CRANFIELD UNIVERSITY

Nicolau Iralal Morar

Investigating dependencies between laser drilling process parameters, recast layer thickness and corrosion-fatigue life for turbine vane cooling film holes

School of Aerospace, Transport and Manufacturing

Doctor of Philosophy (PhD)
Academic Year: 2011 - 2017

Supervisors: Professor Rajkumar Roy & Dr Jörn Mehnen
July 2017

CRANFIELD UNIVERSITY

School of Aerospace, Transport and Manufacturing

Doctor of Philosophy (PhD)

Academic Year 2011 - 2017

Nicolau Iralal Morar

Investigating dependencies between laser drilling process parameters, recast layer thickness and corrosion-fatigue life for turbine vane cooling film holes

Supervisors: Professor Rajkumar Roy & Dr Jörn Mehnen

July 2017

This thesis is submitted in partial fulfilment of the requirements for the degree of Doctor of Philosophy (PhD)

ABSTRACT

Manufacturers of aeroengines are currently being confronted with service related degradation process such as fatigue, thermal fatigue, creep, hot corrosion, wear, corrosion-fatigue and fretting. These degradation modes are causing engine operational disruption, unscheduled maintenance burden, and costly components replacement. Degradation of components and systems is a continuous process that results in loss of function and performance when exposed to fluctuating loads and an adverse operating environment. Understanding of factors and drivers influencing premature degradation and early damage on critical aeroengine mechanical components is needed.

As such, the purpose of the present research was to develop an understanding of the impact of manufacturing process and parameters used on the corrosion-fatigue life of an aeroengine turbine vane based on the past degradation information. Based on the service experience data, turbine vane cooling film holes shown to be life limiting feature, which are exposed to high cyclic stresses and temperatures in harsh environment. Therefore, understanding of fatigue life degradation of turbine vane cooling holes and impact of drilling method and environment provides an insight and knowledge for the changes in effusion cooling holes design and/or optimisation of drilling parameters.

The research has been able to establish the effects of key laser drilling process parameters, such as the influence of peak power, pulse frequency and trepan speed on the recast layer thickness and surface cracks formation in a Ni-base CMSX-4 superalloy angled cooling holes. The results indicate that trepan speed and peak power had significant influence on the thickness of the recast layer and cracks formation around the sidewalls of cooling holes, both statistically and physically. The metallography examinations show that the recast layer has an altered morphology. Furthermore, elemental analysis and nano indentations measurements on the recast layer show that there is change in alloy chemistry and mechanical properties, respectively. Therefore, less resistant to fatigue crack initiation and corrosion than base alloy.

The high temperature corrosion-fatigue of critical components and features such as laser drilled cooling holes has received very little attention. The occurrence of high temperature corrosion is associated with an accelerated oxidation and sulphidation assisted cracking, driven by salt and sulphur concentration. In high temperature

corrosion, formation of thick oxide scale and micro pits in the recast and alloy surface leads to potential early onset of fatigue crack initiation and accelerated crack advance on the pre-existing cracks. Therefore, impacting the life performance of laser drilled components. As such, research into interaction between laser drilling, recast layer thicknesses and high temperature corrosion-fatigue life has been undertaken. The representative laser drilled cooling holes specimens were tested in laboratory with different range of recast layer thickness and representative of service conditions. The corrosion-fatigue in CMSX-4 bare specimens found to give life debit between 20 to 25% from the air fatigue data. Corrosion-fatigue tests result show that laser drilled fatigue specimens provide a fatigue life debit between 30 to 40% from un-drilled specimens tested under similar conditions. The recast layer thickness had significant influence of the corrosion-fatigue strength degradation of cooling holes, particularly in crack nucleation. The role of environment was also significantly in both crack nucleation and short crack growth.

The research work developed in this thesis contributes to the understanding of the role of laser drilling process parameters and recast layer thickness interaction and their effects on the corrosion-fatigue life and surface crack initiation in cooling holes, and how empirical methods can be used to extend the lives of turbine vane cooling film holes.

Keywords: Degradation analysis, corrosion-fatigue, turbine vanes, CMSX-4, laser trepan drilling, cooling film holes, recast layer, and surface cracks.

ACKNOWLEDGEMENTS

First, to all, I would like to express my sincere gratitude to my principal supervisor, Professor Rajkumar Roy for the opportunity given to me for pursuing the doctoral degree, and his invaluable support and continuous guidance throughout the research. Next, acknowledge EPSRC and Rolls-Royce for the financial support during my research.

I would also like to thank Dr Jörn Mehnen, my second supervisor and Professor John Nicholls (subject advisor) for their active guidance and valuable suggestions during the research and journal papers writing.

I am particularly grateful to Mr Andrew Harrison (Rolls-Royce), my industrial sponsor, for his valuable comments, sharing his knowledge in service engineering and providing the data for the analysis. Rolls-Royce Materials team for providing the material and technical resources for completing the research work.

I am also thankful to all staff members at the EPSRC TES Centre, especially Mr Andrew Shaw (Centre's Manager) and Mrs Teresa Bandee (TES Business Support Administrator) for their continuous assistance during this journey.

I am also grateful to Dr Sundar Marimuthu (Research Engineer, MTC), Dr Simon Gray (Research Fellow, Cranfield), Dr Tracey Roberts (Analytical Officer, Cranfield) for the technical support. Without their assistance, I would not able to conduct the experimental work required in completing the thesis.

I would like to express my sincere gratitude to my parents, Iralal Dulobo and Calavanti Bai Maugi and my wife Vandana Nicolau for their patience and endless support.

Finally, my lovely children's Hiral Morar, Chirag Morar, and Jai Morar for being my strongest motivation for completing this thesis.

TABLE OF CONTENTS

LIST OF PUBLICATIONS

1. Redding, L.E., **Morar, N.**, Tiwari, A. (2012). Challenges and Opportunities in Through-life Engineering Services. Proceedings of the 10th International Conference on Manufacturing Research (ICMR), 1, 397-412.

2. **Morar, N.**, Roy, R., Mehnen, J., Redding, L. E., & Harrison, A. (2013). Data Mining and Knowledge Reuse for the Initial Systems Design and Manufacturing: Aero-engine Service Risk Drivers. *Procedia CIRP*, *11*, 130-134.

3. Tapoglou, N., Mehnen, J., Butans, J., & **Morar, N.** (2016). Online on-board Optimization of Cutting Parameter for Energy Efficient CNC Milling. *Procedia CIRP*, *40*, 384-389.

4. **Morar, N.**, Roy, R., Mehnen, J., Nicholls, J. R. and Gray, S. (2017). The effect of trepanning speed of laser drilled acute angled cooling holes on the high temperature low cycle corrosion fatigue performance of CMSX-4 at 850 °C. *International Journal of Fatigue*, 102, pp. 112–120.

5. **Morar, N.I.,** Roy, R., Mehnen, J., Marithumu, S., Gray, S., Roberts, T. and Nicholls, J., (2018). Investigation of recast and crack formation in laser trepanning drilling of CMSX-4 angled holes. *The International Journal of Advanced Manufacturing Technology*, 95 (9), 4059-4070.

6. **Morar, N.**, Roy, R., Gray, S., Nicholls, J. R. and Mehnen, J. (2018). Stress-life fatigue prediction model considering surface flaw size effects. *International Journal of Fatigue*. IJFATIGUE-D-18-00101.

LIST OF FIGURES

LIST OF TABLES

LIST OF ABBREVIATIONS

ANOVA	Analysis of Variance
ERMS	Engine Record Management System
CDN	Crack Number Density
CNC	Computer Numerical Control
DoE	Design of Experiments
DF	Degree of Freedom
EDM	Electrical Discharge Machining
EDS	Energy-Dispersive X-ray Spectroscopy
EGT	Exhaust Gas Temperature
E-N	Strain-Life
EPSRC	Engineering Physical Science Research Council
FE	Finite Element
FOD	Foreign Object Damage
HCF	High Cycle Fatigue
HT	High Temperature
HPT	High Pressure Turbine
IT	Information Technology
LD	Laser Drilling
LTD	Laser Trepanning Drilling
LCF	Low Cycle Fatigue
LCCF	Low Cycle Fatigue Corrosion Fatigue
MRO	Maintenance, Repair & Overhaul
NaCl	Sodium Chloride
Nd:YAG	Neodymium-Doped Yttrium Aluminium Garnet
NGV	Nozzle Guide Vane
OEM	Original Equipment Manufacturer
PF	Pulse Frequency
PP	Peak Power
PPE	Percentage of Prediction Error
R	Stress Ratio
RCI	Resolved Customer Issue

RLT	Recast Layer Thickness
R-R	Rolls-Royce Plc
S	Stress
SE	Standard Error
SD	Surface Damage
SDM	Service Data Management
SEM	Scanning Electron Microscope
S/N	Signal-to-Noise
S-N	Stress (S)-Cycles to Failure (N)
SS	Sum of Squares
SCMM	Standard Cubic Centimetres per Minute
SO_2	Sulphur Oxide
RMSE	Root Mean Square Root
TBC	Thermal Barrier Coating
TEM	Transmission Electron Microscopy
TMF	Thermo-mechanical Fatigue
TS	Trepanning Speed
VPM	Volume per minute

1 INTRODUCTION

This chapter introduces to research background and industrial context. It includes the importance of through-life engineering services in high-value aerospace mechanical components and underlying degradation mechanisms. In addition, the present chapter presents and discusses findings of aeroengines past service experience data mining conducted with industrial partners to define and postulate scope of the research. The chapter finishes with outlining the research aim, objectives and describes the structure of the present thesis.

1.1 Background

The present doctoral research is sponsored by the EPSRC Centre for Innovative Manufacturing in Through-Life Engineering Services (TES) at Cranfield University and Rolls-Royce Plc[1] as an industrial partner. TES Centre focuses in developing engineering solutions and technologies to support UK manufacturers of high-value engineering products (TES, 2012). TES are *"Those technical services that are necessary to guarantee the required and predictable performance of a complex engineering system throughout its expected life with optimum whole-life cost"* (Roy *et al.*, 2013).

TES activities in aerospace sector are becoming crucial because of the increase in popularity of the availability-based contracts for high-value products and systems (such as aircraft engines). It addresses the needs of such high-value systems through its entire life cycle, from conceptual design all the way to end of life. TES through technologies and processes advances the industry capability to deliver high-value products and systems having improved design, availability, predictability and reliability with lowest life cycle cost.

The present research is a flagship to the EPSRC TES Project 3 *"Characterisation of in-service component feedback for system design and manufacturing"* (TES, 2011). The project 3 research covers some of the challenges in through-life engineering services. It

[1] Rolls-Royce (R-R) is a global company providing highly efficient integrated power and propulsion solutions for use in land, sea and in the air. It is one of the world's leading producers of aero engines for large civil aircraft and corporate jets (Rolls-Royce, 2016).

includes the development of a technology demonstrator to semi-automatically capture different types of component degradation data from two different advanced inspection techniques; development of algorithms for prediction of remaining useful life based on past service experience; and to investigate the relationships between in-service component degradation and the manufacturing processes used based on past service data. Latter is the focus of the present research work. The outcomes from this project will be fed in the conceptual design of aeroengine components and are expected to have an impact on reducing the maintenance costs and improving the service performance by providing the needed information to optimise design and process parameters options to improve the integrity of critical mechanical components.

Knowing the component and their critical design features failure mechanisms based on previous service experience and then associate them with respective manufacturing process becomes important to minimise the rate of deterioration[2] process due to manufacturing.

1.2 Research context

At present, increasing competition from both emerging industrial economies and global market manufactures of high-value, products are now looking to build their revenues streams through services. Over half of the revenue in the aerospace sector is coming from TES related activities such as engineering support and services (Roy *et al.*, 2013; Redding *et al.*, 2015). In TES context, "*the customer pays for a service or functionality rather than an asset, and does not think of products and service as separate*" (Tasker, 2016). For companies like Rolls-Royce, who offers service contracts "*power by the hour*" (Smith, 2013), maximising the services cost through the expected operational life of the engine while minimising the maintenance, repair and services cost becomes the main challenge.

Over the past years, aircraft engine manufacturers are confronted with an increase of service costs associated with unexpected engine removals, caused by engine gas temperature (EGT) margin deterioration, life limited parts (LLP) replacement and component mechanical degradation (Meher-homji, Chaker and Motiwala, 2001). Latter

[2] Deterioration can be defined as a gradual decline, as in quality, serviceability, or vigor.

being the focus of the present research work. The component degradation typically arises from parts after being exposed to adverse operating conditions for a lengthy period, and/or in the presence of design errors or manufacturing defects. This could lead to component distress and crack in extreme conditions, component failure. Other causes of engine removal include high engine vibration, excessive engine oil consumption and foreign object damage (Eady, 2000).

Fatigue, corrosion, wear, erosion and fretting are main contributors of aeroengine component degradation (Bagnall, Shaw and Mason-Flucke, 2000; Carter, 2005). These degradation mechanisms are causing engine operational disruption, unscheduled maintenance burden and costly components repair or replacement (Fernandes *et al.*, 2011). The chart in Figure 1-1 shows typical expenditure breakdown in percentage for aeroengine components maintenance, repair and overhaul (MRO) per operator. It shows that the aerofoils related components such as blades and vanes either from the compressor or from turbine hot section have significant large proportion of the total maintenance burden. Moreover, it has been reported that high cycle fatigue (HCF) is the largest cause of aeroengine component failures and have significant economic impact on the maintenance operations, after a review (Cowles, 1996).

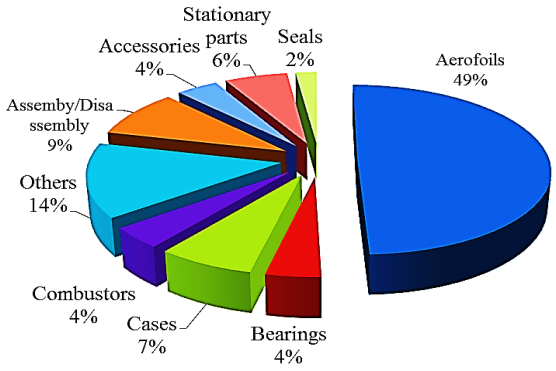

Source: Adopted from TTL Newsletter, Issue 1, 2010

Figure 1-1. Typical aeroengine repair and overhaul component expenditure breakdown.

Another study, reviewed the distribution of failure mechanisms in aeroengines components of a Dutch airliner. Fatigue, both thermal and mechanical was the most prominent damage mechanism by 47 % of total 61 cases reviewed (see Figure 1-2). Fatigue related thermal and mechanical degradation is the most significant problem and thus affecting the service life cycle of aeroengines.

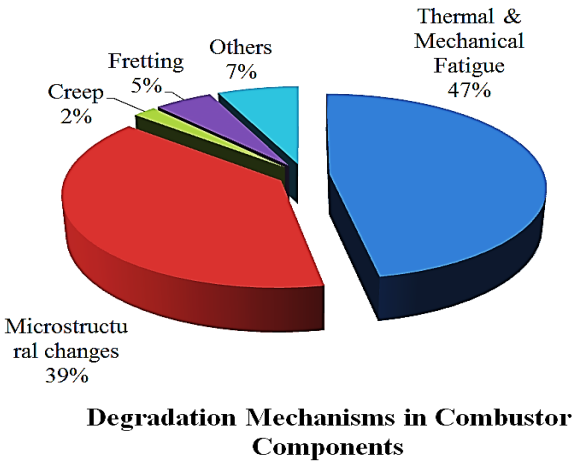

Figure 1-2. Aeroengines damage mechanisms, adopted from (Kool *et al.*, 2008).

In engineering, degradation is defined as: *"a loss of the relevant properties of materials which proceeds gradually due to exposure to in-service conditions"* (Kurzydłowski *et al.*, 2007). Degradation also refers *"to the process of deterioration of characteristics of an object with time, gradual decline in quality and/or breakdown of matter due to the impact of external forces in conformity with the laws of nature and time"* (Roy *et al.*, 2013). The word degradation is derived from Latin "degradatio", meaning reduction; other meaning is process of degrading or being degraded. After a thoroughly literature search, the author defined the degradation in components and systems as *"a continuous process of deterioration that results in loss of intended function and desired performance, when exposed to in-service fluctuating loads and operating environment."*

The degradation in components and systems could lead to a failure state. In this case, the component or system can be considered to have failed if the performance declines to below the critical level, as it will no longer be able to perform the intended function. In aeroengines, physical hardware damage results in degraded component performance such as a change in efficiencies producing an increase in speed, temperatures, pressures, fuel consumption and power output. Moreover, the advance state of degradation above the critical level in components or systems could lead to catastrophic failure if improved inspection techniques and skills are not in place.

Relevant examples from the aerospace industry have been taken to demonstrate the examples of catastrophic failure. The United Flight 232 crash at Sioux City on 1989 took more one hundred lives. The accident was caused by fatigue fracture that started on the

fan disk and subsequently released from an engine into the fuselage. The root cause was attributed to metallurgical defect located in a critical area of the fan disk, induced during the manufacture, and subsequently inappropriate inspection at overhaul and manufacturing stages (NTSB, 1989). Another example is the accident in Florida, United States, Delta Airlines Flight 1288 (NTSB, 1996). The root cause was attributed to metallurgical defect located in a critical area of the fan disk, induced during the manufacture and subsequently inappropriate inspection at overhaul and manufacturing stages.

Moreover, it should mention that the aging of aeroengine and their components is an irreversible process and gradually reduce their performance, reliability and safety over the time. However, the rate of degradation can be influenced by intrinsic factors, external factors or a combination of both (Eady, 2000). The intrinsic factors are unavoidable and outside the control of the engine manufacturers. These factors include engine operational cycles and service operating environment. Whilst, the external factors include materials and manufacturing anomalies, assembly and maintenance errors, engine usage, and design flaws. These external factors are more in the control of the engine manufacturers, airline operators, and repair and overhaul service providers, but these factors cannot be avoided completely. This suggests that the manufacturing and design related degradation information could provide the opportunities for design changes for improving component reliability and availability. Geometry change, material changes, part deletion and manufacturing improvement are some of the design changes proposed by an aeroengine OEM (Jagtap and Johnson, 2011), based on degradation mechanisms.

Understanding components failure modes while in production and in-service have received increasing interest from the aerospace OEM's in the recent years. There are a number of studies available in the literature proposing the use of service data feedback to initial design functions (Jagtap and Johnson, 2010; McFarlane and Cuthbert, 2012; Sanya and Shehab, 2014; Masood *et al.*, 2015), and in developing Life Cycle Cost (LCC) models based on degradation information (Fernandes *et al.*, 2011; Zhao *et al.*, 2011). The collected data enables the designers and reliability engineers to use the experience information for the decision-making process of a new design or manufacturing process generation; and assess better the risks, safety and through-life costs associated with critical engine components and systems. In most of the high-value and safety-critical

aeroengine components, the understanding of degradation mechanisms and the consequences and risk of induced anomalies at manufacturing level is required (see Figure 1-3). This understanding enables to make effective decisions related to design changes and/or manufacturing process improvements that can make components more predictable. Therefore, a systematic and structured methodology is required for assessing the service and manufacturing process related degradation process of mechanical components based on past service historical data, ensuring the optimal levels of performance during its service operation and maintenance level.

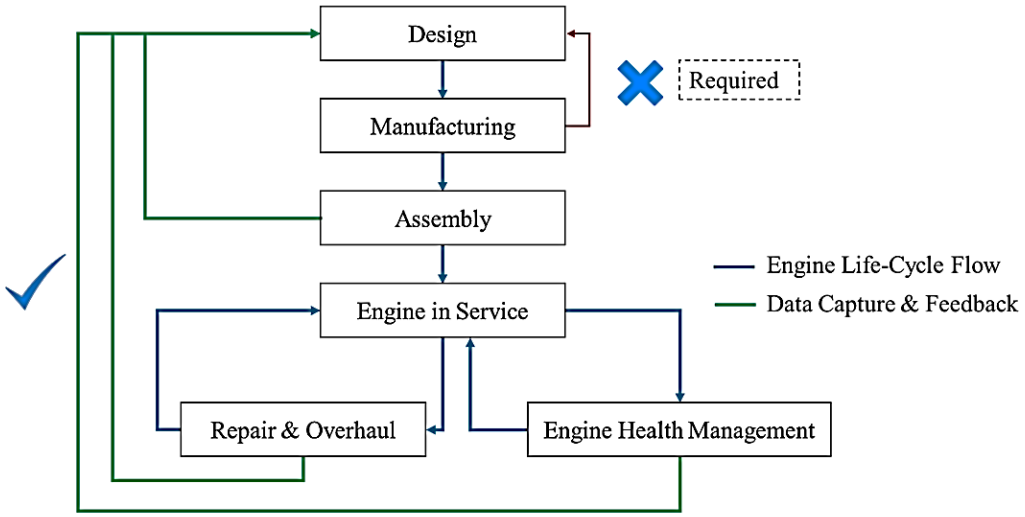

Figure 1-3: Process for effective systems/components design based on service degradation knowledge.

1.3 Research Aim

Based on the research context and industrial requirements, the aim of the research is to ***develop an understanding of the influences of the manufacturing process and parameters used on the fatigue life degradation of a critical aeroengine mechanical component based on past degradation information*** using experimental and analytical techniques to support the design and manufacturing functions.

To accomplish the research aim, the following research questions are formulated:

1. Is it possible to analyse service experience log data and past degradation information to improve critical component life cycle?

2. How current manufacturing methods and process parameters used influences fatigue strength degradation in critical component features?
3. Is it possible to develop prediction model to correlate processing parameters, surface damage and fatigue life of critical component feature?

1.4 Industrial context

This section presents findings of service experience data mining study conducted within the collaborative industry to identify most critical aeroengine mechanical components and associated critical features affected by degradation mechanisms that have a direct impact on through-life performance and engine service availability. This industrial case study attempts to define the path of the research and answer the first research question.

As such, the case study aimed to data capture and analyse past service experience to establish relationships between degradation mechanisms, critical components, critical design features and associated causal drivers. For the data capture a semantic data mining toolkit[3] developed by Roll-Royce was applied to extract terms and concepts related to the service events and degradation mechanisms. The technique was used as a method for a fast and consistent data capture. Details of the steps carried out for the data capture are described and discussed in (Morar *et al.*, 2013)

The service experience event records captured were part of a group of logging data, the first line of customer services in the collaborating company. These event records are known as RCI (Resolve Customer Issues), ERMS (Engine Record Management System) and SDM (Service Data Manager). The event records are logged from different areas of the business divisions, such as from on-wing support, repair workshops, customer services, engine development program, and online engine health monitoring support services. The reason for selection of the data sources above mentioned is due to type of records that contain mentions of entities such as occurrences of engine component issues, underlying component damage or failure information (Okho, C. Roy, R., Mehnen, J. and

[3] 'Entity Recognition' Patent Application in: http://patents.justia.com/patent/20110320186 (Accessed on 21/10/2016

Harrison, 2014). This information collected is based on civil aeroengines partly from a period of five years of service experience.

A total of 23,743 log events were analysed considering the degradation mechanisms and underlying information. Figure 1-4 show distribution of events captured from each service experience database. In general, the analysis highlighted the aeroengines operational problems and a considerable number of degradation mechanisms were found on log data. A total of 112 degradation terms are available in the literature and ontology R-R database, but only 24% had major impact. These events have been breakdown into degradation mechanisms and related components, design features and operational and business impact.

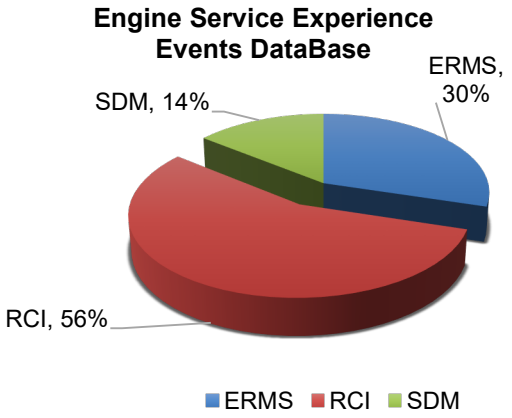

Figure 1-4. Breakdown of service experience records used in data analysis.

In the first analysis, Pareto charts have been put forward and reviewed for top 10: degradation mechanisms, components most affected by degradation, life limiting component design features and effects of degradation in terms operational disruption and business. Figure 1-5 show the cumulative distribution of the degradation mechanisms for all the event cases reviewed. Regarding magnitude, crack term received the highest rate of hits. Nevertheless, others are known degradation mechanisms such as wear, blade release, corrosion, dents and fatigue are most critical symptoms of failure. Remaining 102 mechanisms had a very low count regarding frequency but highlight the range of mechanisms susceptible to cause operational engine disruptions. Moreover, the term '*others*' stated in the events logs were broad in the sense that could cause a damage or crack. It not well defined in event logs review the exact type of degradation mechanism. In addition, seize, shuddering and fretting terms used could also indicate the component

is complete degraded or is beyond the allowable damage limits and it needs removal. There is a level of uncertainty related to these terms utilised in the service field when logging such critical events.

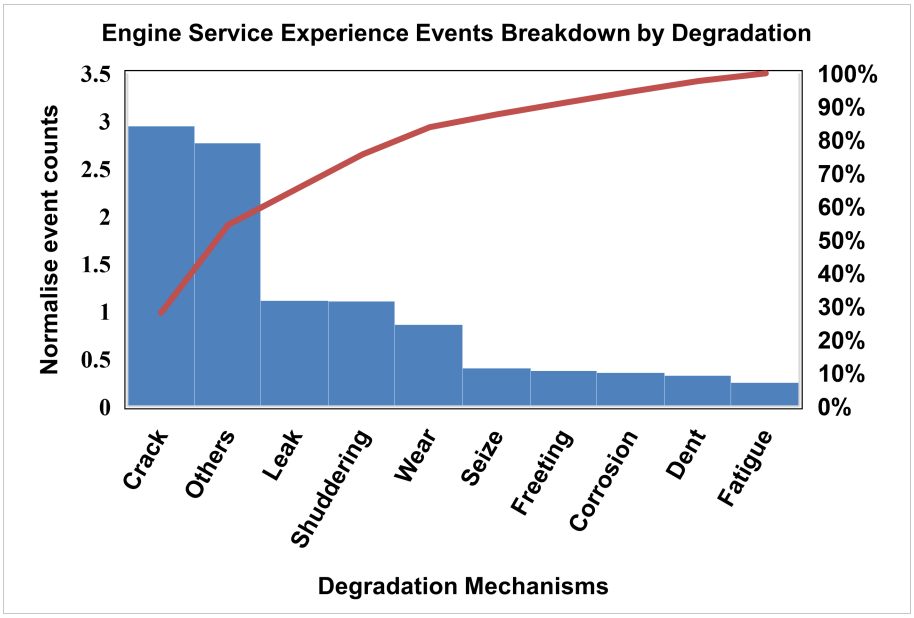

Figure 1-5. Pareto of top 10 degradation mechanisms.

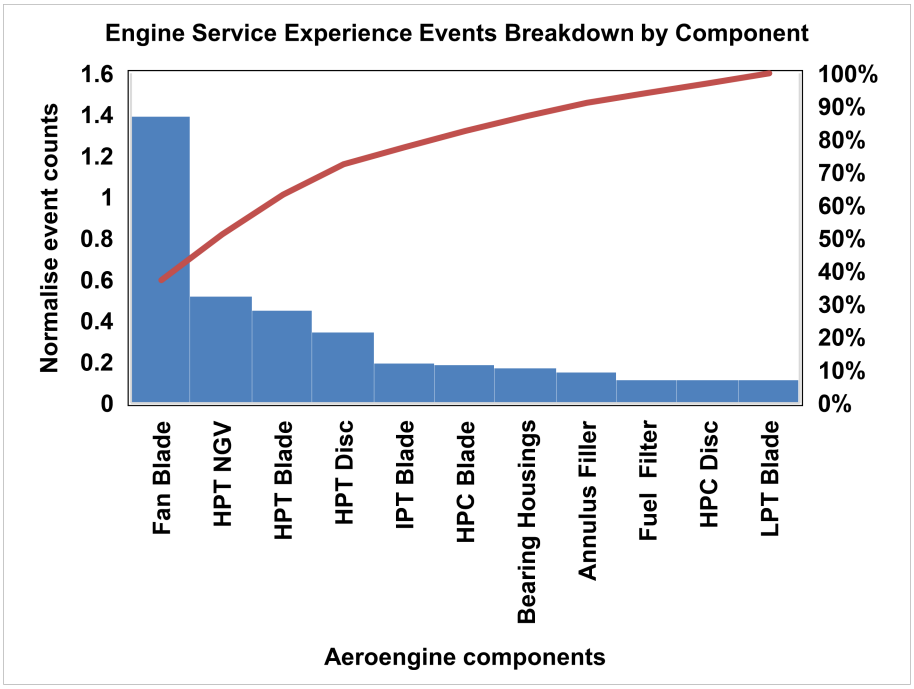

Figure 1-6. Pareto of top 10 aeroengine components affected by degradation.

Figure 1-6 shows the breakdown of components under the events logged. It indicates that top 5 aeroengine components affected by degradation problems are blade related components. These findings are similar to reported in TTL newsletter 2009 and (Cowles,

1996). This Pareto shows that more than 80 % of all cases concern the front engine fan blades are the most affected by the degradation regarding the magnitude of events reported. Besides fan blades, the following are 'usual suspects' such as hot section turbine components including HPT vanes, HPT blades, HPT discs and IPT blades. These findings are very revealing since fan blades are susceptible to damage from bird strikes and solid particles. While, hot section components suffer from hot gases contaminants, erosion, hot corrosion and thermo-mechanical fatigue, thus, more likely to deteriorate at a rate that is not predictable.

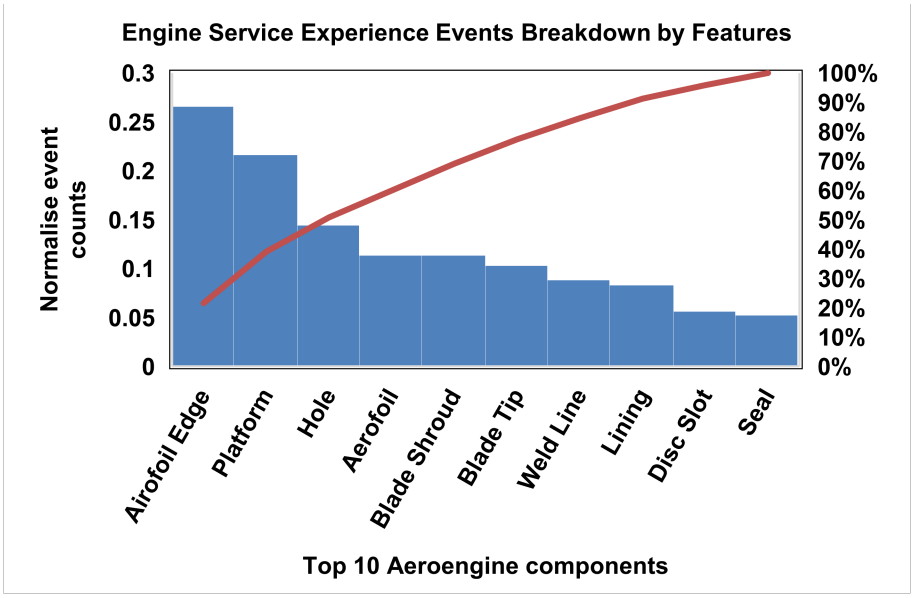

Figure 1-7. Pareto of top 10 critical design features.

Figure 1-7 show Pareto of underlying features of components that are limiting the life in service. The term feature used in this thesis describes the key locations in components defined by design engineers. For example, airfoil edges, platforms, shroud and cooling holes are key locations in a turbine blades and vanes. It can be seen from Figure 1.7 that the edges of the blade, platform and holes are the most critical design features influencing premature damage. Others including airfoil surfaces, shrouds and blade tips are also influencing component deterioration and engine performance. These findings suggest these features are susceptible to promote loss in turbine efficiency, increase the rate of deterioration in components and maintenance burden. Therefore, there is an essential need for understanding and identifying contributing factors that limit the lifetime of such critical features, particularly in the initial design stages.

The second part of the analysis involved combination of critical components to degradation mechanisms relationship. It can be seen from Figure 1-8 that crack is most common degradation mechanism followed by fatigue in all five components. This information indicates that the all blades and vanes from hot-section part of the engine experienced thermal cracking and thermal fatigue (Eady, 2000), except for fan blades which are from cold section of the engine. Latter, fan blades are more susceptible to impact damage causing score, dents and mechanical fatigue (Carter, 2005). Moreover, when considering combination of degradation mechanisms to feature relationship under hot-section turbine components, it can be seen from Figure 1-9 that blade and vane features like airfoil surfaces, platform and holes suffer from cracks, wear and dents. These findings confirm the previous studies conducted on aeroengine components (Kool *et al.*, 2008). Further, it should mention that more than 209 design features were found in logged events to have links with degradation mechanisms, and some of these critical features are inevitable by design. Moreover, the event records analysed did not contain the root-cause analysis information, only provided information related to component symptoms and effects. The root cause failure and analysis information is further explored in the open literature and available industrial reports.

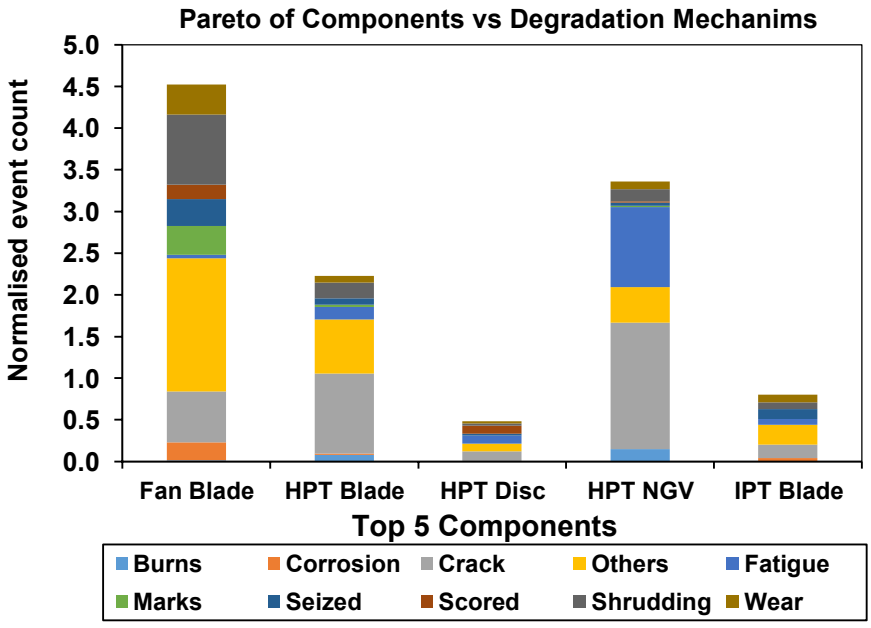

Figure 1-8. Distribution of Top 5 component to degradation relationship.

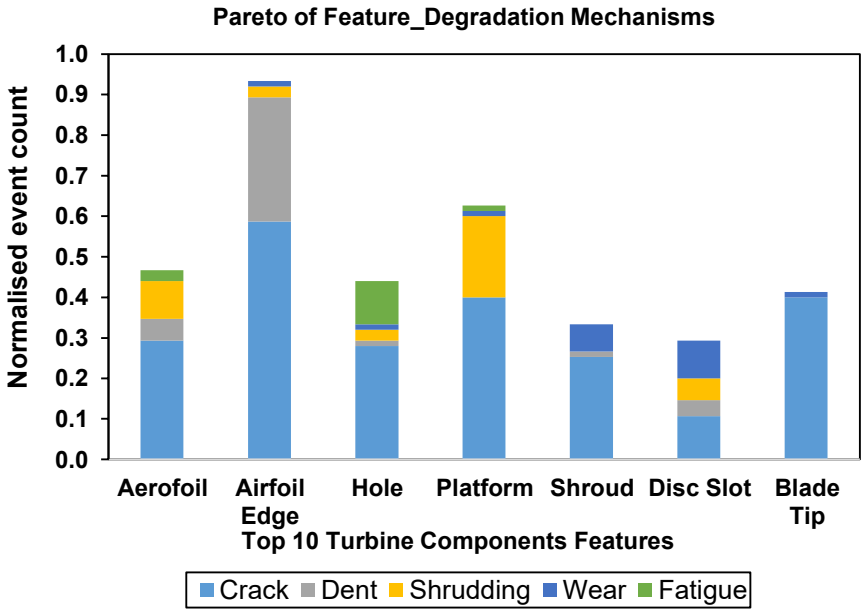

Figure 1-9. Distribution of turbine features to degradation relationship under turbine components.

The following remarks can be drawn based on the past service experience:

1. The findings show a considerable number of different types of degradation mechanisms and life limiting critical design features associated with early component damage. The most common degradation mechanisms were crack, dents, fatigue and wear based on the service experience data.
2. Most the events recorded under degradation information had edge sections of the blade, platform and holes as the top most critical and life limiting design features.
3. The most critical components affected by degradation are airfoil related components, such as fan blade, high pressure turbine vanes and blades, not ignoring the safety critical HPT disc.
4. The study also confirms that there is a lack of structured service degradation and underlying contributing factors and causal information re-used to initial stages of the design.

1.4.1 Remarks

Based on the service experience information and Pareto analysis the research focused on HPT NGV instead of Fan Blade as a component of interest, since latter has been focus of research by Oxford and Swansea University, R-R UTC. The choice of HPT NGVs and

cooling film as feature of interest were based on the industrial requirements and driven by past service experience information. HPT NGVs are exposed to high cyclic stresses and high temperatures in a very adverse environment. As such, cooling film holes are highly stressed and susceptible to early cracking under such conditions.

Past studies have reported early cracking of cooling holes and linked to metallurgical residues produced by manufacturing (Neidel *et al.*, 2005) and service induced damaged by blockage and leading to thermal cracking and burns(Walsh, Thole and Joe, 2006). Moreover, based on the service log data, significant cracking at short lives has been reported on HPT NGV cooling holes both at leading and trailing edges location. Metallurgical and fractography analysis reports that cracks nucleated from surface drilled holes and occasionally from the substrate/coating interfaces around the hole perimeter. In addition, in some cases it has shown some traces of corrosive traces, such as sodium sulphate, sulphate oxides and oxidised layers suggesting occurrence of oxidation and sulphidation assisted cracking.

Therefore, this research focus in establishing relationship between laser drilling parameters, metallurgical residues and corrosion-fatigue life for turbine vane cooling holes.

1.5 Research objectives

Based on the research focus defined in previous section and area of research, following objectives are drawn to achieve the research aim:

1. Characterise metallurgical alterations observed in cooling holes produced by laser drilling, and quantify such residues using existing analytical methods. This enables better understanding of the nature of metallurgical residues produced by laser drilling operations in terms of microstructure, alloy chemistry and properties to the base alloy.

2. Determine how the current key parameters of pulsed Nd:YAG laser drilling influence the metallurgical residues, such as recast layer and surface crack formation.

3. Investigate the effects of different recast layer thickness on high temperature fatigue life of laser drilled cooling holes. The lifing data generated allows to understand the potential impact of such layers on performance of turbine vane cooling holes.

4. Perform metallography of fractured surfaces to better understand degradation behaviour around cooling holes perimeter, and investigate the influence of recast layer and environment on the crack nucleation and crack growth.

5. Develop a general lifing empirical model considering metallurgical damage produced by a drilling method. The model enables to provide lifing data and knowledge for the optimisation of cooling holes design and manufacturing process parameters.

1.6 Organisation of the thesis

The thesis consists of nine chapters and four appendices. Figure 1-10 outlines the flow chart on the research work to achieve the thesis aim. Chapter 1 introduces the research background and through-life engineering service context. The research aim is defined and research questions are postulated. The chapter discusses findings of aeroengines past service experience data capture to define the research scope. Furthermore, outlines the research objectives and thesis structure.

Chapter 2 provides initially an overview of degradation mechanisms and cause of failures in aeroengine components, fatigue life assessment methods, corrosion-fatigue and laser drilling methods for aerospace components. Secondly, the state-of-the-art in literature review on the following subjects: laser drilling in nickel-based superalloys, fatigue life of cooling holes and fatigue life in CMSX-4 superalloys. The chapter ends with outlining the knowledge gaps.

Chapter 3 describes the research methodology, detailing the experiments, testing, modelling and sequence of sample preparations. It includes, the analytical methods used in the research, such as SEM, TEM, EDS and EBDS. In addition, details of material, specimen's layout, design of experiments, statistical modelling, finite element analysis, testing conditions and test matrix are described in this chapter.

Chapter 4 characterises the surface morphology of laser drilled surfaces using analytical microscopy techniques. The microstructure and crystallographic structure of the recast

layer are examined. In addition, elemental analysis and nano indentations tests on the recast layer to the base alloy are discussed.

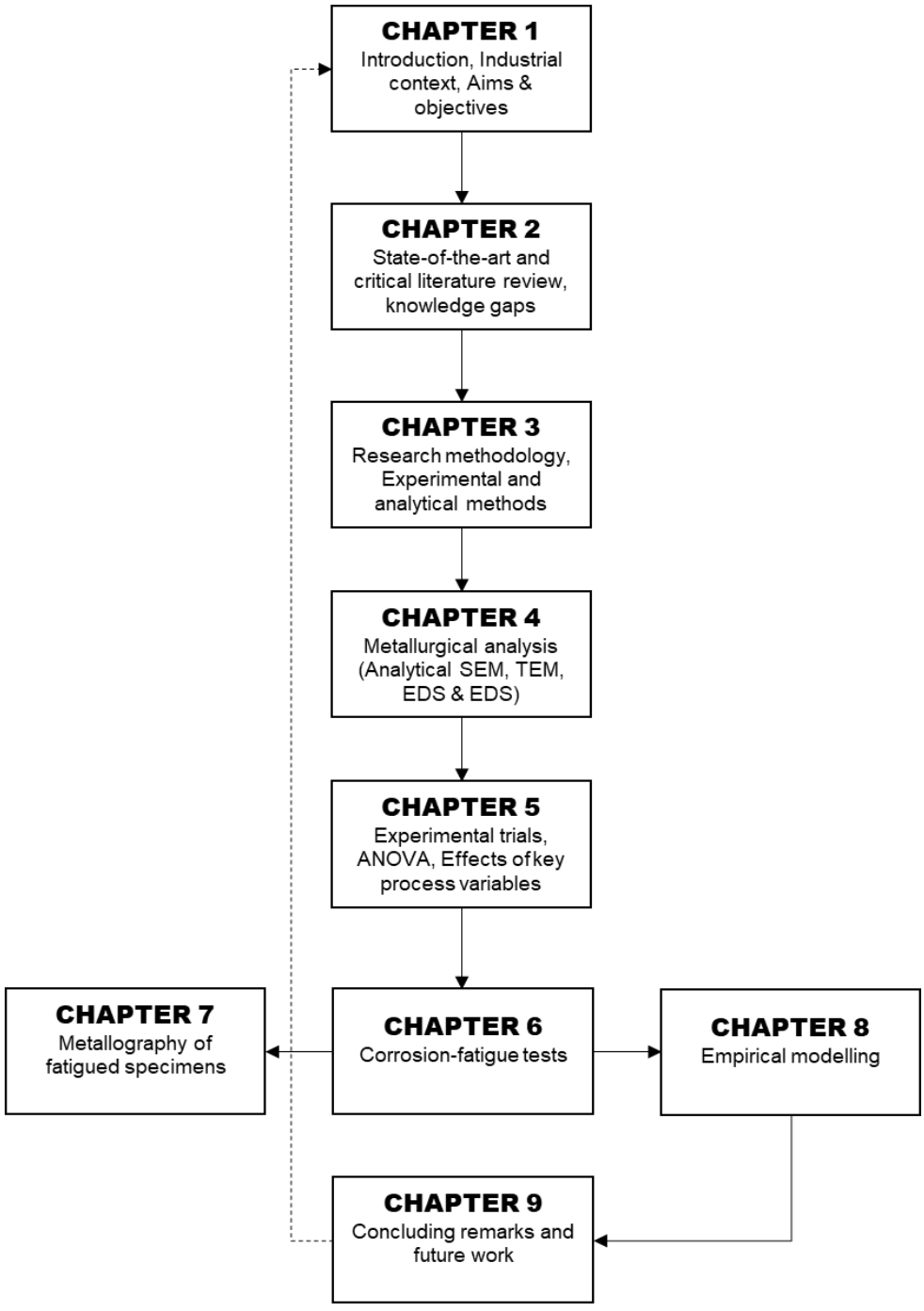

Figure 1-10. Organisation of the thesis.

Chapter 5 discusses the effects of laser trepanning drilling process parameters on the recast layer thickness and surface crack formation in CMSX-4 superalloy angled cooling holes. The process parameters are characterised using Taguchi method and statistical

analysis of variance to determine the significance of key process parameters tested. In addition, the chapter discusses the effects of each parameter on the recast layer thickness and surface cracks formed during the laser drilling.

Chapter 6 evaluates the influence of different recast layer thickness and their effects on corrosion-fatigue performance at different laser trepan drilling conditions. The chapter discusses the tests results and analyse the effect of trepan speeds on the fatigue life performance.

Chapter 7 discusses the results of metallography analysis conducted on the fracture facets. Analytical SEM and EDS. The fracture facet surfaces and sites of crack initiation are examined. Further, elements maps are presented to provide evidences of corrosion compounds and environmental influence on the surface degradation, including: protective scale rupture, de-alloying, corrosion compounds around the crack nucleation, crack tip and crack growth in failed specimens.

Chapter 8 proposes an empirical model to predict residual life of a critical machined feature based on the experimental and lifing data generated. The chapter closes with testing and statistical validation of the model.

Chapter 9 discusses the thesis concluding remarks, starting with research limitation and contribution to knowledge. In addition, the future research work is identified and outlined. The appendices A-D are at the end of the thesis, providing the experimental data and images used in the research work.

2 LITERATURE REVIEW

This section provides a summary of the reviewed literature and current state-of-the-art work for the present research. It is structured in five sections. First, a brief description of working principle of aeroengine and its main modules are given, followed by an overview of degradation mechanisms experienced by main aeroengine components. Second, a literature survey of common causes of aeroengine components failure and damage. Third, laser drilling working principles and key process parameters are reviewed. In addition, review of past studies in laser drilling of nickel based superalloys. Fourth, reviews the fatigue life methods used for aeroengine mechanical components assessment, and followed by a current state-of-the-art review of fatigue life in CMSX-4 nickel-based superalloys and fatigue life in cooling holes. Finally, the last section discusses the knowledge gaps and potential contribution to knowledge.

2.1 Degradation mechanisms in aeroengines

This section provides an overview of failure/degradation mechanisms in aeroengines, and outlines the critical engine sections and components that have the most impact on the engine failure, service and maintenance burden.

2.1.1 Aeroengine

Sir Frank Whittle introduced the aeroengine, also known as a jet engine and aircraft gas turbine engine in 1941. There are several different types of aeroengines and their evolution is described in detail, from military to modern civil engines in (Gunston, 2007). The main function of an aeroengine is to provide the necessary thrust and electrical power to the aircraft. The aeroengine consists of two main sections, namely the cold section and the hot section. The former consists of a Fan and Low Pressure Compressor (LPC) Module. The Fan/LPC assembly contains rotary blades, a disk, inlet guide vanes and compressor casing. The fan blades are generally made of titanium or high strength composites, or both depending on the aeroengine model. The LPC module is typically made of titanium.

The hot section of the engine consists of High Pressure Compressor (HPC), the Combustor, High Pressure Turbine (HPT) and Low Pressure Turbine (LPT) Modules.

The HPC contains series of rotor blades and stator vanes assemblies and is generally made of titanium due to resistance to high temperatures up to 650 ºC and light-weight characteristics. The Combustor assembly consists of multiple annular chambers, fuel nozzles, inner and outer casings. The Combustor main function is to create thermal energy through adding fuel to the compressed air. The Combustor main components are typically made of cast nickel-based superalloys and coated in the ceramic material. The HPT and LPT modules consist of rotor blades and nozzle guide vanes assemblies. HPT modules due to the exposure of high temperatures are made of nickel-based superalloys coated with a ceramic thermal barrier (TBC) coating and internal and external cooling channels. Further, it should be mentioned that the Fan, the Compressor and the Turbine along with Accessory Gearbox assembly are driven by different shafts, conventional twin spool or tripe spool engine design/model. These are generally made of carbon-nitride solution steel with anti-corrosion film coating. In Figure 2-1, the Rolls-Royce aeroengine Trent 900 is shown, and the working principle of an aeroengine is as follow:

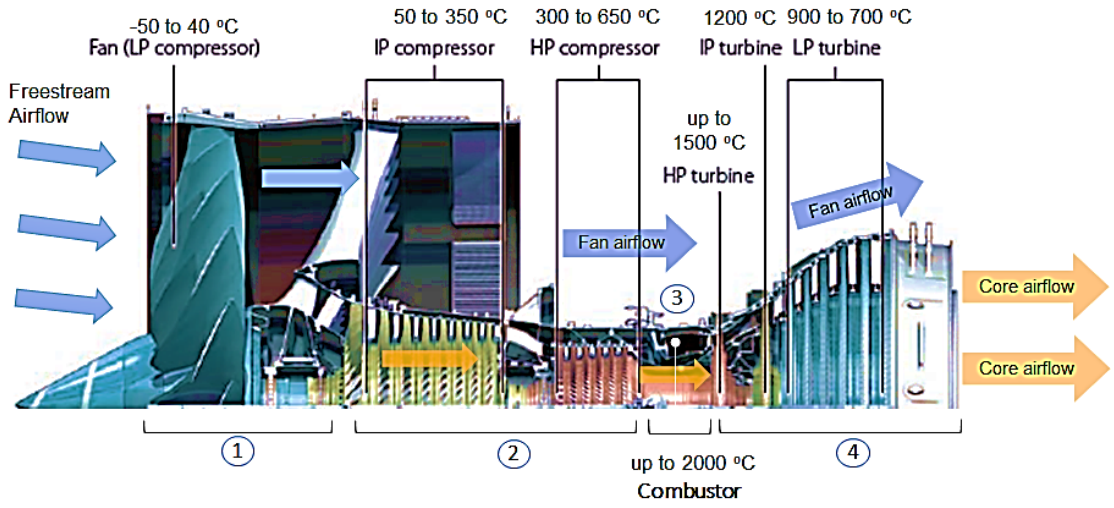

Figure 2-1. Schematic of a cutaway triple-spool aeroengine design model (Rolls-Royce courtesy).

1. Air inlet: The free stream air is extracted by the engine inlet Fan/LPC. One fraction of the airflow bypasses around the core engine providing thrust to engine. The Fan can generate 50%-90% of the total engine thrust depending on the bypass

ratio[4] on the engine model. Other fraction of airflow is downstream to the core engine.

2. Compressor: The downstream airflow is introduced to the IPC and HPC where it is fully compressed, heated up and directed to the combustor chambers through different stages of compressor assemblies.
3. Combustor: Within the combustor chamber, the hot compressed air is mixed with chamber fuel and is ignited, so that the thermal energy generated exits fully expanded and with high force to the Turbine section.
4. Turbine: The HPT, IPT and LPT modules extracts the thermal energy from the combustor hot gases into kinetic energy for driving the fan, compressor and turbine rotor assemblies and along with accessory gearbox through different shafts. Finally, hot gases exit through engine exit nozzle providing also some thrust to the engine.

Moreover, the fan, compressor and turbine rotary assemblies are mounted to different shafts, depending on the engine model. In addition, shafts convert the mechanical energy from the turbines kinetic into electrical energy through a generator for the aircraft. For detailed knowledge, there is a considerable literature available on the fundamentals and design of aircraft jet engines (Rolls-Royce, 2005; Boyce, 2012; Soares, 2015) and performance (Walsh and Fletcher, 2004; Kurz, 2005).

2.1.2 Degradation mechanisms

Aeroengines are considered highly reliable and service failures are low and rare. However, during overhaul, there is a high rate of component rejections as these show evidence and symptoms of initial stages of failure (Carter, 2005). This is due to the rigid inspection regimes used on engines and rigorous criteria applied during component inspections (Harper, 2009). At this stage components are sanctioned from services either by removal or by repairable, preventing service failures. The most predominant rejected components during maintenance are aerofoil-based components, both from the compressor and turbine hot sections, as previously mentioned (see Figure 1-2). The most

[4] Bypass ratio is the ratio of airflow that travels around the core engine over the airflow that travels through the core engine.

common degradation and failure mechanisms experienced by aeroengines have been presented in this section (see Figure 2-2), and described as follows:

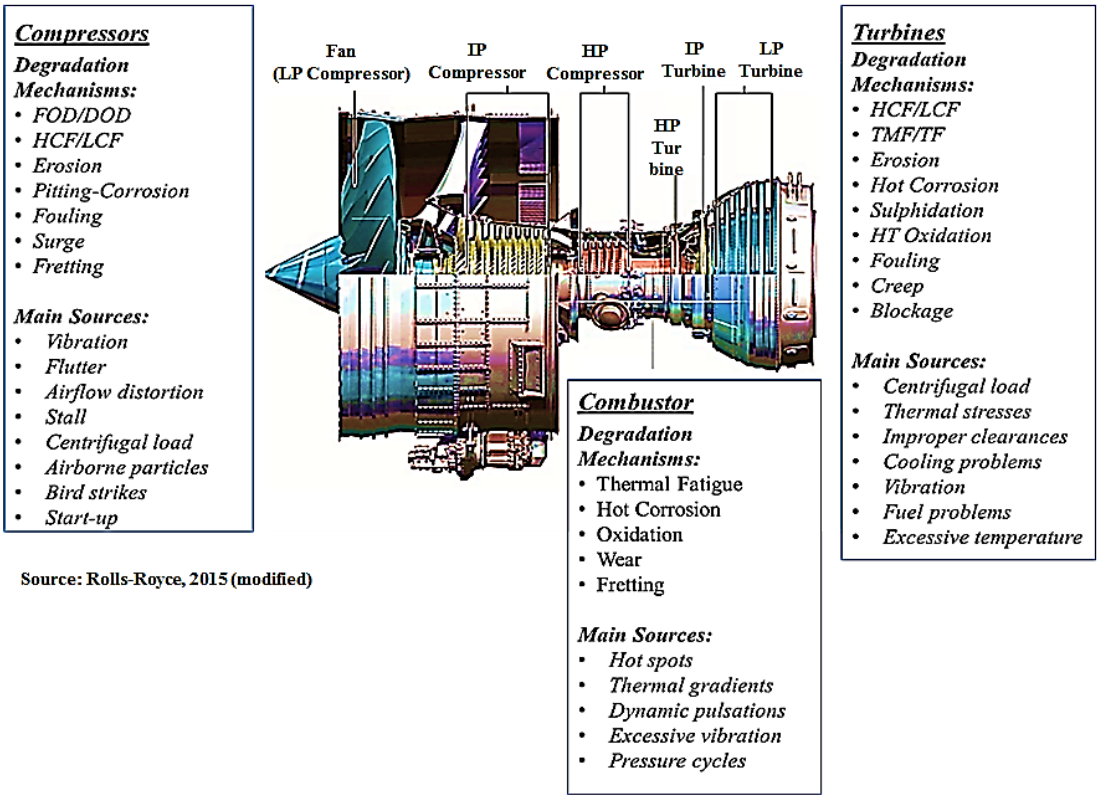

Figure 2-2. Pictorial overview of degradation mechanisms in aeroengine components.

- **Fatigue**[5] **failure** is a general term given to the sudden and catastrophic separation of a machine part into two or more pieces as a result of the application of fluctuating loads or deformations over a period of time (Craig, 2005a). Failure takes place by the initiation and propagation of a crack until it becomes unstable and propagates suddenly to failure. The loads and deformations that typically cause failure by fatigue are far below the static failure levels. The key fatigue drivers are mean stress, operating speed, temperature, corrosion, metallurgical defects and residual stresses (Eady, 2000).

[5] *As defined by ASTM, fatigue is:*
"The process of progressive localized permanent structural changes occurring in a material subjected to conditions that produce fluctuating stresses at some point or points and that may culminate in cracks or complete fracture after a sufficient number of fluctuations."

- **High cycle fatigue (HCF)** results from repetitive loading or fluctuating stresses that can result in the formation of cracks and failure. High cycle fatigue in turbine engines is typically associated with low amplitude vibratory stresses, and aerodynamic excitation or flutter (Meher-Homji and Gabriles, 1998). The deformation will occur in elastic mode once the component has undergone to many cycles greater than 10^7 and the stress levels are above the fatigue strength of the base metal. Further, the temperature gradients, high operating speeds, intrinsic defects, residual stresses, and corrosive environment are among the key drivers that strongly affect the fatigue strength reduction (Eady, 2000). The critical components affected by HCF includes compressor and hot section turbine blades (Carter, 2005).

- **Low cycle fatigue (LCF)** is the most significant and critical degradation mechanism in materials (metallic or non-metallic), when it superimposes the HCF. In LCF, cyclic loads are relatively high, strain cycles are limited to the plastic deformation and low numbers of cycles to failure are exhibited, confined to 10^1 to 10^5 cycles. In aeroengines, the LCF is associated with the engine throttle movements (Rao, Kumar and Prasad, 2014) and potential intrinsic metallurgical defects (Eady, 2000). Moreover, large number of throttle movement results in variation in rotational speed, pressure oscillations, and temperature gradient within the components. This, in turn, could limit the life of component by 10,000 hours or even less (Rao, Kumar and Prasad, 2014). The LCF is predominant in rotating blades and disks from the last stages of compressor and turbine sections, particularly on the bores, cooling holes, and bolt/pin hole locations, where centrifugal and thermal loads are more dominant (Meher-Homji and Gabriles, 1998).

- **Thermal-mechanical fatigue (TMF) and thermal fatigue (TF)** results from high transient or steady state temperature gradients induced in the hot section components (Eady, 2000). This results in intensive differential thermal expansion of the base material. Therefore, the localised high stress-strain levels can cause the formation of cracks and propagate under mechanical loads. If the stress in a component develops without mechanical load, the term thermal fatigue (TF) is then considered. Both, TMF and TF damages are associated with thermal

stresses-strains related to turbine engine start-up and shutdown cycles and rapid throttle movements (Meher-Homji and Gabriles, 1998).

- **Creep** can be defined as a time-dependent deformation of a material under an applied stress at an increasing temperature (Craig, 2005a). Creep damage in aeroengine components results from the long-term exposure to high stress bellow the yield strength of the base material, and at a temperature above 0.4 of the material melting temperature. The deformation is primarily inelastic and rate of deformation always increases with stress and temperature combination rise. This mechanism affects the hot section blade and vane aerofoil mid span region and disk rims of turbine and as well as the final stages of the compressor (Eady, 2000). An example of an excessive creep deformation can be found on aerofoil tip surface eroding the axial working clearances, resulting in creep cracking or rupture. Creep failures are characterised by bulging or blistering in the aerofoil trailing edge of a high pressure nozzle guide vane; intergranular voids, grain-boundary sliding and cracks in the microstructure of the base alloy (Meher-Homji and Gabriles, 1998).
- **Creep-fatigue** is a combination of creep and fatigue damage that can arise from thermal transients, extended operating times, residual stresses, or environmental attack. These factors contribute rise in accelerated creep deformation in combination with the fatigue phenomena (Eady, 2000).
- **Erosion** is the cumulative damage that results from airborne solid particles ingested into the engine, and removes component surface material from the flow path by abrasion. Source of ingested particles vary from small to large solid particles, from the ground as well from the environment such as sand, hail, volcanic ashes, dust and airborne pollutants (Eady, 2000). This results in slight changes in the shape and increase of surface roughness component and will affect in loss of performance and mechanical strength of the component. Erosion is most frequent on the aerofoil pressure side of the compressor and turbine section, as it also reduces the blade tip and leading edge, causing reduction in blade chord width. This has an impact on the blade aerodynamics and pressure losses, leading to blade stall or engine surge (Meher-Homji and Gabriles, 1998).

- **Hot Gas Erosion** occurs in the hot-end section components, such as in first stage nozzle segments, inner platform location. Hot gas erosion results from the hot gases and fuel contaminants in the flow path, which in contact with the blade or vane surface causes erosion damage. This type of degradation is associated with inappropriate cooling or a drop in cooling air film effectiveness (Meher-Homji and Gabriles, 1998).

- **Corrosion** is the deterioration of a metal surface due to chemical reaction with the surrounding environment, typically the metal reacts with oxygen and other corrosive products (Craig, 2006). In aeroengines, corrosion mechanism results from inlet moist air and airborne contaminants, as well as from the aggressive fuel combustion impurities. Corrosion damage can occur in the form of crevice corrosion or pitting corrosion. Crevice corrosion occurs when aggressive contaminants are deposited on the component surface, mostly in the attachment areas acting as abrasives and increasing its clearance. Pitting corrosion is frequently developed from airborne salts and surrounding contaminants, which act as crack causing a reduction in fatigue strength. Both are irreversible degradation process and can lead to a premature LCF failure (Eady, 2000).

- **Sulphidation** is another form of corrosion, predominant in the hot section turbine blades and vanes (Meher-Homji and Gabriles, 1998). This type of corrosion results from the reaction from the surrounding contaminants such as sulphur, sodium chloride, or chlorine with an oxide scale. This causes formation of liquid sodium sulphate droplets (Rao, Kumar and Prasad, 2014). It is the main cause of deterioration in the protective oxide scale/layer and attacking the base alloy, thus, leading to a failure. Sulphidation is critical when is found on the blade root and shroud area, or along the leading edge, causing cooling hole blockage and changing the surface profile and interfering with the heat transfer leading to thermal fatigue (Meher-Homji and Gabriles, 1998).

- **High Temperature Oxidation** is also metal surface loss due chemical reaction between the metal/alloy surfaces and surrounding oxygen in the environment (Kurz, 2005). It occurs when alloys are exposed to temperatures above 538°C, resulting in the protective oxide scales. The oxide scale can be detrimental if the

oxidation continues at a rate that results in a thicker scale and hence spallation or rupture occurs. This consequently leads to reduction of high temperature corrosion and fatigue resistance of the base metal. Typical example is the degradation of thermal barrier coating[6] (TBC) cracking and spalling. High temperature oxidation also can occur in the inner surface of the turbine blade cooling channels and result in blade fracture. Currently there are coatings available to overcome this effect and can be applied both on the blade surface and internal cooling holes (Meher-Homji and Gabriles, 1998).

- **Hot Corrosion** results from a combination of oxidation and sulphidation. It has the detrimental effect on the coatings and the base metal deterioration (Eady, 2000). Two categories of hot corrosion have been identified based on the range of temperatures at which they occur. Type I (high temperature) hot corrosion occurs at temperatures between 825°C to 950°C and is characterised by a denuded zone along with intergranular cracks and sulphide spikes. Type II (low temperature) hot corrosion results from 600°C and 750°C and exhibits a layered type corrosion scale. Both are detrimental to internal and external surfaces for hot section turbine blades and vanes (Meher-Homji and Gabriles, 1998)
- **Fretting and Galling** damage results from relative motion between the surfaces that are close-fitted in contact. These types of surface damage create small cracks due to trapped debris produced between the surfaces, which in turn crack propagates under fatigue cyclic loading. This type of damage is known as a fretting-fatigue mechanism. Fretting affects blade and disk attachments, joints, bolted areas, and riveted or press fitted locations. Galling is frequently found in bearings, induces deep grooves, and tends to reduce LCF. While fretting induces low grooves and tends to reduce HCF (Eady, 2000)
- **Wear** results from the movements of two contacting components due to thermal expansion of the base metal, which leads to rubbing contact and then to adhesive or abrasive wear (Craig, 2005b). This is typically found in blade tip-shroud region,

[6] *TBCs are complex, multifunctional insulating thick films typically 100 μm to 2 mm thick of a refractory material yttria-stabilized zirconia (YSZ) that protect the metal part from the extreme temperatures in the gas temperatures above their melting points* (Clarke and Phillpot, 2005).

and on abradable seals. Temperature is the main factor for the rate of wear in a turbine engine, since the slight increase in operating temperature has negative impact on the relative hardness of contacting materials, the contacting force and lubrication (Eady, 2000).

- **Fouling** occurs due to contaminants adhering to aerofoils and annulus surfaces, causing changes in the blade geometry and increase of surface roughness. Fouling reduces the mass flow rare, power output, and drop in efficiency, thus increasing the fuel consumption and rise in turbine inlet temperature. This type of degradation can accelerate both fatigue and creep, and can be found in compressor and turbine blades. Example in turbine blade and vanes, contaminants may plug into the cooling holes, causing fracture due to overheating. Filtration and regular offline washing or in combination with online washing mitigates the effects of fouling at some extent (Meher-Homji and Gabriles, 1998)
- **Foreign Object Damage (FOD)** results from the ingestion of large solid particles into the engine inlet flow path, such as birds, stones, gravels or even broken ice formed in the engine inlet (Carter, 2005). FOD is common in fan and compressor blades, especially at the sharp leading edges. FOD can induce small dents, nicks or v-notch type defects, which in turn, will act as stress risers and susceptible to crack initiation. The damage caused by FOD also promotes mechanical imbalance, aerodynamic excitation, material loss, and release of small fragments into downstream components (Eady, 2000).

Despite many studies and reports available in the open literature, there is still a lack of understanding of compound degradation such as environmentally assisted corrosion-fatigue and stress corrosion cracking in high-performance materials and design features for critical aeroengine components. Moreover, degradation mechanisms above mentioned have a detrimental impact on the mechanical integrity of the safety-critical aeroengine components leading to a gradual degradation of mechanical properties and loss of performance, hence intended functionality. As such, this research has attempted to review and identify the degradation mechanisms and related casual links to life limiting features of critical components.

2.2 Cause of failures in aeroengines

There has been an increase in a number of occurrences of failures in mechanical components, particularly in the aviation industry (ATSB, 2014). Much of the reports published by the engine OEM's and airline operators have only provided the symptoms of failure, such as oil leakage, in-flight-shut-down, abnormal engine indications, high EGT margin, etc. Therefore, it becomes important to understand the underlying cause of failure mechanisms. There are many causes for the occurrence of such failures in mechanical components. The most common underlying cause of failures are as follows: service operating related damage; design related flaws; manufacturing related anomalies; assembly related errors; and improper maintenance and repairs (Shipley R 2002 pp 79-217).

The following sub-sections reviews the underlying causes of failures which are mainly responsible for the aeroengine compressor and turbine section components. The literature survey used the open literature of reported cases that have contributed to the analysis of failures of aeroengine blades, vanes and discs.

2.2.1 Service related failures

Damages arising during service in aeroengines may result from operating engine conditions and/or service environment (Carter, 2005), such as aerodynamic excitations, combustion instabilities, mechanical vibrations, rotor imbalance (Cowles, 1996), hot corrosion (Eliaz, Shemesh and Latanision, 2002a), and foreign object damage (Chen, 2005). The root cause of failure of an LP turbine blade by thermal-mechanical fatigue in a low bypass turbofan engine was analysed (Mishra, Johney, *et al.*, 2014). Forensic and metallurgical investigations results revealed that the blade surface experienced heavy oxidation, making it weak, more brittle, and prone to crack initiation. High thermal cyclic loading and high mechanical stresses due to high throttle excursion contributed to blade failure. Furthermore, affected overheating, burns and erosion in HP nozzle guide vanes (see Figure 2-3).

Figure 2-3. Photograph of thermal cracking and overheating in nozzle guide vanes (Mishra, Johney, *et al.*, 2014).

Another case, on a root cause analysis of fractured J85 aeroengine turbine blades revealed that excessive and long term exposure of turbine blade to high temperature could led to blade discoloration, intergranular cracking, necking and creep rupture at blade tips (Kim *et al.*, 2008), as shown in Figure 2-3. The overheating effect on the blade surface led to coating peeled-off and direct exposure of the base alloy to a high temperature creep rupture.

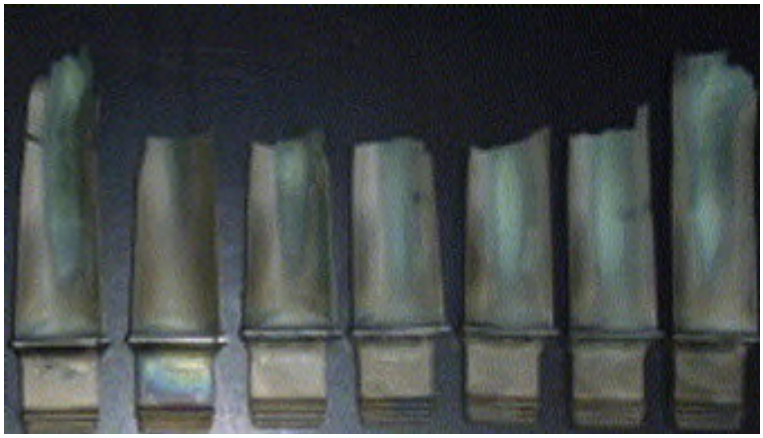

Figure 2-4. Photograph displaying discolorations in blades surfaces due to thermal and corrosion effect (Kim *et al.*, 2008).

The interaction of both creep and fatigue mechanisms is the other main cause of failure in compressors and turbines blades of aeroengines (Infante *et al.*, 2009). Creep damage is a high temperature and time dependent mechanism which results from microstructural changes in the alloy leading to a continuous reduction in the strength of the material

during service mainly due formation of intergranular voids and subsequent cracking (Sklenicka, 1996) and grain boundary sliding (Salam, Tauqir and Khan, 2002).

The failure by creep-fatigue of HP turbine blade in an aeroengine was investigated by metallurgical and stress analysis of the failed blade (Sugianto *et al.*, 2014). The authors found that the blades experienced internal cooling hole cracks in different aerofoil sections assisted by a coating and base alloy degradation due to operation at high temperature. The coating degraded due to high temperature oxidation causing loss of aluminium and coating spalling, resulting in alloy exposure to high temperature. Latter decreased the alloy ductility and toughness facilitated by grain boundary brittleness caused by the formation of a continuous film of carbides on grain boundaries, the degradation of gamma prime due to elongation (rafting) and coalescence, and high thermo-mechanical stress level.

During service, the HP turbine blades suffer also from increasing cracks from blade tip-shroud rub after hundreds of hours of service. This significantly affects the whole engine function, it increases EGT and, thus, engine efficiency and the safety of the aircraft. Another investigation on a premature HPT blade tip cracking found that a combination of mechanical stresses and environmental assisted hot corrosion caused cracking and failure of the blade (Xie *et al.*, 2006). Further, lack of coating of both oxidation-resistance and abrasion-resistance at blade squealer tip also contributed to the problem. This study suggests that having effective coating surrounding critical locations of the blades and re-applying coating during refurbishment could prevent failures.

However, coatings do spall during service, when exposed to high thermal stresses and vibrations (Nissley, 1997). Spalling of TBC's in HP turbine blades is also life-limiting feature. These coatings are applied to insulate the base alloy of first stage HP turbine blades from the hot gas environment (Clarke and Phillpot, 2005). The underlying cause of spalling of TBC is also attributed to the formation of a thermal growth oxide layer and thermal stresses from engine starts/stops (Lowden *et al.*, 2009).

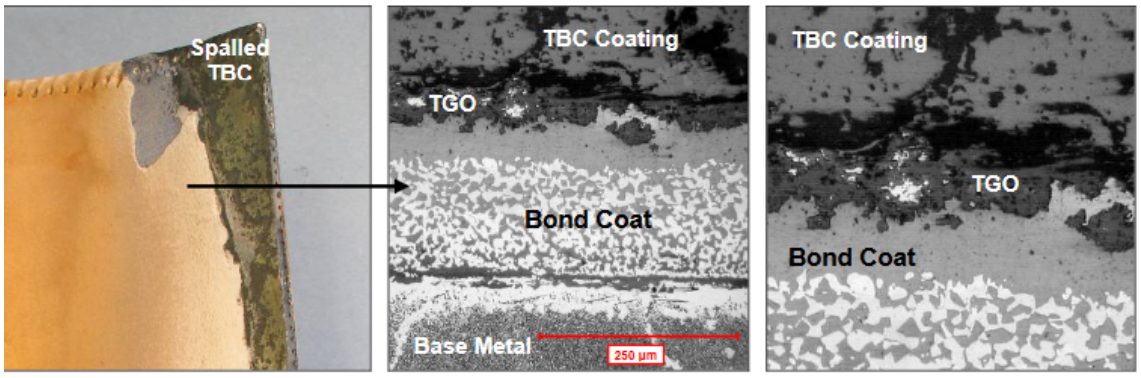

Figure 2-5. Photograph and micrographs displaying the TBC coating degradation adjacent to a spalled region (Lowden *et al.*, 2009).

A case of failure of a platinum aluminide coated LP turbine blade of an aeroengine, revealed that excessive vibration in the engine can also cause cracking in the brittle platinum aluminide coating layer due to excessive bending of blades (Bhaumik *et al.*, 2006). The authors found that the cracks acted as stress raisers and subsequently propagated to base alloy resulting in failure by HCF. Also, a fractography study revealed that the failure of the aeroengine compressor disk was fractured by HCF mechanism due to increased stress/vibration on the compressor disk as a result of changes in the engine behaviour (Suresh *et al.*, 2013).

Aeroengines can be subject to ingestion of small or large hard particles, including sand particles or birds. Civil and military aircrafts are known to be vulnerable to bird strike near to airfields during take-off, approximately 90 % of the bird strikes on civil aircraft and 54 % of those to military aircraft (Neubauer, 1990). This is because military jet engines are particularly vulnerable during the take-off when the engine is at a very high speed and the aircraft is at a low altitude where large group of birds are commonly found flying. Another reason is that majority of the military fields are near coastal area where there is a natural habitat for some of sea birds. Thus, increasing the higher probability of bird-strike impact. Depending on the severity of the impact and weight of the bird, high speed impact can cause considerable damage and even catastrophic failure to the aircraft (Mishra, Ahmed and Srinivasan, 2013).

Compressor blades are also affected by the impact of small debris inducing nicking in form of sharp V notches in the leading edges of the blades, which, in turn, will act as stress raisers susceptible to crack initiation (Nowell, Dini and Duó, 2003). An example of such cases is reported on a fracture analysis of two aeroengine compressor blades,

which identified the impact of debris as a source of crack initiation causing pits on the blades surface and subsequently propagated under HCF mechanism (Silveira, Atxaga and Irisarri, 2008; Infante *et al.*, 2009).

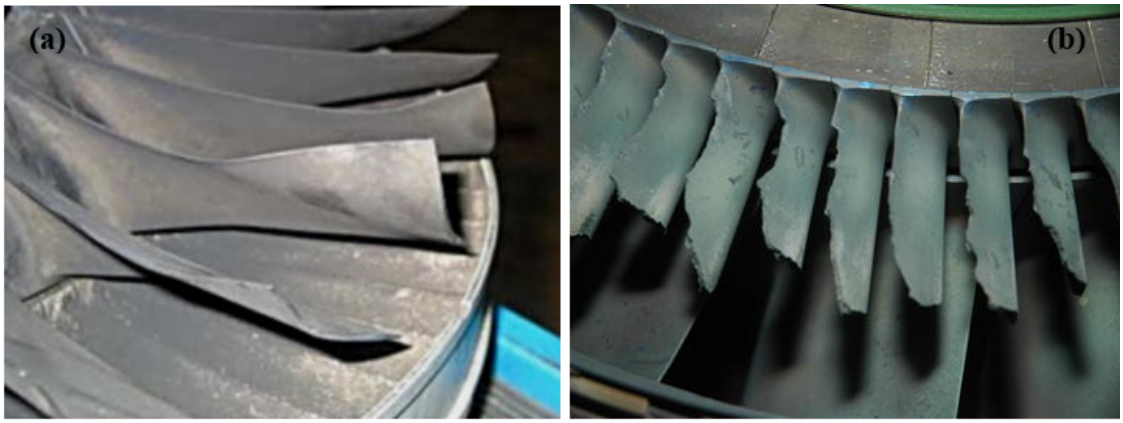

Figure 2-6. Photographs showing a) LP compressor blade distortion due to bird strike, and b) LP turbine blades damage due to over-heating and creep effect (Mishra, Ahmed and Srinivasan, 2013).

On the other hand, turbine blades and vanes experienced domestic object damage (DOD) which could lead to the failure or decrease engine performance. This type of damage arises from a dislodged debris or component from another location of the engine (Suresh, 1998). Table 2-1 summarises the service-induced damages on aeroengine blades and vanes based on the reviewed literature. Lastly, it should be mentioned that in all service related failure cases highlighted the need for an increase in on-wing inspections, periodic baroscopic checks and effective coating solutions.

Table 2-1: Summary of service induced damage drivers.

Service factors	Causal drivers	Mechanisms
Operation environment	High temperature, fuel and air contaminants, solid particles	Thermal fatigue, Creep, Hot Corrosion, Oxidation, Erosion, FOD
High mechanical stresses	Centrifugal load, vibrational and flexural stresses, stall/surge, rotational speed, etc.	Thermal-mechanical Fatigue, High Cycle Fatigue, Low Cycle Fatigue, Fretting-Fatigue
High thermal stresses	Thermal gradients, high thermal transients load (i.e. trips, start-ups and slowing downs), Overheating due to high EGT	Thermal Fatigue, High Temperature Creep, Creep-fatigue

2.2.2 Design related failures

Degradation affects a variety of aeroengine components, but failure in compressors and turbines components affects the integrity and performance of the engine. The origin of design[7] related flaws can be attributed to one or combination of underlying causes such as unintended stress raisers due the excessive sharp edges, resulting in an unexpected high stress concentration and consequently leading to HCF failure, when exposed to excessive vibration and rotational speed. An example of such failure is reported on LP compressor blade, at fillet of blade lugs location (Mishra, Thomas, *et al.*, 2014).

Inadequate geometries could also lead to LCF, as the case of improper tolerance of the dovetail-rim area of the turbine disk (Witek, 2006). Using nonlinear FE analysis, the author found that the shorter radius of the disk slot could lead to high stress concentration and fracture under excessive rotational speed. Other example comes from a design shortcoming resulted in fretting and then LCF failure due to abnormal contact between the LP compressor blade tenon and the LP compressor disk mortise area (Xi *et al.*, 2000). Comprehensive analysis of fracture cause led to inappropriate dimensional tolerance and the over-compensation of centrifugal bend moment responsible of fracture at blade/disc interface. The problem of improper dimensional tolerance on a failed LP compressor and turbine blade due to design is also been discussed in reported cases, respectively (Park *et al.*, 2002; Tang *et al.*, 2009; Lee *et al.*, 2011).

Improper material selection is also considered a design flaw, since it is incapable to provide the required mechanical properties for the application such as resistance to creep, corrosion, fatigue, etc. The cause of HP turbine blade fractured by corrosion-fatigue was investigated by (Xie *et al.*, 2000). The microstructural investigation revealed the presence of a poor alloy microstructural stability, weakening the serration area. The inappropriate alloy led to crack nucleation caused by excessive bending resonance and propagated through intergranular corrosion. FE analysis was used to investigate a fractured HP turbine blade by a mixture of LCF/HCF (Hou, Wicks and Antoniou, 2002). The authors concluded that the poor creep resistance of the turbine blade material contributed to

[7] Design in engineering "is the process of devising a system, component, or process to meet desired needs. It is a decision-making process (often iterative), in which the basic science and mathematics and engineering sciences are applied to convert resources optimally to meet a stated objective."(ABET, 2016)

excessive blade stretch, resulting in the blade tip/shroud rub to fatigue failure. The fretting fatigue is the main mechanism of premature failures in compressor blades (Patil and Shirsat, 2012) and on the turbine blades tip to shroud locations (Liu *et al.*, 2011).

Another critical observation is that much of the design related failures by the researchers are seen on the blade fir-tree/disc dovetail slot and blade tip/casing shroud locations. This suggests that changes in the dimensional tolerances, design of appropriate geometries and selection of materials resistance to high temperature, creep and hot corrosion are important to prevent failures from such design features/locations, sourcing from service conditions such as excessive vibration, pressure dynamics, thermal expansion, and centrifugal load during steady or transient state engine operation. Figure 2-3 diagram shows an example of how a design deficiency could sustain a premature failure from anticipated service condition such as stress level prior to reaching the intended service life.

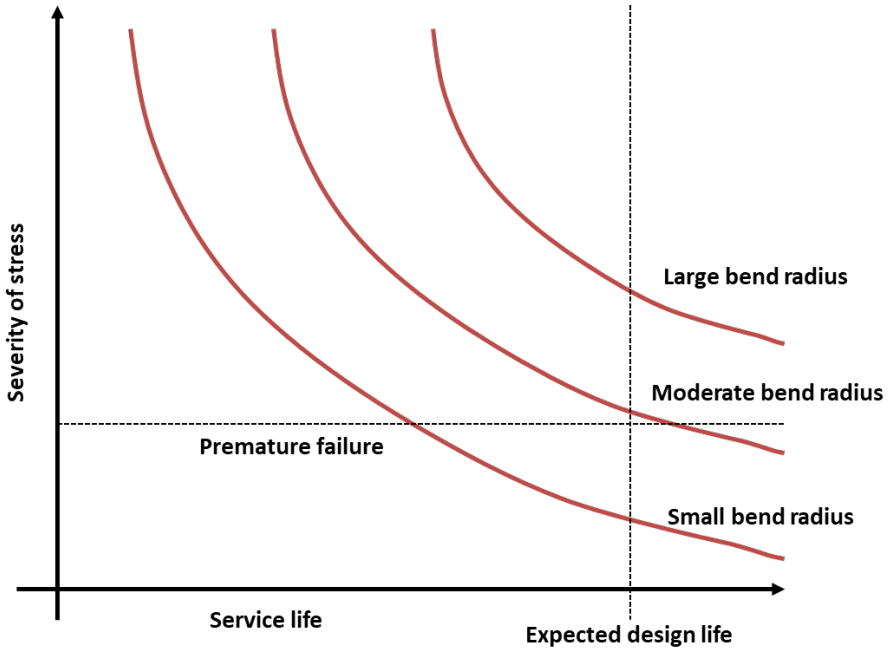

Figure 2-7. Schematic diagram showing an example of life-design flaws plot. It shows the effects of design flaws such as bend radius on service life of a component. Adopted from (Scutti, 2002).

2.2.3 Manufacturing related failures

A wide variety of manufacturing[8] anomalies occurs during materials processing, machining and structural assembly, which could lead to premature component failure (Grandt Jr, 2003). One common type of defect in turbine components is porosity or freckle due to casting defects. From fractography result analysis many researchers have confirmed that crack initiation in HP turbine blades originated from the porosity cavitation and then leading HCF failure (Kim, 2009; Kianicová and Pokluda, 2014). Also, inappropriate columnar grain growth at the blade root during casting could lead to the premature stress rupture (Bhaumik *et al.*, 2002). The improper control of casting parameters is the underlying cause of such failures.

Deficient microstructure caused by primary carbides during the solidification of the alloy can also contribute to blade premature failure. An examination of a set of HP turbine blades found that the fracture of the first blade was initiated at one of the cooling holes, where the large size of carbides was present. These carbides contributed to high stress concentration and crack initiation (Silveira *et al.*, 2009). This implies that micro-voids generation by creep was also easier on this blade and the failure process is accelerated further by thermal-mechanical fatigue.

Machining marks due to abusive drilling are one the main reasons for the surface crack initiation in the discs holes (Yan *et al.*, 2000). The authors through mechanical testing and metallurgical analysis concluded that cracks found in the holes were mechanical driven due to thermal gradients and residual stress produced by abusive machining. Moreover, examples of machining anomalies and inspection techniques used for aeroengine rotor disks are discussed in (Feist *et al.*, 1994; Mook *et al.*, 2006). Machining marks could also cause high stress concentration in tip/shroud location of turbine blades (H. Wang *et al.*, 2007). In such cases, high bending-vibration stress can promote premature crack initiation, resulting in LCF or creep-fatigue failure. Metallurgical analysis of a turbine blade failed by creep has also shown that excessive grinding at blade edges can contribute to change in blade geometry (Ejaz, Qureshi and Rizvi, 2011). This

[8] Manufacturing refers to the process of creating a product from technical documentation and raw materials, generally performed at a factory (Shipley R 2002 pp 79-217).

change generates thin sections on the blade, which makes them susceptible to creep-fatigue at abnormal thermal stress conditions.

Improper surface treatment can lead to premature microstructural degradation of the alloy when exposed to overheating and high thermal stress (Barbosa *et al.*, 2005). During an investigation of fractured compressor blades and vanes, it has found that improper shoot peening of blade surface led to premature fatigue failure. The hardness tests and metallurgical examination showed that high plastic deformation caused by improper shot peening led to early crack nucleation (Lv *et al.*, 2009). Similarly, improper heat treatment can cause crack nucleation and LCF fracture in turbine blades (Song *et al.*, 2007). The metallurgical and chemical analysis of the blades found that improper heat treatment led to segregation of Ti and Mo which then caused the crack initiation. Another example is reported by (Zhang *et al.*, 2004; He *et al.*, 2011) is the improper solution treatment. The authors found that surface recrystallization caused by improper solution treatment led to plastic deformation in the blades surface, and consequently to fatigue failure.

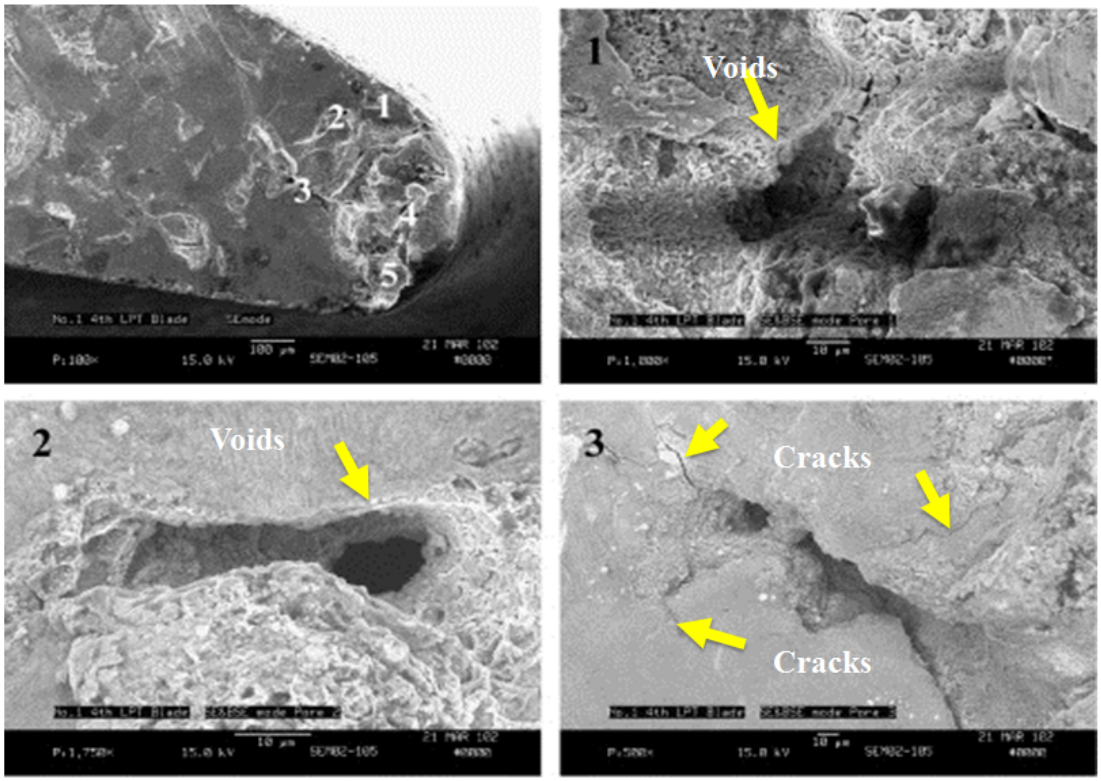

Figure 2-8. SEM micrographs showing example of the casting defects including voids and cracks at the trailing edge section of a turbine blade (Kim, 2009).

The cause of plugging material in cooling holes of a turbine blade was investigated (Mustafa, Badairy and Mehta, 2009). The blades experienced thermal fatigue due to overheating caused by plugging. A detailed analysis of all elements which had an influence on the failure found that the coating material contributed to plugging, suggesting improper coating and poor-quality inspection at manufacturing stage. Other types of the manufacturing anomalies could originate from hot cracking and residual stresses induced by welding (Jahangiri and Fallah, 2011), white layer (Herbert *et al.*, 2012), embrittlement (Nandi *et al.*, 2012), and many more manufacturing anomalies are listed in (Wilby and Neale, 2012) and discussed in (Viswanathan, 1989; Shipley and Becker, 2002). These anomalies also affected the performance of the components, making it more susceptible to premature fatigue failure.

More attention to quality and control during the processing of materials and inspection at manufacturing stages is needed for safety-critical aeroengine components. Further, review of the manufacturing process and stringent quality control practices can eliminate defects if any and can improve the quality of components. Therefore, reduce the risks of engine component failures.

2.2.4 Remarks

There are number of degradation mechanisms causing premature fatigue damage in aeroengine hot gas path components such as thermal fatigue, creep, low cycle fatigue and hot corrosion. These mechanisms are linked to critical design feature of blades, vanes and discs, such as aerofoil leading and trailing edges, blade root, fir-tree and dovetail interface, blade tip and shroud interface, impingement holes and effusion cooling holes, discs slots, holes and mating/joint areas. These were found to be critical and life limiting features influencing engine performance, maintenance and failure of components and engine damage.

High cycle fatigue is predominant, both in the compressor and in turbine section components based on the literature review. Cracking in hot section turbine components in the most of the cases initiates from coating spallation, cracking in cooling holes, microstructural anomalies including porosity and carbides. Crack initiation in hot section turbine components in most cases begins from the surface and subsurface anomalies,

areas of high stress concentrations and microstructural ageing. Crack propagation is driven by mechanical vibration, oxidation and sulphidation attack and transient thermal stress due to abnormal rotational speed and stop/start cyclic loadings.

Overall, the literature survey conducted on the engine failure and analysis reports indicates the service related damage was the highest contributor cause of turbine components failure followed by manufacturing and design related flaws and improper assembly.

2.3 Laser drilling

Laser beam machining is an advanced manufacturing method for drilling micro holes and applies a specific source of energy such as LASER as a material removal mechanism. The LASER is the acronym for light amplification by stimulated emission of radiation. Laser drilling being a non-contact and thermal-based material removal process. Therefore, a relevant drilling technology that is suitable to a wide range of materials such as superalloys and ceramics (Beck, 2011). In addition, laser drilling being a single-point tool holds several advantages compared to mechanical drilling and electrical discharge machining (EDM) such as high processing rate, free-tool wear, manufacture of shapes, holes; being capable of drilling at angles of ≤15 degree through ceramics, being flexible and easy to employ automation (Dahotre and Harimkar, 2008).

In recent years, this process has been extensively used for the drilling of micro-holes for gas turbine hot-section blades, vanes and combustor rings for cooling purposes, hole diameters ranging from 0.3-1.0 mm (van Dijk, 1992). Table 2-2 shows typical whole size for different aeroengine components. These components are typically made from nickel base superalloys and difficult to machine using traditional drilling processes. It has gained much attention in aircraft engine applications owing to the increase towards improving the efficiency of the engines and capable of drilling multi-layer materials with high aspect ratio (see Table 2-3). However, laser drilling alters the surface microstructure around the hole vicinity inducing spatter, heat-affected zone (HAZ) recast layer, burrs and micro-cracking. These are the metallurgical defects frequently observed after laser processing of metals (see Figure 2-9).

Table 2-2. Hole dimensions for different aeroengine components (van Dijk, 1992).

Component	Diameter (mm)	Wall thickness (mm)	Angle (deg.)	No. holes
Blade	0.3 – 0.5	1.0 – 3.0	15 - 30	25 – 200
Vane	0.3 – 1.0	1.0 – 4.0	15 – 30	25 - 200
Afterburner	0.4	2.0 – 2.5	90	40,000
Base plate	0.5 – 0.7	1.0	30 - 90	10,000
Seal ring	0.95 – 1.05	1.5	50	180
Cooling ring	0.78 – 0.84	4.0	79	4,200

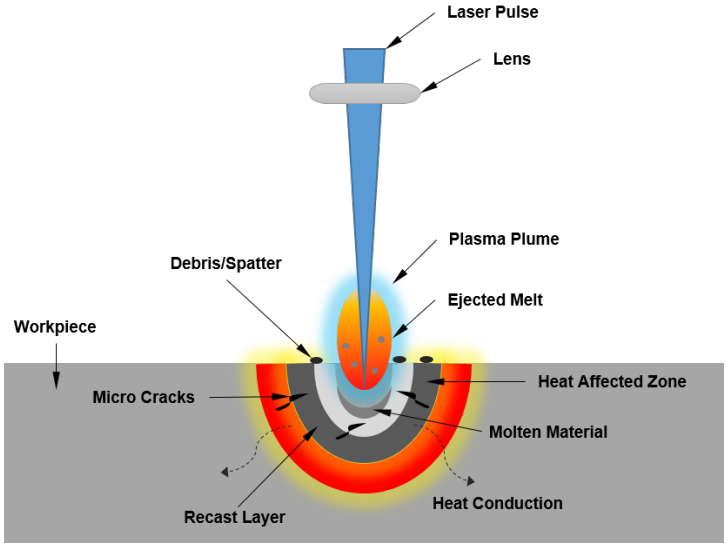

Figure 2-9. Schematic of the physical damages taking place during the nanosecond/millisecond laser drilling process. Adopted from (Dimov *et al.*, 2008).

Table 2-3. Comparison of hole drilling techniques for aeroengine components (Yeo *et al.*, 1994).

	ECM	ECD	EDM	Laser
Minimum				
hole diameter (mm)	0.75	0.5	0.3	0.1
taper (mm/mm)	0.025	0.001	0.0005	0.01
recast layer (μm)	—	—	25	25
angle to surface (degree)	—	15	20	15
surface roughness (μm)	2	6	6	20
Maximum aspect ratio, i.e. depth/diameter	20	250	25	50[a]
Complex shapes	Yes	No	Yes	Yes
Simultaneous drilling	Yes	Yes	Yes	Yes
Tooling complexity	High	High	High	Low
Speed	Medium	Medium	Slow	Fast

[a]Depending on the material thickness

2.3.1 Working principle

The laser drilling works on the principle that when an intensity laser beam is focused on the workpiece surface heats and heat diffusion takes place by absorption and conduction, transforming the work volume into molten. This phase change causes vaporisation and then chemically degrade the irradiated field, making easy to eject away the molten material from the hole (Dubey and Yadava, 2008). A typical power density of 10^6-10^9 W/mm^2 is used for most metal processing by lasers to generate melting and vaporisation (Dutta Majumdar and Manna, 2003). This process happens very fast and usually on time scale of nanoseconds to microseconds (Schulz and Eppelt, 2009).

For generation of laser beam requires: (i) Laser active medium which sends out part of the emitted energy in the form a laser radiation. (ii) Source of energy to excite to stimulate the lasing medium to create light. Flash lamps and more recently doped fiber optics are used as source of energy to excite lasing medium. (iii) Resonator to generate laser radiation. The resonator consists of two mirrors between which the laser beam radiation is reflects back and forth. The resonating mirrors boost the laser efficiency by stimulated emission. One mirror is fully reflective and other partially reflective. (iv) Fiber optics delivers the laser beam produced to the focused head.

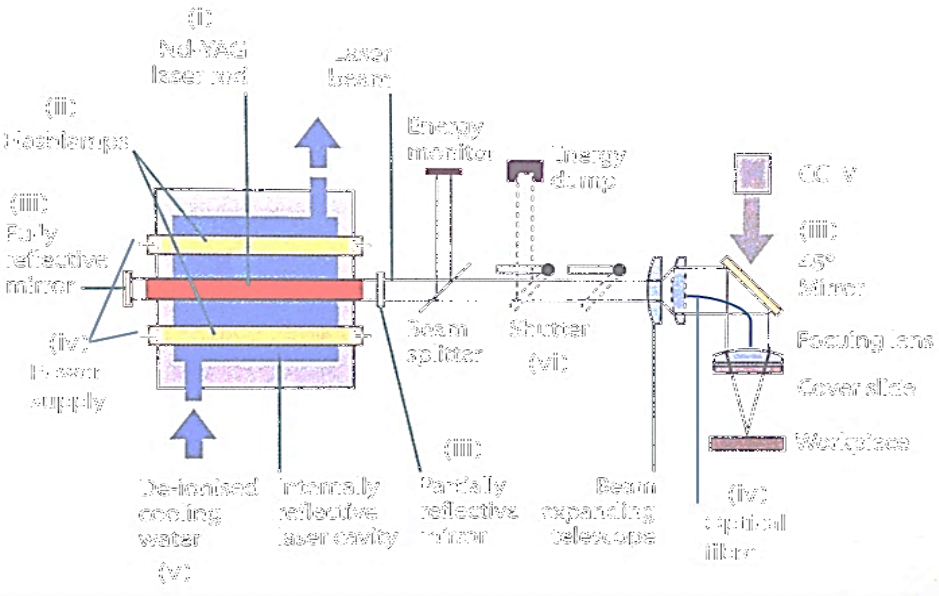

Figure 2-10. Schematic diagram of Nd:YAG laser beam machining (Rolls-Royce, 2005).

Moreover, it should be mentioned that only a minor portion of the energy used is converted into laser radiation, a cooling unit is used to control the laser medium

effectively. Therefore, a power supply unit, water cooling unit and beam shutter system is integrated in most laser beam machines (see Figure 2-10). Power supply unit controls the laser output by controlling the intensity of light emitted by the flash lamp. The water cooling unit to avoid thermal damage of laser cavity, energy source, and lasing medium. Beam shutter is a laser safety switch which allows to control the path (clear or block) for the laser beam.

There two types of laser operating mode, viz. pulse mode and continuous mode. In pulse mode, the laser is basically switched on and off very quickly. The pulsing makes it possible to reduce average energy input into the workpiece. Moreover, the pulse shaping minimise the thermal cycling experienced by the workpiece surface during processing of materials that are prone to cracking, it avoids taper in percussion drilling. Whilst, in continuous mode a constant level of beam intensity is provided. It means that laser beam reflects back and forth between the mirrors is generated continuously and radiation exits the resonator continually through the output coupler.

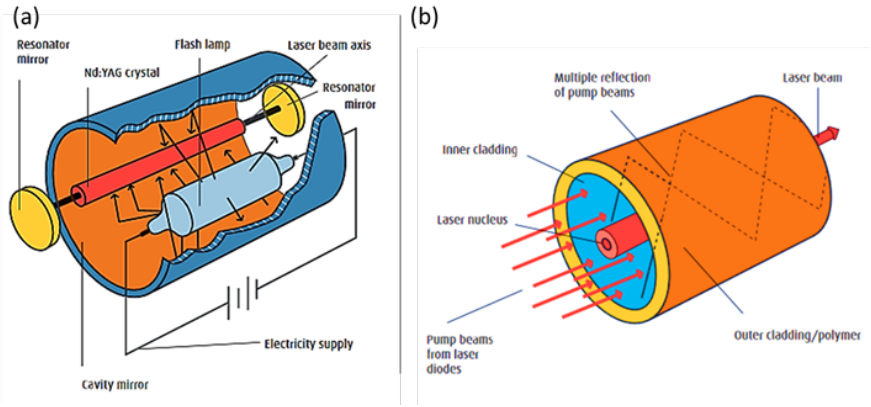

Figure 2-11. Schematic diagram: (a) Nd:YAG laser pump and (b) Yb fiber laser [9].

The available type of lasers includes solid-state, liquid or gaseous state-based and spectral wavelength ranging from ultraviolet to the infrared range (Meijer, 2004). As such, lasers have a variety of applications in different materials processing including forming, cutting, scribing, drilling, and cleaning among others. As shown in Figure 2-11, the pulsed Nd:YAG (neodymium-doped yttrium aluminium garnet) and continuous wave (CW)

[9] Retrieved from: https://www.boconline.co.uk/internet.lg.lg.gbr/en/images/laser-basics410_39552.pdf?v=1.0, accessed in 12/04/2017.

Ytterbium (Yb) fiber lasers are dominating sources of lasing in the aerospace applications for drilling and cutting (Tan, 2013).

Nd:YAG lasers are optically pumped using flash tube and two reflecting mirrors to provide feedback and produced stimulated emission is delivered by fiber optics to focused head as mentioned previously. Nd:YAG laser typically emits light with a wavelength of 1064 nm. It operates in both pulsed and continuous mode. In fiber lasers, Ytterbium (Yb) doped fiber optics is used as laser active medium and are optically pumped using diode and special plugs at the fiber ends as reflective mirrors. The pumped diode light is delivered by active fibre optics where it produces stimulated emission of laser radiation. Ytterbium (Yb) fiber laser typically emits 10.80 nm wavelength of fiber laser. Recent work in fiber laser has shown to deliver good beam quality, high stability, low cost of ownership and higher rate of repeatability (Marimuthu, Antar and Chantzis, 2015).

Other type of laser system such as ultrafast lasers like femtosecond (fs) laser ablation have been put forward for the drilling of nickel alloys in order to eliminate the delamination crack effect on coated interfaces, and holes with negligible spatter, recast layer and HAZ (Das and Pollock, 2009). This only possible due to ultra-short pulses (~100 fs) in low fluence regime causes direct ablation and vaporisation. Hence, no heating and consequent damage zone are induced around the hole vicinity (McDonald J, Ma S, Nees J, Pollock T, 2006). However, the technology advancements have not yet allowed the femtosecond (Ti: Sapphire) lasers to be transferred to the industry in full scale due to the inherent costs and very low material removal rate. Hence, Nd:YAG lasers dominating the automotive and aerospace industry for drilling, welding and cutting applications.

2.3.2 Laser drilling mechanism

The laser drilling and material interaction process have been described in four stages (see Figure 2-2): surface heating, melting, vaporising, and melt ejection (Schneider *et al.*, 2010) . To understand this process, some researchers have used observation techniques such as streak photography (Yilbas, 1985), field emission scanning electron microscope (Garofano, Marcus and Aindow, 2010), and high-speed camera approaches (Schneider, 2007) to explain the material removal mechanism during laser drilling.

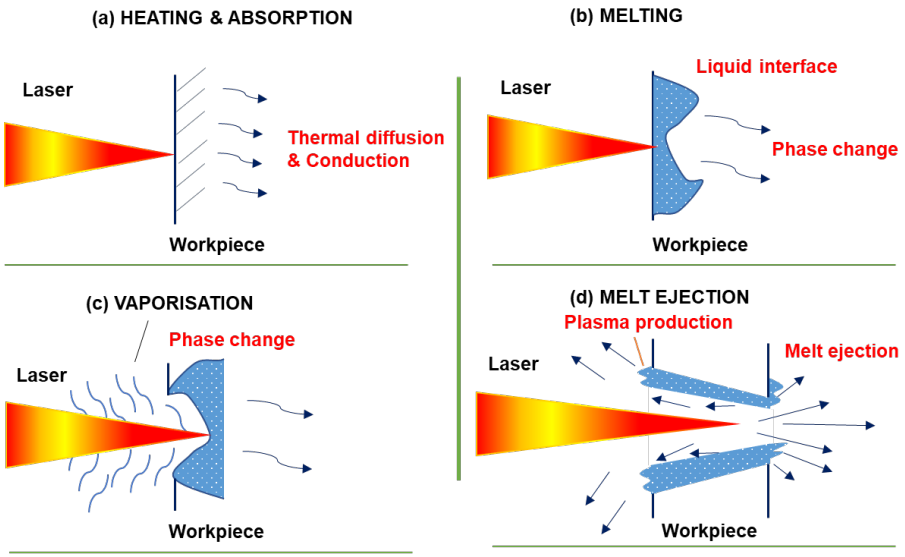

Figure 2-12. Schematic diagram of physical process during the laser drilling.

The physics of laser drilling shown in Figure 2-12 could be explained as described in following sub-sections.

2.3.2.1 *Surface heat and absorption*

The first phase of the laser drilling is the surface heating and absorption of laser intensity by the workpiece. The irradiated focused laser beam onto workpiece surface interacts with heat flow and rapidly converts the laser energy to heat and a portion of that energy is absorbed by workpiece surface (Yilbaş, 1993; Shuja, Yilbas and Shazli, 2007). The amount of energy absorbed depends on the workpiece material properties (thermal conductivity, reflection coefficient and diffusivity), surface temperature, and laser wavelength and beam parameters. The heat flow depends on the thermal diffusivity of the material and temperature of the surface since the absorptivity increases with increase in temperature. The thermal diffusivity (β) can be defined as (Weman, 2003):

$$\beta = \frac{K}{\rho\, c_P} \tag{2-1}$$

Where, K is the thermal conductivity (W/m^{0}K) and it is a measure of the rate at which heat is transferred through a material (Askeland, Fulay and Wright, 2010), ρ is the material density (kg/m^3), c_p is specific heat capacity (J/kg^{o}K) and it is the energy needed

to change the temperature of the material one degree (Askeland, Fulay and Wright, 2010). The surface temperature of the material (T_s) is a function of time (t), thermal conductivity (β), absorbed intensity (I) and ambient temperature (T_0), and can be expressed as (Chryssolouris, 1991).

$$T_s = T_0 + \frac{2\,I}{K}\left(\frac{\beta t}{\pi}\right)^{1/2} \tag{2-2}$$

So, the amount of energy absorbed by workpiece is given by (Steen and J., 2010):

$$E = I\,t_P\,A_l \tag{2-3}$$

Where, t_P is pulse duration, A_l is focal spot area and I is the absorbed laser intensity by the workpiece, and is expressed as Equation 2-3. I_0 is output beam laser intensity and is function of peak power (PP) and focused spot area (A_l). The term A_b in Equation 2-4 is the absorptivity and is given by Equation 2-5. The R_f is reflection coefficient and is given by Equation 2-7.

$$I = A_b\,I_0 \tag{2-4}$$

$$A_b = 1 - R_f \tag{2-5}$$

$$I_0 = \frac{PP}{A_L} \tag{2-6}$$

$$R_f = \frac{\left(1 - n_f\right)^2 + K_e^2}{\left(1 + n_f\right)^2 + K_e^2} \tag{2-7}$$

2.3.2.2 *Surface melting*

The surface becomes molten if the laser intensity and beam interaction exceeds the latent heat of the material. The time of heat flow (t_m) to attain the melting temperature of the material (T_m) can be expressed as in Equation 2-8 (Chryssolouris, 1991) and depth of penetration (Z) of heat is given in Equation 2-9 (Weman, 2003).

$$t_m = \frac{\pi}{\beta}\,\frac{K\,(T_m - T_0)}{2I} \tag{2-8}$$

$$Z = (4\,\beta\,t)^{1/2} \tag{2-9}$$

The required laser intensity to produce deep penetration melt must attain correspondent material threshold of disintegration which is about 10^5 to 10^6 W/cm^2 for metals [88, 89] and ablation threshold fluence is 2100 J/m^2 per each single pulse for Ni-base single crystal superalloys (X. Wang *et al.*, 2007). The applied laser fluence (F_P) is function of absorbed laser pulse energy and laser beam radius (r_b), and is given by Equation 2-10 (Ng, Crouse and Li, 2006):

$$F_P = \frac{2\,E}{\pi\,r_b^2} \tag{2-10}$$

2.3.2.3 *Vaporisation*

At this phase the temperature of the irradiated surface is higher than the material boiling temperature, thus to vaporise. One fraction of the molten material formed in the cavity is vaporised and the corresponding laser intensity threshold for vaporisation is about 10^8 to 10^9 W/cm^2 (Koener *et al.*, 1996). The vapour formed on the workpiece surface in form of clouds expels into the atmosphere due to induced recoil pressure expelling the melt radially from the beam path [ref] The remaining fraction heats the workpiece eroding the edges of the cavity to form a hole (Yilbas and Yilbas, 1988; Yilbas and Aleem, 2004). The vaporisation time (t_v) needed to attain the vaporisation temperature (T_v) is given by Equation 2-11 (Luxon and Parker, 1985).

$$t_v = \frac{\pi}{4}\,\frac{K\,\rho\,c_P^2}{I^2}\,T_v^2 \tag{2-11}$$

2.3.2.4 *Melt ejection*

The molten material removal occurs in both vapour and liquid form. The fraction of molten material which is not vaporised is ejected away due to pressure gradient and recoil pressure in case of laser percussion drilling (Yilbas, 1995). Whilst, in case of laser trepanning drilling it is flushed away from the hole exit with assistance of process gas. The melt ejection is dependent of volume of the melt formed, pulse intensity and pressure

generated by recoil effect and the assist gas. So, higher the pulse intensity greater the pressure, thus to cause faster flow of molten material. The velocity of melt (V_m) can be calculated from Equation 2-12 (Von Allmen, 1976; Ruf *et al.*, 2003)Where, p_r is measured pressure recoil and p_o is measured ambient pressure.

$$V_m = \left(\frac{2(p_r - p_0)}{\rho}\right)^{1/2} \quad (2\text{-}12)$$

2.3.3 Types of laser drilling techniques

There are currently four techniques in laser drilling, namely single pulse, percussion, trepanning, and helical drilling (Walther *et al.*, 2008). In single pulse, drilling the material removal or ablation occurs in a single pulse with high laser energy. A detailed description of the melt ejection process in single pulse laser drilling is given by (Voisey *et al.*, 2003). Percussion and trepanning drilling are the most preferred methods for nickel alloys (Naeem, 2008). Figure 2-13 shows typical methods of laser drilling approaches for turbines, nozzle guide vanes and combustion components (Beck, 2011).

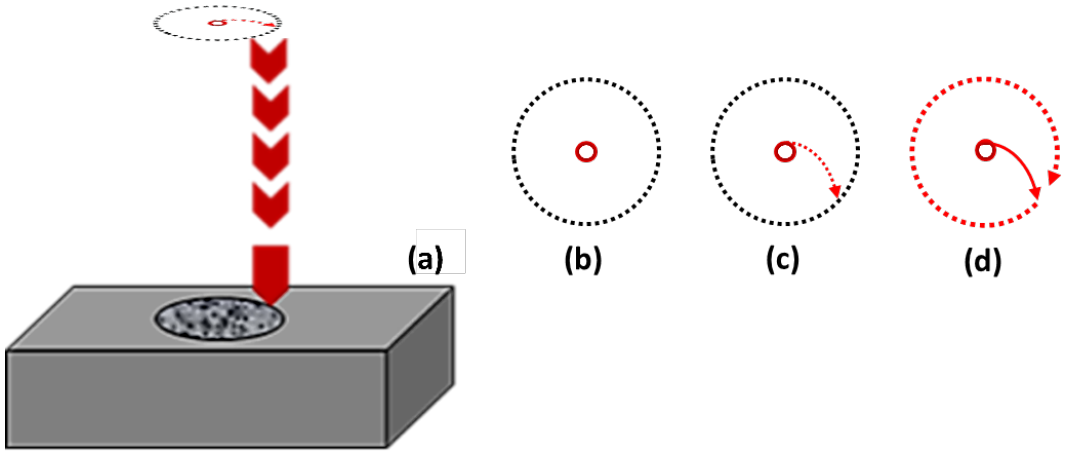

Figure 2-13. Schematic diagram illustrating the laser trepanning drilling operations.

Percussion drilling consists of firing a series of consecutive laser pulses at the workpiece to create a blind hole. Trepanning laser drilling uses a combination of drilling and contour cutting process, in which a blind hole is pierced by percussion drilling and then the through hole is widened to its desired diameter in a circular cutting motion. Percussion drilling holds an advantage of high processing rate over trepanning in general by a factor of four (Sezer *et al.*, 2006) and preferred choice of past research studies. Conversely,

trepanning gives a better hole geometry such as hole taper, roundness and desirable metallurgical aspects such as thin recast layer and a negligible HAZ (Dhar, Saini and Purohit, 2006) .

2.3.4 Metallurgical defects

The metallography examination of a section of the surface layer produced by laser drilling process shows changes to the surface morphology of the sidewalls of the hole (Sezer *et al.*, 2006; Chien and Hou, 2007; Leigh *et al.*, 2010). Two to three distinct layers are formed above the substrate, as shown in Figure 2-15. In addition, spatter and burrs are found adhered on the top surface and hole exit, respectively (see Figure 2-14). Spatter is also one of the intrinsic defects in laser drilling, which results when the ejected molten material expels upwards, falling onto the workpiece surface, and then solidifying and adhering around the periphery of the hole (Low, Li and Byrd, 2003). The characteristics of spatter and burrs formation and prevention under different laser drilling parameters on nickel alloys are already grounded in the literature by (Low, N. Li and Byrd, 2001) and (Duan *et al.*, 2014) respectively.

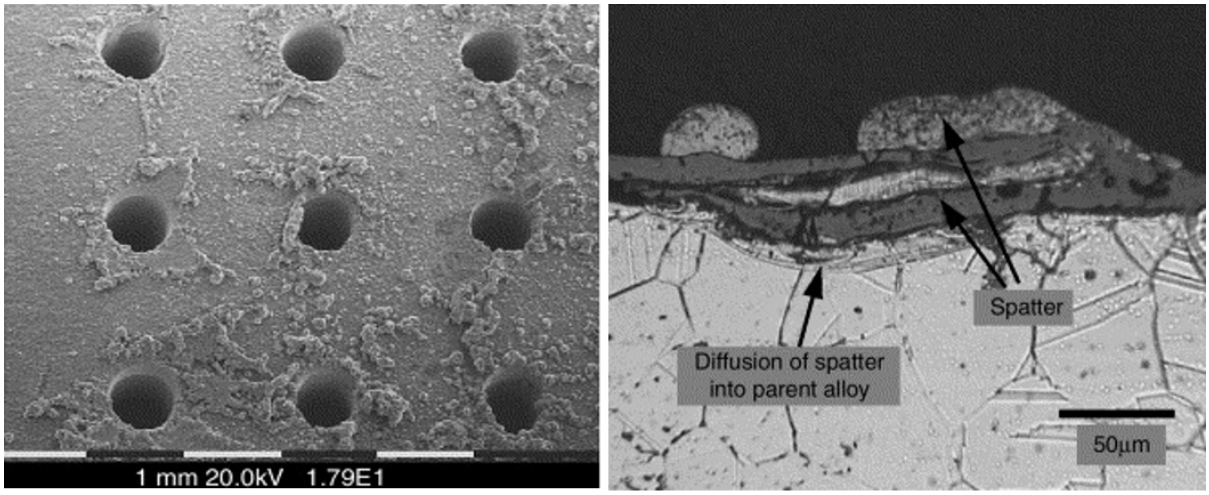

Figure 2-14. Typical SEM micrographs showing: (a) array holes with spatter formed after laser drilling and (b) a cross section micrograph of spatter deposited on the surface periphery of the hole (Low, Li and Byrd, 2003).

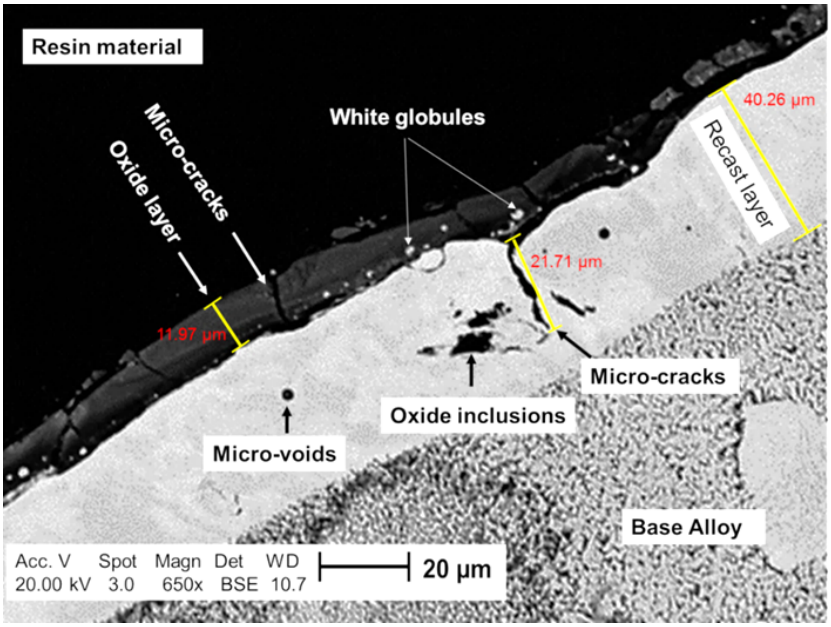

Figure 2-15. SEM micrograph of physical damages taking place during the nanosecond and millisecond laser drilling process.

First layer is the thin oxide layer and it is formed due to exothermic reaction when oxygen is used as process gas. This layer is attached to the recast layer and it is brittle, contains micro cracks and can easily be removed (Sezer *et al.*, 2006). A research work, found that by applying low gas pressure or increasing the nozzle stand-off can reduce the oxide layer (Leigh *et al.*, 2009). However, this could reduce the molten ejection rate and potential increase in the recast layer thickness. Prevention of oxide layer while maintaining the molten ejection efficiency is needed.

The second layer is the recast layer also known as white layer. The laser drilling process alters the metallurgical microstructure and characteristics in the recast layer. It is formed by the molten material that was not expelled and rapidly resolidifies by the cooling effect of assist gas. In addition, surface cracks can form in this brittle and micro-segregated layer. This is highly undesirable particularly the presence of micro-cracks in the recast structure since the propagation of the cracks from the recast layer into the parent material could occur in service, leading to failure and, thus to compromise the integrity and lifetime of the drilled component.

Limited number of studies have attempted to characterize the recast layer microstructure in laser drilling (Wang *et al.*, 2004; Garofano, Marcus and Aindow, 2009, 2010). These studies found the recast layer structure to be amorphous and brittle, and in some cases

with polycrystalline structure and a columnar structure of dendrites. The presence of thick recast layer showed to be detrimental to fatigue failure.

The last layer is the heat-affected zone (HAZ), which has only been heated but not melted. It is being found to be negligible in laser trepanning drilling (Hongyu Zhang *et al.*, 2016). The thickness of the oxide layer, recast layer and the heat-affected zone dependents on the power density applied and interaction between other laser beam parameters, material thickness, and assist gas and optics settings (see Figure 2-16).

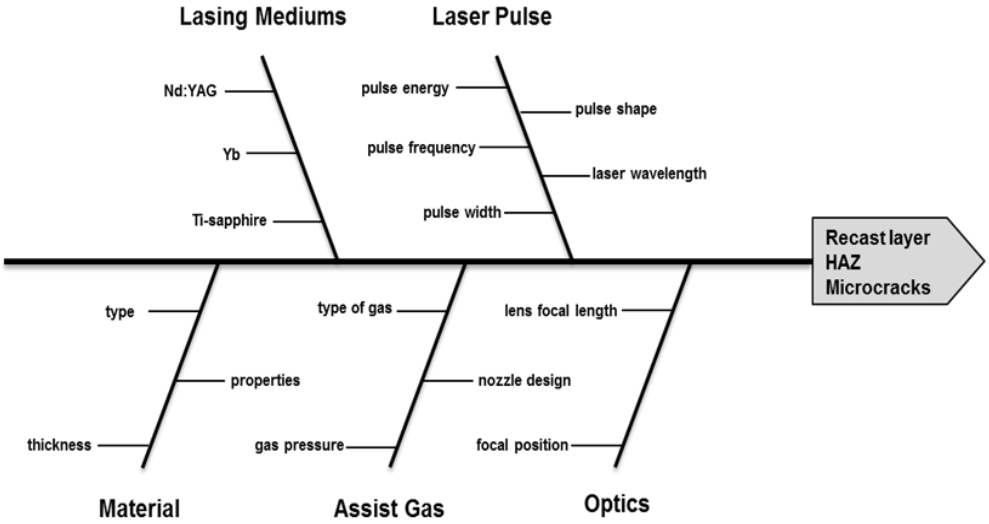

Figure 2-16. Schematic of fishbone cause and effect diagram showing the various processing parameters affecting the oxide layer, recast layer and micro cracks formation in laser-drilled holes.

2.3.5 Process parameters

2.3.5.1 *Peak power*

Peak power refers to the output amount of laser beam intensity used in laser drilling (Ready, Farson and Feeley, 2001), measured in units of kilowatts. It is the key process parameter for heating, melting and vaporisation stages in laser trepanning drilling. During each pulse, the power increases until it reaches a defined set level, which is expressed as the peak power. Peak power is an output of pulse energy and pulse duration interaction and is given by Equation 2-13. In both laser percussion drilling and laser trepanning drilling, the amount of pulse energy and pulse energy is dependent of surface area of the drill and type of material. Latter, is associated with set material thermal conductivity and

diffusivity, enthalpy of vaporisation and melting temperature. This in turn, leads to power density and focal beam spot area needed for cut, and can be expressed as Equation 2-14. Depending of type of material, higher pulse energy and short pulse duration is used to reduce the molten material, thus, less material resolidifies in sidewalls of the hole. Higher peak power improves the vaporisation rate, but too excessive peak power leads to large variation in the recast layer thickness and oxide layers (Yeo *et al.*, 1994; Bandyopadhyay *et al.*, 2002).

$$PP = \frac{PE}{PD} = \frac{Joules}{miliseconds} \tag{2-13}$$

Where, *PP* is peak power (kW), *PE* is pulse energy (J) and *PD* is pulse duration (ms). The power density is given by:

$$I_P = \frac{PP}{Focal\ spot\ area} = \frac{kilowatts}{mm^2} \tag{2-14}$$

$$Focal\ spot\ area = \frac{\pi d^2}{4} \tag{2-15}$$

Where, I_P is power density and *d* is the diameter. Power density is also known as intensity and radiance.

2.3.5.2 *Pulse duration*

Pulse duration is temporal distribution of laser beam energy applied at different time scales (Rockstroh, Chen and Lotshaw, 1996), and expressed in units of milliseconds. Pulse duration is also known as pulse width and pulse length. Since the laser drilling in this research work is done in pulsed mode, the pulse duration and repetition rate (frequency) per second are important for the amount of energy applied during each pulse for metal heating, melting and vaporisation. This energy is controlled by the laser peak power and the pulse duration (see Figure 2-17). The longer the pulse duration, more molten material will be formed and hence more material resolidifies. The resulting recast layer will be thicker than the shorter pulse duration (Goyal and Dubey, 2014). The longer pulse duration also allow more heat to diffuse and spread into the material creating more

melt in case of material with good thermal conductivity. Whilst, material with low thermal conductivity allow less laser energy absorption and spread resulting in localised high heat and thermal tensile residual stress into the sidewall of the hole, which could lead to formation of surface cracks. On the other hand, if pulse duration is too short, it will affect the stability of the cut front in laser trepanning drilling (Duan *et al.*, 2014).

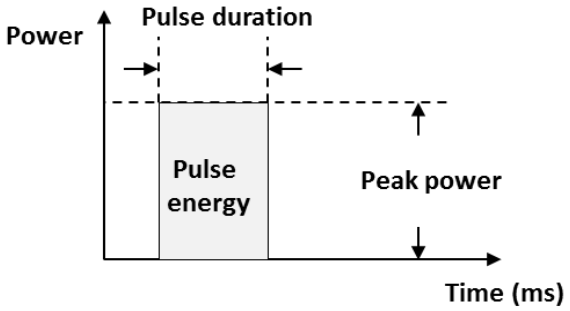

Figure 2-17. Pulse duration in millisecond pulsed laser drilling.

The pulse duration can greatly affect the laser energy and material interaction during the laser drilling operations, since it allows the molten material to be ejected away by the flow of assist-gas pressure and melt will partially be vaporised (Nowakowski, 2005). Typical ranges are from 0.2 to 1.2 ms for gas turbine cooling film holes (Beck, 2011b).

2.3.5.3 *Pulse frequency*

Pulse frequency is the number of pulses per second. It is also known as repetition rate and is expressed in Hertz (Hz). Figure 2-18 show a diagram of the pulse frequency when laser is used in pulsed mode. Pulse frequency can be calculated by Equation 2-16. Combining the pulse energy and pulse frequency defines the average power (see Equation 2-17). It is an averaged power per pulse and is associated with beam stability and hole taper (Antar *et al.*, 2016).

$$PF = \frac{1}{Pulse\ period} \tag{2-16}$$

$$Avg.Power = PE\ (J) \times PF\ (Hz) \tag{2-17}$$

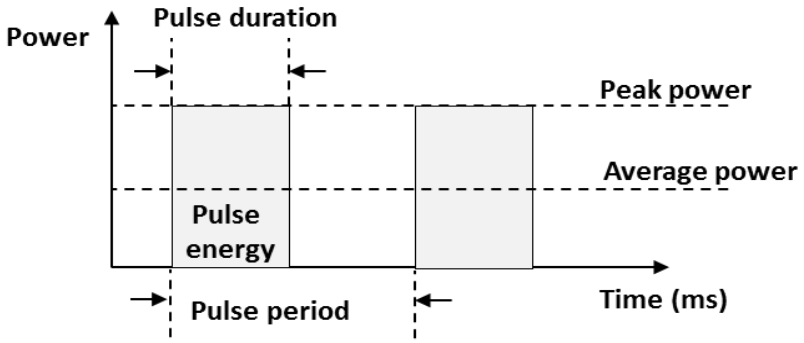

Figure 2-18. Pulse frequency in millisecond pulsed laser drilling.

The relationship between pulse frequency and recast layer thickness was studied in laser percussion drilling (Leigh *et al.*, 2009) and laser trepanning drilling (Chien and Hou, 2007; Duan *et al.*, 2014). The higher the pulse frequency, more energy is absorbed, thus, may cause more molten material (Mishra and Yadava, 2013a). Shorter pulse frequencies found to improve vaporisation rate and molten material ejection. Typical range between 10 to 30 Hz produces thinner recast layer with less thermal damage to the workpiece (Bandyopadhyay *et al.*, 2002; Chien and Hou, 2007; Leigh *et al.*, 2010).

2.3.5.4 *Pulse shape*

Pulse shaping is temporal energy distribution profile. It allows for control of hole geometry quality, such as hole roundness and taper (P. W. French *et al.*, 2006). There are two main types of pulse shaping most frequently used for laser drilling of cooling holes, viz. intra-pulse and inter-pulse shaping. The intra-pulse shape includes standard rectangular pulse shaping (also, known as normal delivery pattern, NDP), treble pulse shaping, and ramp-up and ramp-down modulated pulse shapes. The intra-pulse includes sequential pulse delivery pattern control (SPDPC), as shown in Figure 2-19.

It can be seen from Figure 2-4 shows that the energy delivery pattern in SPDPC the peak power of sequential pulses is increased linearly throughout the pulse train needed for hole drilling until it reaches pre-set level. Whilst, in NDP the peak power in successive pulses remains constant throughout the laser drilling. The standard rectangular pulse has showed to improve vaporisation rate and reduce recast layer thickness than SPDPC (Low, L. Li and Byrd, 2001).

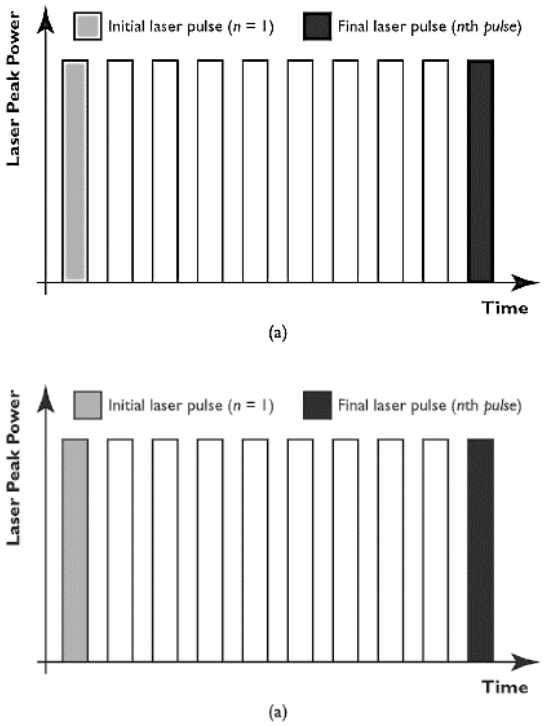

Figure 2-19. Representational diagram of the (a) normal delivery pattern (NDP) and (b) sequential pulse delivery pattern control (SPDPC) (Low, L. Li and Byrd, 2001).

In another study, ramp-up modulated pulse shape found to provide efficient molten material ejection than standard rectangular pulse shape in laser percussion drilling (P. M. W. French *et al.*, 2006). This is due to initial pre-heat and rapid rise in heating of material caused by sharp trail which leads to higher intensity to vaporise and expel the molten material faster (Duan *et al.*, 2016). However, ramp-up and ramp-down pulse shape showed no influence on the recast layer thickness (Corcoran *et al.*, 2002). It has also shown that modulated pulse shaping can reduce recast layer. This is due to increased absorptivity of laser caused by the pre-melting and increased in vaporization pressure results in more molten material being expelled, thus, less molten material to resolidify as recast layer (Duan *et al.*, 2016).

On the other hand, sequential pulse delivery pattern control (SPDPC) showed to improve the hole taper and reduction of spatter due to low beam intensity formed (Low, Li and Byrd, 2000). Moreover, it should be mentioned that most of the pulse shapes above mentioned are used in laser percussion drilling than laser trepanning drilling. Most common pulse shaping used in laser trepanning drilling is standard rectangular pulse shape due to provide controlled hole taper and recast layer thickness.

2.3.5.5 *Trepan speed*

Trepan speed is rotating scan speed of laser beam (Grafton-Reed, 2008). It is one of the main process variable in laser trepan drilling since it affects the distribution density of laser pulse along the scan path and time (Duan *et al.*, 2014). It means that energy absorbed during the hole drilling at different trepan speed will vary and this is because that there is relationship between the pulse frequency, trepan speed and energy absorbed during laser drilling, as given in Equation 2-18:

$$E_{abs} = \rho_P l \, PE \tag{2-18}$$

$$\rho_P = \frac{PF}{TS} \tag{2-19}$$

Where, E_{abs} is energy absorbed by the workpiece, l is the scan path, ρ_P is pulse density, PE is the pulse energy and PF is the pulse frequency. As such, increase in trepan speed leads to decrease in the pulse density so as less energy is absorbed into the workpiece, thus to cause more localised molten material to resolidified on sidewall of the hole. Past studies, have reported that high trepan speed leads to thicker recast layer (Chien and Hou, 2007; Goyal and Dubey, 2014). This is due to poor molten ejection rate when the beam interaction time or pulse density is too short. At low trepan speed, energy absorbed may cause more heat diffusion and more molten material, however, denser pulse density distribution increases the flow of molten material along the sidewall of the hole. Therefore, resulting in improved molten ejection, hence less to resolidify. Typical trepan speeds ranging between 50 to 75 mm/min reported thinner recast layers in laser trepan drilling of nickel-base alloys (Chien and Hou, 2007; Duan *et al.*, 2015; Hongyu Zhang *et al.*, 2016).

2.3.5.6 *Focal length and position*

Refers to the distance between the minimum spot diameter and material surface. FPP has significant influence on the hole taper. FPP determine the laser beam energy intensity to the workpiece material. The focal position could be zero to the surface, above the surface (positive) or below the surface (negative). The former FPP yields minimum focal spot

size leads to maximum energy density, hence to improve the depth of cut and reduced hole taper (Yilbas, 1997). Figure 2-20 depicts the effects of different FPP on the hole quality and past studies has showed that FPP positioned on the surface or just below the workpiece surface yields good hole quality (Johnson and Pfledderer, 1989; McNally, Folkes and Pashby, 2004).

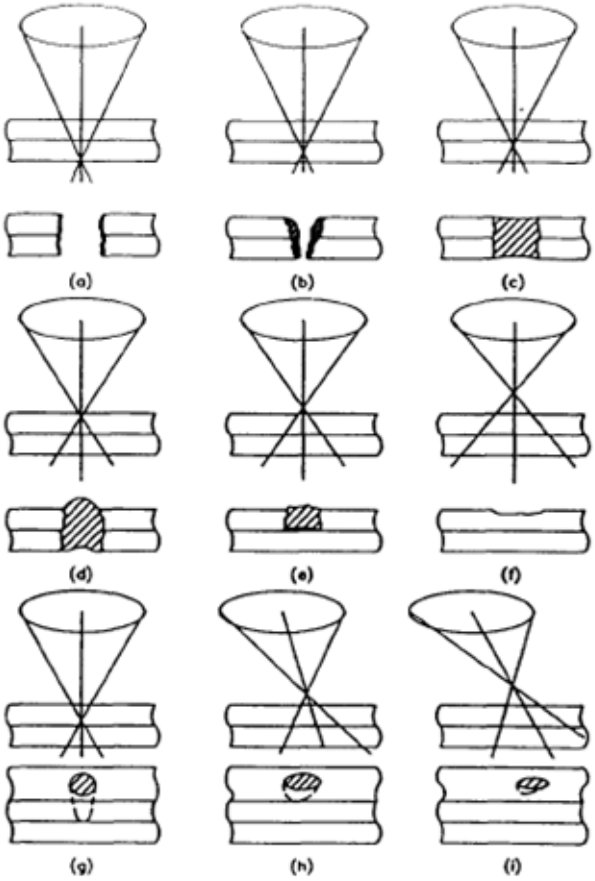

Figure 2-20. The effect of depth of focus and focal position on the quality of the holes (M. Ruselowski, 1987).

Moreover, there is strong relationship between depth of focus and lens focal length, which in turn, is associated with spot diameter and FPP. The depth of focus and lens of focal length can be expressed as (McNally, Folkes and Pashby, 2004):

$$DOF = \frac{2\,\theta\,f^2}{D_i} \tag{2-20}$$

Where, *DOF* is depth of focus, *f* is lens of focal length, θ is focal beam divergent and *Di* is the unfocused beam diameter. The schematic representation of the DOF and lens focal

length is shown in Figure 2-21. Larger DOF leads to larger focal spot size resulting in low power density and affecting the vaporisation rate and consequently the hole taper.

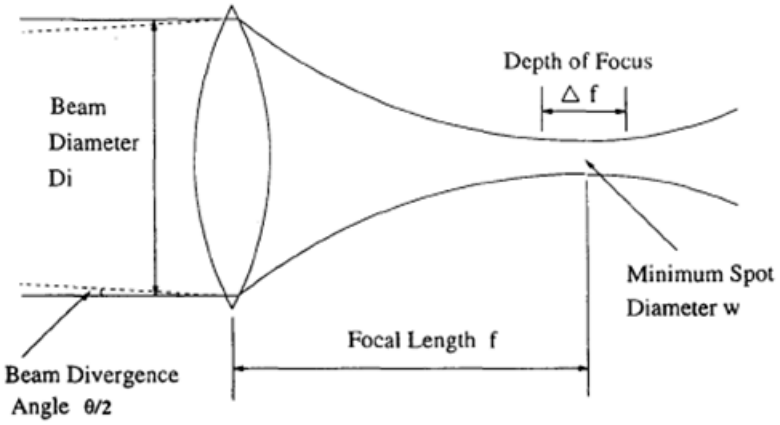

Figure 2-21. Schematic diagram of converging lens (Johnson and Pfledderer, 1989).

An ideal laser beam has greatest intensity in the center and tails off at the edges, following a Gaussian profile (Ready, Farson and Feeley, 2001), as show in Figure 2-22. This is known as the TEM_{mn} or fundamental output mode, which in turn determines how small beam waist can be focused. The TEM acronym stands for transverse electromagnetic modes and subscripts m and n symbolises the number of nodes in horizontal and vertical directions to the beam propagation, respectively. Ideally lower divergence and higher radiance will produce good quality holes. The quality of a laser beam is specified using the M^2 (M squared) factor, and can be estimated as follows (Ready, Farson and Feeley, 2001):

$$M^2 = \frac{\pi D \theta}{4\lambda} \tag{2-21}$$

Where, θ is divergence angle (radians), λ is the wavelength, and D is the unfocused beam diameter (mm). M^2 is a beam propagation ratio that indicates how close a laser is to being single mode TEM_{00}. For the perfect Gaussian TEM_{00} condition has $M^2 = 1$, particularly in YAG laser systems. M^2 values less than 1.1 are suitable for laser drilling since it provides good beam quality and small focal spot size (Steen and J., 2010).

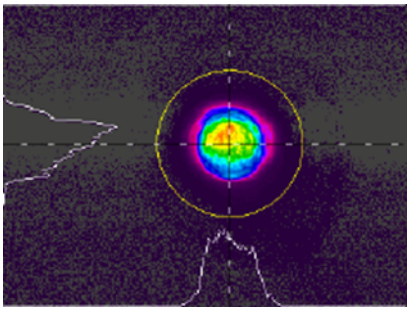

(a) **(b)**

Figure 2-22. Examples of Gaussian mode plots: (a) representation of different types of Hermite-Gaussian modes[10] in 3D and 2D, (b) beam profile of a JK 704 laser system (Naeem, 2008).

2.3.5.7 *Assist gas*

Assist gas refers to co-axial process gas through the beam nozzle to expel the molten material away from the hole and also act as shield to protect the beam nozzle from spatter and molten debris (Low, Li and Byrd, 2000; Sezer, Li and Leigh, 2009). The type and pressure of assist gas also has strong influence on the hole quality in terms of geometrical and metallurgical aspects (D. K. Y. Low, Li and Corfe, 2000). There are three types of process gases most frequently investigated, viz. oxygen, argon, and nitrogen (Willach *et al.*, 2003).

Oxygen as an assist gas found to increase the amount of energy absorption, vaporisation and improve in melt ejection (Patel and Brewster, 1991). Another study, showed that using oxygen assist gas generates oxidise layer on the sidewalls of the hole (Ng, Crouse and Li, 2006) and spatter morphology is more viscous than the argon (D. K. Y. Low, Li and Corfe, 2000; Willach *et al.*, 2003). This due to exothermic reaction and high peak power interaction when oxygen is used as assist gas.

Studies conducted by (D K Y Low, Li and Corfe, 2000; D. K. Y. Low, Li and Corfe, 2000) showed that spatter accumulated around the hole entrance was less adhesive and slightly thick when applying oxygen assist gas in comparison to argon and nitrogen in percussion drilling. In addition, oxygen reduces the cooling rate during the drilling

[10] Retrieved from http://www.optique-ingenieur.org/en/courses/OPI_ang_M01_C03/co/Grain_OPI_ang_M01_C03_5.html, Accessed on 12/01/2017.

process, thus to extent the melt time. Argon cools faster and solidifies the molten material rapidly, resulting in multiple recast layers during each sequential pulses. Conversely, other studies found that argon found to be the most effective process gas when it comes to reducing the thickness of the recast layer (Horn *et al.*, 2000; Lugscheider *et al.*, 2005). The presence of cracks and inclusions in the recast layer where prominent when oxygen process gas was used. However, use of oxygen found the avoid closures, melt droplets and formation of burrs compared to argon (Willach *et al.*, 2003; Kreutz *et al.*, 2007). These studies suggest that different solidification rates may generate different recast layer characteristics.

One important consideration for melt expulsion at the hole exit in trepanning drilling is the faster flow of molten material at each sequential pulses and downward mechanical force to expel away the melt to form the hole (Duan *et al.*, 2014). As such, assist gas pressure may create high downward mechanical drag force to eject away molten material easily. However, excessive gas pressure may increase the cooling cycle gradually preventing the molten material eject away. Therefore, resulting in rapid solidification of the molten material on the hole wall and formation of burrs in the hole exit periphery (Von Allmen, 1976; Voisey *et al.*, 2003).

2.3.6 Laser drilling of nickel-based superalloys

The literature review of pulsed Nd:YAG laser drilling for nickel-base superalloys shows a considerable number of studies conducted focused on the percussion drilling compared to the trepanning method (see Table 2-4). The effect of pulsed Nd:YAG laser percussion drilling process parameters on the geometrical and metallurgical quality characteristics have been established in previous studies by (Bandyopadhyay *et al.*, 2002; Pandey, Shan and Mohandas, 2006; Mishra and Yadava, 2013a) and (Corcoran *et al.*, 2002; Leigh *et al.*, 2009; Bathe and Padmanabham, 2014), respectively.

On the other hand, pulsed Nd:YAG laser trepanning drilling of nickel-base super alloys has received little attention. This is mainly due to drilling speed. Horn examined the effects of three assist gases nitrogen, argon, and oxygen on the recast layer thickness (RLT) and cracking in coated CMSX-4 laser trepanned drill holes at an acute angle up to 60 degrees to the surface (Horn *et al.*, 2000). The results showed that the RLT was at least

two to three times less when using argon assist gas in comparison to oxygen and nitrogen during trepanning laser drilling. The presence of cracks and bubbles in the recast layer were observed when using oxygen, and argon found to be the most effective process gas when it comes to reducing the thickness of the recast layer. However, argon gas produces difficult to remove burrs.

Table 2-4. Research in pulsed Nd:YAG laser drilling of Ni-base superalloys.

Drilling Method	Workpiece *Coated	References
Percussion	Inconel 718	(Yilbas, 1985, 1997); (Tam et al., 1993); (Bandyopadhyay et al., 2002, 2005);(Mishra and Yadava, 2013b)
	CMSX-4	(Trippe et al., 2004); (Leigh et al., 2009, 2010); (Sezer et al., 2006)
	Nimonic 263	(Low, Li and Byrd, 2000); (D. K. Y. Low, Li and Corfe, 2000); (Petronić et al., 2010)
	C263	(French, Naeem and Watkins, 2003; P. W. French et al., 2006); (Naeem, 2008); (Pandey, Shan and Mohandas, 2005, 2006)
	IN1000	(Garofano, Marcus and Aindow, 2009, 2010)
	*Various	(Voisey K, Thompson J, 2001; Voisey and Clyne, 2004)
	*Nimonic 263	(Kamalu, Byrd and Pitman, 2002); (Sezer et al., 2005, 2006; Sezer, Li and Leigh, 2009)
	*Rene 80	(Corcoran and Sexton, 2000; Corcoran et al., 2002)
	Haynes 188	(Guinard et al., 2012)
	Inconel 718	(Bathe and Padmanabham, 2014)
Trepanning	Inconel 718	(Rockstroh, Chen and Lotshaw, 1996); (Rockstroh X, 1996); (Chien and Hou, 2007); (Wang et al., 2012); (Kumar, Dubey and Pandey, 2013); (Goyal and Dubey, 2014)
	CMSX-4	(Willach et al., 2003) Willach et al., 2003
	CMSX-4 Coated	(Horn et al., 2000); (Lugscheider et al., 2005); (Kreutz et al., 2007); (Walther et al., 2008)
	Miscellaneous	(H. Zhang et al., 2016)

Willach examined the effects of assist gas pressure, nozzle diameters and nozzle distance on trepanning kerf and the recast layer thickness during laser trepanning drilling of CMSX-4 (Willach *et al.*, 2003). The results revealed that the high assist gas pressure, larger nozzle diameter improves the melt expulsion and reduces the RLT. Further, an increase of nozzle distance to the workpiece surface leads to a thicker recast layer. Lugscheider and other authors applied finite volume method to investigate the gas jet of

the conical nozzle positioned above the workpiece surface and found that lateral offset of the nozzle yields a smaller recast layer at the trepan kerf surface during angle drilling (Lugscheider *et al.*, 2005). Kreutz presented 5-axis trepanning drilling process for low-angled and fan shaped holes with minimum damage to the coated CMSX-4 substrate (Kreutz *et al.*, 2007). They found that 5-axis trepanning of shaped holes yields high reproducibility and thin recast layer thickness. They also suggested that the use of oxygen assist gas prevents closures, melt droplets, and formation of burrs compared to process argon. However, the choice of gas does not reflect the current industrial practice across the number of applications (Grafton-Reed, 2008).

Chien and Hou applied Taguchi method to investigate the parameters that exert more influence on the recast layer formation during laser trepanning drilling of Inconel 718 (Chien and Hou, 2007). The experimental results showed that gas pressure, peak power, and focal length are significant factors affecting the RLT. Further experiments and analysis concluded that the minimum recast layer thickness could be obtained by adjusting the values of the assist gas pressure and the trepanning speed. Wang used the Taguchi method to examine the influence of laser trepanning drilling parameters (peak power, pulse width, and pulse frequency) on a Ni-base superalloy (Wang *et al.*, 2012). They found that the pulse width (duration) had a significant effect on the RLT. In addition, laser post-processing by chemical etching can remove the residual recast layer completely.

More recently, Kumar et al., 2013 developed a computer-aided hybrid methodology of multi-variable regression and genetic algorithm for multi-objective optimisation (CGAMO) to predict the recast layer at the entrance and exit of Inconel 718 laser trepanned drill holes. They used the published experimental data (Chien and Hou, 2007) for training, testing and for validating the software toolset. The CGAMO toolset suggested that based on the range of values used the low RLT at entrance hole could be achieved at lower values of peak power and higher values of assisting gas pressure, and low recast layer at the exit hole could be obtained at lower values of nozzle diameter as well as low values of peak power.

Goyal and Dubey adopted artificial neural network and genetic algorithm to obtain optimal laser drilling parameters for better hole circularity and reduced taper on the

Inconel 718 alloy (Goyal and Dubey, 2014). They found that the higher values of pulse frequency and trepanning speed resulted in better hole taper and circularity. Also, in previous studies (P. W. French *et al.*, 2006) found that the pulse shaping improves hole taper and improve metallurgy. Lately, Zhang and Zhou developed a quantitate method to characterise hole geometry such as conicity and circularity, and surface quality such as the recast layer, spatter, and micro cracks (H. Zhang *et al.*, 2016). They found that developed method aids to optimise parameters such as laser power and beam expanding ratio.

2.3.7 Remarks

The current research work on laser trepan drilling in different nickel-based materials based on Table 2-1 can be summarised as follows:

1. Much work has been focused to the laser percussion drilling process in terms of recast layer thickness, taper ratio and material removal rate (see references on Table 2-3).
2. A number of investigations have been conducted on the modelling and optimisation of the recast layer thickness (Chien and Hou, 2007; Kumar, Dubey and Pandey, 2013), development of automated five axis laser trepan drilling process in CMSX-4 (Horn *et al.*, 2000; Willach *et al.*, 2003; Kreutz *et al.*, 2007; Walther *et al.*, 2008).
3. Others have investigated the impact on hole geometry (Goyal and Dubey, 2014), dimensional deviation (H. Zhang *et al.*, 2016), and drilling speed (Marimuthu, Antar and Chantzis, 2015; Antar *et al.*, 2016).
4. There is still very limited work on the understanding of influences of laser trepan key process parameters to minimise the surface crack formation in the recast layer and how it impacts on the performance of laser drilled components.

2.4 Fatigue life assessment methods: an overview

High cycle fatigue, thermal-mechanical fatigue, corrosion-fatigue and creep-fatigue are among the most critical forms of fatigue failure potentially occurring in cast nickel-based

turbine blades and vanes (Seerangan, Walunj and Kumar, 2012). The existing fatigue life assessment approaches and predictive damage models are still challenging considering the accuracy and environmental effect such as from oxidation and corrosion challenging (Bagnall, Shaw and Mason-Flucke, 2000). There have been numerous investigations on the fatigue life assessment and life prediction of cast nickel-base alloys for aeroengine applications published in International Journal of Fatigue, Journal of Materials at High temperature, Superalloys 2012 Proceedings, etc., by use of deterministic or probabilistic methods. The purpose of this review is focused on presenting a summary of the mechanisms of fatigue failure, fatigue life methods, and status of high temperature fatigue life of single crystal (SC) nickel-base CMXS-4 alloy.

2.4.1 Mechanism of fatigue failure

Fatigue also refers to the progressive accumulation of damage in a material under a repeated cycling of stress[11] and strain[12] at constant or variable temperature. There are three distinct stages of fatigue failure (see Figure 2-23). The first stage is the crack initiation nucleation (stage I), which it is at the microscopic level in the component or material. Second, the crack propagation (stage II) characterised by the short crack growth and long crack growth. Finally, the last stage is the material failure by fast fracture or tensile overloading.

Crack initiation in materials usually occurs from (Gell and Leverent, 1973):

- Microstructural defects, from casting porosity, white layer, carbide inclusions, segregation, etc.
- Stress raisers including holes, radii, and discontinuities.
- Environmental assisted cracking, such as hot corrosion and oxidation.
- Surface flaws such as scratches, machining marks.

[11] Stress (S or σ, sigma) is the load per unit area or the force (F) applied per cross-sectional area (A) perpendicular to the force (ASTM E6, 2000).
[12] Strain is elongation change in dimension per unit area (ASTM E6, 2000).

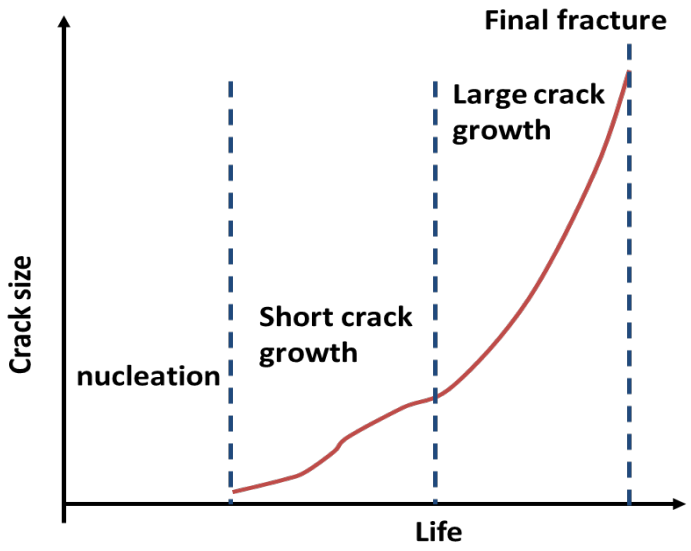

Figure 2-23. Schematic diagram showing different stages of fatigue crack mechanism to failure.

The crack nucleation (stage I) usually starts with a faceted surface and then follows through striation type pattern (river lines, beach marks, etc.) at different stages of the crack growth (stage II). The crack growth at elevated temperatures is ductile and is controlled by the stress intensity factor (K_{ic}) at crack tip (Duquette and Gell, 1971). The final stage of failure by fast fracture will occur when the remaining cross-section of the material after a continuous cyclic load is insufficient to carry more load/stress. The final fracture morphology is characterised by cleavage, ductile shear or brittle fracture (Brooks and Choudhury, 2002).

Also, it should be mentioned that fatigue crack initiation and growth could be characterised by intergranular fracture mode or transgranular fracture mode (Shipley and Becker, 2002).

- **Intergranular fracture**: The crack propagation of travels along the boundaries of the metal or alloy, typically due to elemental depletion at the grain boundaries or weakening of grain boundary due to chemical, corrosion and oxidation attack.
- **Transgranular fracture:** The crack propagation results from the repeated breaking of atomic bonds along specific planes and the crack travels through the actual grains (see Figure 2-24).

Moreover, there is a comprehensive literature available on the basics of fracture mechanisms of metals and alloys (Gayda and Miner, 1983; Antolovich, 1996; Liu, 2005; Campbell, 2012).

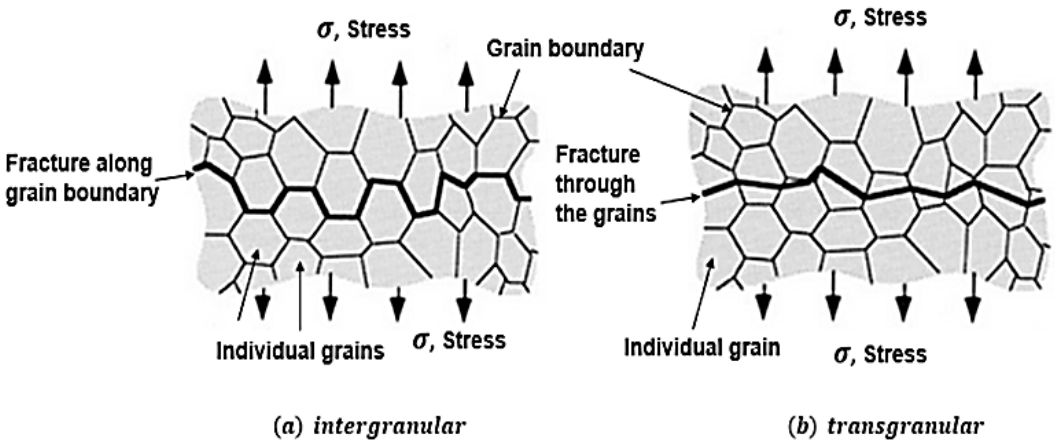

Figure 2-24. Schematic of mechanisms of fracture in polycrystalline alloys: (a) intergranular fracture and (b) Transgranular fracture. Modified from (Campbell, 2012).

2.4.2 Fatigue life methods

This section briefly introduces three fatigue analysis methods including stress-life approach, strain-life approach and the fracture mechanics approach. These methods have their own area of application with some degree of similarities among them, the stress-life and strain-life approaches that are also considered to be the total-life approach.

2.4.2.1 *Stress-life approach*

Stress-life (S-N) approach was one of the first analytical methods developed to determine the fatigue life. It was developed in the 19th century using standard laboratory tests (Wöhler, 1867). The tests were cyclic based such as rotating and cantilever bends, axial pull-up tests and torsion tests. The experimental data analysed the applied stress (S) to the number of load cycles to failure (N); hence known as S-N curve (Wöhler, 1870). This enabled the design engineers to accurately predict fatigue life and derive material's

fatigue limit[13] from this curve. Later, the finite life region of the Wöhler's S-N curve was represented by Basquin Function (Basquin, 1910). Basquin Function was also later modified by introducing an extra parameter, the fatigue limit (Stromeyer, 1914).

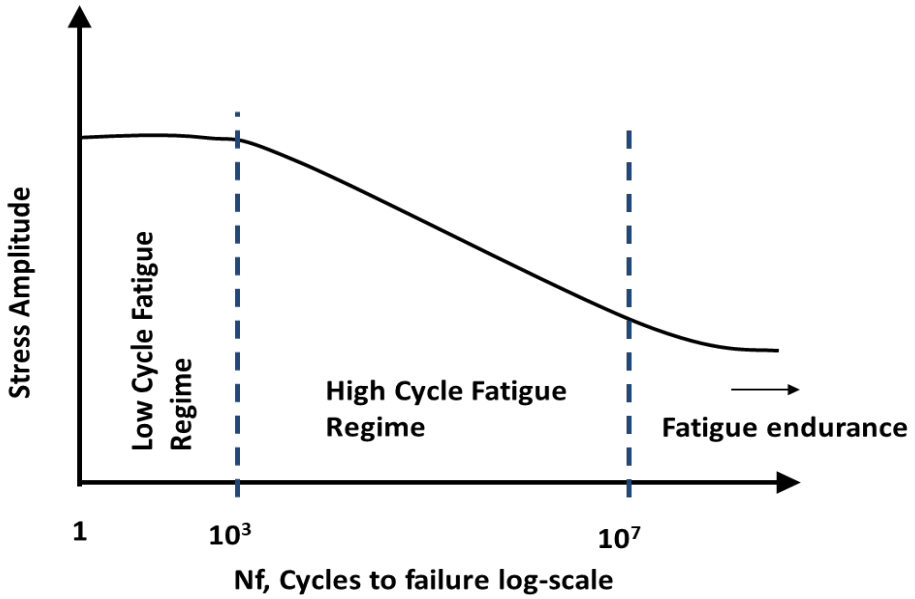

Figure 2-25. Schematic diagram of S-N curve showing the HCF and LCF life cycles to failure regions. Adopted from (Suresh, 1998).

To demonstrate the effect of stress ratio ($\sigma_{min}/\sigma_{max}$) on the fatigue life, the equivalent stress model was proposed (K. Walker, 1970). This model considers the mean stress effect on the stress cycle, as shown in Figure 2-25. Moreover, Basquin Function is limited to zero mean stress conditions, not representing the real-life loading conditions. For non-zero mean stress conditions, different combinations of the stress amplitude and mean stress is plotted through Morrow relation (Morrow, 1968), Söderberg relation (Soderberg, 1939), Goodman relation (Goodman, 1899) and Gerber relation. Among these models, Gerber gives better life prediction for tensile mean stresses. Söderberg gives a conservative prediction of the fatigue life. Further detailed discussion of these models is available in the open literature (Suresh, 1998; Campbell, 2008).

There are also other factors that affect S-N fatigue curves such as stress concentration; surface finish; surface treatments; load types; shape and distribution of inclusions; grain

[13] Fatigue limit or endurance is maximum fluctuating stress a material can endure for an infinite number of cycles (ASTM E6, 2000)

size and direction; frequency; temperature and environment. These factors have been considered and discussed in (Cui, 2002). These factors have a detrimental impact on the fatigue life of cast and machined components by a debit of approximately 35-50% (Fuchs, Stephens and Saunders, 1981; Milella, 2013).

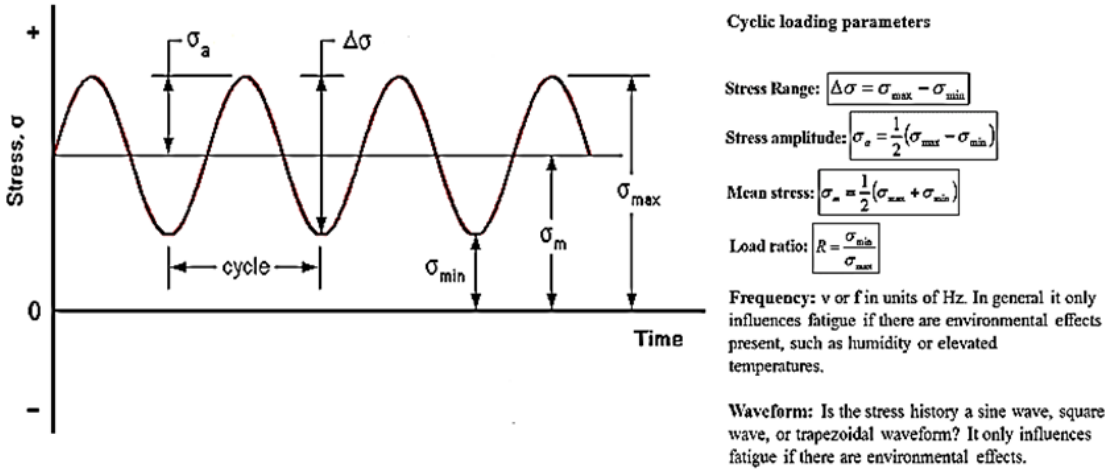

Figure 2-26. Schematic diagram of cyclic loading parameters and variation of stress vs. time (t). Adopted from (Suresh, 1998), page 225.

The S-N approach is widely used for high cycle fatigue tests. Where, in most of the cases a low amplitude cyclic stress is applied to induce mainly elastic deformation in a cross-section of a specimen or component (Suresh, 1998). The test methods for determining the Stress-life (S-N) response and fatigue testing are outlined in detail in ASTM standards E466-E468 and STP 91-A (American Society for Testing Materials, Philadelphia).

2.4.2.2 *Strain-life approach*

Strain-life (E-N) approach, also known as local strain method or low cycle fatigue approach (Fuchs, Stephens and Saunders, 1981). It is applicable for situations involving primarily plastic stress where high stress, high temperatures or stress concentrations (i.e. notches) are involved (Suresh, 1998). The E-N approach is widespread use in the automotive industry, and more recently in aerospace and power generation industries. A typical strain-life diagram is shown in Figure 2-27.

The strain-life method developed in the 1960s through Coffin-Manson expression (Coffin, 1954; Manson, 1954) which was mainly concerned with the thermal fatigue problems, and later with the crack initiation stage. Mean stress effects have also been

incorporated into the E-N (Strain-life) approach for prediction of fatigue life by Morrow relationship (Morrow, 1968), Walker strain relation (K. Walker, 1970) and Smith Watson Topper relation (Smith, Watson and Topper, 1970).

The prediction of fatigue lives for notch members has also found increasing usage in E-N approach. (Suresh, 1998), since it is more convenient to relate the notch tip field to crack initiation phase. The theoretical stress and strain concentration factors under plastic deformation are given by Neuber's criterion (Neuber, 1961) to fatigue loading conditions. Based on this criterion, models developed by some researchers provided acceptable predictions of the fatigue behaviour of notch members (Topper, Sandor and Morrow, 1969; Dowling, Brose and Wilson, 1977). Moreover, multi-axial fatigue variable amplitude cyclic strains and cycle counting related to theoretical strain-life approach has also been discussed in detail in (Cui, 2002). Further, a comprehensive discussion and applications of Strain-life approach have been provided in chapter 8 of (Suresh, 1998) and other authors (Fuchs, Stephens and Saunders, 1981; Fang and Berkkovits, 1994; Dowling, Calhoun and Arcari, 2009; Ince and Glinka, 2011).

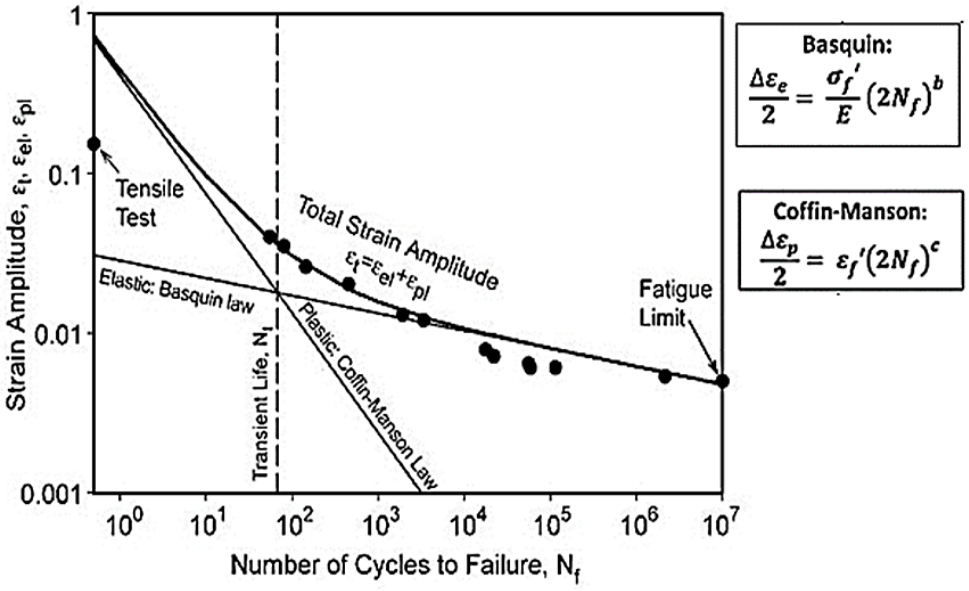

Figure 2-27. Schematic diagram of strain-life curves. Adopted from (*Nanocrystalline Materials: Fatigue Part 1 (Nanotechnology)*, 2016).

The E-N tests are mostly carried out in strain control than control load. Strain control testing uses the output from the strain gauge to provide the feedback to the typical servo-controlled test rig. Whilst, load control is carried out with cycling applied load without strain gauges and it is a simplest and quickest test procedure. In aerospace and power

generation industries, theoretical strain-life approach and thermal-mechanical fatigue (TMF) tests are mostly used for representing features in turbine components such as complex radii, slots and holes (Harrison and Winstone, 1996; Cai *et al.*, 1999; Bagnall, 2008; Blanchard, 2011). TMF failure occurs when plastic strains cannot be accommodated at low temperatures and creep and oxidation deformation occurs at high temperatures (Moverare, Johansson and Reed, 2009).

Thermal-mechanical fatigue tests are conducted according to ASTM Standards (ASTM E2368-10, 2010). The testing encompasses cycling of the temperature and mechanical strain with different phase shifts, viz. out-of-phase (OP) or in-phase (IP). A diagram of the stress–strain behaviour corresponding to OP-TMF is given in Figure 2-28. The E-N test is typically performed on polished cylindrical specimens. In some cases, tests are performed on machined notches in rectangular cross-section specimens to simulate cracks. Further detailed test procedures are described in ASTM Standards E606/E606M (ASTM E606, 2012).

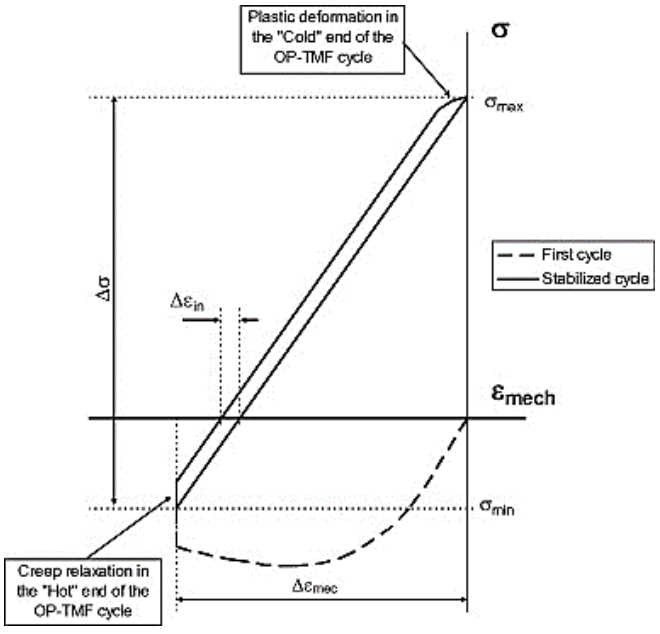

Figure 2-28. Schematic diagram of TMF curves (Moverare, Johansson and Reed, 2009).

2.4.2.3 *Fracture mechanics approach*

The fracture mechanics approach finds its application to predicting the propagation life from an initial crack or surface flaw in a material. Basics of fracture mechanics started with experimental studies by Griffith criterion in 1920's (Griffith, 1920) and have since

then developed in various directions (Irwin, 1948; Orowan, 1949). Later, Irwin developed the method of linear elastic mechanics (LEFM) which relates the growth of an initial crack of size to the number of cycles to failure. Irwin also described the systematic assessment of the toughness of a material and demonstrated the relationship between the crack shape and stress intensity concept (Irwin, 1960).

Fracture toughness is an indication of the amount of stress required to propagate a pre-existing flaw and stress intensity factor is used to determine the fracture toughness (N.E.R, 2011). The stress intensity factor is a function of loading, crack size and structural geometry. Fracture toughness is a very significant material property since the occurrence of defects is not entirely avoidable in the processing, manufacture, assembly or service of a material/component (N.E.R, 2011). Moreover, the strength of a material is typically dependent on the initial crack size that in turn is limited to the size of defects. These defects may appear in the form of cracks, voids, inclusions, weld defects, machining marks or design discontinuities. Therefore, application of fracture mechanics principles is essential to aerospace and power generation components, particularly in the development of novel materials and failures analysis related to critical design features or manufacturing related defects (Farahmand, 2001).

In the linear elastic fracture mechanics (LEFM) approach, the number of fatigue cycles or time to propagate the crack from initial size to some critical dimension is considered the useful fatigue life. The critical defect size is that dimension above which unstable fast fracture occurs (Holdsworth, 1980). The choice of critical defect size for fatigue crack may be based on the fracture toughness of the material (see Figure 2-29), loading geometry and permissible strain or change in the compliance of the material/component (Suresh, 1998). The critical value of fracture toughness is determined directly by laboratory pre-crack specimens with length and thickness of sufficient size to satisfy the linear elastic requirements of ASTM E399.

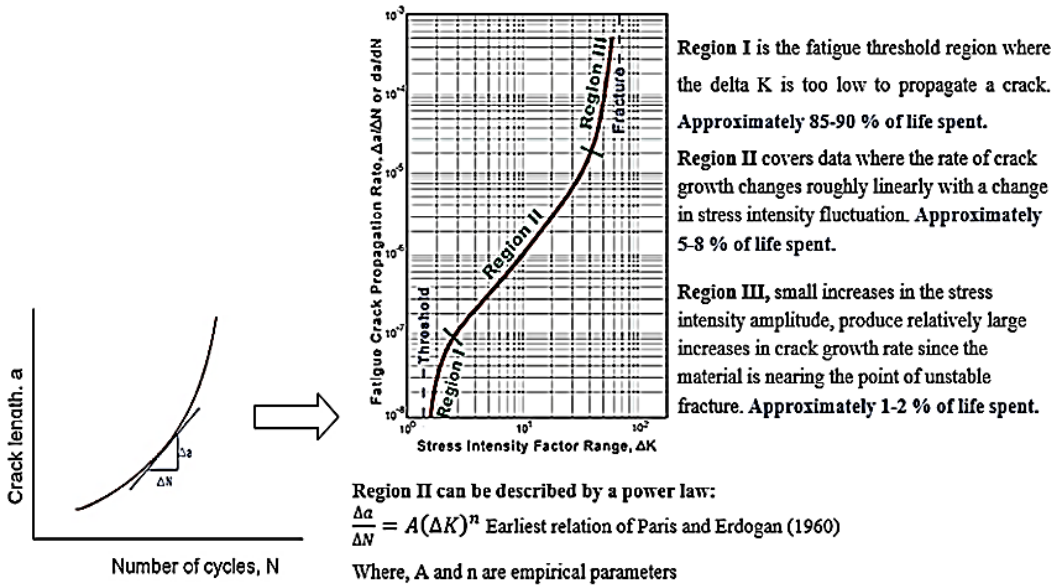

Figure 2-29: Typical fatigue crack growth versus life curve and crack growth behaviour. Modified from (Motarjemi, A. and Shirzadi, 2006).

The prediction of crack propagation life using fracture mechanics approach involves the use of crack growth empirical laws. Paris's law (Paris and Erdogan, 1963) has been widely used for the estimation of fatigue crack growth applications where catastrophic failures may occur. Further, the range of stress intensity factor present in the Paris empirical expression can be determined by Broek criterion (Broek, 1986). There is a considerable number of literature available on the state-of-the-art review of fracture mechanics principles (Anthony, 2007; Broek, 2012; Zhu and Joyce, 2012; Ransom, Glaessgen and Ratcliffe, 2013). The fatigue crack growth tests are generally carried out on standard compact tension (CT) specimen, according to ASTM standards (ASTM E399-12, 2013; ASTM E1820-15a, 2015; ASTM E647 − 15e, 2015).

2.5 CMSX-4 superalloy

CMSX-4 is trademark name of Cannon-Muskegon and a second-generation rhenium containing single crystal (SC or SX) nickel-based superalloy. It is widely used in the hot gas path of aeroengines and industrial gas turbines components, in particular, turbine blades and vanes (Stekovic, 2005). The CMSX-4 provides superior creep performance, stress rupture, fatigue, oxidation and high temperature corrosion resistance at elevated

temperatures, typically of at least 1150°C (Sengupta, A., Putatunda, S. K., Bartosiewicz, L., Hangas, J., Nailos, P. J., Peputapeck, M., Alberts, 1994).

The superalloy may be categorised as either chromia or alumina former, depending the alloy composition and application. CMSX-4 is an alumina former. The chromia and alumina improves resistance to hot corrosion and high temperature oxidation resistance, respectively. Therefore, including these element into the alloy chemistry with purpose of growing either chromia protective layer or alumina protective scale. One reason use of alumina formers is that less proactive layers are formed below 900ºC, thus, ideal for high temperature applications greater than 900ºC. But this at the expense of reduction of chromium content into the alloy, reducing the hot corrosion and corrosion-fatigue resistance. Chromia former tend to the used at temperatures below 900 ºC due to chromia forming is volatile above 900 ºC (Goebel, Pettit and Goward, 1973).

The microstructure of CMSX-4 superalloy consists of two-phase ($\gamma + \gamma'$). In the as-cast condition, the superalloy is characterized by gamma γ matrix, gamma-prime γ′ phase precipitates, and ($\gamma + \gamma'$) eutectic regions (Szczotok and Chmiela, 2014). A detailed description of CMSX-4 metallurgy and microstructure is available in (R.C. Reed, 2006).

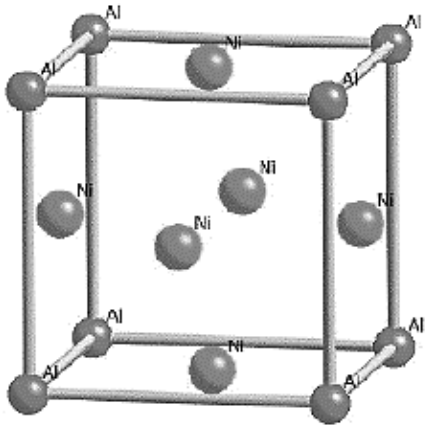

Figure 2-30. Schematic diagram of crystal structure of gamma-prime[14].

The gamma phase work as a matrix and is a continuous matrix faced centric cubic (FCC) crystal structure Ni-based austenitic phase that usually contains high percentage of solid solution element such as chromium, cobalt, molybdenum and tungsten (R.C. Reed, 2006).

[14] Retrieved from: http://www.phase-trans.msm.cam.ac.uk/2003/Superalloys/superalloys.html, accessed in 12/03/2016.

Gamma prime is ordered $L1_2$ FCC crystal structure with nickel atoms as face of the cube and aluminium and titanium as the corners of the cube (see Figure 2-30) Gamma-prime precipitate is intermetallic compound with volume fraction of 77% and cube length of 0.5 µm and size of gamma channels surrounding gamma-prime is about 0.1 µm (R.C. Reed, 2006).

CMSX-4 is a vacuum-melted cast superalloy and the chemical composition of the superalloy (in wt.%) is 9.0 Co, 6.5 Cr, 6.0 W, 5.6 Al, 1.0 Ti, 6.5 Ta, 0.6 Mo, 3.0 Re, 0.1 Hf, and a Ni balance. Rhenium (Re) in CMSX-4 improves the creep life by a factor of at least two, with further benefits for fatigue performance at high temperature (Mottura and Reed, 2014). Other alloying elements such as cobalt (Co) increases the gamma prime (γ′) phase solution temperature, providing resistance to high temperatures; Chromium (Cr) is aiming to improve their oxidation resistance; and Molybdenum (Mo) increases mechanical strength entering into solid solution in the matrix or forming carbides (R.C. Reed, 2006).

Moreover, crystal orientation also influence on the mechanical properties, such as fatigue and creep since are strongly crystal orientation dependent. Ni-base single crystal superalloys are highly anisotropic materials. It means that they have different properties in different crystallographic directions. Figure 2-31 shows a stereographic triangular indicating a crystal planes of a CMSX-4 sample analysed on the EBSD. In [001] direction, tensile yield strength is greater than [011] and [111] directions. Thus, better creep properties and preferred upward direction for gas turbine blade applications.

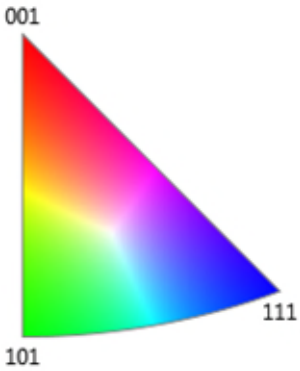

Figure 2-31. Example of an EBSD stereographic triangle showing the different [001], [101] and [111] crystal orientations.

Microstructural degradation in CMSX-4 superalloy at high temperature generally occurs through creep deformation (i.e. rafting of the γ′ structure, twining, etc.), recrystallization,

oxidation diffusion, microstructure defects (i.e. porosity, segregation, recast, etc.) and hot corrosion attack (Fullagar *et al.*, 1996; Cox *et al.*, 2003; Carter, 2005; Neidel *et al.*, 2005; Sidhu, Prakash and Agrawal, 2006). Typical microstructure of aged CMSX-4 is shown in Figure 2-32. It can be seen that there is deterioration of gamma-prime due to rafting. Rafting is a directional coarsening degradation of gamma-prime precipitates due to exposure to high temperature and high centrifugal load, thus to reduce creep resistance (Reed *et al.*, 1999). Two types of rafting exists, first the P-type which rafts lies parallel to the load direction and second lies transverse to the load direction (Fedelich *et al.*, 2012).

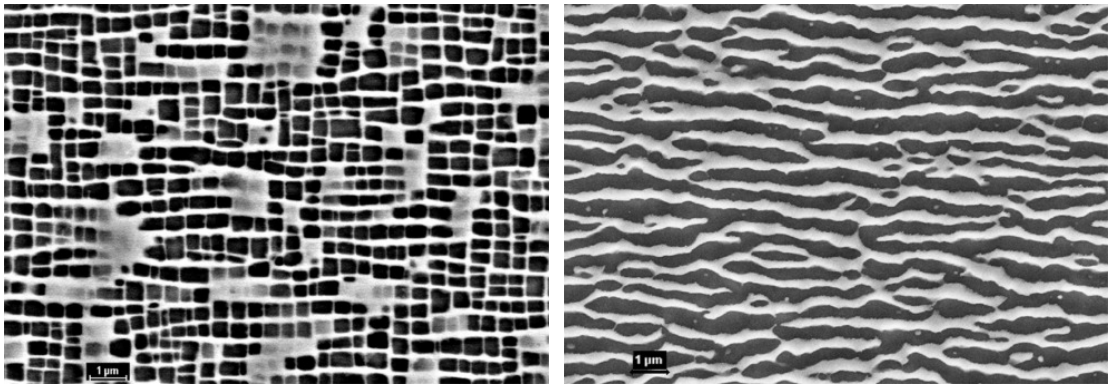

Figure 2-32. Example of secondary electron image showing single crystal Ni-base microstructure: (a) before the test and (b) after creep exposure at high temperature. adopted from (Giorgetti, 2017).

2.6 Review of fatigue life in CMSX-4 superalloy

This section presents the state-the-art review on fatigue life of CMSX-4 nickel-based superalloy for high temperature applications. The review covers most of the research work conducted on thermo-mechanical fatigue, creep, low cycle fatigue, stress rupture and hot corrosion fatigue. Further, a brief introduction to nickel-based CMSX-4 superalloy is given below.

2.6.1 Thermo-mechanical and low cycle fatigue

There have been a lot of investigations on thermo-mechanical fatigue damage evaluation of CMSX-4 material using the traditional strain-life method or the low cycle fatigue approach for optimising the design procedure (Marchionni, 2002a). Some researchers adopt the out-of-phase (OP) conditions to guide the crystal orientation on deformation behaviour and fracture life for turbine component design. In TMF, microstructural stability plays an important role since there are a strong correlation and interactions

between the degradation mechanisms occurring at high and low temperatures. Recently, a study in OP TMF found that inelastic strains clearly occurred in gamma (γ) phase microscopically and asymmetric deformation causes ratcheting deformation in γ and gamma prime (γ') phases of CMSX-4 tested at 200 to 800°C (Mukai Y, Kagawa H, 2015).

Another study revealed that the material degradation (i.e. rafting) during OP TMF with a maximum temperature of 1000 °C led to different mechanical behaviour when the minimum temperature was reduced from 400 to 100 °C (Arrell *et al.*, 2004). This change in temperature resulted in crack initiation life reduction by a factor of 3. It is also found that highly localized twinning can cause deformation during OP TMF cycling (Moverare, 2007; Moverare, Johansson and Reed, 2009).

A comparative study on OP TMF (400 to 950ºC) and isothermal LCF (950ºC) behaviour of CMSX-4 alloy have been investigated through triangular and trapezoidal waveform, respectively (Hong *et al.*, 2011). OP TMF life exhibited less than a half of LCF life. The localized twins provided a preferential crack path and accelerated surface crack propagation through OP TMF cycling. LCF deformation was largely dependent on the oxide diffusion. Whilst, OP TMF deformation was dominated by partial dislocation movement of [111], [112] slip system. Similar results were also reported in (Kang *et al.*, 2011).

In-phase (IP) TMF behaviour of CMSX-4 is also being investigated. Seo and Kim studied the IP TMF behaviour in the temperature range of 500 to 1000ºC in the air. The authors found that IP TMF loading resulted in formation of creep cavities adjacent to internal interdendritic pores which eventually coalesced to nucleate subsurface fatigue cracks (Seo, Yandt and Kim, 2013).

The influence of crystal orientations also has an impact on the alloy deformation and fracture. There are a number of isothermal low cycle fatigue assessments reported on CMSX-4 considering various crystal orientations (Arakere N, 2002; Hou *et al.*, 2008; Xu, Reuter and Rothkegel, 2008; Scholz *et al.*, 2009). A study investigating uni-axial strain controlled loading configurations at 750°C and 950°C in CMSX-4 specimens found that the specimens can experience hardening or softening cycling depending on the temperature and loading configuration (Barnard *et al.*, 2012). Through an examination of fatigue fracture surfaces, it was found that the fracture surfaces at 750°C were highly

faceted and cracks highly inclined to [111] orientations. Whilst, fractures at 950ºC in [001] specimens demonstrated to remain perpendicular to the applied tensile stress.

A new micromechanics model has also been proposed to predict the TMF and LCF lives (Okazaki and Sakaguchi, 2008), applying the Eshelby's theory (Eshelby, 1961) and the Mori-Tanaka's averaging approximation (Mori and Tanaka, 1973). The model enabled to successfully estimate not only the unique characteristics in the TMF and LCF failures but also the effect of γ' geometry on the LCF lives. Coppola aiming to simulate the real high-power transient conditions in aeroengines investigated clockwise and counter-clockwise diamond cyclic loading on bare and coated CMSX-4 specimens to investigate their influence on the TMF, creep and LCF in the range of 750ºC to 1050ºC (Coppola *et al.*, 2008). The findings found to be in agreement with open literature data (Strangman, 1992; Thomas, 1994; Fullagar and et Al., 1996).

The effect of different γ/γ′-morphologies on the LCF behaviour, namely cuboidal γ′-particles, γ/γ′-rafts perpendicular and γ/γ′-rafts parallel to the stress axis have been studied in the past (Ott and Mughrabi, 1999). The LCF tests under strain-controlled and high temperature (950ºC and 1050ºC) showed that the fatigue lives were reduced for specimens with γ/γ′-rafts perpendicular to the stress axis and extended for specimens with γ/γ′-rafts parallel to the stress axis. Specimens with cuboidal γ/γ′-particles exhibited intermediate fatigue lives.

Cyclic dwell LCF behaviour of CMSX-4 under strain-controlled at 1100ºC has been studied (Yandt *et al.*, 2012). Microstructural analysis revealed that no-dwell fatigue induced isotropic coarsening of the γ′ precipitates, while compressive dwell loading led to the formation of discontinuous γ′ rafting parallel to the loading direction. The localised oxide attack from the specimen surface promoted the fatigue crack nucleation. Further, compressive dwell fatigue lives were four to fifteen times shorter than no-dwell loading.

Stekovic presented a study on the low cycle fatigue (LCF) properties and degradation mechanisms of uncoated and coated CMSX-4 tested at two temperatures, 500°C and 900°C (Stekovic, 2005). Results have shown that at 500°C the coating had a detrimental effect on the fatigue life while at 900°C the coating improves the fatigue life of the superalloy. The ductile to brittle transition temperature contributed to early cracking of

the coating hence reducing the fatigue life, while the positive effect of the coating at 900°C resulted in a slower propagation of cracks.

2.6.2 Creep and low cycle fatigue

Creep is known to deteriorate the mechanical properties such as yield stress and reduce LCF life nearly by a factor of 10 (Epishin *et al.*, 2010). The high temperature creep-fatigue behaviour on CMSX-4 has been studied by many researchers such as effects of rafting at 1150ºC (Reed *et al.*, 1999; Epishin *et al.*, 2005; Klingelhöffer, Epishin and Link, 2009). The authors found that the decrease of LCF life correlates with the formation of rafted γ/γ′ microstructure.

Other researchers have investigated the fatigue damage related to the growth of micro cracks originating from initial casting defects such as porosity. A damage model has been developed for predicting the creep-fatigue life of CMSX4 specimens at 950°C under LCF conditions and of 450-950°C for TMF conditions (Koster, Alam and Rémy, 2002). The model considered the distribution of the pore size and their propagation due to fatigue and creep loading. The results suggest that large near surface pore may develop into a surface crack and the weakening of material through oxidation embrittlement could accelerate its propagation. Another study found that fracture surfaces induced by creep damage is internal and cracks nucleates from the pores and in the fatigue damage typically initiates from the external surface and propagates inward in stages I, II and III (Marchionni, Goldschmidt and Maldini, 1993). These findings were based on the tests performed in the range of 500 to 1100 °C under creep, low-cycle, and thermo-mechanical fatigue conditions.

Similarly, TMF (at 250 to 750 °C, 450-950 °C and 550-1050 °C), LCF and creep life (at 750, 950 and 1050 °C) of CMSX-4 specimen at [0 0 1], [0 1 1] and [1 1 1] were assessed through four-point bending tests (Scholz *et al.*, 2008). Later, developed a predictive model for creep deformation based on Garofalo equation and a Larson–Miller approach has developed (Scholz *et al.*, 2009). The model considered cyclic elastic-plastic deformation and fatigue behaviour. The tests were conducted on CMSX-4 samples at different temperatures (850-1050ºC) and at the typical crystallographic orientations [0 0 1] and [1 1 1].

The stress-rupture behaviour of CMSX-4 has been modelled using a damage-mechanics technique (MacLachlan and Knowles, 2000). The model considers the level of damage required to cause failure is delineated by the effective stress reaching the materials ultimate tensile strength (UTS). The authors found this technique reliable to ensure the short-term rupture data extrapolate back to the UTS.

A finite element model based on the slip system approach is used to demonstrate the effects of rotation and bending on specimens (Gunturi, MacLachlan and Knowles, 2000; MacLachlan *et al.*, 2001). For validity of these simulations, authors compared with the results of creep tests performed on CMSX-4 specimens in several different orientations at 950°C. Also, a viscoelastic constitutive model has been developed to predict the degradation effect of rafting on the mechanical behaviour of CMSX-4 in the temperature range of 850-1100°C and its kinetics during complex loadings (Fedelich *et al.*, 2012). The microstructure analysis revealed that the rafting kinetics is driven by the reduction of the internal stresses.

2.6.3 Fatigue lifetime based on notches

A deterministic fracture mechanics approaches are applied to the analysis of the fatigue behaviour of CMSX-4 notched specimens (Wu *et al.*, 2005). The effect of pore shape, size and position on the residual life of notch CMSX4 specimens at 650 °C and 725 °C in air and vacuum have been investigated (Reed and Miller, 2008). The initial results show the role of interdendritic porosity in initiating fatigue in both alloys, and the number of initiation sites is found to directly impact on the fatigue life debt. In the air in CMSX-4, the cracks do initiate at subsurface pores, whilst, tests under vacuum conditions demonstrates that cracks initiate at surface porosity. The model also explains the observed scatter in notch fatigue lifetimes.

Strain control fatigue response and notch fatigue behaviour of three alloys including CMSX-4 at 800 ºC were explored (Marchionni, 2002b). The authors through measured crack growth data and pore sizes, it was found that fracture mechanics approach was more appropriate for predicting the residual lives at 650ºC. Further, Walker strain predictions of notch lives at 800ºC were more meaningful because it considered the stress relaxation effect at the casting pores (Evans *et al.*, 2009). Moreover, non-linear FEM modelling has also been used to identify fatigue damage parameters at 950ºC on the notch LCF

behaviour (Filippini, 2011b) and creep-fatigue behaviour (Filippini, 2011a) for the application of turbine engine components.

2.6.4 Hot Corrosion and corrosion fatigue

A significant number of investigations on hot corrosion assessment of CMSX-4 have been conducted by use of isothermal cyclic tests (Nicholls, Simms and Encinas-Oropesa, 2007; Orosz *et al.*, 2007; Matsumoto *et al.*, 2011; Lortrakul *et al.*, 2014; Sumner *et al.*, 2014). Based on the mass change data and metal loss data from CMSX-4 hot corrosion tests, a simple furnace-based approach has been developed to map the temperature dependence of hot corrosion for alloys in the temperature range 600–1000 °C (Haight *et al.*, 2015). A probabilistic assessment based on Weibull statistics has been proposed considering the transition from incubation lifetime to propagation rates of CMSX-4 and IN738LC samples, which assists in the development of quantitative hot corrosion damage models (Sumner *et al.*, 2014).

An investigation on the effects of fuel gases contaminants on bare and in the platinum aluminised (Pt-Al) coated CMSX-4 samples was conducted using traditional mass change method (Encinas-Oropesa *et al.*, 2014). The authors carried out type II hot corrosion tests as per reported procedure (Simms *et al.*, 2001). Results indicated that the uncoated CMSX-4 was more sensitive to damage by alkali sulphates than Pt-Al coated CMSX-4 samples at 700 ^{o}C, in combustion environment with sulphur and chloride deposits. The sulphur and chlorine gaseous contaminants are extremely corrosive, forming deposits of sulphates, which in turn can form in a molten state on the surface of the components. These molten deposits can promote accelerated corrosion and degradation, known as hot corrosion (Sumner *et al.*, 2013). This phenomenon can cause a gradual loss in turbine efficiency and reliability of hot gas path turbine blades and vanes (Encinas-Oropesa *et al.*, 2014).

A systematic study of the effects of various salt deposits, salt concentration, and sulphur level on the cyclic oxidation of CMSX-4 in the air at temperatures above 1000°C has been presented by (Pahlavanyali *et al.*, 2014). The alloy was tested both in the bare and in the Pt-Al coated conditions. It was found that cyclic oxidation with the addition of salt offers an accurate, flexible, reproducible and above all realistic method of assessing the life of turbine components.

A dimensional metrology approach in a probabilistic content to predict hot corrosion damage in terms of metal loss was proposed (Simms, Encinas-Oropesa and Nicholls, 2008). The authors used pre-exposure contact measurements and post-exposure measurements of features on CMSX-4 polished cross-sections. These measurement methods permitted distributions of damage data to be determined and allowed different approaches to corrosion modelling to be explored and their practicality to be assessed.

A considerable literature on fundamentals of hot corrosion in nickel-based alloys been published in the open literature (Pettit *et al.*, 1984; Tatlock, Hurd and Punni, J, 1987; Eliaz, Shemesh and Latanision, 2002b; Sidhu, Prakash and Agrawal, 2006; Deodeshmukh and Gleeson, 2008; Nicholls and Simms, 2010; Sumner *et al.*, 2013). However, there is a scarce number of publications in the high temperature corrosion-fatigue behaviour of nickel-base alloys for gas turbine blades and vanes applications, particular in the CMSX-4 alloy (Sato *et al.*, 1995).

Most of the available publications relate to hot section nickel-based disc alloys (Gabb *et al.*, 2010; Rosier *et al.*, 2014; Child, Meldrum and Onwuarolu, 2016; G. J. Gibson *et al.*, 2016). Others on hot corrosion and low cycle fatigue behaviour of IN718 (Mahobia *et al.*, 2014), Nimonic-263 (Sahu *et al.*, 2015), DZ125 (Yang, Li and Qi, 2015), Rene 80 (Rahmani and Nategh, 2010), Udimet 500 (Pieraggi, 1987) and IN738LC (Jianting *et al.*, 1984).

2.6.5 Remarks

The CMSX-4 nickel-base superalloy was developed initially for the use as a structural material in blades and vanes of aircraft gas turbine engines for the aerospace industry. Later, used in the industrial gas turbine industry due to its superior mechanical properties, good corrosion resistance, oxidation, creep resistance at high temperature (Fullagar *et al.*, 1996; Ford *et al.*, 1999). In past, considerable number of publications have reported improved characteristics of CMSX-4 superalloy focusing on the thermal-mechanical fatigue, creep-fatigue interaction, hot corrosion, and fatigue crack growth behaviour under different temperatures and crystal orientations. These studies have demonstrated that a variation in the microstructure, metallurgical defects, different environments and

variable loading can impact on the lifing performance and rate of degradation of CMSX-4 nickel-based components.

A significant number of investigations on fatigue assessment of turbines materials including nickel-based CMSX-4 superalloy has been conducted by use of the strain-life and fracture mechanics approach, such as Larson-Miller Parameter, Cofin-Manson and Paris law. Finite element modelling (FEM) has also been in used for assisting in the development of predictive fatigue and damage modelling for turbine components design. It has the advantage of providing the exact sites, directions, and magnitudes of high stresses concentration and the map of stress distribution in the entire region of the specific feature being considered.

Another critical observation is that there is very limited work on the corrosion-fatigue behaviour of CMSX-4 superalloy. The next section describes the corrosion-fatigue process in alloys and a state-of-the-art literature review of fatigue life studies in cooling film holes.

2.7 Corrosion-fatigue

The corrosion-fatigue is an emerging degradation mechanism experienced by aeroengine hot-section components, such as turbine blades, vanes and discs. The current demands of high efficiency led to an increase in turbine inlet temperatures (TIT). In past, TIT's were low and ranging between 650 to 900 degrees Celsius, so there has no or little mechanical interaction. In recent years, TIT's have gone up to 1200 degrees Celsius and mechanical interaction has increased since, thus to rise in corrosion-fatigue cracking. To sustain high temperatures, materials have been developed to have high temperature resistance and creep strength. However, at expense of reducing chromium content in superalloys, thus to decrease in hot corrosion resistance. One example is nickel-base CMSX-4 superalloy, an alumina former. In addition, impurities in fuel and air-intake has increased over the years. Increase in the heat and airborne salt flux also causes rate of deposition of corrosion elements in the superalloy (Leyens, Wright and Pint, 2001).

The nickel-based superalloys when exposed to salts and sulfur compounds at elevated temperatures can lead to hot corrosion fatigue crack growth in aeroengine hot-section components. Once micro pits are formed under hot corrosion environment, these serve as

stress concentration sites where cracks can initiate and propagate to failure under subsequent cyclic loading (Chan *et al.*, 2016). As such, corrosion-fatigue has been defined by National Association of Corrosion Engineers (NACE) as *"a result of the combined interaction between alternating or cyclic stresses and corrosive environment"*.[15] The corrosion-fatigue mechanism can be characterised in three stages (see Figure 2-33).

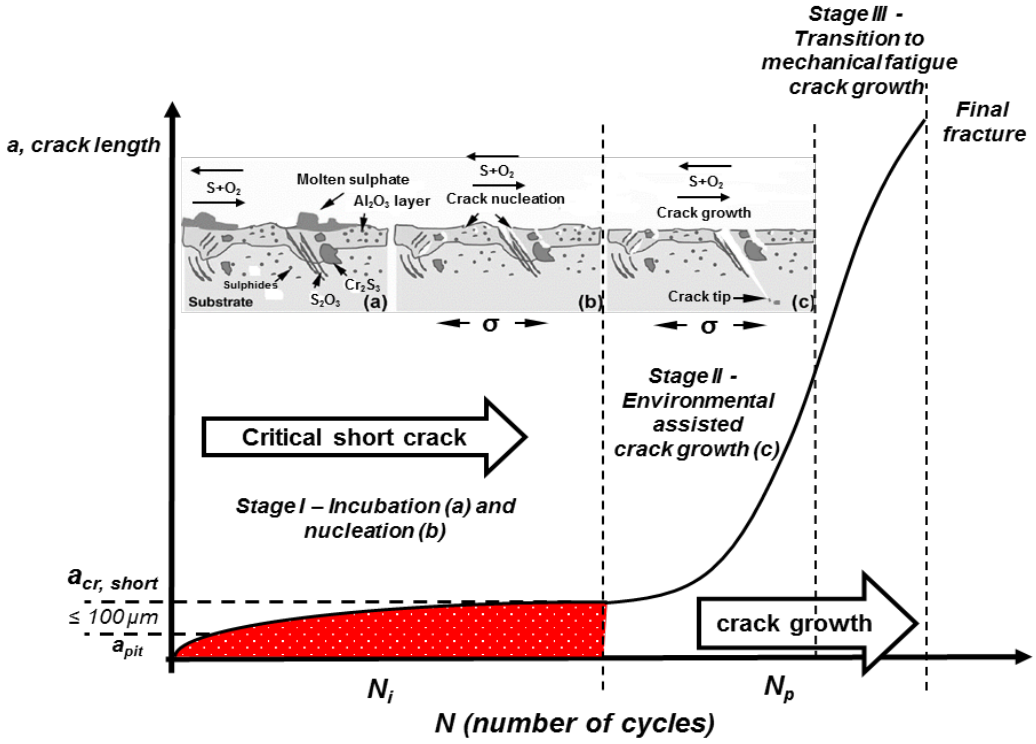

Figure 2-33. Schematic diagram of corrosion-fatigue stages in gaseous environment. Modified from (Chan, Enright and P. Moody, 2013) and (Qining *et al.*, 2015).

The stage I – incubation and nucleation, before crack initiation a protective scale is formed which changes with exposure time and the formation and growth of pits on the alloy surface (Chiang, Pettit and Meier, 1983). The protective layer is mostly consisted of oxide rich in aluminium, chromium and nickel (Al_2O_3, Cr_2O_3 and Ni_2O_3). The dissolution of protective oxide is caused by molten sulphates followed by fatigue crack nucleation at corrosion pits. Multiple cracks initiates at the surface of protective scale through stress-assisted corrosion. The cracks remain small, less than 100 microns, or taken by corrosion front forming pit like features with increasing exposure time. In

[15] https://www.nace.org/Corrosion-Central/Corrosion-101/Corrosion-Fatigue/, accessed in 20/01/2015.

presence of high cyclic stresses triggers a transition from pitting to corrosion-fatigue crack growth. The incubation and nucleation process is similar to static hot corrosion and stress corrosion cracking mechanism, (Pettit *et al.*, 1984) and (Gangloff, 2005), respectively. Figure 2-34 illustrates initial oxidation of chromium and aluminium formers in nickel-base superalloys.

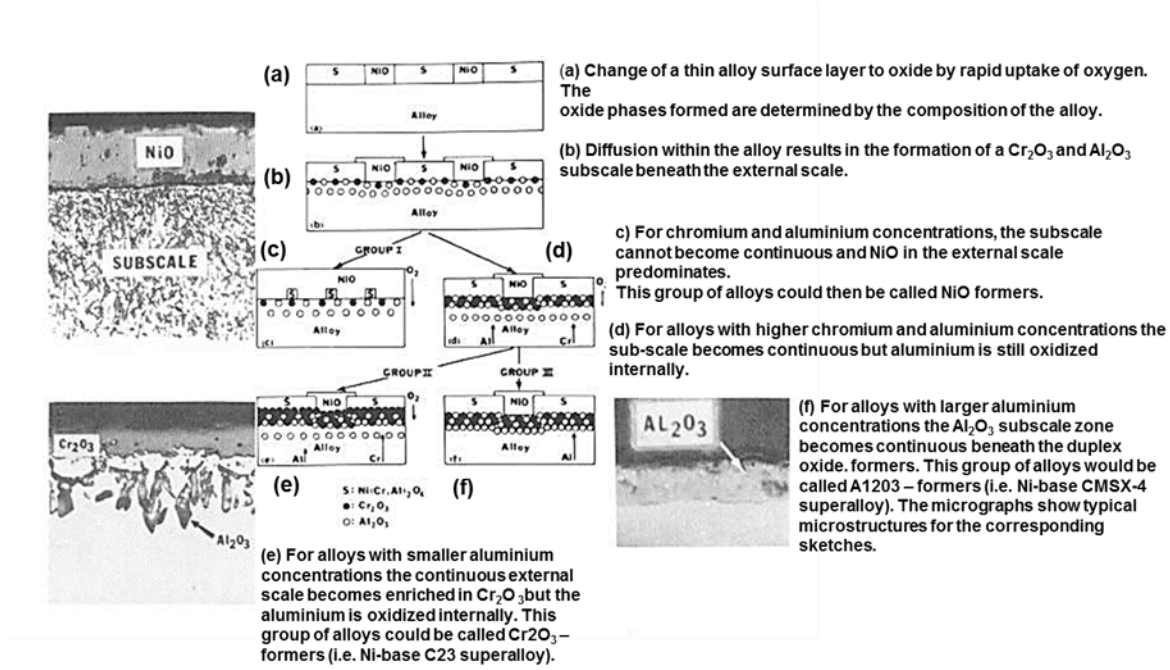

Figure 2-34. Schematic diagram to illustrate oxide scale formation in nickel-based superalloys. Modified from (Pettit and Meier, 1984). Used with permission of The Minerals, Metals & Materials Society.

Existing literature suggests that more than one driver exists causing breakdown of the protective scale at the end of incubation stage. These includes as follows (Pettit, 2011)

- Heat flux and temperature influences the rate of deposition of salts and corrosive species, such as sodium, sulphur and vanadium.
- Acidic and salt fluxing of the scale, plays important role in depletion of protective scale, such as nickel oxide and alumina scale.
- Thermal gradients between metal surface and gas flow.
- Salt chemistry and rate of deposition which could be dependent of pressure.
- Mechanical cracking of protective scale due to thermal cycling.
- Impurities in the fuel and intake air, as well as fuel/air ratio.

The impurities in the atmosphere including sea air leads to formation of deposits rich in sodium sulphate/vanadium in surface of the engine components. The deposits are in liquid or semi-liquid at temperatures ranging between 550ºC-900ºC, causing enhance metal/alloy deterioration due to oxidation and sulphidation reaction.

Corrosion-fatigue stage II, propagation is characterised by sulphur/oxidation embrittlement. It is linearly proportional to exposure time and sulphate concentration. Internal sulphidation beneath protective scale forms sulphide oxides (Cr_2O_3 and Ti_2O_3) which leads to depleting of the surroundings alloy elements. The sodium sulphate, sulphide oxides and oxygen absorption across the crack tip act as stress raiser, enhancing the rate of corrosion-fatigue crack growth.

The stage III of corrosion-fatigue is the transition mechanical fatigue, one crack reaches a critical threshold. The transition is gradual with a mix of corrosion-fatigue and mechanical fatigue being relatively small cracks. The mechanical fatigue dominates at larger cracks size and crack growth behaves more cyclic driven than exposure time-based. The final fracture mode occurs in tensile mode.

2.8 Fatigue life of cooling holes

Laser drilling process is known to induce localised stress concentrations, thermal damage, microstructure alterations around the hole surrounding area (Beck, 2011). Therefore, decreasing the operating life of laser drilled components in service owing to their brittle recast layer and susceptibility to hot cracking (Neidel *et al.*, 2005). Interestingly, past studies related to nickel-base cooling film holes for turbine blades and vanes applications have focused on the hole geometry, film-cooling effectiveness and effects of holes shape on thermal fatigue and creep life. For example, more recently comparative analysis of different laser drilling process including picosecond and nanosecond process were used to assess the fatigue life of DZ2125 superalloy cooling holes (Liang *et al.*, 2016). The fatigue tests were conducted at 900ºC and on single and multiple hole. The picosecond laser drilling has shown to provide better life performance than nanosecond. This is due to high quality holes produced by picosecond process. In addition, the authors found that different laser drilling process leads to slightly different fracture morphologies. This result found to be similar to fatigue lives of EDM specimens and high-speed EDM

specimens, where EDM specimens found to have better fatigue life characteristics (Wen *et al.*, 2017). These findings suggest that the drilling methods that produce better surface quality holes in terms of geometry and metallurgy will certainly have improve fatigue resistance.

The creep damage evolution models have been reported on nickel-based DD6 superalloy cooling holes (Jianwei and Zhixun, 2015). The models are based on finite element simulation and crystal plasticity theory. The authors (Jianwei and Zhixun, 2015) found that creep damage and resolved shear stresses were more pronounced in specimens with holes at 0, 15 and 45 degrees to surface than 30 degrees to surface. The study concludes that the 30 degrees angled cooling film hole has the longest creep failure life. Another study (Ai *et al.*, 2014), shown at 950ºC that there is nearly 50% creep life debit of specimens with cooling holes than specimens without cooling holes when the stress was kept at 377 MPa. Creep performance can also be influence by cooling holes arrangement, where by decreasing the horizontal distance of the holes results in poor performance, whilst, increasing the vertical distance of the holes improves the creep performance (Li *et al.*, 2013).

A study on the creep behaviour of a nickel-based single crystal has been investigated at 980 °C with two different crystallographic orientations (Yu, Yue and Wen, 2008). The authors in this study found that crystallographic orientations and cooling holes have significant influence on the stress rupture behaviour. In addition, FEM results reveal that stress and strain concentration near the holes edges are high, which indicates the crack nucleation and crack advance path in elliptical cooling holes (Wang *et al.*, 2013).

Effect of electro-chemically machined (ECM) acute angled cooling holes on tensile behaviour was also been investigated (Zhou *et al.*, 2015, 2017). The authors found that the maximum strain concentration was shown at the acute side of specimens drilled at 30 degrees angle than of 90 degrees to surface. These findings suggest that acute corners of the holes are sites of high stress/strain concentrations, hence potential sites of fracture in turbine blades and vanes.

The effects of roundness error on the cooling film holes through the experimental and finite element modelling have been also investigated (Chen *et al.*, 2014). The results shown that irregularities on the contour profile of the laser drilled hole caused by recast

layers could significantly decrease the life of the drilled holes. Moreover, the larger the roundness error, the shorter the low cycle fatigue life.

Another study used a damage model to characterise the fatigue lifetime (Degeilh, Bonnand and Pacou, 2013). The authors investigated laser drilling effects on three different hole diameters. The model consisted of a 3D averaging method that considers the material microstructure and hole shape. The results showed that small holes diameter under 0.4 mm had a better performance less than compared to large holes diameter under 0.8 mm and EDM holes of a diameter of 1.0 and 2.0 mm. The difference between the laser and EDM drilling fatigue life was caused by the difference in the microstructure, the thickness of the heat affected zone, and surface roughness of the specimens. Further studies were conducted to assess thermal-mechanical properties of thin-walled cylindrical specimens with laser-drilled holes. One study, shown that the TMF lives under similar conditions the laser drilled specimens were four times shorter than the smooth plain specimens (Kersey *et al.*, 2013). Whilst, another study (Pan, Bischoff-Beiermann and Schulenberg, 1999) used a local stress approach for assessing the fatigue life of laser drilled holes at high temperatures ranging between 700^{o}C and 900^{o}C. The metallographic analysis suggested that the micro cracks induced by laser drilling had no significant influence on the total live of the specimen under low cycle fatigue regime (10^5 cycles).

Moreover, in the late seventies used fracture mechanics to predict the life of different cooling hole configurations formed by laser drilling, EDM, and ECM under thermal-mechanical fatigue conditions (Gemma and Phillips, 1977). They found that the defects introduced by the different drilling techniques generate different initial defect sizes and that this knowledge could be used to estimate the life of cooling holes for each drilling technique. However, no details were reported on the different methods of drilling conditions and potential initial defect sizes produced.

2.9 Knowledge gaps

The following gaps from the literature review are summarised as follows:

1. There is a need for developing an understanding of laser drilling process parameters influence on the recast layer thickness and how to minimise the surface cracks formation in nickel-base effusion shaped cooling holes.

2. The effects of recast layer thickness on high temperature fatigue produced by laser drilling process is very limited. The existing literature does not fully detail the influence of process parameters on the fatigue life.
3. There is a scarce research related to corrosion-fatigue of nickel-base CMSX-4 superalloy using stress-life (S/N) approach, when considering the application for gas turbine blades and vanes design. Majority of related fatigue life assessment on CMSX-4 superalloy are limited to TMF, LCF, creep-fatigue interaction and mass loss due to hot corrosion.
4. The corrosion-fatigue behaviour in nickel-base superalloys has received very little attention, particularly in a gaseous environment. The need for investigating the effects different load cycles, effects of salt chemistry and different gases (NaCl, SO2, etc.). In addition, influence of pressure on corrosion-fatigue crack growth (CFCG).
5. Existing fatigue empirical and damage models do not capture the influence of key process variables and fatigue life interaction at initial stages of product design.

In view of the gaps found in the literature, this research attempts to investigate the correlation between laser drilling process parameters, recast layer thickness and corrosion-fatigue behaviour of CMSX-4 effusion cooling holes in a simulated laboratory environment. In addition, there is an attempt to develop an empirical model considering the effects of surface defects and applied stress for estimating the residual life of cooling holes at the initial design and manufacturing stages.

3 RESEARCH METHODOLOGY

This chapter presents research methodology used for this thesis. The chapter details the experimental procedures, techniques and equipment used throughout the research. It includes laser drilling experiment details, metallography sample preparation and analytical microscopy used for the characterisation, corrosion-fatigue testing details, statistical techniques and modelling approaches employed.

3.1 Experimental details

3.1.1 Workpiece

The base material used as the workpiece is a single-crystal CMSX-4 nickel-base superalloy, which is used in the gas turbine blades and vanes due to its high temperature fatigue and corrosion resilience characteristics. Table 3-1 provides the nominal composition of the CMSX-4 superalloy. The plates of about 65 mm x 8.0 mm x 2.0 mm in size were used for the entire experimental trials, as displayed in Figure 3-1. The thickness of 2.0 mm used is approximately the leading edge wall thickness that used for turbine vane and used in previous studies (Leigh *et al.*, 2009).

Table 3-1. Nominal composition (wt %) of the CMSX-4 superalloy (Sengupta et al., 1994).

Element	Nomenclature	Composition
Chromium	Cr	6.5
Cobalt	Co	9.6
Tungsten	W	6.4
Rhenium	Re	3.0
Molybdenum	Mo	0.6
Aluminium	Al	5.6
Titanium	Ti	1.0
Tantalum	Ta	6.5
Hafnium	Hf	0.1
Nickel	Ni	Balance

Before laser drilling, an anti-spatter silicon-based coating (Silkolene®) was applied on the top and bottom surface of the samples, creating a protective layer against spatter/debris. The coating requires a curing time of a minimum of 12 hours at room temperature, and it can be easily removed by a hot water wash. Figure 3-2 shows the coated flat plate samples before and after laser drilling.

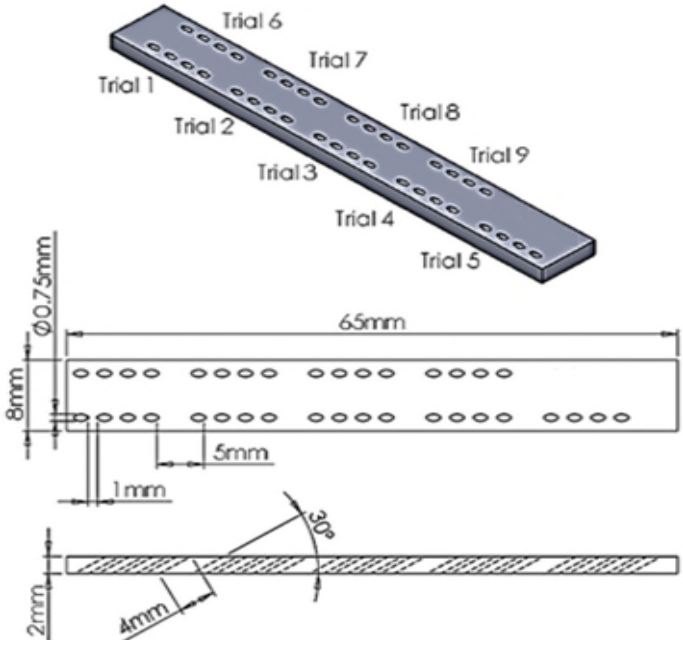

Figure 3-1. Schematic layout of the Ni-base CMSX-4 specimen's arrangement for laser drilling (dimensions not to scale).

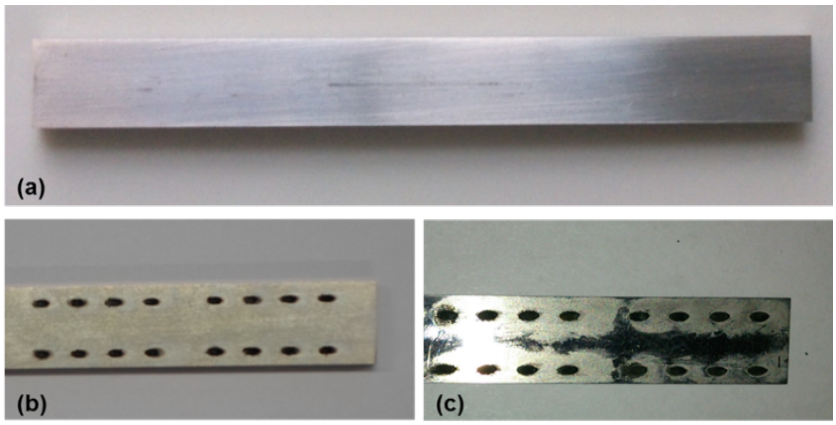

Figure 3-2. Example of a section of CMSX-4 sample (a) before laser drilling; after laser drilling: (b) with anti-spatter coating and (c) with anti-spatter coating removed.

3.1.2 Laser system

A 5-axis LASERTEC 80 PowerDrill machine (see Figure 3-3), fitted with a 300 Watts millisecond pulsed Nd: YAG laser source at a wavelength of 1.064 μm was used for the experiments. All experiments performed on a laser beam angled at 30^{o} to the workpiece surface. Typical beam profile characteristics in DMG machine is shown in Figure 3-4. A beam profiler measures the beam spatial energy density distribution. It provides an understanding of the beam spatial characteristics such as beam focus spot size, peak

position, peak power, beam divergence, beam propagation (M^2), mode structure, and stability and wavefront analysis[16].

Figure 3-3. Laser machine used for the drilling of the samples.

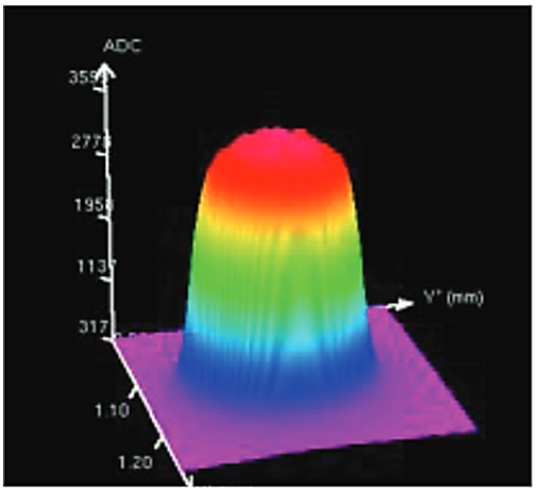

Figure 3-4. Typical beam profile of DMG laser system used (Antar *et al.*, 2016).

3.1.3 Design of experiments

The effect of input parameters on any performance characteristics can be analysed by (i) traditionally varying one factor at the time while keeping others factors constant; (ii)

[16] http://www.laserfocusworld.com/articles/2010/02/beam-characterization.html, accessed on 28/01/2018.

design of experiments techniques such as full factorial, central composite design and Taguchi orthogonal array based. Taguchi method design of experiments L9 orthogonal array (OA) was employed and found to be suitable for the selected three main control factors and their ranges based on the available literature (Ross, 1998; Roy, 2010). This method allowed the number of trials required to be minimised compared to the classical combination method with the full factorial experiment, which would have required 36 experimental runs to capture the influencing parameters.

The L9 OA had 3 columns and 9 rows providing 8 degrees of freedom to manipulate three control parameters with three levels, see Table 3-2. The control factors and their levels are presented in Table 3-3, which includes peak power, pulse frequency and trepanning speed. The input parameters and their values were selected based on the industrial consultation and literature review. It enabled to decide the range of values for each input parameters would achieve similar range of recast layer thickness and extent of cracks observed in actual laser drilling operations. The remaining laser drilling processing parameters held constant are presented in Table 3-4.

Table 3-2. L9 Orthogonal array design of experiments.

Trial No.	Control Parameters			Responses							
				RLTmax (µm)				CND			
	Peak power (Level)	Pulse freq. (Level)	Trepan speed (Level)	R1	R2	R3	R4	R1	R2	R3	R4
1	1	1	1	-	-	-	-	-	-	-	-
2	1	2	2	-	-	-	-	-	-	-	-
3	1	3	3	-	-	-	-	-	-	-	-
4	2	1	2	-	-	-	-	-	-	-	-
5	2	2	3	-	-	-	-	-	--	-	-
6	2	3	1	-	-	-	-	-	-	-	-
7	3	1	3	-	-	-	-	-	-	-	-
8	3	2	1	-	-	-	-	-	-	-	-
9	3	3	2	-	-	-	-	-	-	-	-

Table 3-3. Control factors and their levels.

Symbol	Control parameters	Level 1	Level 2	Level 3
A	Peak power (kW)	8.3	10	12.5
B	Pulse frequency (Hz)	20	22.5	25
C	Trepanning speed (mm/min)	75	100	125

Table 3-4. Laser beam parameters.

Constant parameters	Output
Laser	Nd:YAG
Mode	Trepanning
Operating mode	Pulsed
Wavelength	1064 µm
Beam angle	30 degrees
Lens focal length	170 mm
Stand-off distance	10 mm
Nozzle type	conical
Nozzle exit diameter	~2.5 mm
Spot diameter	0.190 mm
Assist gas type	Oxygen
Gas pressure	100 psi/0.68 MPa
No. of orbits	2
Maximum average power	130 watts
Pulse energy	5 Joules

The minimum and maximum value of power density (defined as the laser power per unit area) for the present range of peak power has found to be 2.9 x 10^{11} W/m^2 and 4.1 x 10^{11} W/m^2, respectively using below equation:

$$\boldsymbol{Power\ density} = \frac{\boldsymbol{Peak\ power}}{\frac{\boldsymbol{\pi d^2}}{\boldsymbol{4}}} = \frac{\boldsymbol{Watts}}{\boldsymbol{m^2}} \quad \textbf{(3-1)}$$

3.2 Microscopy

3.2.1 Sample preparation

After laser drilling, the laser-drilled samples were cleaned in hot running water and vapour blasted to remove the anti-spatter coating and excess of debris, respectively. The laser drilled plate, containing nine trials with four holes replication was cross-sectioned on a cutting machine with coolant to a single trial sample, as shown in Figure 3-5.

Each sectioned trial sample was cleaned with isopropanol and firmly clamped with laser-drilled holes facing outside. This position enables the cross-section view of drilled holes in an optical microscope. Then, each sectioned sample were clamped and mounted in a Bakelite material using an automatic hydraulic hot compression mounting press machine

(ATA® Opal 410), as displayed in Figure 3-6a. The procedure followed is outlined in the machine manual, and the mounting parameters used are listed in Table 3-5.

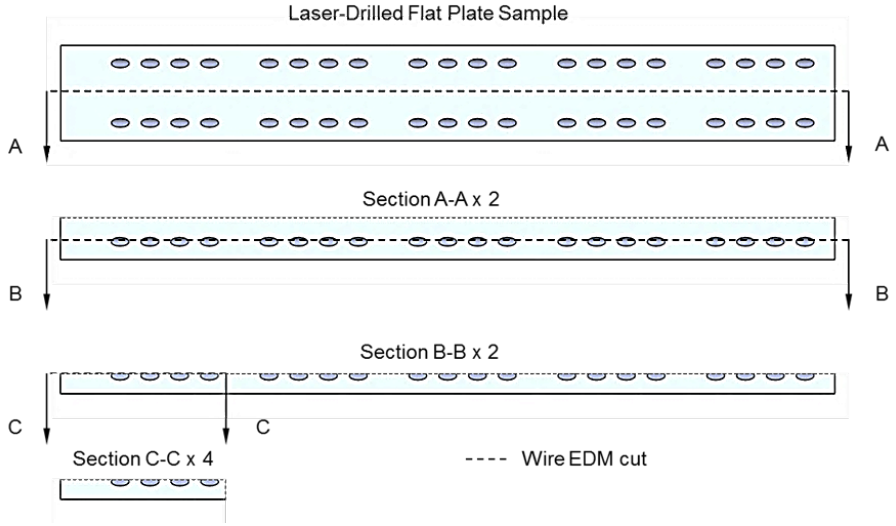

Figure 3-5: Schematic illustration of sectioning operations carried out on the laser-drilled samples. A Wire EDM machine was used to cut samples in two parts, section A-A, and then to section B-B, and lastly to section C-C.

The grinding and polishing was performed on an automatic Beuhler Metaserv Motopol 12 machine (Figure 3-6b). The sequence followed for the grinding and polishing operations are outlined in Table 3-6. The polished samples were rinsed with isopropanol and blown dry. This cleaning process removes any impurities that can cause scratches. The mounted samples were then etched through a suggested electrolytic etching technique procedure (Sezer *et al.*, 2006), as outlined in Table 3-7. The final mounted resin sample is shown in Figure 3-7. Finally, the samples were ready for detail observation of cross sections of angled drilled holes on SEM.

Table 3-5. Compression mounting operation procedure for 30 mm mould.

Moulding Parameters	
Type of Resin/Form	Phenolic/Granular
Colour	Black
Moulding powder	3 – 4 scoops
Moulding temperature	185ºC
Holding time at temperature	4 minutes
Curing time	8 minutes

Table 3-6. Procedure for grinding and polishing the mounted resin samples.

Step	Operation	Grit paper	Time	Speed	Load	Lubricant
1	Grinding	Silicon carbide 1200 grade	2 min	150 rpm	5 lb/per sample	Water
2		Silicon carbide 2500 grade	3 min			
3	Polishing	6 µm Microcloth®	2 min		4 lb/per sample	Colloidal silica solution, 0.05 µm
4		3 µm Microcloth® disc	4 min			

Table 3-7. Etching procedure for the mounted acrylic resin samples.

Technique	Composition	Conditions
Electrolytic etching	30 ml Deionised water	Etch the solution with 2.5 Volts DC for approximately 20-25 seconds in order to reveal the recast layer microstructure
	10 ml Phosphoric acid	
	15 ml Sulphuric acid	

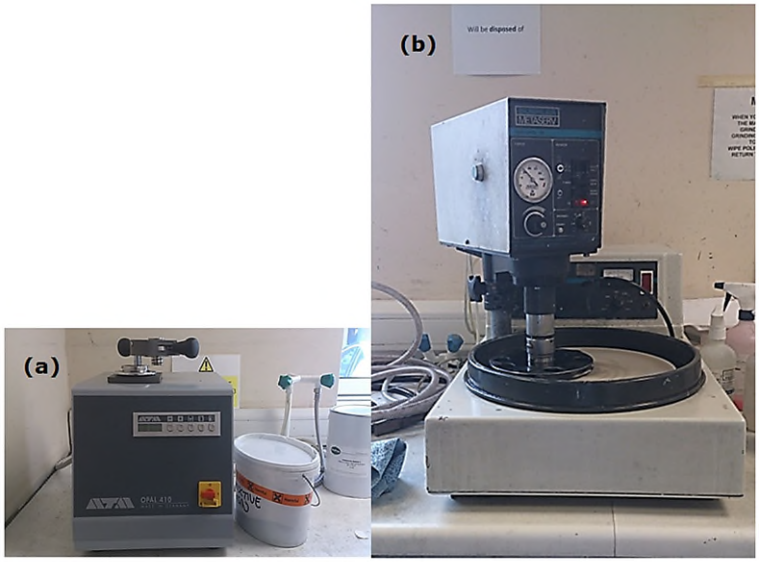

Figure 3-6. Digital images of (a) Opal 410 automatic hot mounting press and (b) Beuhler Metaserv Motopol 12 machine for grinding and polishing.

Figure 3-7. Resin mounted laser drilled sample for metallography examination.

3.2.2 Recast layer and surface cracks measurements

The experimental responses such as the recast layer thickness and crack number density on the laser drilled surfaces were initially imaged by Nikon Eclipse ME600 confocal optical microscope micrographs of various samples at different magnifications (from 5x to 10x). Later, the examination and measurements were conducted by SEM. Four laser-drilled holes were analysed for each drilling trials to minimise the measurement errors. The quantification of the recast layer was performed through measurement of the thickness at sixteen equally spaced points along the leading and trailing edges of the holes (see Figure 3-8). The recorded values of the recast layer thicknesses are presented in Appendix B. Only an averaged of maximum thickness values of the recast layer were analysed (see equation 3-2) and these values are presented in Chapter 5.

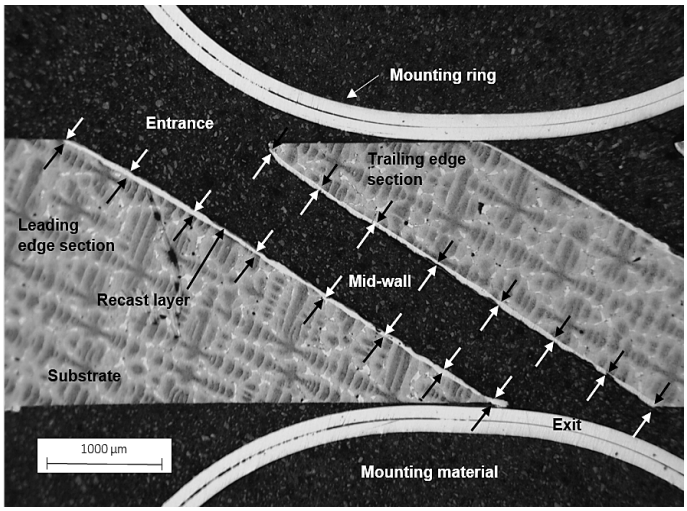

Figure 3-8. Optical micrograph showing the recast layer thickness measurement at different points on the cross-section of a laser drilled hole.

$$\boldsymbol{Ave.RLT_{max}} = \frac{\boldsymbol{RLT_{max_{Hole1}}} + \boldsymbol{RLT_{max_{Hole2}}} + \boldsymbol{RLT_{max_{Hole3}}} + \boldsymbol{RLT_{max_{Hole4}}}}{\mathbf{4}} \quad (3\text{-}2)$$

Further, the micro cracks examination was performed through cross-sectioned profile by SEM with backscattered electron detector. Each cross-sectioned profile of the hole was divided into eight sections, resulting in 8x4 SEM micrographs per sample trial. The SEM/BSE magnifications varied from 100x to 2000x. The number of micro cracks, length

and their orientation found on each trial sample were recorded. Two types of crack orientation were observed, viz. transverse and longitudinal (see details in chapter 4).

To evaluate the severity of cracks, only maximum transverse crack numerical density was used for the analysis. In this work, crack numerical density is defined as the number of micro-cracks in a unit area (μm^2), as shown in Equation 3-3 (Crack number density calculation). The unit area for SEM/BSE micrographs was fixed and it will consider 4000 μm^2, which is the depth of the hole times the long axis of the hole (see Figure 3-9).

$$CND_i = NC_i/A_i \tag{3-3}$$

Where CND_i is number density of cracks, NC_i is number of cracks from cross-sectioned hole profile and A_i is the defined unit area from cross-sectioned hole profile (see Figure 3-9).

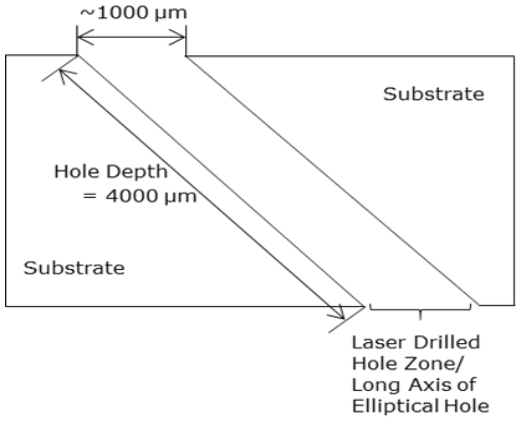

Figure 3-9. Schematic of cross-sectioned profile showing the examined area of unit for crack number of density.

3.2.3 Scanning electron microscopy

Scanning electron microscopy (SEM) is a microscopy technique in which a beam of electrons in a vacuum scan across the surface of the sample in a straight line to deliver images with information. At this stage, electron beam has an energy ranging from 100 eV to 30 keV. The signals emitted from the sample irradiated by electrons are secondary electrons (SE), backscattered (BSE) and X-rays. SE are used for topographical images and have the small sampling volume which gives the best spatial resolution (Gabriel, 1985). BSE are mostly used for elemental compositional and diffraction (i.e. electron

backscatter diffraction, EBSD). X-rays signals are produced to determine chemical compositions in the form of elemental maps or spot chemical analysis, using an integrated energy dispersive detector (EDS).

SEM typically operates at voltage ranging from 5 to 30 kV (Hafner, 2007). At this lower voltage electrons accelerated have a short wavelength. Therefore, increases topographic contrast and reduce sample charging and beam damage. The SEM enables magnifications ranging from 20 times to approximately 100,000 times to be made, and resolution about 10 nm. SEM detailed fundamentals and working principles are available in (Gabriel, 1985; Brandon and Kaplan, 2008a). Figure 3-10 illustrates a layout of internal diagram in a SEM.

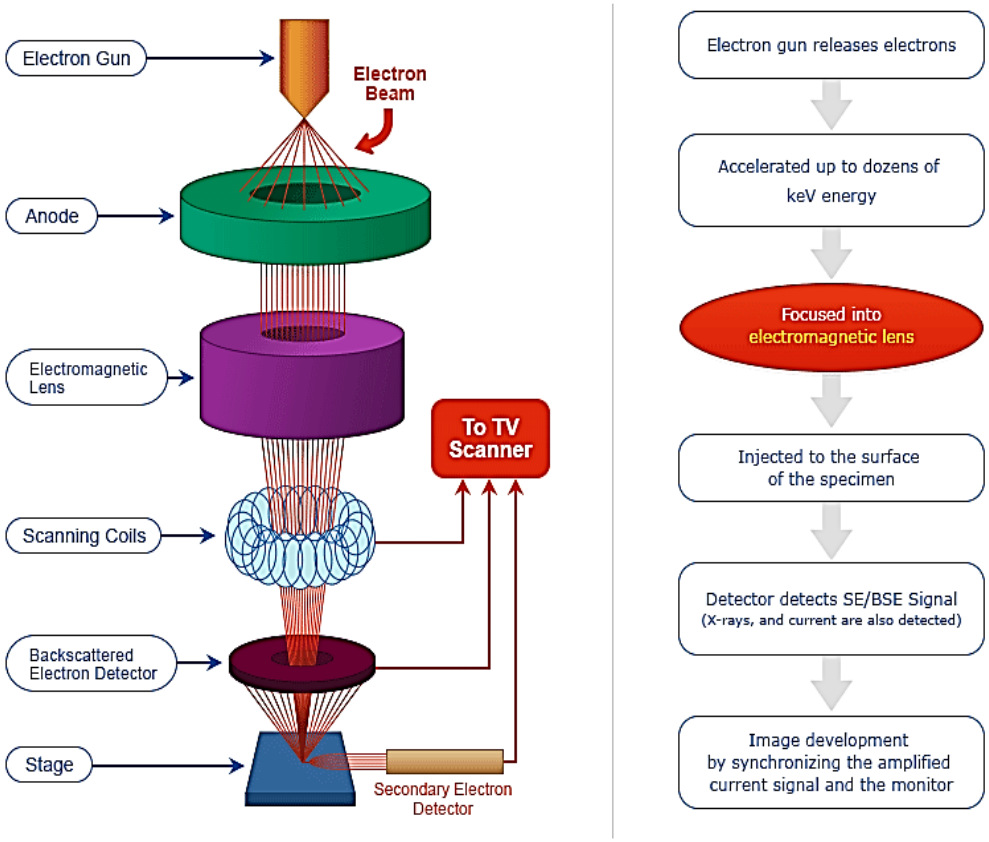

Figure 3-10. Schematic diagram of the SEM components[17].

[17] Retrieved from http://www.nanoimages.com/sem-technology-overview/, accessed on 25/01/2018.

3.2.3.1 *Equipment and examination approach*

The recast layer and surface cracks on the laser drilled samples were examined using Oxford FG-16 scanning electron microscopy. The cross-sections of the laser drilled holes were acquired by backscatter electron detector using accelerated voltages of 20.0 kV with a 20-60 μm aperture and 5-10 mm working distance. The BSE was selected due to higher atomic mass elements show sharper so it is visually easier to differentiate between the substrate and the recast layer.

3.2.4 Energy dispersive x-ray spectroscopy

Energy dispersive x-rays spectroscopy (EDS) is a quantifiable technique used to measure chemical elements present within the sample to be examined. EDS system is commonly coupled with SEM and TEM systems. EDS use X-rays generated from sample atoms exited by electrons to identify the elemental composition in the sample. By determining the energy rates of X-ray characteristics emitted, elements present in the sample can quantified (D, 2008). In SEM, EDS sampling depth images ranges from 0.1-3 μm, and lateral resolution of 0.1 μm. EDS data collected are displayed as histograms of counts versus X-ray energy.

3.2.4.1 *Equipment*

In this research, EDS was used to establish which elements were present within the recast layer and oxide layer produced by laser drilling. In addition, was to state the chemistry and traces of corrosion in specific areas of fracture facets of fatigued specimens. Points spectra's and elemental maps were collected using beam energy of 20-30 keV with 40-60 μm and working distance of 5.0 mm. An Oxford Inca EDS system analysis software was used in this research.

3.2.5 Electron backscattered diffraction

Electron backscattered diffraction (EBSD) is a crystallographic characterisation technique used for analysing the crystalline structure of materials, such as crystal orientation and phase identification of material. EBSD can also be used to quantify the features within a microstructure such texture analysis and grain size (Goodhew,

Humphreys and Beanland, 2001). EBSD detector is coupled in SEM on millimetre to a nanoscale.

EBSD signals originates from the inelastic scattering of the returning electrons emitted from the sample. Such interactions cause the formation of kikuchi bands or lines, which are the basis of crystallographic orientation identification (Williams, David B., Carter, 2009). Example of how Kikuchi bands are formed is depicted in Figure 3-11. As an electron beam hits crystallographic planes in the sample, it is scattered in all directions, radiating in conical shape. This gives rise to scattered paths, A and B, which both satisfies the Bragg equation for diffraction (Williams and Carter, 2009a) on each of the nearest planes. This is seen on the display as two parallel lines, and is repeated for different crystallographic planes at different positions on the display. An image of typical Kikuchi pattern is shown in Figure 3-12.

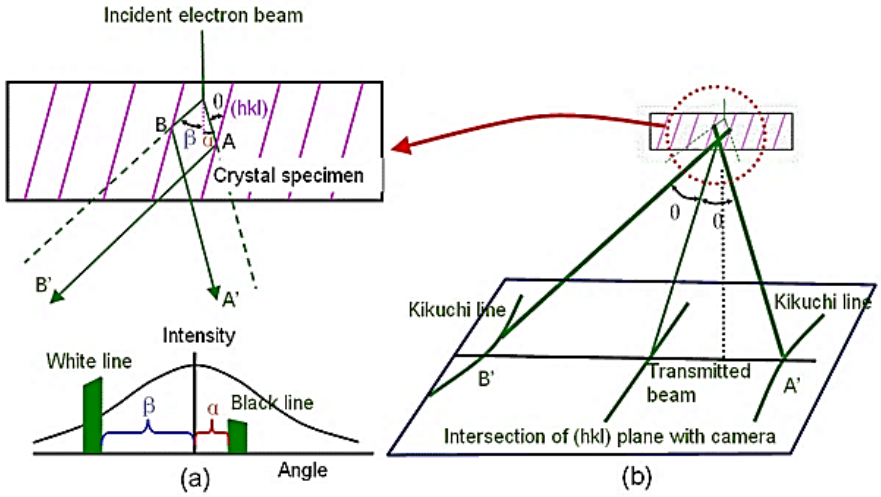

Figure 3-11. Schematic diagram of the formation of Kikuchi lines where θ is the Bragg's angle[18].

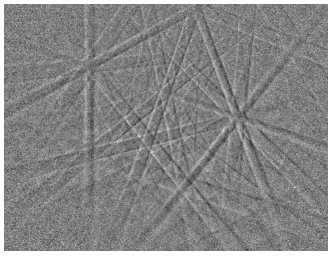

Figure 3-12. Example of Kikuchi pattern extracted from a single crystal Ni-based CMSX-4 superalloy by EBSD.

[18] Retrieved from: http://www.globalsino.com/EM/page4130.html, accessed on 27/01/2018.

3.2.5.1 *Sample preparation and equipment*

In this research programme the EBSD coupled in SEM was only used to determine the state of the crystal orientation of the fatigue specimen. This enabled to crystal orientation in relation to the load direction. For EBSD analysis, prepared sample was cut from a section of the supplied bar of CMSX-4. The sample preparation is similar to sequence described in section 3.2.1.2 with an additional fine polishing up to 25 minutes using a colloidal silica solution. EBSD data was collected and manipulated with same Oxford Instruments[19] software used for the EDS analysis.

3.2.6 Transmission electron microscopy

Transmission electron microscopy (TEM) is another analytical tool allowing characterisation and visualisation in realms of microscale (1 µm) to nanoscale (1 nm). This technique uses a beam of electrons which is transmitted through an ultra-thin section of the sample within a high vacuum to form an image. This image is magnified and focused by the electromagnetic fields. The focused and magnified image is displayed onto fluorescent or phosphorescent screen or CCD camera by electromagnetic lenses (Brandon and Kaplan, 2008b). Figure 3-13 shows a general layout of a TEM describing the path of electron beam in a TEM system.

TEM typically operates at a voltage up to 80-200 kV to illuminate an area of 5-70 µm at which electrons are accelerated two thirds of the speed of light and electrons travel under the short wavelength. The wave nature of electron in TEM can be viewed in a similar way to how light travels through a lens or slide projector. The short wavelength enables imaging in TEM to resolve in nanoscale. TEM provides atomic resolution imaging and chemical analysis, revealing atom columns and crystalline structure of materials (Williams and Carter, 2009b). Overall, there are three main applications of TEM: (i) imaging, internal microstructure; (ii) diffraction, identifies crystalline orientation and phases; (iii) spectroscopy, gives the chemical analysis.

---

[19] Retrieved from: http://www.ebsd.com/solving-problems-with-ebsd/ebsd-advancement, accessed on 27/01/2018.

3.2.6.1 *Sample preparation and equipment*

In order to get a better deeper understanding of the recast layer microstructure in the laser drilled surfaces, a JEOL 2000FX transmission electron microscopy (TEM) was used. TEM samples were prepared using FEI Nova Nanolab 600 Dual Beam Focus Ion Beam system. A focused ion beam (FIB) system is nearly identical to a SEM, but has an extra ion column mounted and instead of beam of electrons uses beam of gallium ions. These ions at higher beam current can sputter or mill the sample surface under examination with high precision (in nanometers). In addition, can be used for imaging using secondary ions emitted from the sample surface at low beam current.

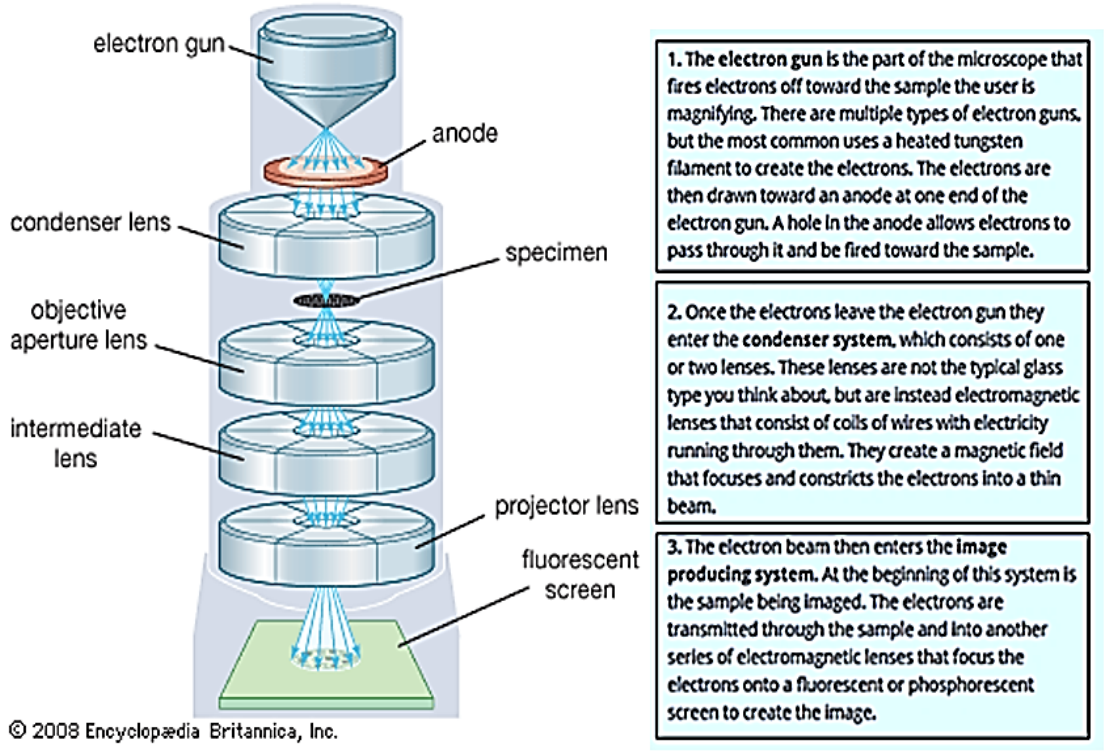

Figure 3-13. A generalised layout diagram of the internal structure of a TEM[20].

[20] Adopted from https://www.britannica.com/technology/transmission-electron-microscope, accessed on 25/01/2018 and https://study.com/academy/lesson/transmission-electron-microscopy-theory-applications.html, accessed on 25/01/2018.

3.2.6.2 *Sample preparation and equipment*

In order to get a better deeper understanding of the recast layer microstructure in the laser drilled surfaces, a JEOL 2000FX transmission electron microscopy (TEM) was used. TEM samples were prepared using FEI Nova Nanolab 600 Dual Beam Focus Ion Beam system. A focused ion beam (FIB) system is nearly identical to a SEM, but has an extra ion column mounted and instead of beam of electrons uses beam of gallium ions. These ions at higher beam current can sputter or mill the sample surface under examination with high precision (in nanometers). In addition, can be used for imaging using secondary ions emitted from the sample surface at low beam current.

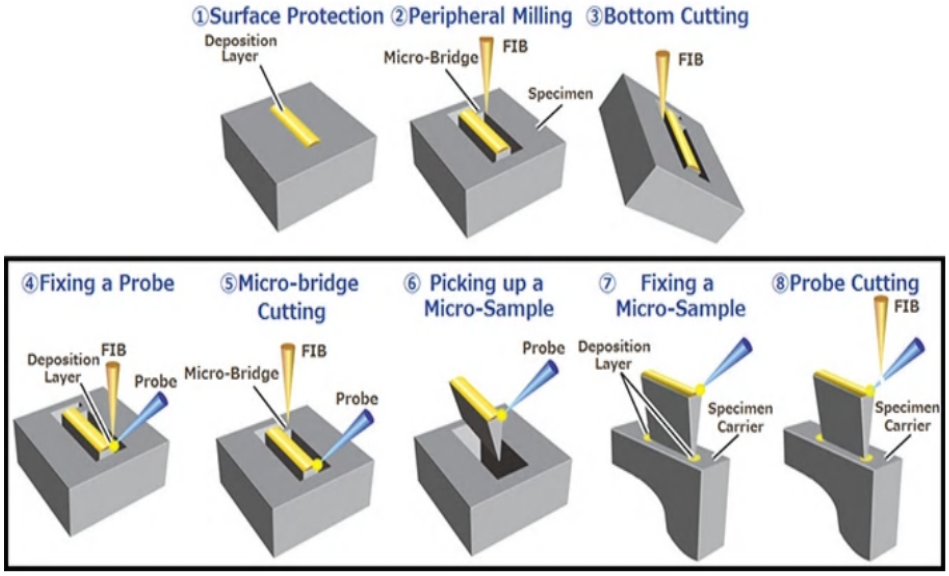

Figure 3-14. TEM sample process flow illustrating FIB milling to final grid attachment[21].

The sequence for TEM sample preparation is illustrated in Figure 3-14, and summarised as follows:

1. First, after defining the area to be examined a protective layer of platinum or tungsten is deposited on the top of the defined area to highlight the underlying surface to be milled.
2. Next, a peripheral milling using ion beam to mill trenches on the both sides of the area of interest to the appropriate depth. Typical micro samples have a depth of 5-

[21] Retrieved from https://www.hitachi-hightech.com/global/about/news/2015/nr20151105.html, accessed on 25/01/2018.

10 µm. The remaining material is removed using low ion beam currents at 53 degrees tilt until both sides of the deposited layer is clean and sample is approximately 1-2 µm thick, leaving also a small ligament to the bulk sample.

3. Then, bottom cutting of the micro sample at 7 degrees tilt using the ion beam.
4. After cutting, a micro manipulator Omniprobe (tungsten extraction needle) is inserted in the chamber with caution until it touches the micro sample. Then, a protective layer is deposited (welded) to fix the probe to the micro sample corner.
5. Once the probe is welded, the ion beam is then used to mill away the final attached section of the micro sample to be examined to the bulk sample.
6. Next, micro sample is lift-out from the bulk sample using 1 µm stage movements, and then aligned with sample carrier (prong of a cooper grid for TEM).
7. The micro sample is welded to sample carrier by depositing layer of tungsten or platinum.
8. Again, ion beam is used to detach the probe by milling away the deposited joins, followed by thinning of each sides of the micro sample to electron transparency (100-200 nm) using lower ion beam currents.
9. The milling parameters to generate the sample after lift-out are as follow: i) initial thinning at beam current of 1nA, sample up to 800-750 nm; ii) polishing at beam current of 0.5 nA, sample reduced to a thickness up to 500 nm; iii) final polishing at beam current of 0.1 nA, sample reduced to thickness to 100-200 nm.

The final prepared micro sample for TEM analysis is depicted in Figure 3-15c. Moreover, it should mention that before starting, the bulk sample requires a holder to be fixed on the base of the mounted resin. Then, followed by a cleaning of the surface of the sample by rinsing with ethanol to remove any unwanted deposits, dirt or dust. In this work, milling of the sample to examine was at operating voltage of 10kV and aperture between 19-25 µm. A platinum layer of 1.5 µm was deposited on the top surface at 52 degrees tilt and at a final stage attached to a probe like a ‘needle’ to enable the prepared sample to be removed. See Figure 3-15a for cutting direction details. Sections of 22 µm x 10 µm were used for TEM analysis as well as diffraction patterns to specify the structure of the recast layer and bulk material.

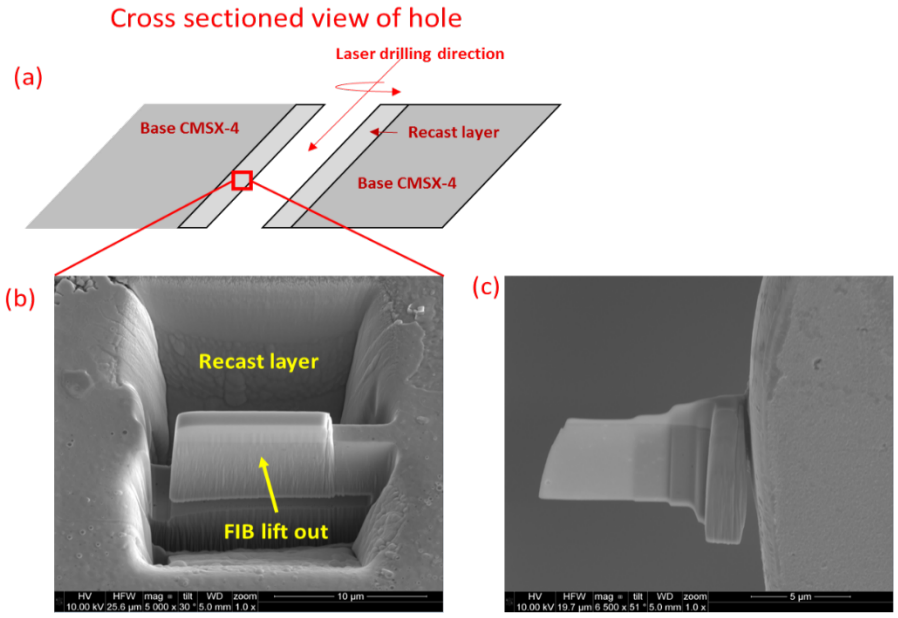

Figure 3-15. Schematic view of cross-sectioned of laser drilled hole:(a) bulk sample, (b) FIB lift-out of the micro section, and (c) final micro sample for TEM analysis.

3.2.6.3 *Diffraction pattern*

In this research, two diffraction patterns were collected at two different by TEM, viz recast layer and base CMSX-4. Diffraction pattern was carried out to compare the state of the crystal orientation and phases of recast layer produced by laser drilling to base CMSX-4 FCC structure. In TEM, diffraction patterns indexing is carried out by measuring the two different spots on a pattern R_{hkl} (R_1-R_2 and then R_1-R_3) which is related to the spacing d_{hkl} for the plane of Braggs indexes hkl (θ_{12} and $\theta_{1\text{-}3}$), see diagram in Figure 3-16. Then, by using equation 3-4 (Shongwe *et al.*, 2012) diffraction pattern index values can be determined or by matching to a crystal structure database (Williams, David B., Carter, 2009) to index each pattern.

$$\boldsymbol{R_{hkl}d_{hkl} = L\lambda} \tag{3-4}$$

Where, L is the camera length and λ is the beam wavelength. R is the radius of spot and d is spacing for the planes of Bragg's indices hkl. The calculations are most typically processed using available analytical software's or matching with available diffraction patterns database (Williams and Carter, 2009b).

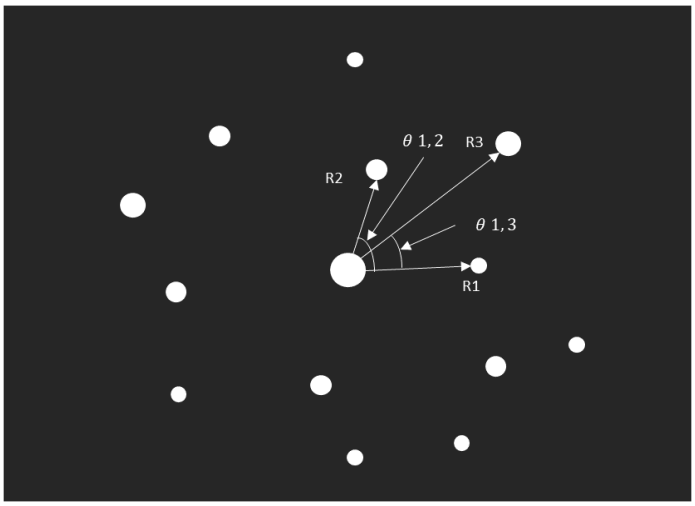

Figure 3-16. Schematic diagram showing the measurement of spot distances and angles. Adopted from (Shongwe *et al.*, 2012).

3.3 Corrosion-fatigue testing

3.3.1 Fatigue specimens

The single crystal CMSX-4 was used for this study in the form of cylindrical bars of 9.0 mm diameter with the [001] orientation along the long axis. The bars were from a solution heat treatment, precipitation hardened and hot isostatic pressing (HIP) batch in accordance with company internal practices. Solution heat treatment is carried out to achieve balanced chemical composition and dissolve potential eutectic regions formed during casting process. Precipitation hardened provides the material with desired mechanical properties (i.e. resistance to creep and corrosion). HIP is typically used for supressing the porosity formed during the casting. After machining and laser drilling the fatigue specimens were subjected to diffusion treatment for stress relieve and as this latter heat treatment improves the coating diffusion. The mechanical properties of the alloy are given in Table 3-8.

Table 3-8. Mechanical properties of CMSX-4 (Sengupta *et al.*, 1994).

Properties	At 20oC	At 800oC
Tensile strength	1150 MPa	1050 MPa
Elasticity of modulus	123,286 MPa	92,326 MPa
Poison's ratio	0.35	0.37

The drilling was performed at an angle of 30 degrees to the fatigue specimen's surface by laser trepanning drilling and electrical discharge machining (EDM). The laser drilling was conducted on a PowerDrill 80 CNC Nd:YAG laser drilling machine at facilities of Manufacturing Technology Centre (MTC), Ansty. The Die-sink EDM drilling was performed on an HAULT® machine at Cranfield University.

Before laser drilling fatigue specimens, some trials were conducted on 2.0 mm thick plates of CMSX-4. The laser drilling parameters employed were selected based on results reported in chapter 5. The three trepanning speed settings were used for the assessment since it had the most significant effect on the RLT response. Remaining process parameters were kept constant. This ensured that the recast layer thickness after LTD set's A, B, and C achieves a maximum average values of ≤50 µm; between >50 µm and ≤65 µm; and ≥75 microns, respectively. Post drilling operations including ultrasonic cleaning, grit blasting and heat-treatment were conducted per the company standard procedures, as this would reflect the current practices in the manufacture of cooling holes of HPT NGV. The details of the post-drilling processes are company proprietary data.

The drilling parameters used and the results of the trials in terms of average values of RLT_{max} at each condition are provided in Table 3-9 and Table 3-10, both for laser drilling and Die-sink EDM, respectively. A total of five groups of specimens were investigated. The non-drilled CMSX-4 and Die–sink EDM specimens were used for benchmark purpose.

Table 3-9. Laser parameters used for the drilling of fatigue specimens.

Input Parameters	Laser drilling conditions		
	LTD set A	LTD set B	LTD set C
Trepanning speed	125 mm/min	75 mm/min	150 mm/min
Peak power	10 kW	10 kW	10 kW
Pulse frequency	25 Hz	25 Hz	25 Hz
No orbits	2	2	2
Nozzle distance	10 mm	10 mm	10 mm
Focal position	0	0	0
Assist gas	Oxygen	Oxygen	Oxygen
Gas pressure	100 psi	100 psi	100 psi
Ave. RLTmax, Predicted	50 < RLT ≤ 65 µm	≤ 50 microns	≥ 75 microns
Ave. RLTmax, Trials	63.2 µm	49.2 µm	76.8 µm

Table 3-10. Die-sink EDM parameters used for the drilling of fatigue specimens.

Input Parameters	EDM conditions
	EDM set D
Pulse on-time	7 seconds
Pulse off-time	4 seconds
Pulse current	0.5 Amps
Dielectric fluid	Kerosene
Output response	EDM set D
Ave. RLT_{max}, Predicted	≤ 25 microns
Ave. RLT_{max}, Trials	24.2 µm

Hollow cylindrical shape LCF fatigue specimens were used for the tests, see Figure 3.17. The specimens and fatigue tests did not follow any national or international standard procedure. The tests were at the request of the OEM, thus not subjected to an international standard. However, the test methodology was consistent for each specimen. Each fatigue specimen had a gauge section of 20.0 mm length and 6.0 mm diameter. The three holes were drilled at an acute angled of 30 degrees in gauge section with a diameter of 0.75 mm, and a depth of 4.0 mm, as shown in Figure 3.17. The spacing between drilled holes is similar that found on the cooling holes of HPT NGV leading edge section.

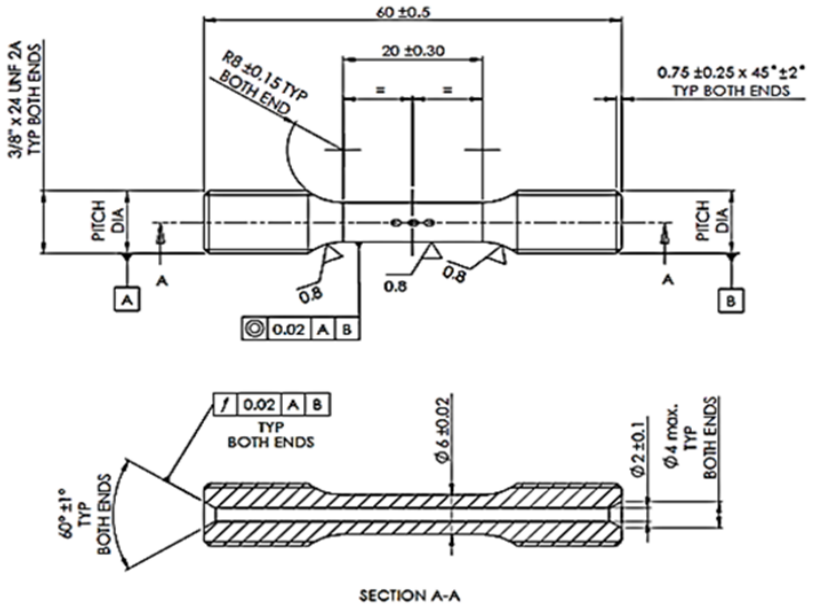

Figure 3-17. Schematic of fatigue specimen simulating acute and angled holes used for the HT LCCF tests (all dimensions are in mm).

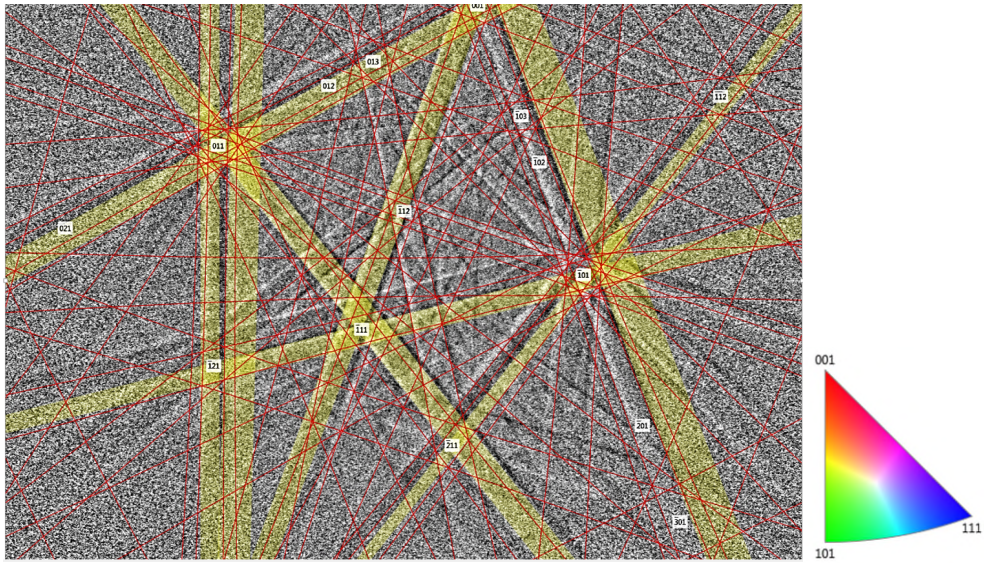

Figure 3-18. EBSD micrograph of Kikuchi pattern obtained at 20 keV for the supplied CMSX-4.

Figure 3-18 shows kikuchi patterns with crystallographic orientations in single crystal CMSX-4 superalloy sample prepared (cut, ground and polished) from a top section of the cylindrical bars supplied by the industrial partner. EBSD analysis confirms that is the case of all fatigue specimen's crystallographic orientation is at [001] in the applied load direction for corrosion-fatigue testing (see Figure 3-18).

3.1.1 Environmental fatigue rig

A servo-hydraulic environmental fatigue rig was used to perform HT CF tests at 850 ^{o}C, under low cycle fatigue regime, see Figure 3-19. The environmental rig in Figure 3-19 has a capacity of 100 kN load in mechanical tension and compression. The rig has a capability of testing specimens up to 1100^{o}C by means of thermocouples wires attached inside the environment gas chamber. The temperature control and settings inside the chamber is conducted through an external thermal control unit linked to main pc controller/software. In the specimen is gripped inside the chamber on both sides of the rod, where the bottom rod is fixed and linked to a load cell. Whilst, top rod coupled with piston rod is free to pull the specimen in tension and compression.

The air+SO^2 is delivered to the environmental chamber by a system of pipes link to the main gas supplies outside the corrosion lab. The chamber enables to mimic hot corrosion environment. The rig has a cooling system which is delivered through a continuous flow

of coolant water at the top and bottom load cells and through internal walls of the rods by a series of pipes to keep it below 60º C. The cooling system avoids the rig's internal components to overheat and damage. The external furnace insulates the environmental gas chamber along with the specimen inside it. The furnace ensures full insulation to keep the inside chamber temperature meets the testing conditions. EFR rig can run fatigue tests up to a frequency of 10Hz in LCF regime.

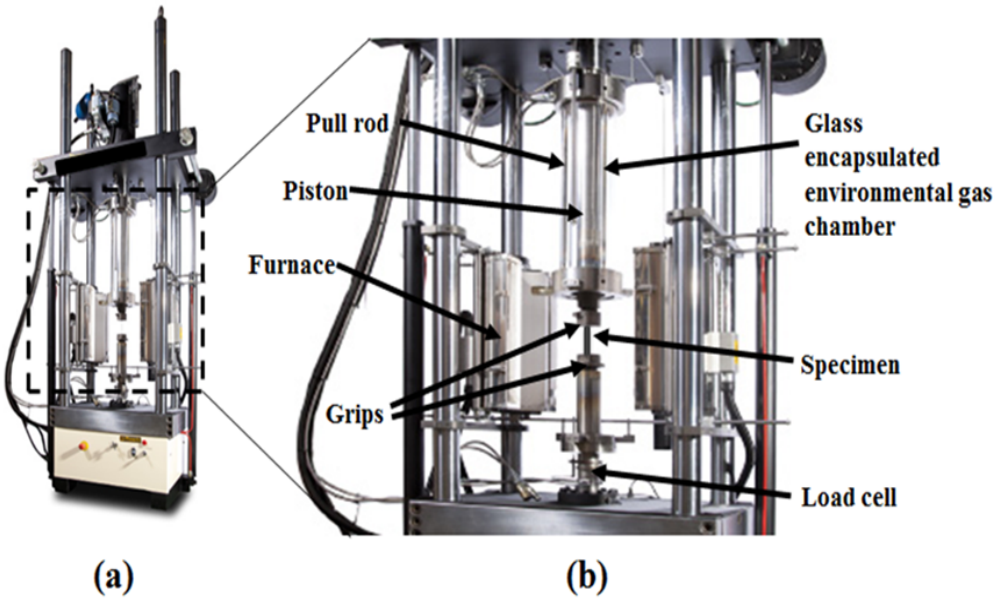

Figure 3-19. Image of a servo-hydraulic environmental fatigue test rig used in this study (a) and (b) annotation of main parts of the test rig.

3.1.2 Testing conditions

High temperature corrosion-fatigue tests were carried out at 850 ºC, under low cycle fatigue regime. The rig provided a continuous flow of pre-mixed Air+SO_2 with concentration of 300 vppm (volume parts per million) at flow rate of 80 cm^3/min, pre-heated to test temperature. Before testing, the specimens were sprayed evenly around the gauge length with 0.2 mg/cm^2 with a mix of salt solution consisting of a fully saturated 98% Na_2S0_4 + 2% NaCl mixture (Haight *et al.*, 2015). The purpose of coating the specimen with the salt is to mimic the sea air ingested by the engine which is partially downstream for cooling hot section components. Figure 3-20 illustrates the apparatus for the salting process and Figure 3-21 depicts the fatigue specimen in bare and salted coated condition.

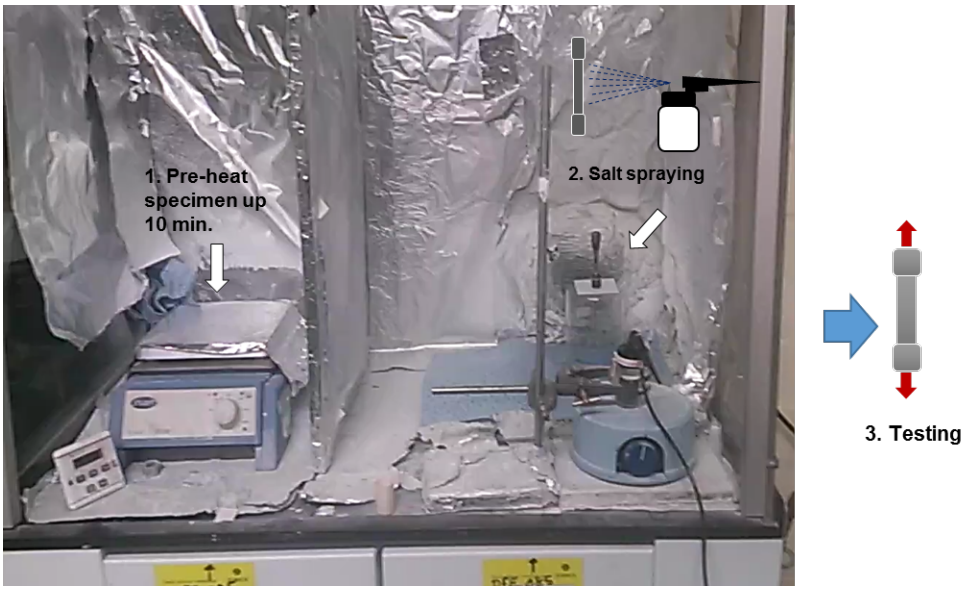

Figure 3-20. Schematic illustration of salting apparatus for fatigue specimens.

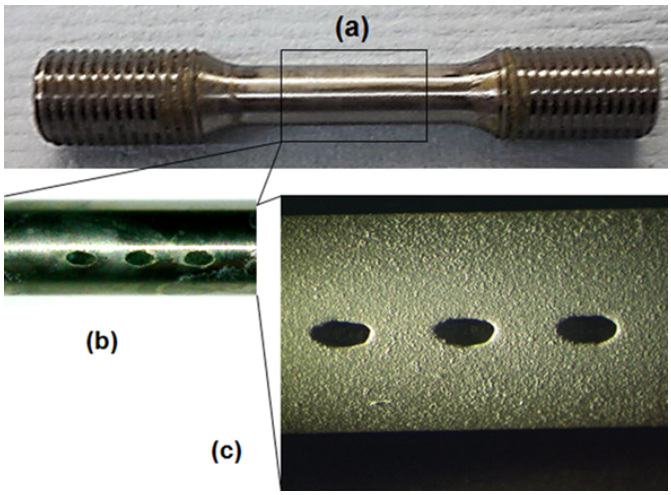

Figure 3-21. Images of (a) bare CMSX-4 fatigue specimen, (b) laser drilled section and (c) after post-processing and then coated with salt mixture.

The problem of high temperature corrosion on the aeroengine hot section components arises from the presence of salts such as Na_2S0_4, NaCl and $S0_2$ discharge from the combustion chamber (Eliaz, Shemesh and Latanision, 2002a). These compounds deposit on the surface of engine components and accelerating degradation, known as high temperature hot corrosion (Nicholls and Simms, 2010). Therefore, specimens were sprayed with salt mixture (NaCl) prior to the test and a continuous flow Air+$S0_2$ at 850^{o}C conditions during the tests in the laboratory. These tests were used to mimic the bleed air form the compressor to internal walls of cooling holes with corrosive environment experienced by internal walls of HPT NGV's.

High temperature hot corrosion (HTHC) occurs in the temperature range of 750 ^{0}C to 950 ^{0}C (Nicholls and Simms, 2010). In film cooling holes, cool stream of air is bled from the compressor stages through combustor bypass. The bypass air is directed to the internal passages of the turbine vanes and discharged along the external surface of the turbine vanes (Walsh, Thole and Joe, 2006). This air provides a thin layer of downstream coolant and insulating blanket against the hot gas stream, at a temperature range from 725 ^{0}C to 1025 ^{0}C (Rolls-Royce, 2005). Based on the technical specialist expert advice and guidance, a temperature of 850 ^{0}C was used in all tests, as this would simulate nearly the temperature experienced by the top surface of the side wall of the cooling film holes during the engine in operation.

Twenty-four high temperature LCCF tests with three to four levels of stress were chosen to assess the fatigue lives in the range between 100 and 110,000 cycles, or a history of 110,000-120,000 cycles at which point the testing was stopped and considered to be run-out. The level of stresses was applied by varying the increments in decreasing order of a 50 MPa with lowest stress of 290 MPa to evaluate the HT LCCF performance of laser drilled holes at three different laser processing conditions along with associate recast layer thickness. The tests were started at 550 MPa because it is the approximately 50 % of the UTS of the CMSX-4 superalloy at 800 ^{o}C (Sengupta *et al.*, 1994).

In view of the actual cooling film holes service environment conditions exposed and levels of stresses experienced, the tests were conducted under LCF load control at 850^{o}C, a stress ratio (R) of 0 was set for all the tests with a 1-1-1-1 second standard trapezoidal waveform at a frequency of 0.25 Hz applied at each stress level. Load control was used since the strain control tests were not possible due to the test environment, specimens are enclosed in the chamber and its containment not being conductive for suitable strain measurement. The stress loading ratio applied in the tests is sufficiently representative of the loading experienced by the critical geometrical features of the static HPT nozzle guide vanes, i.e. platform, shroud, internal walls of aerofoils and inner walls of cooling holes. The stress concentrations generated by such geometrical features such as inner walls of cooling film holes cause the material behaviour to be controlled by the tensile deformation in the main engine cycles. Therefore, performing stress load controlled tests with stress ratio R = 0 reproduces the actual component behaviour.

Table 3-11. Summary of the corrosion-fatigue test matrix.

No.	Specimen ID	Material	Process	Temp. (°C)	Trapezoidal Waveform	SO_2 flux	R	Stress (MPa)
1	FAT233	CMSX-4	LTD set A	850	1-1-1-1 sec	80 sccm	0	550
2	FAT239	CMSX-4	LTD set A	850	1-1-1-1 sec	80 sccm	0	450
3	FAT245	CMSX-4	LTD set A	850	1-1-1-1 sec	80 sccm	0	450
4	FAT293	CMSX-4	LTD set A	850	1-1-1-1 sec	80 sccm	0	350
5	FAT241	CMSX-4	LTD set A	850	1-1-1-1 sec	80 sccm	0	350
6	FAT266	CMSX-4	LTD set B	850	1-1-1-1 sec	80 sccm	0	550
7	FAT236	CMSX-4	LTD set B	850	1-1-1-1 sec	80 sccm	0	550
8	FAT307	CMSX-4	LTD set B	850	1-1-1-1 sec	80 sccm	0	450
9	FAT299	CMSX-4	LTD set B	850	1-1-1-1 sec	80 sccm	0	400
10	FAT270	CMSX-4	LTD set B	850	1-1-1-1 sec	80 sccm	0	350
11	FAT09	CMSX-4	LTD set B	850	1-1-1-1 sec	80 sccm	0	350
12	FAT253	CMSX-4	LTD set B	850	1-1-1-1 sec	80 sccm	0	290
13	FAT258	CMSX-4	LTD set B	850	1-1-1-1 sec	80 sccm	0	290
14	FAT247	CMSX-4	LTD set C	850	1-1-1-1 sec	80 sccm	0	550
15	FAT264	CMSX-4	LTD set C	850	1-1-1-1 sec	80 sccm	0	450
16	FAT290	CMSX-4	LTD set C	850	1-1-1-1 sec	80 sccm	0	450
17	FAT250	CMSX-4	LTD set C	850	1-1-1-1 sec	80 sccm	0	350
18	FAT257	CMSX-4	LTD set C	850	1-1-1-1 sec	80 sccm	0	290
19	FAT309	CMSX-4	Bare	850	1-1-1-1 sec	80 sccm	0	1000
20	FAT311	CMSX-4	Bare	850	1-1-1-1 sec	80 sccm	0	750
21	FAT313	CMSX-4	Bare	850	1-1-1-1 sec	80 sccm	0	600
22	FAT315	CMSX-4	EDM Die-sink	850	1-1-1-1 sec	80 sccm	0	550
23	FAT316	CMSX-4	EDM Die-sink	850	1-1-1-1 sec	80 sccm	0	450
24	FAT317	CMSX-4	EDM Die-sink	850	1-1-1-1 sec	80 sccm	0	350
24	N/A	CMSX-4	Bare	850	1-1-1-1 sec	Air	0	1010
24	N/A	CMSX-4	Bare	850	1-1-1-1 sec	Air	0	940
24	N/A	CMSX-4	Bare	850	1-1-1-1 sec	Air	0	898
24	N/A	CMSX-4	Bare	850	1-1-1-1 sec	Air	0	870
24	N/A	CMSX-4	Bare	850	1-1-1-1 sec	Air	0	840
24	N/A	CMSX-4	Bare	850	1-1-1-1 sec	Air	0	750
24	N/A	CMSX-4	Bare	850	1-1-1-1 sec	Air	0	700
24	N/A	CMSX-4	Bare	850	1-1-1-1 sec	Air	0	655

Trapezoidal waveform was selected due to flexibility in controlling the various periods of applied load at 1-1-1-1 second (see Figure 3-22). More, it is the preferred waveform used by the OEM and previous investigators (Barnard *et al.*, 2012; Sun, Heffernan and Helmink, 2012; G. Gibson *et al.*, 2016) instead of sinusoidal waveform to have small amount of dwell.

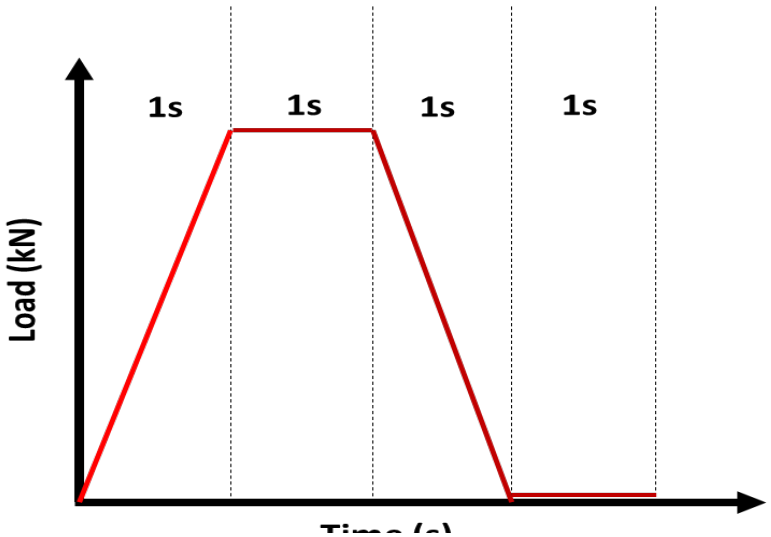

Figure 3-22. Typical 1-1-1-1 second trapezoidal waveform.

As it can be seen from Figure 3-22, the 1-1-1-1 second trapezoidal waveform describes a 1 second load increasing period with 1 second at maximum load hold, followed by 1 second load decreasing and finally 1 second at the minimum load hold period.

3.1.3 Sample preparation for fracture analysis

After testing, all failed specimens were inspected via Philips XL30 SEM equipped with electron dispersive x-ray spectroscopy (EDX) to confirm the crack initiation site, fracture morphology, and to identify the corrosion compounds on the fracture surface. Furthermore, fractured specimens were cross-sectioned for measuring the actual recast layer thicknesses. The metallographic preparation procedure is identical described in section 3.2.1.2, with attention to sectioning, grinding and polishing with an oil-base lubricant to minimise the loss of the main corrosion elements for the chemical analysis.

3.1.4 Nano hardness

Nano-indentations measurements were taken using MicroMaterials Nano-test machine system. The indentations were aligned 30 degrees and 90 degrees perpendicular to the surface in a grid of 3x7 indents with a spacing of 10 microns each indent up to indentation depth of 90 microns, and then 1x4 with the spacing of 30 microns up to remaining indentation depth. The total indentation depth was of 190 microns. The indentations range from the surface over the main re-cast layer to the bulk material. The indentations were performed on cut sections of a laser drilled sample, under LTD parameters set B. The sample prior to indentation was cross-sectioned, grinded, polished and mounted on a hard resin block according to the standard metallographic procedures. The continuous load applied during the indentation was of 100mN. The hardness and Young's modulus is evaluated by using following functions (Oliver and Pharr, 1992):

$$\boldsymbol{H = \frac{P}{A}} \tag{3-4}$$

Where, H is the Hardness; P is the applied load; and A is the projected contact area. For Berkovich indenter is about $24.5h_c^2$, obtained from (Fischer-Cripps, 2011):

$$A = 3\sqrt{3}h_p^2 tan^2\theta = 24.5h_c^2 \tag{3-5}$$

Where, h_c is contact depth and θ is 65.3°, thus,

$$\boldsymbol{H = \frac{P}{24.5h_c^2}} \tag{3-6}$$

The reduced modulus can be calculated as (Oliver and Pharr, 2004):

$$E_r = \left[\frac{1-v_s^2}{E_s} + \frac{1-v_i^2}{E_i}\right]^{-1} \tag{3-7}$$

$$or\ E_r = \frac{dP}{dh}\frac{\sqrt{\pi}}{2\sqrt{A_c}} \tag{3-8}$$

Where, E_r is reduced modulus; E_s is modulus of substrate; E_i is modulus of the indenter (1141 GPa); v_s is poison's ratio of the substrate (0.3); v_i is the poison's ratio of the indenter (0.001); A_c is the contact area; dP is change in the load and dh is the change in depth of penetration (see Figure 3-23 for guidance). These values are computed by the system and nano-indentation results are presented in Chapter 4, section 4.2.5.

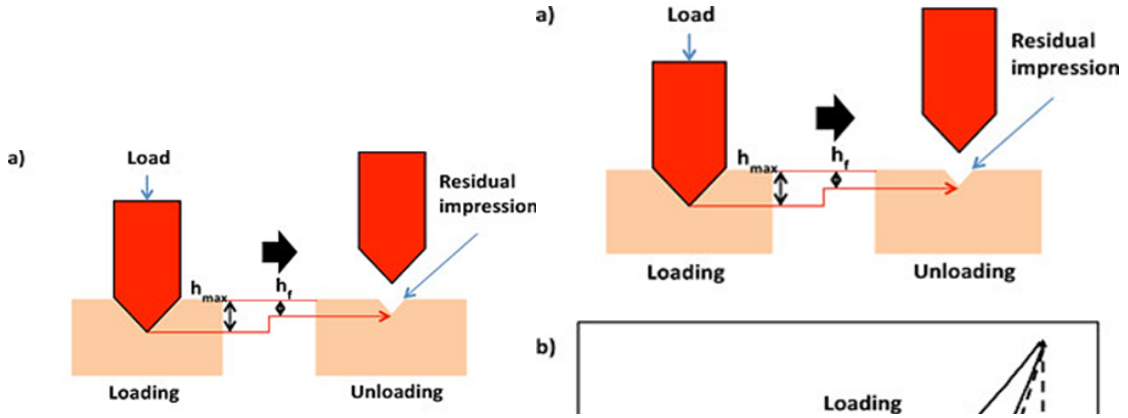

Figure 3-23. Schematic illustration of nano indentation: (a) illustration of working principle, (b) detailing the displacement curve (He et al., 2015).

3.4 Modelling

In this research the modelling divides in two subject areas. First, finite element modelling to investigate the local stress field and potential sites of crack initiation around the vicinity of angled cooling holes. Second, to determine the fitting parameters for the stress-life fatigue prediction model. Both approaches are commonly used in the scientific research for simulating local stress concentrations and developing empirical models, respectively.

3.4.1 Finite element modelling

3.4.1.1 *Geometry and meshing*

In this research the purpose of the finite element (FE) is to determine the areas of high stress concentration and crack initiation in CMSX-4 fatigue cylindrical specimens with angled holes. A linear elastic FE analysis using the software Abaqus® was carried out to determine the stress regions under uniaxial tension loading, at 350 MPa. The mechanical properties of CMSX-4 at 820 °C were considered (Białas, 2008). The Young's modulus (E) of 92,326 MPa, the Poisson's ratio (ν) of 0.37, and density of 8.90 g/cm^3. A default automatic Abaqus linear tetrahedral mesh generator C3D4 is used as shown in Figure 3-24. The mesh contained 4691 total number of nodes and 20679 total numbers of elements[22].

[22] Getting Started with Abaqus: Interactive Edition, accessed on 02/02/2018.

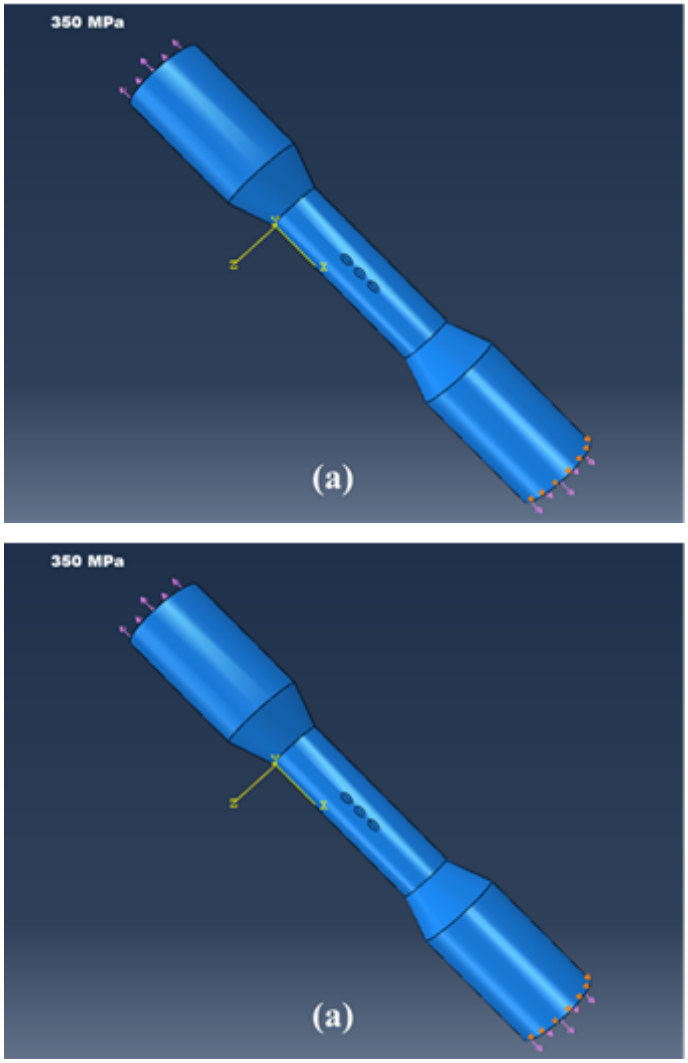

Figure 3-24. 3D CAD images: (a) geometry of the fatigue specimen CAD model showing the applied load direction at the top of the specimen face and bottom face constrained, and (b) CAD model with meshed geometry.

3.4.2 Statistical modelling

3.4.2.1 *Regression analysis*

As mentioned previously regression technique is used for determining the fitting parameters for the developed stress-life fatigue prediction model. Furthermore, it is first used for prediction model of recast layer thickness response by multiple regression analysis approach. Regression analysis is a well-established approach to develop complex linear and non-linear mathematical models to predict the performance characteristics (Freedman, 2005). It models a relationship between a response variable and one or multiple predictor variables.

There two types of regression viz. simple regression and multiple regression (see Figure 3-25). The simple regression considers only two variables at time, one independent and one dependent. Whilst, multiple regression considers more than two variables at time. In the present research, multiple regression analysis (MRA) is used both for prediction modelling of recast layer thickness and determining the fitting coefficients for the stress-life prediction model.

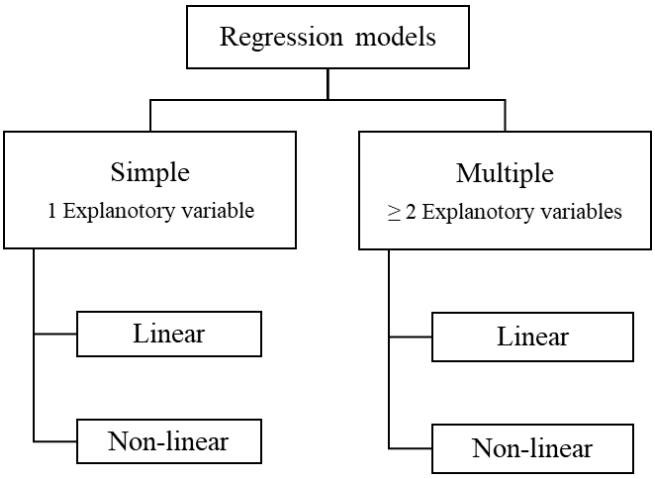

Figure 3-25. Types of regression models.

There are two variants of multiple regression analysis, namely linear or non-linear (Montgomery and Runger, 2012). The regression is linear between variables when the fitting curve is a straight line. Whilst, regression is non-linear between the variable when the fitting curve is not straight line. The liner MRA general equation is as follows:

$$y_i = \beta_0 + \beta_1 x_1 + \beta_2 x_2 + \ldots \beta_i x_i + \varepsilon \quad (3\text{-}9)$$

Where, y_i is the response/dependent variable term for the i th case; β_0 is the intercept, the independent term; β_1, β_2 and β_i are the fitting coefficients for the explanatory variables; x_1, x2, and xi are the independent terms for the i th case; and ε is the random error term. The error term denotes the amount of variations not estimated by the slope and coefficient terms. The non-linear MRA can be represented by the following equation:

$$y_i = \beta_0 + \beta_1 x_1 + \beta_2 x_2^2 + \varepsilon_i \quad (3\text{-}10)$$

Other forms of non-linear models are presented in the Table 3-10. Detailed understanding and application of MRA is available in the open literature (Levine, Szabat and Stephan, 2008).

Table 3-12. Other MRA functional forms (Montgomery and Runger, 2012).

Double-log	$logy_i = \beta_0 + \beta_1 logx_1 + \beta_2\, logx_2 + \varepsilon_i$
Semi-log (ln x)	$y_i = \beta_0 + \beta_1 lnx_1 + \beta_2\, lnx_2 + \varepsilon_i$
Semi-log (ln y)	$lny_i = \beta_0 + \beta_1 x_1 + \beta_2\, x_2 + \varepsilon_i$
Polynomial	$y_i = \beta_0 + \beta_1 x_1 + \beta_2 x_2^2 + \beta_2 x_3^3 + + \varepsilon_i$
Exponential	$y_i = e^{\beta_0} + x_1^{\beta_1} + x_2^{\beta_2} + \varepsilon_i$

The validity and adequacy of the regression model is commonly checked by regression coefficient root squared statistics (R^2), ANOVA parameters and normal probability plot of residuals. ANOVA is the statistical technique applied to determine the significance of the regression model and also provides an indication of which process parameters are statistically significant (Roy, 1990; Bower, 2000). According to this technique, F-ratio and P-value are vital for testing the adequacies of the models. If the calculated value of the F-ratio of the model exceeds standard tabulated value of F-ratio for the desired level of confidence (95 per cent), then the model can be considered adequate within confidence limit (Ramesh, 2009). In addition, when the calculated P-value is less than 0.05 for the desired level of probability (95 per cent), the regression model becomes adequate within the confidence levels.

R^2 statistics is a measure of the amount of reduction in variability of the response obtained by using the regression variables in the model (Frost, 2013). It also measures the goodness of the fit of the model (Mason, Gunst and Hess, 2003), in other words how well the values fit the data. The R^2 values closer to 1.0, better is goodness of the fit of the model (i.e. values ≥ 0.9).

Normal probability plot of residuals indicates how the error terms are distributed. It is a graphical representation to identify outliers, normality, skewness, etc. The data is normally distributed when the data points are closer to the linear straight line. The data is typically plotted against the theoretical normal distribution. Examples of normal probability plot of residuals are shown in Figure 3-27. In this research, regression analysis, ANOVA and normal probability of residuals are computed from Microsoft Excel Analysis Toolkit.

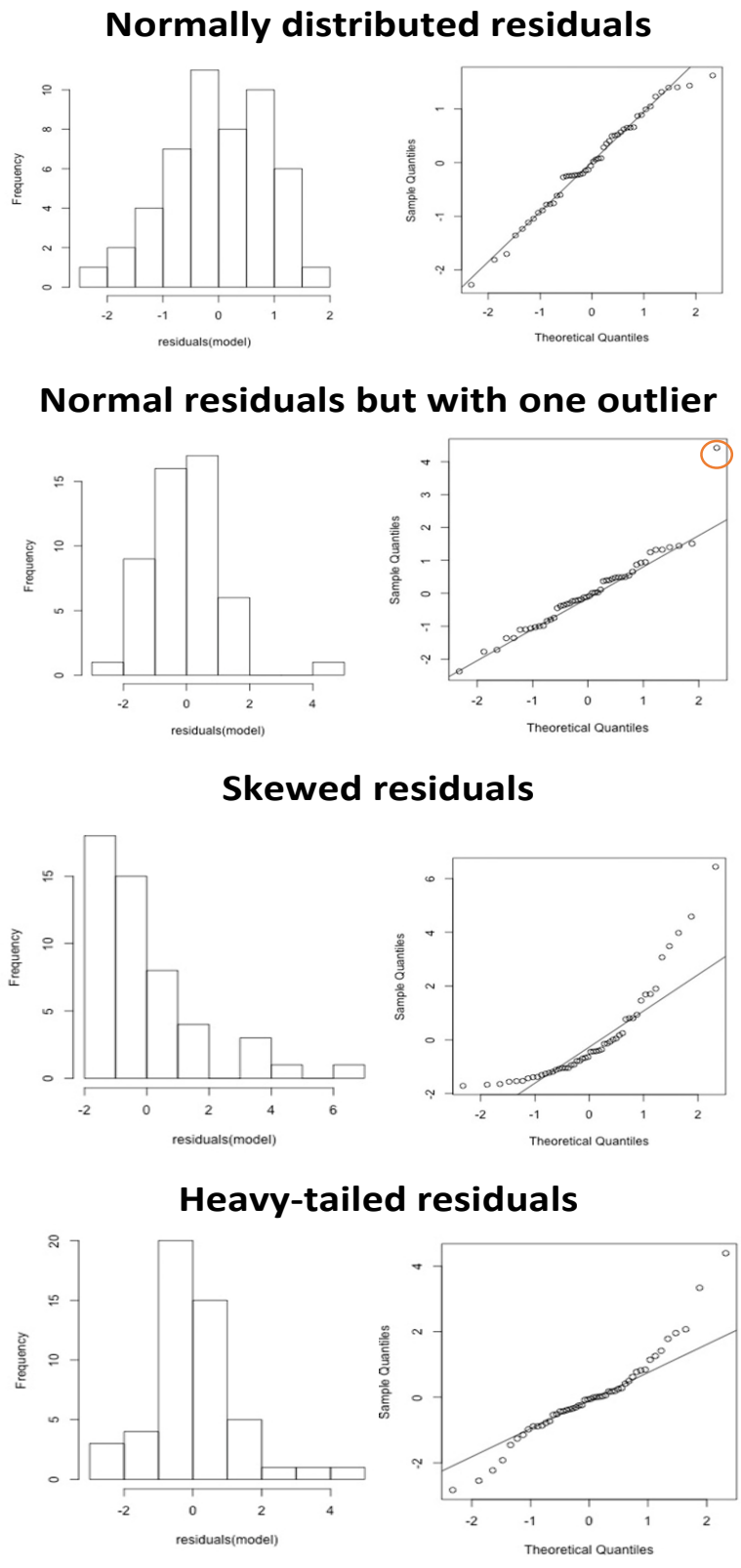

Figure 3-26. Examples of normal probability of residuals plot[23].

[23] Modified from: https://onlinecourses.science.psu.edu/stat501/node/281, accessed on 2/02/2018.

3.5 Summary

This chapter presented details of the experiments, analytical microscopy techniques, testing details and modelling approaches applied in this research. The laser drilling experimental trials were based on statistical design of experiments. All metallography analysis was carried out by SEM for surface characterisation and measurement, and EDS for elemental analysis. Further, transmission electron microscopy (TEM) was used to characterise the grain structure and phases present in the recast layer and base alloy. Later, fractography and corrosion mapping by means of SEM and EDS to determine the site of crack nucleation and presence of corrosion species around the crack tip region. Nano-hardness tests was carried out to compare the properties recast layer to base alloy. Finite element modelling to determine the region of high stress concentration and site of potential crack nucleation in angled holes. Statistical techniques approach to determine the significant process parameters affecting the recast and cracks formation. Furthermore, multiple regression analysis approach for prediction model of surface recast layer thickness, and to determine the fitting parameters for stress-life prediction model.

The next chapter discusses the surface alterations produced by laser drilling processing using analytical SEM, EDS and TEM metallography techniques.

4 METALLURGICAL ALTERATIONS PRODUCED BY LASER DRILLING IN A CMSX-4 ANGLED COOLING HOLES

4.1 Introduction

The laser drilling being thermal-based material removal process generates metallurgical, mechanical and chemical alterations on the sidewalls of laser drilled surfaces. Past studies (Sezer *et al.*, 2006; Leigh *et al.*, 2010), characterised the laser drilled surfaces by presence of recast layers, oxide layers, spatter, dross, surface cracks and heat-affected zone. Metallurgical alterations such as recast layers and surface cracks induced by laser drilling have been known to reduce both fatigue strength and corrosion resistance in laser drilled components in service (Neidel *et al.*, 2005). The understanding of these metallurgical anomalies and surface morphologies obtained after laser drilling becomes crucial to assess the potential impact of recast layers on the fatigue life performance of angled cooling holes.

The metallurgy of laser drilling surfaces have been investigated by limited number of researchers (Schneider, 2007; Garofano, Marcus and Aindow, 2009, 2010; Schneider *et al.*, 2010). In view of that, the purpose of this chapter is to characterise and discuss metallurgical changes on the drilled surface, focusing on the recast layers generated by process of laser trepanning drilling (LTD) of a Ni-base CMSX-4 superalloy. The evaluation of such metallurgical alterations was conducted through analytical SEM, EDS, EBSD, TEM and Nano-indentations measurements.

4.2 Results and discussion

4.2.1 Surface morphology

Metallography of all laser drilled samples was performed by using initially SEM and afterwards TEM for in-depth characterisation of the recast microstructure. An example of a typical laser drilled hole cross-sectioned is shown in Figure 4-1. There are two main distinct layers along with substrate alloy, depending on the laser drilling settings employed. First, oxide layer the upper darkest layer which is heavily oxidase during the drilling process. The formation of the oxide layer above the recast layer is due to

exothermic reaction and rapid cooling effect, when oxygen is used as assist gas (Leigh et al., 2010). The oxide layer poorly adheres around the recast layer periphery as displayed in Figure 4-1.

The oxide layer is highly brittle, flaky and with a high percentage of carbon, increasing the tendency for cracking during the laser drilling operations. Thus, oxidised layer on the laser drilled CMSX-4 surface of effusion cooling holes may be highly detrimental to fatigue strength. However, industrial practice is to remove the oxide layer after the laser drilling process by grit blasting process. This type of post-processing enables not only to remove the oxidised layer as well as trim some of the recast layer thickness. In the present study, oxide layer was found to be patchy and in some cases stratified layers with average less than 15 µm. Second, the recast layer which is formed on the sidewalls of the hole due to re-deposition and re-solidification of the molten material which is not vaporised and ejected away by the combined action of recoil pressure and assist gas pressure at the hole exit, during each pulse. Moreover, a continuous heating and cooling cycles during the laser drilling could lead to the microstructure segregation and brittle phases in the recast layer, thus to increase the probability of micro cracks formation in the recast.

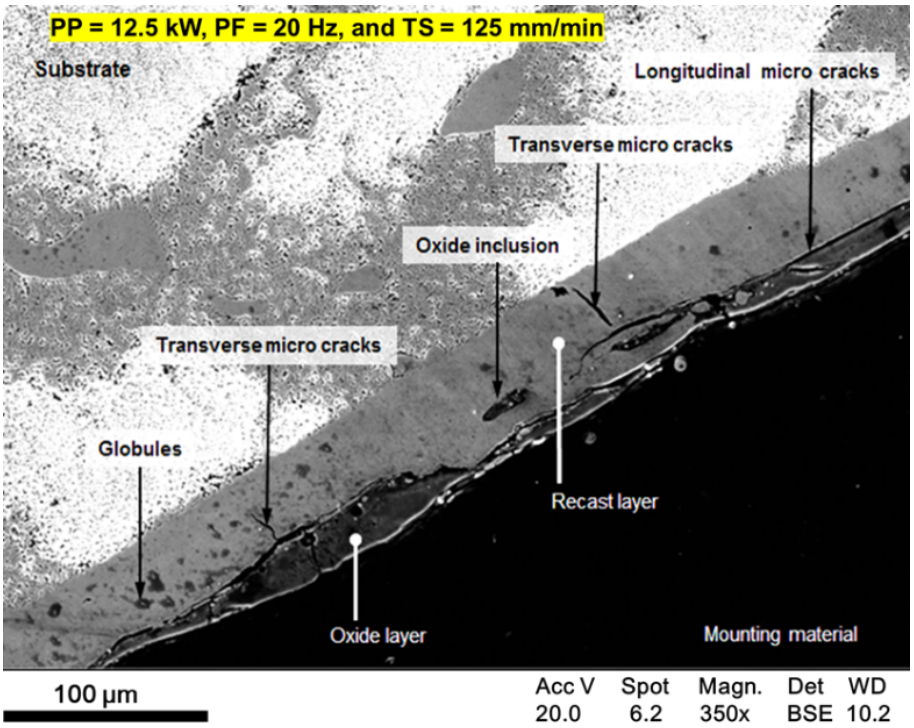

Figure 4-1. Example of a cross-sectioned sample showing typical defects associated with laser drilling of acute angled holes, sample TM 7.

The recast layer is known to contain metallurgical residues such as oxide inclusions, globules and micro cracks (Garofano, Marcus and Aindow, 2009; Leigh *et al.*, 2010). The presence of oxide inclusions, micro-voids, droplets and globules in the recast are caused by low re-solidification rate as the power density increases results in the entrapment of assist gas oxygen in the molten pool during the laser drilling process. Degree of concentration of such metallurgical residues and recast layer thickness varies as the set of processing parameters levels changes, such as laser beam parameters (pulse energy, pulse duration, pulse frequency, trepan speed) , focal parameters, assist gas type and pressure, material properties, hole shape and depth of the drill interaction. Past studies, have characterised the recast layer microstructure as porous, viscous, amorphous or with a dendrite microstructure (Garofano, Marcus and Aindow, 2009, 2010). In the present study, the recast layer thickness found to be unevenly distributed and varied depending on the different laser drilling settings tested (see Figures 4-2 and 4-3).

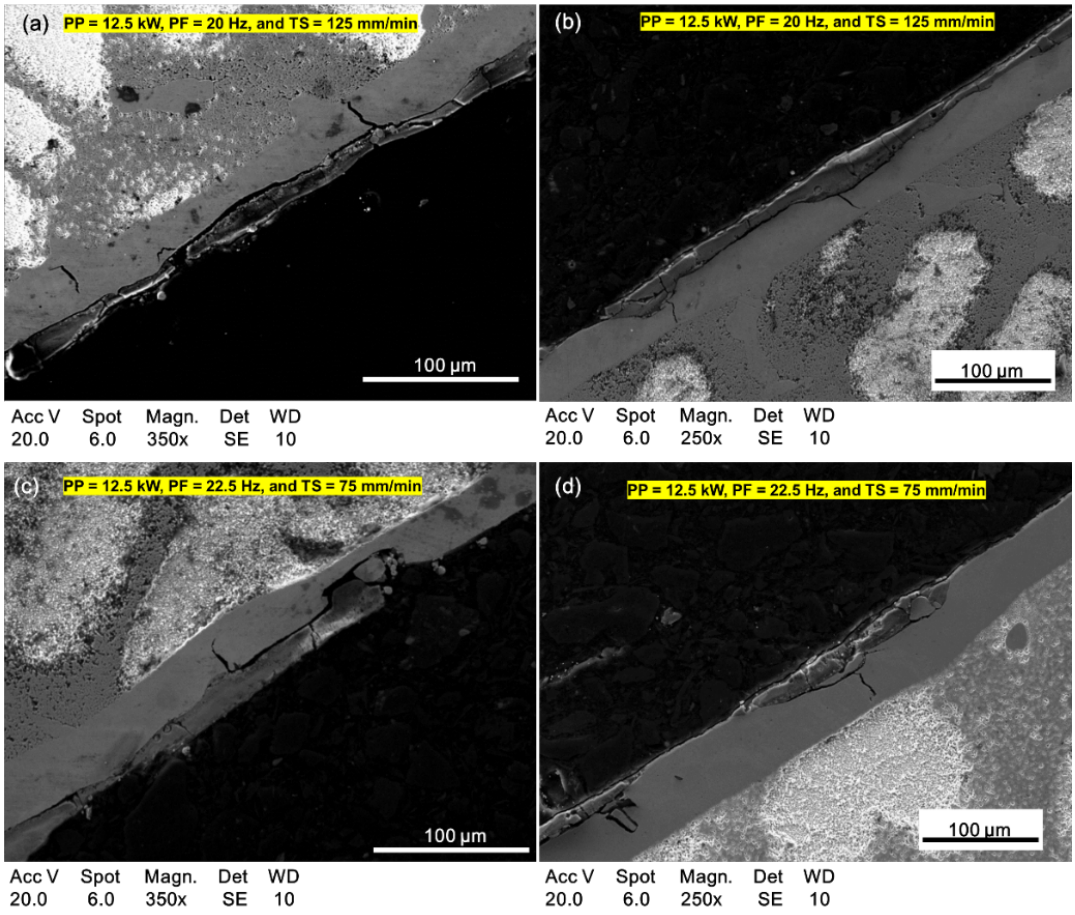

Figure 4-2. SEM micrographs showing surface morphologies of cross-sectioned CMSX-4 laser trepanned drilled samples at: (a-b) Trial TM7, leading-edge and trailing edge sidewalls, respectively; (c-d) Trial TM8, leading-edge and trailing edge sidewalls.

The recast layer of a laser drilled surface becomes more detrimental in the presence of cracks. These cracks are susceptible to reduce the fatigue strength under service. The cracks annotated in the Figure 4-2 are formed due to thermal mismatch between the high laser beam energy, cold workpiece and subsequent rapid cooling effect induced by an assist gas flow during the laser drilling. The high intensity energy and cold gas flow causes more contraction in the molten material than on the unaffected substrate, resulting in an increase of localised thermal tensile stress. This leads to microstructure segregation and brittle phases as aforementioned. It means that when the thermal tensile stresses inflicted by the laser beam energy exceeds the ultimate tensile strength of the material in these phases, results in crack formation. In the present study, two types of micro cracks were observed viz. transverse and longitudinal. The transverse cracks were perpendicular to the recast layer making them vulnerable to extend towards the base material, hence, detrimental to fatigue resistance. Whilst, longitudinal cracks were parallel to the laser drilling angle direction, thus, less detrimental than the former crack type.

Figure 4-2(a) to (d) shows evidence of heavily oxidise layers above the recast layer. The oxide layer found to be patchy and randomly distributed across the sidewalls of the hole, and in some cases with sub-layers. The presence of cracks and voids within the oxide layer was mostly observed on trials with higher peak power. The mount of oxide layer was reduced by lower trepan speed and lower peak power levels, as shown in Figure 4-3(a-b). Another observation from Figure 4-3(a) is that there was also cracking in the thinner oxide layers, as was the case in trials tested at lower peak power (8.3 kW and 10 kW). It can be assumed that the cracking initiate from the oxide layer and depending on the thermal damage inflicted, the cracking extends to the recast layer. The thicker oxide layers produced in trials 7 and 8 as shown in Figures 4-2(a) to (d) are directly linked with higher peak power setting used and oxygen assist gas interaction which in turn burns and oxidises the outer layer of re-solidified material. Moreover, oxide inclusions within the recast layer were observed in majority of samples, as it can be seen Figures 4-3(d). These inclusions are mainly caused by the diffusion of oxide particles into the recast during the re-solidification process as aforementioned.

Figure 4-2(a-d) and Figure 4-3(a-d) shows evidence of micro cracks within the recast layer. The magnitude of such cracks was dependent of processing parameters such as pulse energy and pulse duration interaction which yields the output beam peak power.

The micro cracks were observed when the laser peak power levels of 10kW and 8.3 kW were used. At these settings, the pulse durations were longer, thus, increasing the thermal cycling and the tensile stresses inflicted on the recast layer rises, resulting in crack formation. Past studies, have reported that shorter pulse duration minimises the thermal damage and crack formation in laser drilled nickel-based holes (Goyal and Dubey, 2014), and that was the case of trials tested at 12.5 kW where the pulse length was shorter. In present work, majority of these cracks were longitudinal and not much detrimental as the transverse (radial) cracks which could advance towards the base alloy. The maximum length of transverse crack observed was up to 60-75 % thickness of the recast layer and no micro cracks were observed in the recast layer.

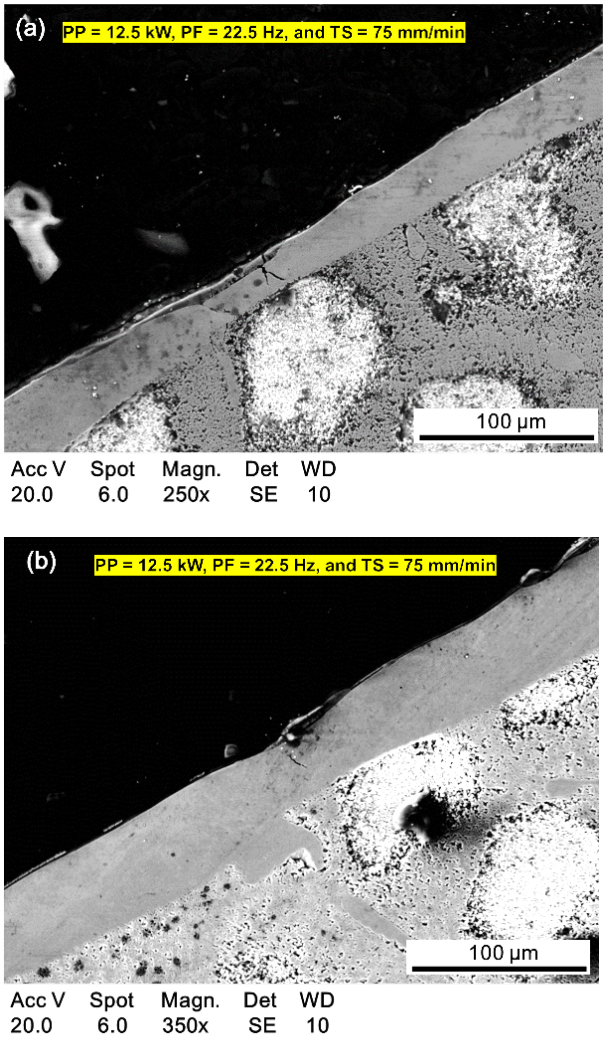

Figure 4-3. SEM micrographs showing surface morphologies of cross-sectioned CMSX-4 laser trepanned drilled samples at: (a) Trial TM4, trailing-edge sidewall; (b) Trial TM6, trailing-edge sidewall.

Another critical observation in all samples was that at the leading-edge side of the holes the recast layer was in average thicker compared to counterpart side wall (trailing-edge side). This could be explained as follows: in the laser trepanning drilling mode, the molten material is typically ejected away from the hole exit. Therefore, the downward force exerted by assist gas pressure to eject away the molten material is more effective at the trailing-edge side of the hole when it comes to angled holes. This phenomenon in laser percussion has been observed and reported in previous studies (Sezer *et al.*, 2005). There is still a need of understanding of the dynamics of melt ejection mechanism on laser trepan drilling of acute angled holes, at 10 to 15 degrees to the workpiece surface.

The recast layer thickness (RLT) and cracks were measured according to details described in Chapter 3 using SEM. Figure 4-4 shows measured recast layer thickness for CMSX-4 laser trepan drilled holes. It can be seen from Figure 4-4 that the laser trepan drilling generated a highest value of average of RLT_{max} of 78 µm and the lowest of 49 µm, based on the process parameters used and range of values tested. The variation observed in the recast layer is caused by the laser beam energy instability, which directly linked to power density and pulse density applied, and in turn, these parameters are linked to the amount of molten pool formed, vaporised, ejected away and re-solidified during the laser trepan drilling (Walther *et al.*, 2008).

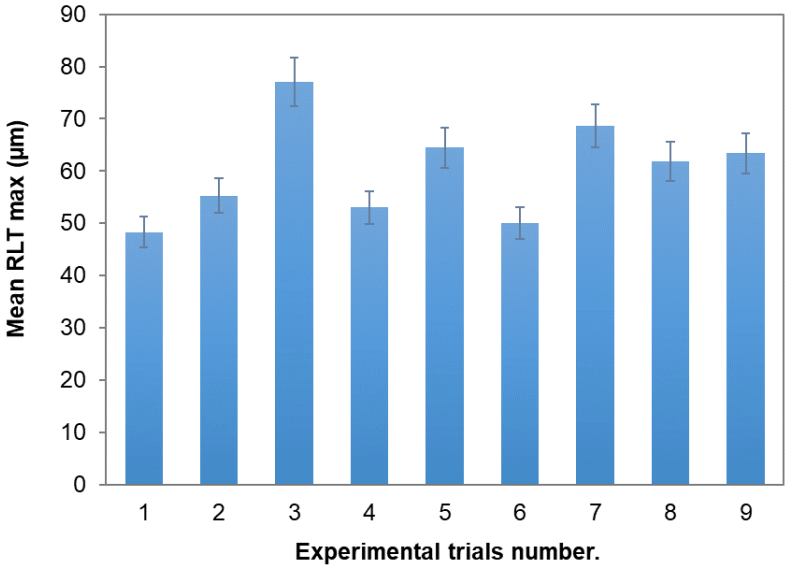

Figure 4-4. Recast layer thickness of laser drilled samples.

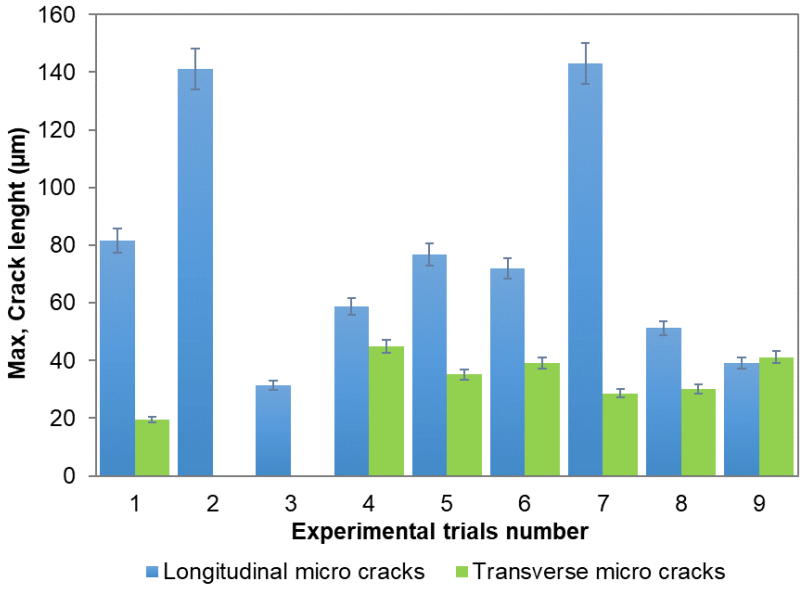

Figure 4-5. Surface cracks in the recast layer thickness.

It can be seen from Figure 4-5 that in most the cases, the longitudinal cracks had the longest lengths compared to the transverse cracks. However, transverse cracks had an average length of 36 µm, which is greater than 60 % of the recast layer thickness in most of the cases. This is undesirable since these type cracks could propagate under the adverse loads, either mechanical or thermal load. Therefore, limiting the life of laser drilled components. No cracks have been detected in the base alloy in this study. The maximum number of cracks was higher from trials 1-6. This could be due to increase in selected input parameters, as previously discussed.

Moreover, in spite of heat-affected zone (HAZ) not being detected in the samples analysed, it has been reported by some researchers that HAZ may present in nickel-based laser drilled surface and in the range of 5-10 µm (Sezer *et al.*, 2006). HAZ is found below the recast layer and is defined as the microstructural altered region but not melted on the sidewalls of the hole and adjacent to base alloy. In this research work, HAZ was not in the scope of this research work.

4.2.2 Recast layer microstructure

To further understand the recast layer microstructure, analytical SEM, TEM and elemental analysis was conducted to characterise the recast microstructure. In addition, nano indentations tests were performed to determine the change in mechanical properties.

4.2.2.1 *Scanning electron microscopy*

SEM observations show that the recast layer on laser drilled surface has multiple layers under high laser peak power. These multilayers are result of molten material build-up and rapid solidification associated with high laser intensity and laser beam interaction time which results in accumulation and re-solidification of molten material on the existing recast layer. The cross-sectioned of the recast layer of sample TM2 (PP = 12.5 kW, PF = 22.5 Hz, TS = 100 mm/min) are shown in Figure 4.6a-d. Four distinct sub-layers along with oxide layer and base alloy are observed in the Figure 4-6a. The upmost layer is thin, patchy and largely oxidise due to exposed high laser intensity inflicted on the surface continuously at each pulse. It is typically dense oxidise and amorphous layer with micro cracks extending to recast sub-layers. The up-most recast sub-layer is thin ranging between 3 to 5 µm with mix of fine and coarse dendrites (see Figure 4-6, annotation A and B). This type of sub-layer is likely associated with solidification of molten material in an undistorted form during laser trepanning drilling.

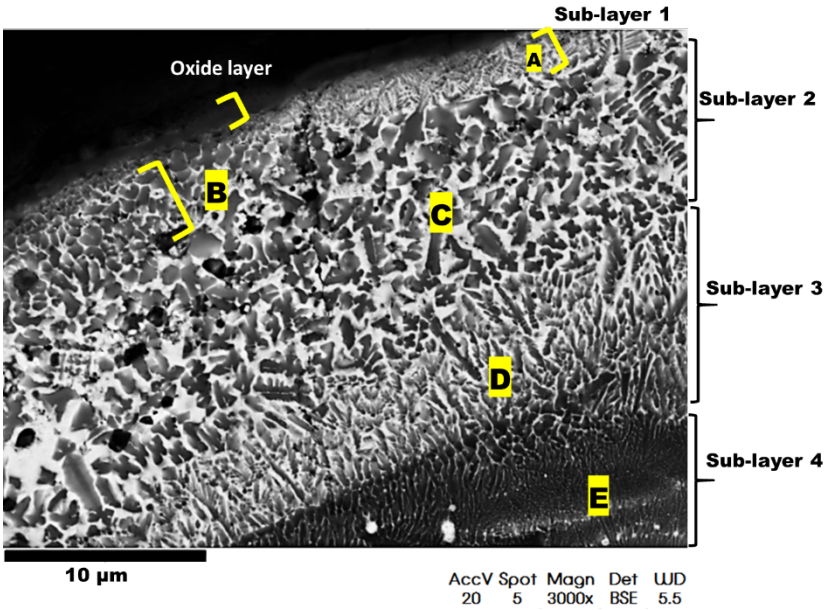

Figure 4-6. Cross-sectioned SEM micrograph showing recast layer microstructure of Ni-base CMSX-4 laser drilled hole (sample TM2).

The second recast sub-layer consist of large and coarse dendrites in different orientations. This type of sub-layer found to have maximum thickness between 10-12 µm. This type of sub-layer likely to undergone to segregation and rapid cooling during solidification, resulting in rapid dendrite growth (see Figure 4-6, annotation C). Third recast sub-layer ranging thickness from 5-10 µm consist of thin columnar dendrite structure (see Figure

4-6, annotation D). Forth and inner-most sub-layer found to be relatively fine cellular dendrite type structure (see Figure 4-6, annotation E). Latter, sub-layer varied thickness ranging from 10-15 µm. Moreover, these observations were consistent with samples at high peak power. However, the thickness of recast sub-layers varied slightly with change in pulse frequency and trepan speed. Interestingly, samples with intermediate peak power shown to have similar recast microstructure, but only consisted of two sub-layers. First, coarse dendrite structure with thickness ranging from 25-45 µm. whilst, second has a thin and fine dendrite structure with sub-layer ranging from 5-10 µm.

Another critical feature in the recast layer is the presence of oxide inclusions (globules) as previously stated. The abundance of oxide inclusions is more evident on the samples laser drilled at high peak power than counterpart samples. These globules are formed by oxidise molten droplets which are diffused randomly during the solidification and then re-solidifies on the recast layers (see Figure 4-7). Figure 4-8a show the microstructure of base alloy with typical dendrite structure at low magnification and Figure 4-8b showing the FCC crystallographic structure with clear gamma matrix and gamma-prime precipitates.

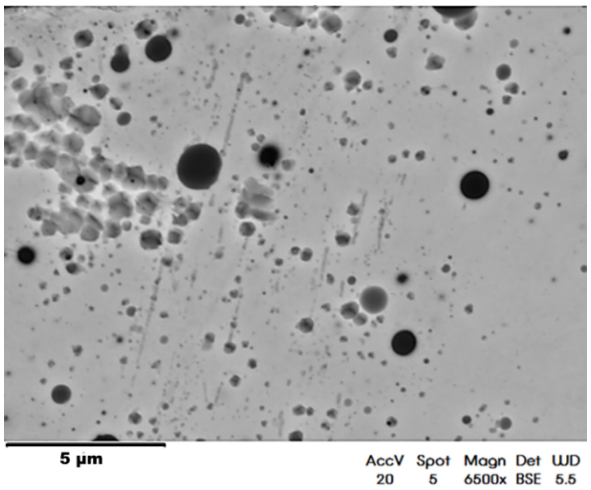

Figure 4-7. SEM micrograph showing an example of oxide inclusions in the recast layer.

Microstructural examinations of the recast layer formed in Ni-base CMSX-4 angled holes under different laser trepan drilling conditions have shown that the recast microstructure depends on the recast layer thickness formed. The laser drilling parameters such as peak power and trepan speed enables to control the recast layer thickness but it is the variation in the thickness that determines the formation of the recast sub-layers at different laser drilling conditions.

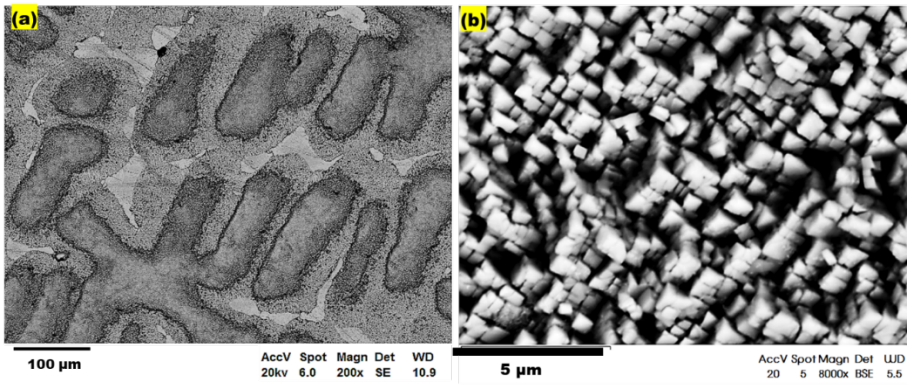

Figure 4-8. SEM micrograph showing CMSX-4 microstructure: (a) dendrite structure at high magnification and (b) gamma matrix (in black) and gamma prime precipitates (bright cuboids) at a lower magnification.

Microstructural examinations of the recast layer formed in Ni-base CMSX-4 angled holes under different laser trepan drilling conditions have shown that the recast microstructure depends on the recast layer thickness formed. The laser drilling parameters such as peak power and trepan speed enables to control the recast layer thickness but it is the variation in the thickness that determines the formation of the recast sub-layers at different laser drilling conditions.

4.2.2.2 *Transmission electron microscopy*

TEM analysis was conducted to further determine crystallographic microstructure of the recast layer. The bright-field (BF) TEM micrograph of the recast layer morphology is shown in Figure- 4-9. Again, it clearly shows that the morphology of the recast layer is very different from the base alloy. The recast layer morphology consists of nano-crystalline structure with random discrete regions of γ' phase and γ matrix. The γ' phase appear dark and the γ matrix are the lighter lines under the acquired BF TEM imaging (see Figures 4-9 and 4-10). The size of precipitates formed within the recast layer is between 25-50 nm, under electron backscattered diffraction (EBSD) examination.

Figure 4-11 shows EBSD image of recast layer and base alloy cross-sectioned view where it can be seen distinct grains orientation and size. One reason for reduction of the grain size in the recast layer is due to continuous impingement of high laser intensity leads to re-crystallisation state where re-precipitation occurs, forming precipitated grains in nano scale size. Figure 4-9 also shows presence of particles located almost at the γ' phases, under bright white circles (highlighted in yellow triangles). EDS data obtained from such

particles/oxide inclusions revealed that they are Al-rich, formed during the melting and solidification process.

Selected electron diffraction patterns (SADP's) were also obtained from the analytical TEM as shown in Figure 4-9b and 4-10b. Indexing show that both SADP's corresponds to a FCC crystal structure of [112] planes, suggesting the diffraction pattern (DP) of the recast is of similar to the base alloy on the selected γ' phases.

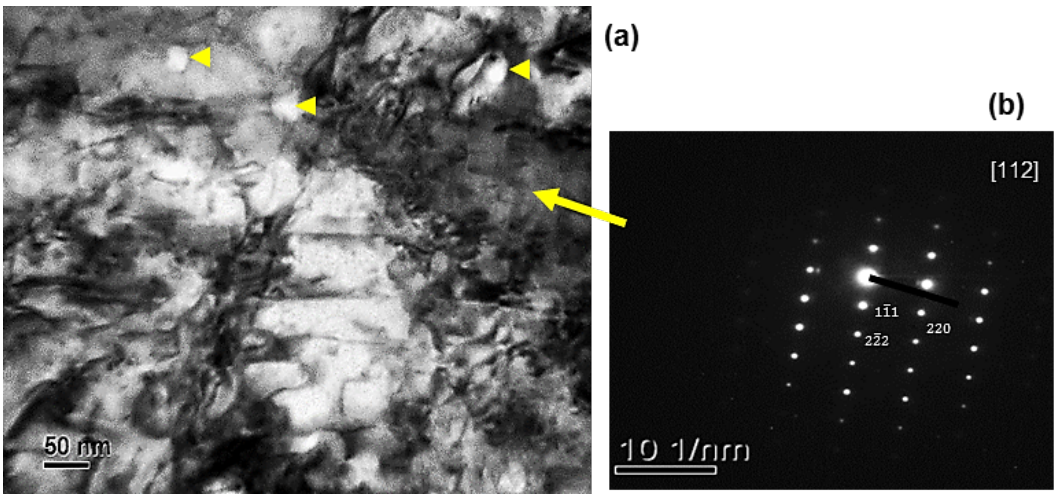

Figure 4-9. TEM data obtained from: (a) BF TEM image of the lamella extracted from the recast layer, (b) Diffraction pattern showing FCC crystal [112] plane. The yellow arrow points out the select region for diffraction pattern analysis.

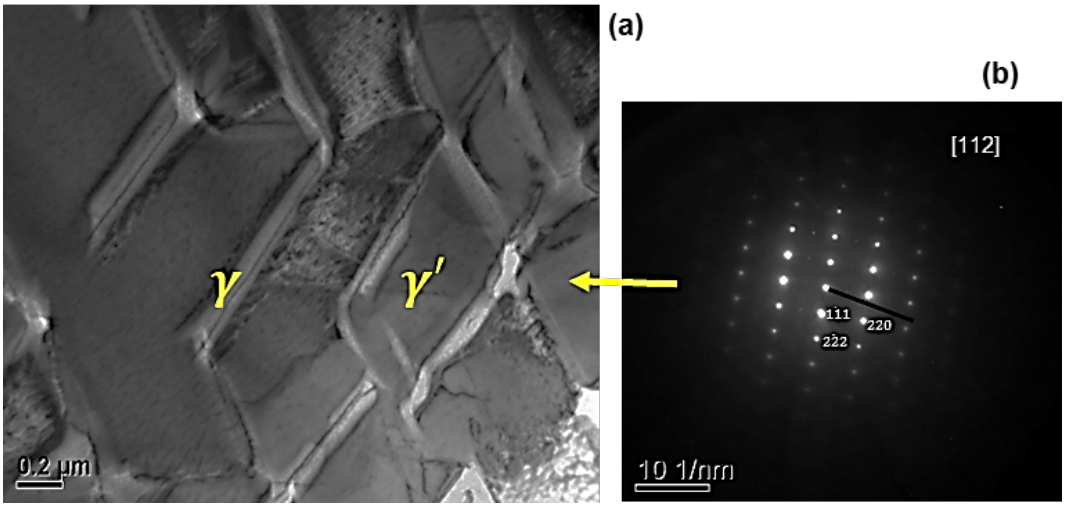

Figure 4-10. TEM data obtained from: (a) BF TEM image of the lamella extracted from the base alloy, (b) Diffraction pattern showing FCC crystal [112] plane. The yellow arrow points out the select region for diffraction pattern analysis.

The DP's obtained were indexed by comparing the pre-existing database of FCC crystal planes (Williams and Carter, 2009a). In addition, diffraction patterns taken from different location from the same sample in the γ' phase which not depicted here were identical. These DP's suggests the nano crystalline nature of the recast layer. The results from the TEM analysis suggests that despite morphological changes in the laser drilled surface there is no alterations to the crystalline phase of recast layer to the base alloy. This is because in laser drilling process the melting and solidification of the molten alloy occurs under the protection of the inert gas such as oxygen prevents foreign elements to diffuse into recast layer, thus, preventing formation of new phases (Fu *et al.*, 2016).

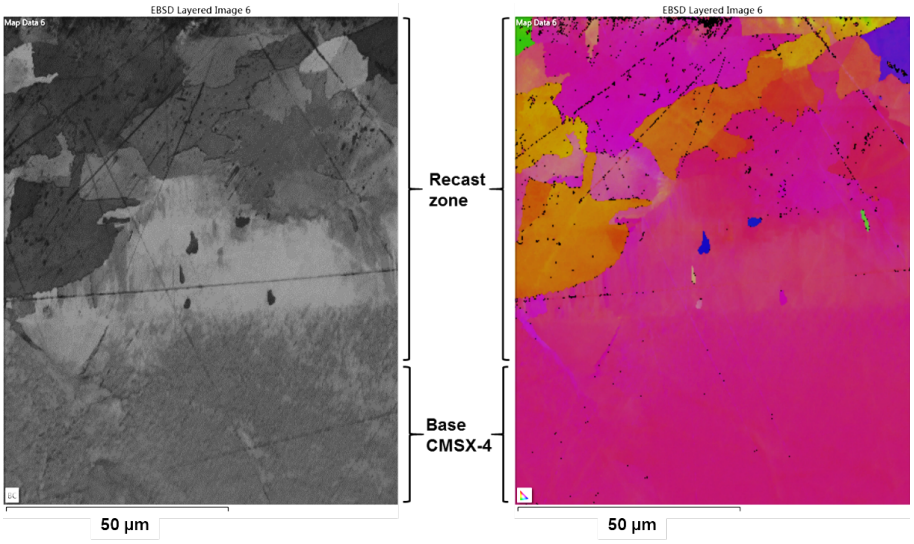

Figure 4-11. EBSD imaging of inverse pole figures (IPF) in laser drilling extracted hybrid sample, showing the recast/base alloy interface at cross-section of laser drilled hole entrance. Precipitated grains larger than 150-250 nm are evident within the recast layer.

4.2.2.3 *Energy-dispersive X-rays spectroscopy*

Energy dispersive X-ray spectroscopy was used to analyse elemental composition of the recast layer and the base alloy CMSX-4. Spot scan was used to acquire the elemental data shown in Figure 4-12 and elemental plot is given in Figure 4-13. The concentration profiles of oxygen and carbon show high in the oxide layer and then completely falloffs in the recast layer, as expected. This is associated with use of oxygen as an assist-gas during the laser drilling process which greatly diffuses into the top layers and oxidising them to an uncertain thickness. Furthermore, concentration profiles of aluminium (Al) and nickel (Ni) show also variation in the oxide layer, recast layer and base alloy. The

concentration profile of Al is enriched in the oxide layer and drops in the recast layer. The concentration profile of Ni shows inverse variation when compared to that of Al. The concentration profile of chromium (Cr) in the oxide layer is slightly high to recast layer and base alloy. The dissolution of Ni and enrichment of Al and Cr is caused by high laser beam energy and molten material interaction on the upper layers during solidification process. These observations are similar to reported elsewhere (Sezer *et al.*, 2006; Hongyu Zhang *et al.*, 2016). The concentration profiles of other key elements such as cobalt (Co), and titanium (Ti) show little variation in the recast layer and base alloy region. The dissolution or micro segregation of key elements such as Ni, Al, Ti and Cr inside the recast layer may be the root cause of the reduced fatigue strength and corrosion resistance in the recast layer produced by laser trepan drilling.

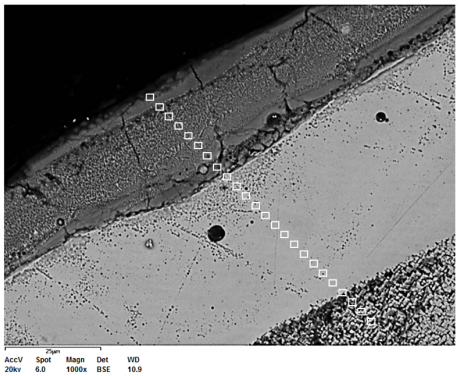

Figure 4-12. SEM micrograph showing spot scan selected for acquiring elemental data (un-etched TM2 sample).

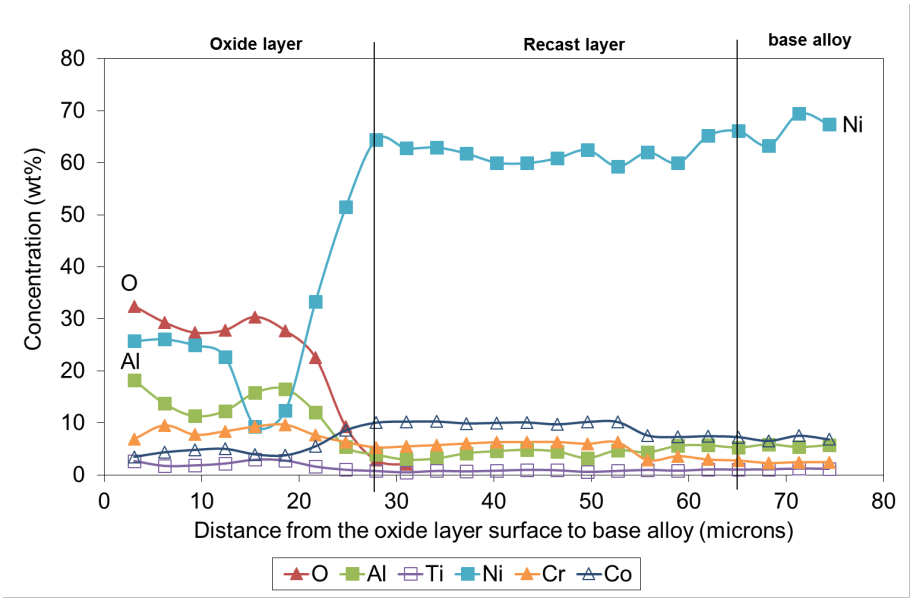

Figure 4-13. Elemental profile of laser drilled layers in CMSX-4 superalloy.

In addition, Figures 4-14 shows the micrograph of sample TM5 and selected elemental spots for the elemental analysis, respectively. EDS elemental results in the Table 4-1, spectrums 2, 3 and 4 show similar elemental trend to TM2 sample in Figures 4-15. The elemental analysis indicate change in alloy chemistry, particularly in Ni, Al, Cr, Co and Ti, hence to potential change in mechanical properties.

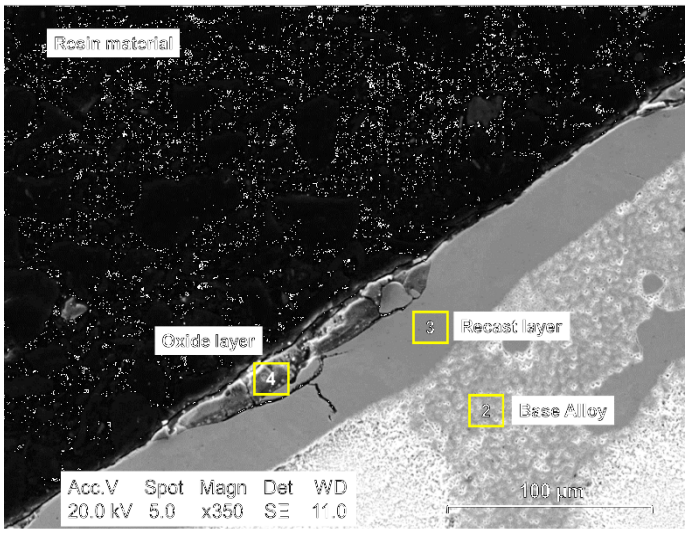

Figure 4-14. SEM micrograph showing selected spot areas including oxide layer, recast layer and base alloy (un-etched TM5 sample).

Table 4-1. Weight % elements in different zones of laser trepan drilled CMSX-4.

Zone	Ni	Al	Cr	Co	Ti	Mo	Ta	W	Re	Hf	O
Oxide layer	14.8	26	6.0	2.8	3.2	0.2	7.8	2.9	0.0	0.1	30.6
Recast layer	61.1	4.8	6.5	10.2	0.9	0.5	6.7	6.3	3.0	0.0	0.0
Base Alloy	67.7	6.8	2.5	7.7	1.5	0.3	8.2	5.2	0.0	0.0	0.0

4.2.2.4 *Nano-hardness*

To further understand the mechanical properties of the recast layers, nano-hardness of a laser drilled sample was measured by nano-indentation using MicroMaterials nano-test system. Three indentations were performed at same depth and equally 10 µm spacing between two indentations around the recast zone and 30 µm around the base alloy zone to minimise the measurement errors. A maximum load of 100mN was used for each indentation. Figure 4-15 show the hardness of laser drilled sub-surface layers. The measured nano-indentations of the recast layer found to be between 6 to 7 GPa which is slightly higher than of measured nano-hardness of the base alloy (CMSX-4) of 5 GPa and

4 to 5 GPa measured elsewhere (J. Gibson *et al.*, 2016). The metallurgical transformations such as re-crystallisation and phase transitions taking place during rapid heating and faster cooling are likely to be the potential reasons of the higher hardness of the recast layer as compared to the base alloy CMSX-4. As result, this could induce fatigue debit associated with alterations in the microstructure produced by laser drilling process. Further hardness tests are required to confirm this trend since the sample population was limited to one laser drilling conditions and only one load was used for this analysis.

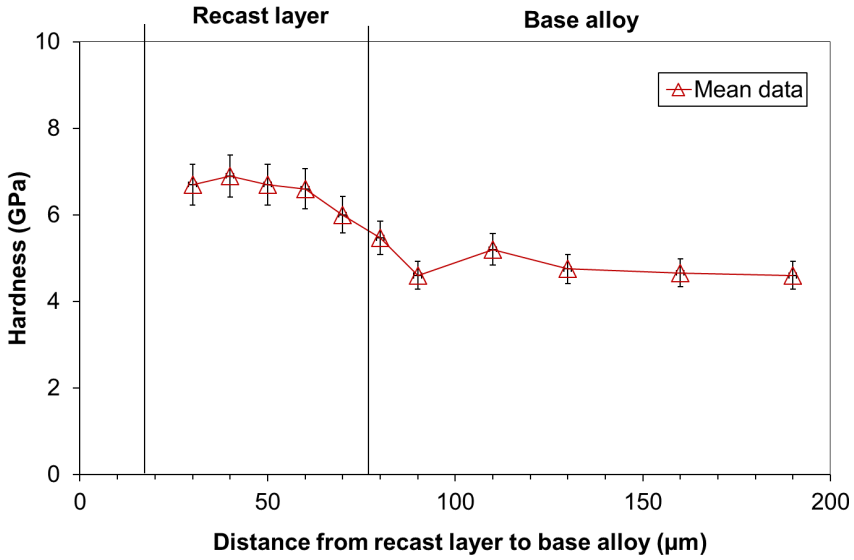

Figure 4-15. Variation in the nano-hardness measured between the recast layer zone and bulk material.

Table 4-2. Hardness results.

Zone	Average, Hardness (GPa)	Average, Young Modulus
Recast layer	6.7 ± 0.34	248.1 ± 12.4
Base alloy, CMSX-4	4.8 ± 0.28	218.7 ± 9.6

4.3 Summary

This chapter characterised and discussed metallurgical alterations produced by LTD, focusing on the recast layer structure. The evaluation of the RL was conducted through analytical SEM, EDS, EBSD, TEM and nano-hardness measurements. The results of this analytical identified critical metallurgical features such surface cracks within the recast,

change in the chemistry and re-precipitated grain size, variations in the hardness and thickness of the recast layer.

The main findings from this chapter are as follows:

1. SEM examination has shown that indeed the laser drilling can produced undesired metallurgical defects on cooling holes such as recast layers, oxide inclusion and even micro cracks within the recast layer. Such metallurgical defects are detrimental for fatigue strength and service life of laser drilled components.
2. The variation in the recast layer morphology was linked to laser beam parameters and oxygen process assist-gas employed and range of levels tested. The SEM observation has shown that higher the peak power greater is the thickness of the recast layer and formation of an oxide layer on the upper layer of the recast.
3. Two types of micro cracks were found in the study, viz. longitudinal and transverse. The transverse (radial) cracks were found to be more detrimental than longitudinal. These cracks were formed due to thermal mismatched during the laser drilling melting and rapid cooling stages. SEM observation show that majority of transverse crack lengths formed were 60 to 75% of its recast layer thickness.
4. EDX spectroscopy examination has shown that concentration of profile of nickel is low in the oxide and recast layer. The concentration profiles of aluminium and chromium were relatively higher than the base alloy. Oxygen has shown to be higher within the oxide layer and then declining towards the recast layer. The EDS analysis suggests that the dissolution and micro segregation of key elements in the recast layer is the root cause of reduced fatigue resistance.
5. TEM and EBSD analysis has shown that the recast layer is of nano-crystalline structure with re-precipitated grains of 150 to 250 nm. This re-precipitation is caused by recrystallization during the laser drilling melting and re-solidification stages where at the molten state there is dissolution and segregation and then afterwards during the rapid re-solidification re-precipitation occurs and small grains are formed in the recast layer.

6. DP's analysis show that both base alloy and recast layer have similar FCC crystal structure. Based on the existing databases the corresponding indexed FCC structure is of 111 plane. Therefore, it can be concluded that the recast layer does result in change in microstructure but not in end phase of the base alloy.
7. Changes in the grain size has an impact on the hardness variation and hence fatigue strength, making the recast layer brittle and vulnerable to early cracking. The nano indentation measurements in the recast layer found to be about 1.4 higher than the base alloy CMSX-4.

The results of this chapter provide an understanding of the recast layer morphology and surface cracks formation in laser trepan drilling of cooling holes and how altered properties may influence the fatigue life performance in service. The next chapter investigates the effects of laser trepan drilling parameters such as peak power, pulse frequency and trepan speed on the recast layer thickness and crack number density by Taguchi method.

5 EFFECTS OF LASER TREPANNING DRILLING PARAMETERS ON THE RECAST LAYER AND SURFACE CRACKS FORMATION IN CMSX-4 ANGLED HOLES

5.1 Introduction

The laser trepanning drilling (LTD) process plays a key role in the manufacturing of cooling film holes for aerospace industry. However, service life of laser drilled components is highly influenced by the surface integrity generated during melting, vaporisation, and molten ejection stages (Voisey *et al.*, 2003). The laser trepan drilled surfaces has many metallurgical defects such as oxide layer, recast layer, oxides, and micro cracks. These metallurgical defects have been characterised and discussed in Chapter 4.

In this research, recast layer and surface cracks formed during the LTD process are evaluated. Much of past studies have focused on the hole taper, drilling speed, optimisation and modelling of surface integrity. A limited number of studies have reported detailed investigation of process parameters and surface crack interactions in laser trepan drilling of angled micro holes (see Chapter 2, see 2.3.6).

In view of that, the novelty of the present work is to further extend the understanding the of influence of pulsed Nd:YAG laser trepanning drilling key process parameters on the recast layer thickness and surface cracks formation on nickel base effusion cooling angled holes. There are number of key process variables in LTD that influence the recast layer thickness and crack formation within the recast layer. In this research, three of these parameters such as peak power, pulse frequency and trepan speed were selected based on the literature review and industrial consultation as aforementioned (section 3.1).

Taguchi method was used to evaluate the key process parameters influencing the thickness of the recast layer and cracks formation of laser drilled surfaces. The sample configuration, experimental setup and design of experiments matrix are detailed in section 3.1 of this thesis. Statistical techniques such as signal-to-noise (S/N) ratios and analysis of variance were employed to determine the main influencing process parameter(s).

Overall, the aim of this chapter is to understand the processing parameters, recast layer and surface cracks formation relationships in laser drilling of CMSX-4 angled cooling

holes so that effort is made to minimise such defects and improve life expectancy of laser drilled components.

5.2 Results and discussion

5.2.1 Analysis of recast layer thickness

5.2.1.1 *S/N ratios*

Table 5-1 shows the S/N responses obtained for the average of maximum recast layer thickness (RLT_{max}). Based on L9 OA, nine different experimental combinations of input parameters were tested four times on the workpiece. The recast layer thickness was measured as per method described in Chapter 3 (section 3.2.2) and provided in Appendix B. the S/N ratios in Taguchi analysis are commonly used to evaluate the variability in a product or process by minimising the effects of uncontrollable factors (Ross, 1998). It also provides a measure of the impact of control factors on the performance or experimental objective. Since the recast layer thickness and cracks formed within the recast layer have great influence on the mechanical properties and service life of laser drilled components, therefore, the smaller is the better (SB) quality objective characteristic was employed for the present analysis. The equation for SB calculation is given by (Roy, 2010):

$$\eta = -10\log\left[\frac{1}{n}\sum_{i=1}^{n} y_i^2\right] \therefore -10\,log\left(\frac{1}{n}(y_1^2 + y_2^2 + y_3^2 + y_4^2)\right) \quad (5\text{-}1)$$

Where, η is signal to noise ratio (S/N ratio), y_i is the ith response of the experiment, n is the repeated number of the ith experimental trial. For example, S/N for trial no.1 of column of Table 5-1 is as follows:

$$\eta_1 = -10\,log\left(\tfrac{1}{4}(44^2 + 48^2 + 53^2 + 48.2^2)\right) = -33.67 \quad (5\text{-}2)$$

The S/N ratios of trial no. 2 to 9 are similarly calculated using equation 5-1 and shown in last column of Table 5-1.

Furthermore, the mean S/N ratio effects plot displays the means response for each input parameter. The opportunities for minimising the recast layer thickness can be easily determined from these plots based on the small is better criteria, see Figure 5-1. The

findings suggest that the intermediate level of peak power (10 kW, A2), higher level of pulse frequency (25 Hz, B3) and a lower level of trepanning speed (75 mm/min, C1) can achieve an average RLT_{max} less than 50 µm. The peak power of 10 kW with set constant pulse energy provides enough laser power for effective processing rate. A pulse frequency at 25 Hz provides enough input average power for efficient melting. Moreover, trepanning speed at 75 mm/min can deliver a more robust process at cut front. However, manufacturing demand the highest trepanning speed which can be achieved at an acceptable *RLT* (Grafton-Reed, 2008). The influences of each process parameter tested on the recast layer thickness is discussed in section 5.2.1.3.

Table 5-1. The results of the recast layer thickness values with related S/N ratios.

Trial No.	Control Parameters			RLTmax (µm)				Mean	MSD	S/N ratio (db)
	PP (kW)	PF (Hz)	TS (mm/min)	1	2	3	4			
1	8.3	20.0	75	44	48	53	48.2	48.3	3.7	-33.67
2	8.3	22.5	100	61.6	48.2	49.8	53.6	55.3	6.0	-34.85
3	8.3	25.0	125	69.2	79	78.1	82.3	77.1	5.6	-37.74
4	10	20.0	100	53.0	52.8	42.8	51.2	53.0	4.8	-34.48
5	10	22.5	125	83.0	62.0	60.0	53.0	64.5	12.9	-36.19
6	10	25.0	75	55.6	43.5	48.2	49.5	50.0	5.0	-33.97
7	12.5	20.0	125	73.0	71.0	62.0	*	68.7	5.9	-36.73
8	12.5	22.5	75	76.7	71.5	46.6	52.3	61.8	14.6	-35.81
9	12.5	25.0	100	63.8	69.6	55.6	64.7	63.4	5.8	-36.04
Peak Power (PP); Pulse Frequency (PF); Trepan Speed (TS); Mean Standard Deviation (MSD)										

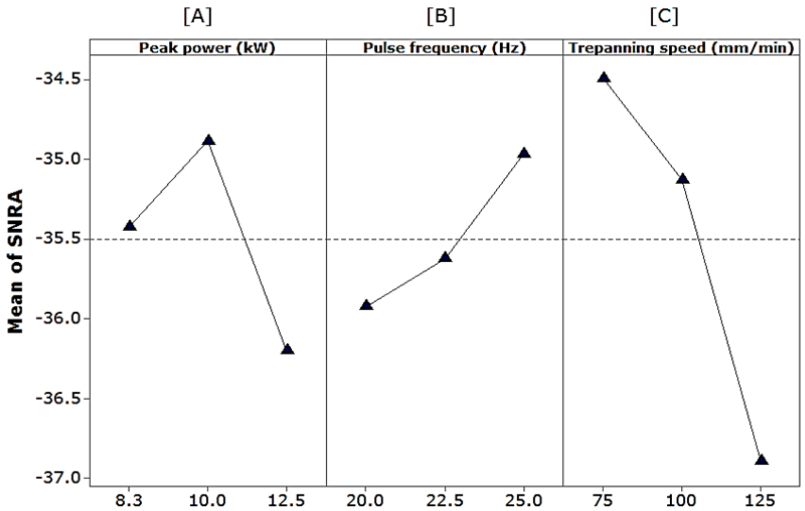

Figure 5-1. Effects of process parameters on S/N ratio (SNRA) for mean RLT_{max}.

Table 5-2. Mean response table for RLT_{max}.

	RLT_{max} (dB)		
Levels	[A] *PP* (kW)	[B] *PF* (Hz)	[C] *TS* (mm/min)
1	-35.42	-34.97	-34.49
2	-34.89	-35.62	-35.14
3	-36.20	-35.92	-36.89
Delta	1.31	0.96	2.40
Rank	2	3	1

5.2.1.2 *ANOVA*

Analysis of variance (ANOVA) is a statistical method to determine the individual interactions of all the control parameters in the experimental design (Ross, 1998). In this work, ANOVA was used to analyse the influences of peak power, pulse frequency, and trepanning speed. ANOVA results for the experimental responses are shown in Tables 5-3, under 95 % confidence limits. The significance of control parameters in ANOVA is determined by comparing the statistic F-values of each control parameter (Roy, 1990). In addition, percentage contributions of each control parameters were computed and are provided in the last column of the Table 5-3.

Table 5-3. ANOVA response for the average RLT_{max}.

Variance Source	DF	Adj SS	Adj MS	F-Value	% Contribution
[A]	2	116.16	58.08	1.83	16.34
[B]	2	70.45	35.22	1.11	9.81
[C]	2	460.51	230.25	7.25	64.80
Error	2	63.53	31.76	-	8.93
Total	8	710.64	-	-	100

As per the Table 5-3, ANOVA results indicates that the trepanning speed is the most statistically significant input parameter influencing the RLT_{max} response with a higher F-value than other input parameters. Based on the degrees of contribution and mean S/N ratios results (see Table 5-2), it was found that the trepan speed (factor C) has the largest degree of contribution, followed by peak power (factor A) and pulse frequency (factor B).

5.2.1.3 *Regression analysis*

In this research work, non-linear regression was used for obtaining the empirical model for RLT_{max}. The relationship between the RLT_{max} response and laser drilling parameters has been determined based on the full quadratic with two-way interaction log-level regression model of second order. The insignificant terms have been removed by backward elimination of terms method, removing P-values less 0.05. The regression analysis was conducted using both Microsoft Excel analysis toolkit and Minitab 16 to determine the regression coefficient and residual plots. The obtained coefficients to correlate the recast layer thickness with respect to laser drilling process parameters are tabulated in Table 5-5. The data used for obtaining regression coefficients for formulating the relationship is shown in Table 5-4.

Table 5-4. Laser drilling data used for RLT_{max} regression analysis.

	Input parameters			Response	
Trial	PP (kW)	PF (Hz)	TS (mm/s)	RLT_{max} (µm)	ln RLT_{max}
1	8.3	20	1.25	48.3	3.88
2	8.3	22.5	1.67	55.3	4.01
3	8.3	25	2.08	77.1	4.35
4	10	20	1.67	53.0	3.97
5	10	22.5	2.08	64.5	4.17
6	10	25	1.25	50.0	3.91
7	12.5	20	2.08	68.7	4.22
8	12.5	22.5	1.25	61.8	4.12
9	12.5	25	1.67	63.4	4.15

Table 5-5. Coefficients for RLT_{max} regression model.

Terms	Coefficients	Standard Error	t Stat	P-value
Intercept	3.62	0.06	50.6	0.000
PP^2	0.01	0.00	5.42	0.003
TS^2	0.44	0.07	6.23	0.002
*PF*TS*	-0.11	0.02	-4.88	0.004

The regression equation for RLT_{max} is given below:

$$\ln SD_{RLT} = 3.62 + 0.01PP^2 - 0.04TS^2 - 0.002\,PPTS \quad (5\text{-}3)$$

The estimates performed according to regression Equation 5-3 are shown in Table 5-6. R^2 statistic and R^2 adjusted values of 0.95 and 0.92 obtained for the RLT_{max} regression model shows that data fits well the observed data under 95% confidence intervals. The analysis of variance results for regression equation is shown in Table 5-7. The P-value for the regression model is less than 0.05, indicating that model is statistically significant. Furthermore, the residual plots in Figure 5-2 confirm that the model fit well the experimental data. It can be observed from the normal probability plots that the experimental points are close to the straight reference line, which means that the data follows a normal distribution. Hence, the residuals of RLT_{max} regression model follow the normality assumption. The calculated root mean square error (RMSE) of 0.003 indicate that prediction accuracy is adequate, thus, acceptable for determining coefficient parameters for estimating life of cooling holes considering surface flaw produced by laser drilling (i.e. recast layer).

Table 5-6. Prediction confidence limits responses for transformed ln RLT_{max}.

Trial No.	Predicted, ln RLT_{max}	Residuals	Standard Residuals	95% CL Lower	95% CL Upper
1	3.85	0.02	0.84	3.78	3.93
2	4.00	0.00	0.05	3.95	4.06
3	4.31	0.03	1.7	4.21	4.41
4	4.00	-0.03	-0.80	3.95	4.05
5	4.22	-0.06	-1.54	4.16	4.29
6	3.92	-0.02	-0.44	3.87	3.98
7	4.21	0.01	0.35	4.12	4.30
8	4.14	-0.02	-1.21	4.03	4.25
9	4.09	0.05	1.37	4.03	4.17

Table 5-7. Analysis of variance for the RLT_{max} regression.

Source	DF	SS	MS	F-Value	P-Value
Regression	3	0.182	0.061	30.4	0.001
Error	5	0.01	0.002	-	-
Total	8	0.192	-	-	-
S = 0.044		R^2 = 0.95		R^2 adjusted = 0.92	

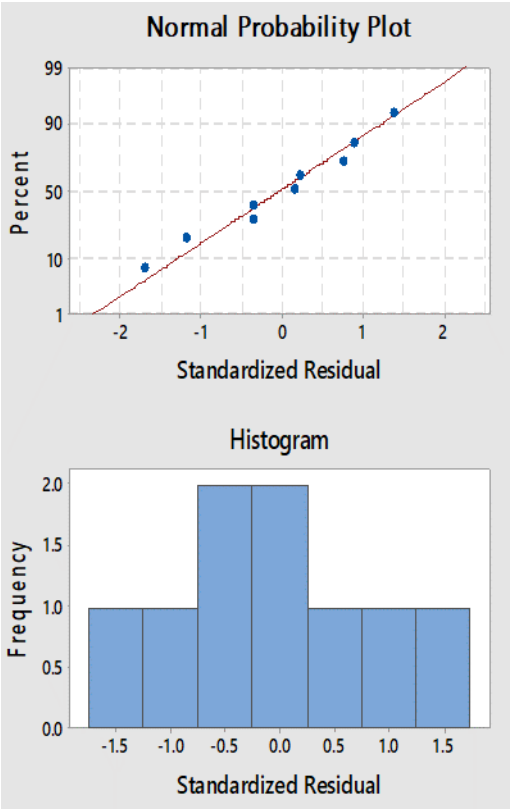

Figure 5-2. Residual plots for the RLT_{max} predicted responses.

5.2.1.4 *Effects of process parameters*

5.2.1.4.1 Peak power

Peak power had a moderate effect on the recast layer thickness within the range of values tested. In general, peak power and power density have major role in the recast layer thickness (Yeo *et al.*, 1994). The peak power corresponds to amount of laser beam intensity delivered into the surface workpiece on a single pulse during the laser processing, in units of joules per milliseconds (Tam *et al.*, 1990). The influence of peak power on the average RLT_{max} is shown in Figures 5-3. It shows that the average RLT_{max} increases as the peak power increase.

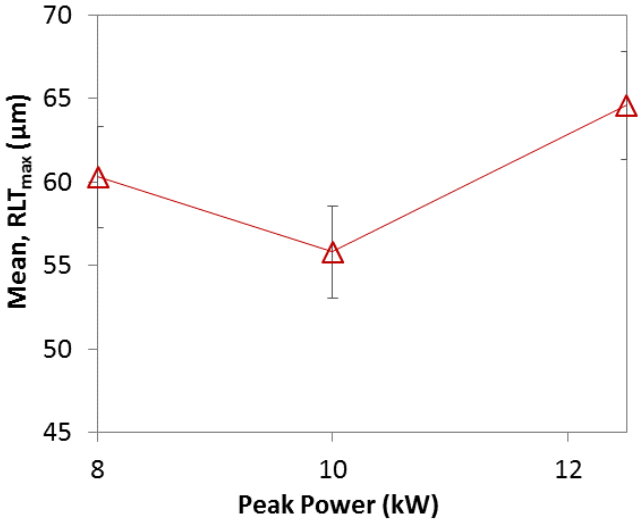

Figure 5-3. Effects of peak power on mean RLT_{max}.

In the present study, a pulse energy of 5 Joules was kept constant through entire experiments and the pulse duration varied from 0.4 to 0.6 milliseconds. As previously mentioned, peak power is output of pulse energy per pulse duration. Therefore, the amount of laser intensity increases as the pulse duration decreases. In general, higher the peak power, higher will be melting or vaporisation rate. In this work, high peak power resulted high molten pool than vaporisation. This is because the thermal conductive in nickel-based alloys is low and thus less heat is diffused through the workpiece, resulting in more heat and melting around sidewalls of the hole. An example of this case is when a setting of 12.5 kW (5 J/ 0.4 ms) is tested, resulting in a thicker recast layer in overall. On the other hand, if the peak power is too low, it will cause the molten pool to accumulate on the sidewalls of the hole due to the low vaporisation rate. As this was the case when tested at a lower setting of 8.3 kW (5 J/ 0.6 ms) yielding also thicker recast layer (see Figure 5-3). This study shows that the better peak power setting for producing high quality angled cooling holes with a diameter of 0.75 mm and depth of 4.0 mm on a CMSX-4 workpiece should be at a moderate laser beam intensity setting of 10 kW (5 J/ 0.5 ms). This setting can be characterised by a vaporisation dominated process and generating less molten pool, thus, thinner recast layer.

Moreover, it should be mentioned that pulse duration had a direct influence on the applied peak power (Leigh et al., 2009). The pulse duration is the amount of time allowed to deliver laser energy in laser drilling, on a single pulse (Duan *et al.*, 2015). A typical a range between 0.2 to 1.0 ms is practised in the aerospace industry depending on the hole

diameter and depth, as well as the type of material for optimising the hole quality in aeroengine components (Beck *et al.*, 1997). The present study confirms that the shorter pulse duration has also a major role in the reduction of the recast layers, as reported studies elsewhere (Sezer *et al.*, 2006; Chien and Hou, 2007; Goyal and Dubey, 2014). The selected input values for the pulse duration varied from 0.4 ms to 0.6 ms in this study, as previously mentioned to yield range of peak power values 8.3 to 12.5 kW. The range of values tested were based on the existing constraints experience during the manufacture of film cooling holes due to back-wall damage problem in the airfoil section of turbine vanes.

Overall, in pulsed Nd:YAG laser drilling suitable pulse duration and pulse energy along with efficient pulse frequency deliver an optimal peak power per pulse (McNally, Folkes and Pashby, 2004; Grafton-Reed, 2008; Marimuthu, Antar and Chantzis, 2015).The optimal peak power enables enough temporal distribution for efficient heat absorption in the workpiece, thus, vaporises more molten material without inflicting thermal damage to the surface workpiece, resulting in less molten material in sidewalls of the hole.

5.2.1.4.2 Pulse frequency

The influence of pulse frequency on the mean RLT_{max} is shown in Figure 5-4. There is a slight decay in the mean RLT_{max} response as the pulse frequency increases. In pulsed laser drilling, pulse frequency determines the laser off-time between the pulses and energy consumed by the material per unit time (Leigh *et al.*, 2009). The maximum value of pulse frequency in this experiment was limited to 25 Hz. This setting ensured the output average power remained below 130 Watts. The output average power value is a function of the pulse energy and pulse frequency (Leigh *et al.*, 2009). As the matter of fact, a suitable pulse frequency will provide enough melt off-time for efficient material removal and the rapid evaporation of the melt, resulting in a thin recast layer. The results obtained from the experiment show that an increase of output average power from 100 to 125 W, improved melting and vaporisation rate, resulting in a slight decrease in the mean RLT_{max}.

A study elsewhere (Duan *et al.*, 2014), demonstrated that a higher pulse frequency greater than 30 Hz produces thicker recast layer. This is because an increase in the pulse frequency increases the laser average power being transferred to the substrate material,

and the time between successive pulses becoming too short to allow the molten material to be completely removed before the start of the subsequent pulse. Therefore, this could result in a poor vaporisation rate and, consequently causing a thicker recast layer. In this study, the highest setting of pulse frequency (25 Hz) provided an overall thin recast layer under the range of values tested.

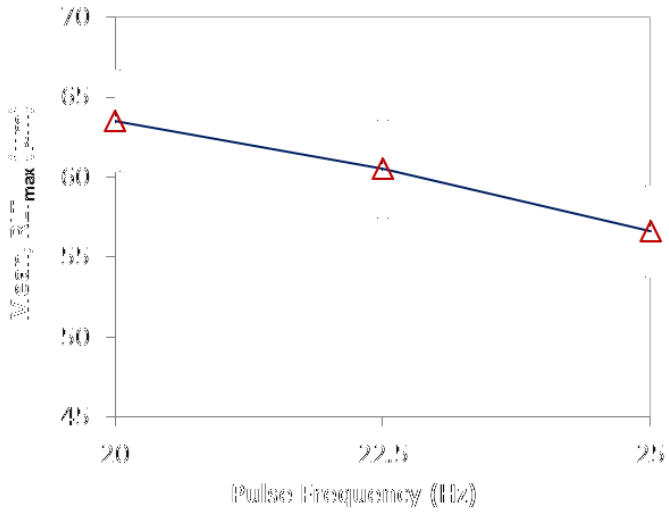

Figure 5-4. Effects of pulse frequency on mean RLT_{max}.

5.2.1.4.3 Trepan speed

The trepan speed is the rotational beam scan speed or the beam motion of the laser beam that enables to cut or pierce the targeted material, making it an important parameter in the laser trepanning drilling. For this study, three trepan speed settings were investigated with an increment of 25 mm/min, starting with 75 mm/min. The effects of laser drilling parameters on the *RLT* responses are shown in Figure 5-5 and show that the recast layer thickness increases with increasing trepanning speed. This trend is also observed elsewhere (Chien and Hou, 2007; Goyal and Dubey, 2014). A higher trepanning speed shortens the amount of interaction time at the cut front, reducing the molten material ejection rate and vaporisation rate. Therefore, a large portion of the molten material re-solidified remains on the sidewalls of the hole, forming thicker recast layer.

On the other hand, lower trepanning speed generally results in more interaction time between peak power and scan speed, thus, effective energy absorption and heat dissipation of the laser beam intensity into the workpiece (Chien and Hou, 2007) and

slower beam motion generates better hole geometry (Antar *et al.*, 2016). Hence, lower trepanning speed promotes effective pulse density. The pulse density is pulse frequency over the trepanning speed (Duan *et al.*, 2014). For example, a high pulse density, a combination of low trepanning speed and high pulse frequency yields vaporisation dominated process. Therefore, less molten material on sidewalls of the holes, resulting in a thinner recast layer. In the present study, lowest trepanning value tested of 75 mm/min yielded a thinner recast layer in overall. Past studies have also observed similar results when laser trepan speed ≤ 75 mm/min was used for drilling cooling holes (Goyal and Dubey, 2014; Antar *et al.*, 2016).

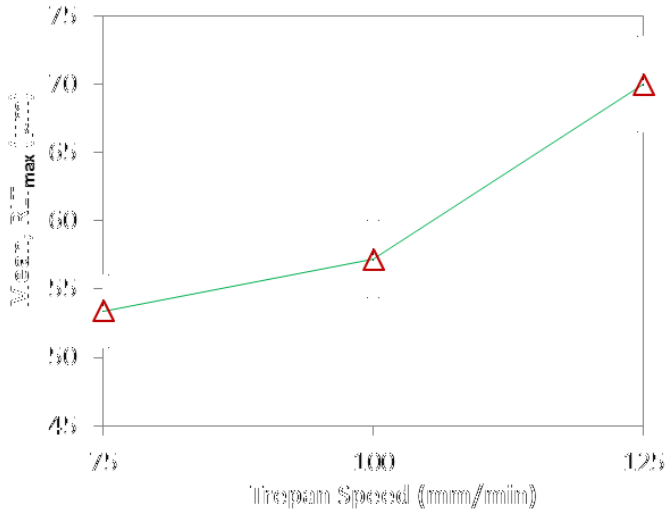

Figure 5-5. Effects of trepan speed on mean RLT_{max}.

Pulsed Nd:YAG laser drilling is a complex process and the recast layer thickness responses obtained in this work suggests that the trepan speed and peak power interaction played an important role in the recast layer thickness. Figure 5-5 show the interaction effects between the peak power and trepan speed on the recast layer thickness. According to trends in the Figure 5-4, it is clear that the increase in peak power in combination with an increase of trepan speed leads to thicker recast layer thickness. This is because when the trepan speed is faster and high peak power is high result in short interaction time and more molten material on the sidewalls of the hole. This shorter interaction time result in poor molten material removal, thus, increase in the recast layer thickness. However, interesting observation when high peak power in combination with high trepan speed (12.5 kW, 125 mm/min) yields less thick recast layer than peak power levels at 10 kW and 8.3 kW. This is because at high trepan speed the interaction time also restricts the

excessive heat and thermal damage on sidewalls of the hole and its periphery (Goyal and Dubey, 2014). Furthermore, laser trepanning drilling with a lower level of peak power is shown to be less stable (Grafton-Reed, 2008; Antar *et al.*, 2016). That was indeed the case, when peak power of 8.3 kW was tested.

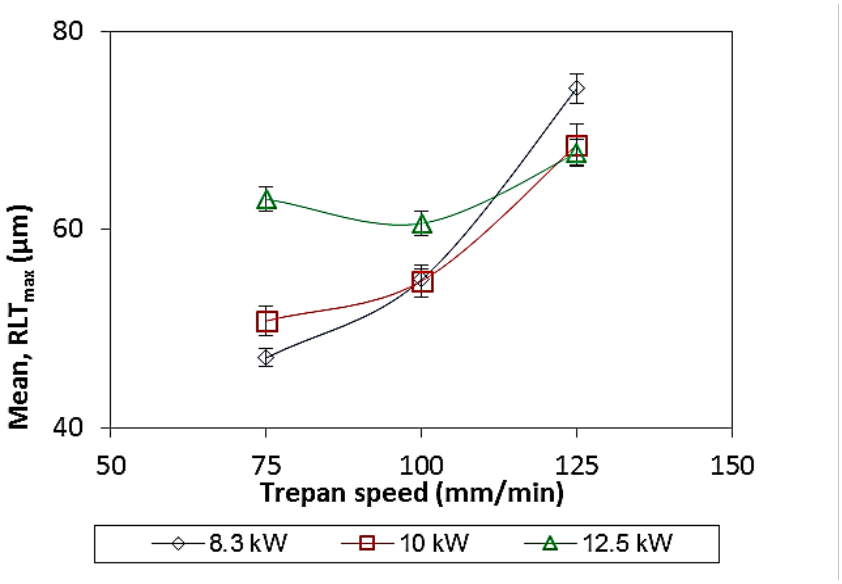

Figure 5-6. Effects of trepan speed and peak power interaction on *RLT$_{max}$*.

5.2.1.4.4 Number of trepanning speed

One more parameter involved in the laser trepanning drilling is the number of trepan orbits, also known as beam rotation or motion. In this post-experiment, the effects of one to four rotations were tested. The remaining parameters were held constant including the pulse duration (0.5 ms), pulse frequency (25 Hz), trepanning speed (75 mm/min), and remaining parameters held constant. Figure 5-7 show that the no. of trepan orbits had no influence on the recast layer thickness. This can be explained by the fact that most of the molten material in the hole has been ejected during the first rotation, and the subsequent rotation will only trim slightly the molten material on the sidewall of the hole. Therefore, the molten material after third and subsequent rotations will mainly flow along the sidewalls, increasing the probability of the multi-layered re-solidified material, resulting in the thicker recast layer. The current experimental results confirm that this is indeed, the case. Moreover, multiple orbits also result in the increase of drilling time (Antar *et al.*, 2016), thus, making them undesirable for drilling hundreds of cooling holes in turbine vanes.

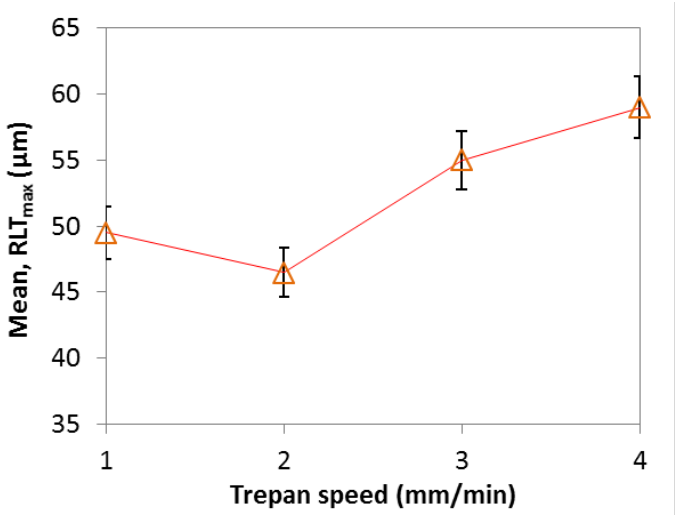

Figure 5-7: Influence of number of trepanning orbits on the average RLT_{max}.

5.2.1.4.5 Assist gas

Assist gas pressure is the main element of the ejection of molten material through the exit hole during the laser processing. The assist gas pressure act as a rigid downward mechanical force, which works in synergy with the sequential melting and vaporisation during the impingement of continuous laser pulses to form a hole (D. K. Y. Low, Li and Corfe, 2000). The flow of assist gas also acts as a protective shield for the nozzle exit diameter of the laser beam against debris and spatter (Low, Li and Byrd, 2000). Moreover, the types of assist gas also have an impact on the surface morphology of the laser drilled surface as previously mentioned. Most common assist gas used for laser trepanning drilling of nickel-base alloys is oxygen, among the argon and nitrogen. The previous studies have shown that the argon is the most effective when it comes to reducing the thickness of the recast layer (Horn *et al.*, 2000). Whilst, others (Kreutz *et al.*, 2007; Walther *et al.*, 2008) indicated that the use of oxygen as an assist gas yields in generally better surface morphology. Overall, these studies indicate that the different type of assist gas and pressure values can generate different solidification rates and hence different surface recast morphology.

The range of assist gas pressure employed by previous studies above cited ranged from 72 psi to 145 psi, independent of the type of assist gas. It should be mentioned that the assist gas pressure effectiveness depends on the material thickness and depth of the drill. Furthermore, it is being established that higher assist gas pressure may lead to an effective

downward force, resulting in the molten material to eject out more easily (Palumbo, De Chiara and Marrone, 2009). However, excessive gas pressure gradually prevents molten material from ejecting outside due to increasing cooling rate, which rapidly re-solidifies the melt on the sidewalls of the hole by means of forced convection (Tam *et al.*, 1993), resulting in a thicker recast layer thickness.

In the present experiments, the pressure of 100 psi was used through entire experiments. The decision was based on the literature and the range of values used in the industrial practice, for laser drilling of turbine engine components. In current manufacturing, oxygen and air are the two main gases used as this gives an acceptable balance of process speed and the metallurgical result (Grafton-Reed, 2008).

5.2.2 Analysis of surface cracks

SEM observation of the laser drilled cross-sectioned samples reveals that the surface cracks were longitudinal and transverse type micro-cracks. In the present study, only transverse cracks were used for the analysis. As previously, stated, transverse cracks are perpendicular to the recast layer making them vulnerable to advance towards the base alloy, hence, detrimental to fatigue life. Since transverse cracks act as the initiation point of failure, it is essential to quantify the degree of cracking in terms of standard measure. In this study, crack number density (CND_i) is applied to evaluate the severity of cracking (see Equation 3-9).

5.2.2.1 *S/N ratios*

The S/N ratios of trials 1 to 9 were calculated using the Equation 5-1, as described in Section 5.2.1.1., and S/N ratio results for transverse CND_{max} is given in Table 5-8. Figure 5-8 show the mean effects plot for transverse CND_{max}, for each input parameter tested. It can be seen from Figure 5-6 that the peak power appears to have significant effect on the transverse crack density. This mainly associated with input laser intensity to thermal gradients and tensile residual stress caused by cold assist gas pressure and work surface at room temperature. In this research, the high peak power tested inflicted less thermal damage to the sidewalls of the hole, thus, less cracks formed within the recast layer. This mainly due to short pulse duration setting at that high peak power level.

Table 5-8. The results of the transverse crack number density values with S/N ratios.

Trial No.	Control parameters			CND_{max} (no./mm^2)					
	PP (kW)	PF (Hz)	TS (mm/min)	Hole 1	Hole 2	Hole 3	Hole 4	Mean	S/N ratio (db)
1	8	20	75	0.25	0.25	1.25	0.75	1.25	0
2	8	22.5	100	0.5	1	2.25	0.75	2.25	-6.02
3	8	25	125	1.5	0.5	-	1	1.5	-1.938
4	10	20	100	1.5	0.5	0.25	0.5	1.5	-3.521
5	10	22.5	125	2.25	2	2.75	2	2.75	-8.786
6	10	25	75	2.25	0.25	2.5	2.5	2.5	-7.958
7	12.5	20	125	1.25	0.5	0.75	0.5	1.25	-1.938
8	12.5	22.5	75	0.5	-	0.25	0.5	0.5	12.041
9	12.5	25	100	0.5	-	0.5	0.75	0.75	6.02

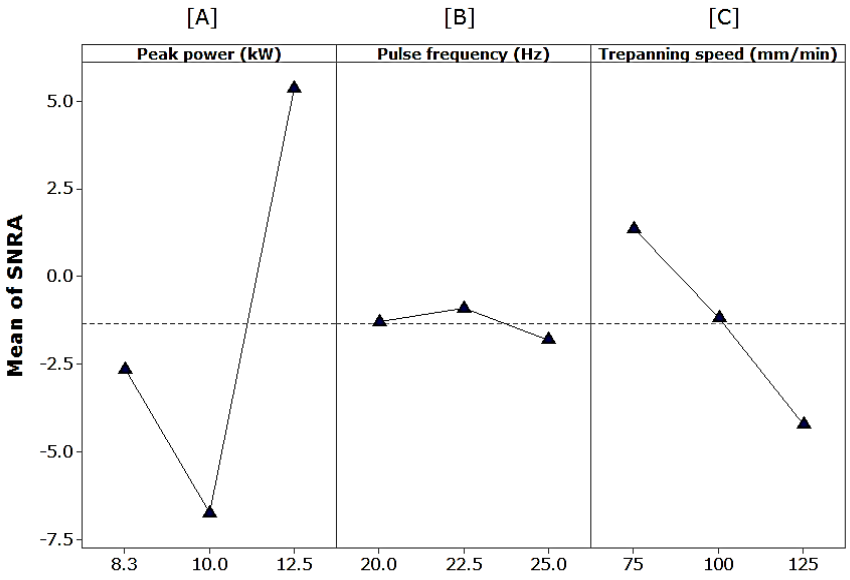

Figure 5-8. Effects of process parameters on mean S/N ratio (SNRA) for transverse *CND_{max}*.

Plots in Figure 5-6 suggest that the high level of peak power (12.5 kW, A1), intermediate level of pulse frequency (22.5 Hz, B2) and a lower level of trepanning speed (75 mm/min, C1) could minimise the transverse cracks within the recast layer. The influences of process parameters on the crack formation are discussed in the next section.

5.2.2.2 *ANOVA*

ANOVA results from Table 5-9 confirms that peak power is the most statistically significant factor affecting the transverse CND_{max} with highest percentage contribution of 79 %, followed by pulse frequency (12.4 %) and trepan speed 0.6 %, latter being insignificant factor under the range of values tested. The percentage error was significantly low at 8.93 % and 7.72 % for both average RLT_{max} and CND_{max} respectively.

Table 5-9. ANOVA response for the transverse CND_{max}.

Variance Source	DF	Adj SS	Adj MS	F-Value	% Contribution
[A]	2	5.54	2.77	10.23	79.1
[B]	2	0.87	0.43	1.62	12.4
[C]	2	0.041	0.020	0.08	0.58
Error	2	0.541	0.270	-	7.72
Total	8	7.0	-	-	100

5.2.2.3 *Effects of process parameters*

5.2.2.3.1 Peak power

Figures 5-9 show how CND_{max} varies with changes in the peak power, pulse frequency and the trepanning speed. The mean effects plots and ANOVA shows that the peak power has a major effect on the transverse CND_{max} response. It shows that the transverse CND_{max} tends to be insignificant when laser drilling with a high peak power of 12kW (5 J/ 0.4 ms). This is opposite to mean RLT_{max} responses. This is because shorter pulse duration generates less thermal damage to the sidewalls, hence, less cracking. On the other hand, the pulse frequency and the trepanning speed had very little statistical significance in the formation of transverse CND_{max}.

The peak power is the function of pulse energy and pulse duration, as previously stated. From the mean plot, as shown in Figure 5-9, the transverse CND_{max} increases significantly as the peak power decreases. This is because the pulse duration varies in the increasing order as the peak power decreases, when the pulse energy is held to 5 joules throughout the entire tests. The results show that an increase of pulse duration to 0.5 ms and 0.6 ms had significant influence on the cracks within the recast layer. It means that shorter the pulse duration, less thermal stress is inflicted on the workpiece surface and thus cracks

tend to not appear when laser drilling with high peak power, based on the range of values tested. However, there are two constraints using high peak power setting. First, the back-wall damage on the blade and vane airfoil. Second, thermal conductivity of the material and the recast layer thickness correlation. The material with thermal conductivity tends to diffuse heat away from the localised heat region faster to the material surroundings. Therefore, resulting in less localised molten pool and hence thinner recast layer, as well as less tendency for cracking. Since nickel base superalloys have lower thermal conductivity, peak power will have significant influence on the surface crack formation.

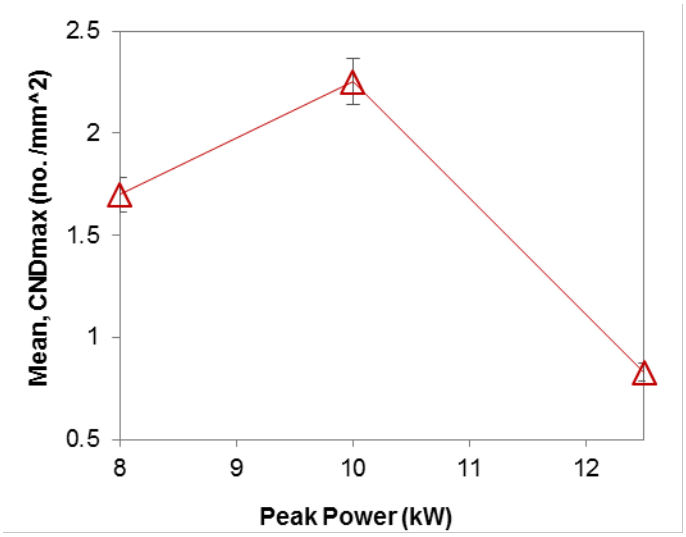

Figure 5-9. Variation of transverse CND_{max} with peak power.

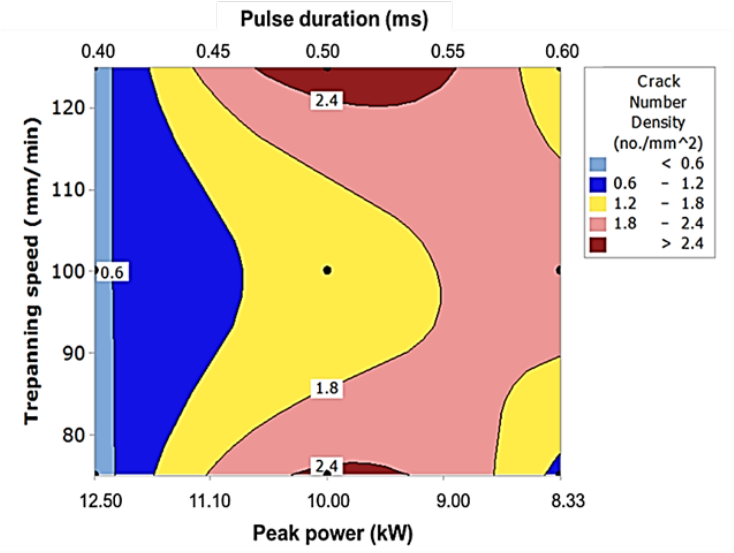

Figure 5-10. Contour graph shows the effect of peak power, pulse duration and trepanning speed on the transverse CND_{max}.

Figure 5-10 show a contour map of the transverse CND_{max} based on the experimental responses. It shows how the variation in laser beam parameters such as pulse energy and pulse duration interaction affect the output peak power and in turn in the variation in the crack formation. The contour map can be used for controlling the surface damage and optimisation of processing parameters. However, this map is constrained by the range of values tested, diameter of the hole and drill depth. Therefore, an investigation into the surface crack formation is needed if a further understanding is to be obtained to control cracking during laser drilling of acute and angled effusion cooling holes.

5.2.2.3.2 Pulse frequency

Although pulse frequency had small influence on the transverse CND_{max} under the range of values tested, as shown in Figure 5-11. In general, higher the pulse frequency, greater is the thermal damage to the workpiece surface that can be obtained in pulsed laser drilling. This is because at higher pulse frequency the time between two successive pulses is not long enough for heat to dissipate to the workpiece surroundings and leads to high localised residual heat and greater thermal gradient. Therefore, resulting in crack formation.

The increase in pulse frequency has shown to slight influence the RLT_{max} as well transverse CND_{max} response when increasing from 20 Hz to 22.5 Hz. This is because a slight rise in the pulse frequency stabilises the laser energy and output average power inflicted on the workpiece, thus, reducing the localised residual heat. However, an increase in the pulse frequency to a higher levels greater than 30 Hz could cause an increase in the recast layer thickness, based on the work reported elsewhere (Chien and Hou, 2007; Duan *et al.*, 2014). Therefore, a range between 15 to 26 Hz can be used depending on the thickness of the material and type of material and their properties such as thermal diffusion and absorptivity.

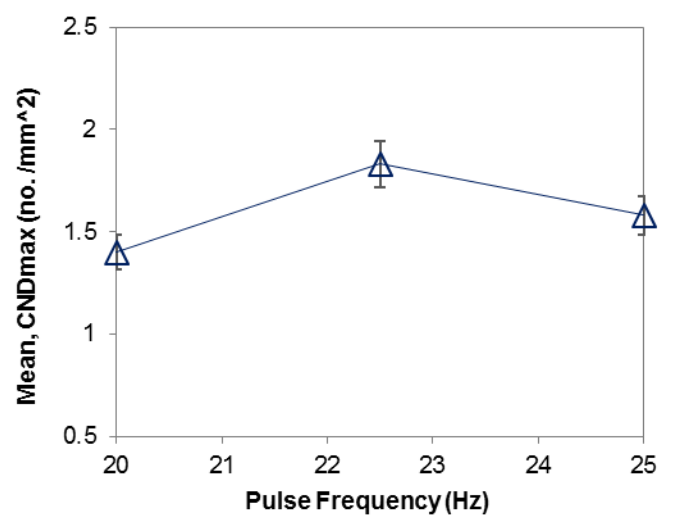

Figure 5-11. Variation of transverse CND_{max} with pulse frequency.

5.2.2.3.3 Trepan speed

Figure 5-12 show that the increase in trepan speed slightly increases transverse CND_{max}. This is due to interaction between the peak power and laser beam scanning speed. The lowest values of transverse CND_{max} were at 75 mm/min for all trepan speed values tested. One reason is the high residual stresses and adverse heat transfer behaviour. In general, high trepan speeds can lead to an increase of thermal residual stresses on the sidewalls of the hole due to reduce time available for effectively disperse the residual heat to the workpiece surroundings to avoid the localised thermal cracking during the re-solidification. Although increasing peak power has been shown to reduce the cracks, increasing pulse duration increases the amount of residual heat on sidewalls of the hole during laser drilling. This may also explain why cracks were found in the oxide layers. In this study, surface cracks are significantly reduced at low trepan speed and peak power interaction at short pulse duration. Moreover, the low trepan speed increases the laser beam interaction time for effective heat dissipation, vaporisation and molten ejection rate, thus, reducing the recast layer thickness and potential cracking.

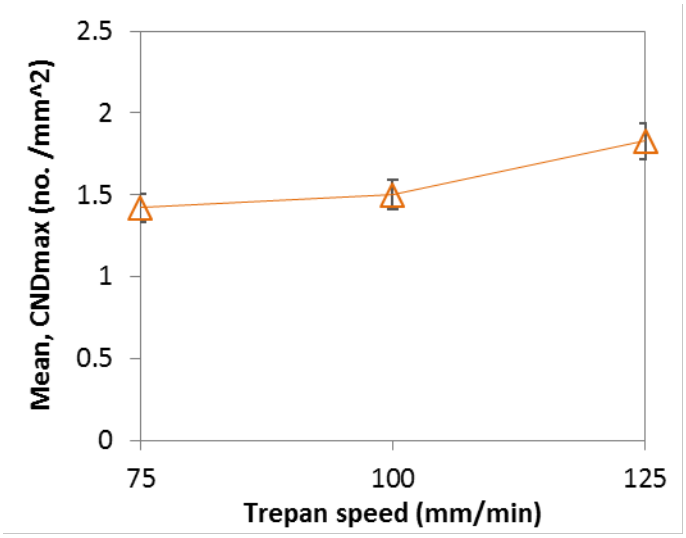

Figure 5-12. Variation in CND_{max} with trepan speed.

5.2.2.3.4 Assists gas

Based on previous studies elsewhere (Horn *et al.*, 2000; Lugscheider *et al.*, 2005), authors reported that each type of assist gas influences the surface crack formation, such as argon, nitrogen and oxygen. Latter, avoid closures, melt droplets, and formation of burrs compared to the argon (Kreutz *et al.*, 2007; Walther *et al.*, 2008). Although, this study and the discussion presented attempted to provide an understanding of this phenomenon by considering the characteristics of the pulsed Nd:YAG LTD process along with key process parameters such as peak power, pulse duration, pulse frequency and the trepanning speed, but there is still a need for better understanding of the effects of oxygen assist gas pressure and mass flow rate on the surface cracks.

5.3 Summary

The following key observations could be drawn from this experimental investigation based on the input parameters and range of values investigated:

1. The SEM examination has shown that there is variation in the recast layer and surface cracks depending on the peak power and trepan speed levels tested. Increase in peak power found to be influent on the formation of oxide layer and recast layer thickness.

2. The formation of the recast layer is mostly influenced by the trepanning speed and followed by peak power. An increment of 60 % was observed from an increase of 75 to 125 mm/min. An intermediate level of peak power showed to be the most effective for reducing the RLT_{max}. The pulse frequency has been found to be less significant. For the entire experiments, average RLT_{max} observed varied from 48 µm to 77 µm.
3. The crack number density is most influenced by the peak power. Pulse frequency and trepanning speed were found to be insignificant. In comparison to crack orientation, the transverse cracks in the recast layer are found to be highly detrimental compared to longitudinal, as the foremost cracks could penetrate to the substrate, consequently reducing the resistance to fatigue crack mechanism.
4. The number density of transverse crack was found to decrease from 2.75 no./mm^2 to 0.25 no./mm^2, when incrementing the peak power from 8.3 to 12.5 kW. This is due to by rapid heating and cooling cycles causing distress in the molten area and tensile residual stress during the re-solidification.
5. Majority of the cases, transverse maximum crack length values had exceeded 40 to 60 per cent of its recast layer thickness. This is detrimental, since it may limit the life of laser drilled components during in-service.
6. Based on the ANOVA results, the percentage contribution of key process parameters on the recast layer thickness has found to be higher for trepanning speed (65%), followed by peak power (16.3%) and pulse frequency (10%). Whereas, the percentage contribution of key process parameters on the transverse CND_{max} has found to be higher peak power (79%), followed by pulse frequency (12%) and trepan speed (0.6%).
7. The optimum settings for minimum surface damage including the recast layer thickness and the transverse crack number density could be obtained at intermediate pulse duration and pulse energy combination, a higher level of pulse frequency, and low level of trepanning speed.
8. Overall, long pulse duration and thick recast layer are two main factors that lead to more crack formation, hence, the transverse CND_{max} response in this study.

9. The knowledge gained in this experiment enables to determine the range of the recast layer thickness and crack number density formed during a commercial laser drilling of nickel-base angled holes, leaving for potential opportunities for review of the current parameters settings, allowable recast layer thicknesses tolerances and parameters optimisation.

The next chapter uses present chapter knowledge and data to evaluate the effects of different recast layer thicknesses on high temperature corrosion-fatigue of nickel-based angled cooling holes, yielded on at different laser drilling settings.

6 EFFECTS OF RECAST LAYER THICKNESS ON HIGH TEMPERATURE LOW CYCLE CORROSION FATIGUE LIFE OF LASER DRILLED CMSX-4 ANGLED COOLING HOLES

6.1 Introduction

This chapter presents research work related to investigation of effects of different recast layer thickness on high temperature (HT) corrosion-fatigue (CF) of angled cooling holes produced by laser drilling. Through a series of mechanical tests in simulated environment, this chapter discusses the potential fatigue life debit due different recast layer thickness produced. This study makes use of previous chapter results for selection of most significant laser drilling parameter influencing the recast layer, so that it can be used to yield the range of recast layer thickness for this study. Fatigue specimen's preparation and laser drilling settings for initial trial plates and fatigue specimens are described in chapter 3.

Nevertheless, studies reported in the existing literature and discussed in chapter 2 (section 2.8) have not fully detailed the laser drilling conditions and their influence on corrosion-fatigue life. More, the past research studies have focused on thermal mechanical fatigue and creep behaviour of cooling film holes, given that the cooling holes are not only exposed to high temperature but also to hot gases and sea air ingested from inlet engine. As such, this chapter attempts to fill the gap in the literature related to the effects of recast layer thicknesses on the HT CF life of laser drilled CMSX-4 angled holes.

6.2 Results and discussion

6.2.1 S-N Corrosion-fatigue data

For the first time, HT CF tests under low cycle fatigue regime have been carried out to analyse the influence of laser drilling process and the different recast layer thickness produced interaction. Three different laser trepanning drilling conditions were used for this study (see Table 3-9). Table 6-1 to Table 6-4 shows the results obtained from the corrosion-fatigue tests and the S-N plot is depicted in Figure 6-1.

Table 6-1. Results of HT LCCF tests performed on the LTD set A specimens.

Specimen Code	Specimen No.	Stress (MPa), S	Cycles to failure, Nf	Observations
FAT233	LTD 01	550	6,353	Fail
FAT239	LTD 02	450	50,089	Fail
FAT245	LTD 03	450	58,891	Fail
FAT293	LTD 04	350	97,247	Fail
FAT241	LTD 05	350	110,000	Unbroken

Table 6-2. Results of HT LCCF tests performed on the LTD set B specimens.

Specimen Code	Specimen No.	Stress (MPa), S	Cycles to failure, Nf	Observations
FAT246	LTD 06	550	19,604	Fail
FAT236	LTD 07	550	17,716	Fail
FAT307	LTD 08	450	80,768	Fail
FAT299	LTD 09	400	110,000	Unbroken
FAT270	LTD 10	350	110,000	Unbroken
FAT09	LTD 11	350	120,000	Unbroken
FAT253	LTD 12	290	110,000	Unbroken
FAT258	LTD 13	290	120,000	Unbroken

Table 6-3. Results of HT LCCF tests performed on the LTD set C specimens.

Specimen Code	Specimen No.	Stress (MPa), S	Cycles to failure, Nf	Observations
FAT247	LTD 14	550	4,333	Fail
FAT264	LTD 15	450	36,694	Fail
FAT290	LTD 16	450	39,978	Fail
FAT250	LTD 17	350	89,076	Fail
FAT257	LTD 18	290	110,000	Unbroken

Table 6-4. Results of HT LCCF tests performed on the plain CMSX-4 and EDMed specimens.

Specimen Code	Specimen No.	Stress (MPa), S	Cycles to failure, Nf	Observations
FAT309	Bare 01	1000	110	Plain (not drilled), Fail
FAT311	Bare 02	600	131,304	Plain (not drilled), Fail
FAT313	Bare 03	700	5,626	Plain (not drilled), Fail
FAT315	EDM 01	550	15,690	EDM Die-sink, Fail
FAT316	EDM 02	450	45,021	EDM Die-sink, Fail
FAT317	EDM 03	350	110,000	EDM Die-sink, Unbroken

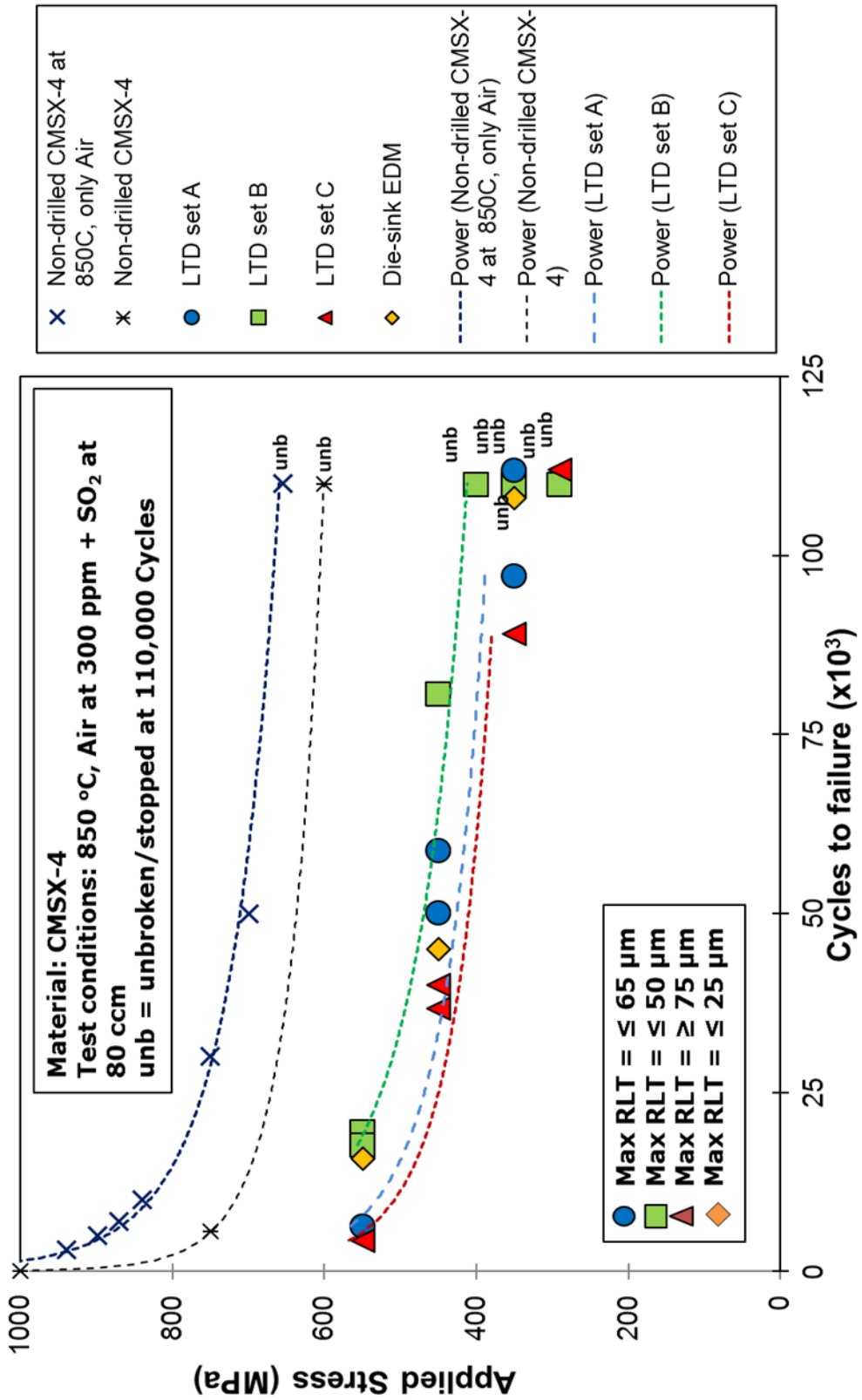

Figure 6-1. Corrosion-fatigue S-N curves of CMSX-4 drilled and undrilled specimens tested.

The corrosion-fatigue S-N data of specimens tested at three different laser drilling conditions, one Die-sink EDM condition, and in non-drilled conditions both in the air/SO_2 simulated lab environment is shown in Figure 6-1. Five sets of experimental data include: LTD set A (blue circle); LTD set B (green square), LTD set C (red triangle) and Die-sink EDM (orange diamond). Last one, trend-line for non-drilled tested specimens is depicted in black line and has been tested at three different stress levels (1000 MPa, 750 MPa and 650 MPa) under 850 ºC similar testing conditions. In addition, a set of data tested in air at 850ºC was used for comparison and it was supplied collaborative company. The air data is represented as doted lines with blue cross marks.

Examining the S-N data in Figure 6-1, in general, all laser drilled fatigue specimens have experienced a reduction in life compared to un-drilled specimens, under similar test conditions. The data suggest that the corrosive environment had an impact on the fatigue life debit about 15% on CMSX-4 un-drilled (bare) specimens when comparing to bare data tested in air at same temperature. Moreover, it can be seen from S-N curves of laser drilled specimens were significantly influenced by the recast layer thickness. The shorter lives between laser drilling tested specimens at each stresses level were associated with a thicker recast layer. The measured mean recast layer thickness varied up to a maximum of 63.2 µm for LTD set A, 47.8 µm for LTD set B and 77.9 µm for LTD set C. Therefore, in overall, LTD set B tested specimen had better life performance compared to counterpart LTD set A and C.

Another critical observation was that the specimens of LTD set B tested at lower stress levels (i.e. 350 MPa and 290 MPa) were unbroken at 120,000 cycles, thus, re-tested again to verify the fatigue strength up 10^7 cycles. The re-tested specimens tested at 400 MPa and 350 MPa did not fail again at 120,000 cycles. As such, strongly suggests that corrosion-fatigue strength up to 10^7 cycles is closer at 350 MPa, which about 60-90 MPa higher than the counterpart laser is drilling conditions A and C, also re-tested at 290 MPa. However, more tests are required to confirm these trends.

Although the number of EDMed drilled tested specimens used for the comparison was very limited, the test results show a life that is similar to the LTDed tested specimens LTD set A and C. EDMed drilled specimens had measured mean RLT_{max} of 25.5 µm. In general, EDM drilling produces an average of recast layer thickness ranging between 10-

15 μm for holes with a diameter range between 0.5-1.0 mm (Degeilh, Bonnand and Pacou, 2013). Therefore, better corrosion fatigue life characteristics than the laser-drilled specimens would be expected. This is because the metallurgical residues and microstructural alterations induced on the drilled surface by EDM may be detrimental than the laser drilling. In addition, electrode tube material such as brass or cooper used as drilling tool and type of dielectric fluid employed (deionised water or kerosene) can migrate on the recast layer, thus, reducing the fatigue resistance under hot corrosion environment. Additional tests are required to understand the metallurgical alterations produced by EDM on mechanical properties of cooling holes, such as corrosion-fatigue strength.

6.2.2 Effects of trepan speed on corrosion-fatigue

Furthermore, the S-N data was used to analyse the lives of laser drilled tested specimens in terms of different trepanning speed and applied stress levels interactions, as shown in Figures 6-2(a-b) and 6-3(a-b). It can be seen from the plots the low trepanning speed had a beneficial effect on the HT CF performance. On the other hand, life becomes more pronounced as the value of the trepanning speed increases from 75 mm/min to 150 mm/min, adversely affecting the HT CF performance. This is directly related to pulse density and peak power interaction at each trepanning speed settings tested. The variation of recast layer thickness with respect to change in trepan speed is discussed in Chapter 5 (Section 5.2.3.3).

Figure 6-2a show that the laser drilled specimens tested at 550 MPa had shorter lives, below 20,000 cycles. This suggests that the applied cyclic stress was dominant, independent of the recast layer thickness and hence levels of trepan speed employed. This also suggests that at applied stress levels above 550 MPa, the mechanical fatigue is main driver for crack advance and failure. Variation in HT CF life begins to be more prominent at intermediate applied stress tested, 450 MPa (see Figure 6-2b). At this stress level, corrosion-fatigue and recast layer thickness interaction influenced the live performance of tested specimen's. The specimen's laser drilled at low trepan speed (75 mm/min) had better life performance compared to counterpart specimen's laser drilled at 125 mm/min and 150 mm/min by approximately 70%.

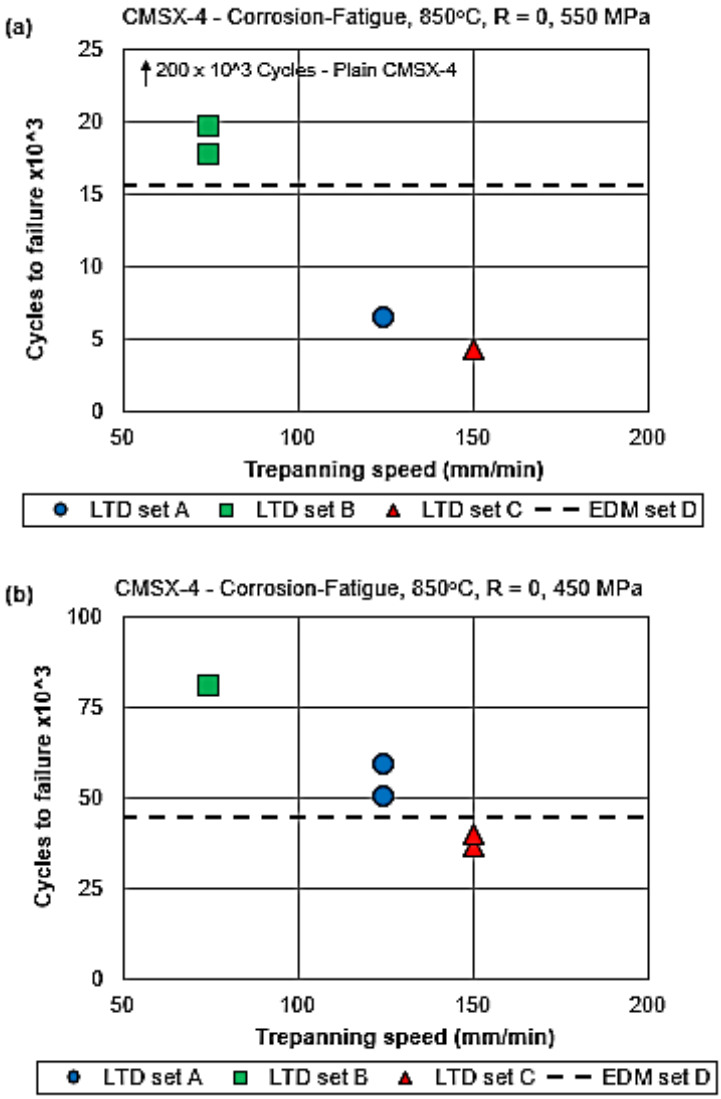

Figure 6-2. Effect of trepanning speed on the HT LCCF life of CMSX-4 laser drilled acute angled holes at (a) 550 MPa and (b) 450 MPa.

As can be seen from Figure 6-3a-b, at stresses below 350 MPa the laser drilled specimens had significantly longer lives. These results point out the importance of both thinner recast layer generated by low trepan speed and environmental effect on crack initiation time and growth rate at low stress levels. Moreover, it should be mentioned that presence of pre-existing cracks generated during the laser drilling may have influenced the lives of specimens drilled with LTD set A and C. Another critical observation was the corrosion-fatigue life of all specimens tested improved as the stress reduced to 290 MPa, suggesting endurance limit bellow 300 MPa for laser drilled and EDMed specimens independent of recast layer thicknesses. Overall, the results suggest that the higher drilling speed may be compromised over the hole quality and precision, based on the fatigue performance data.

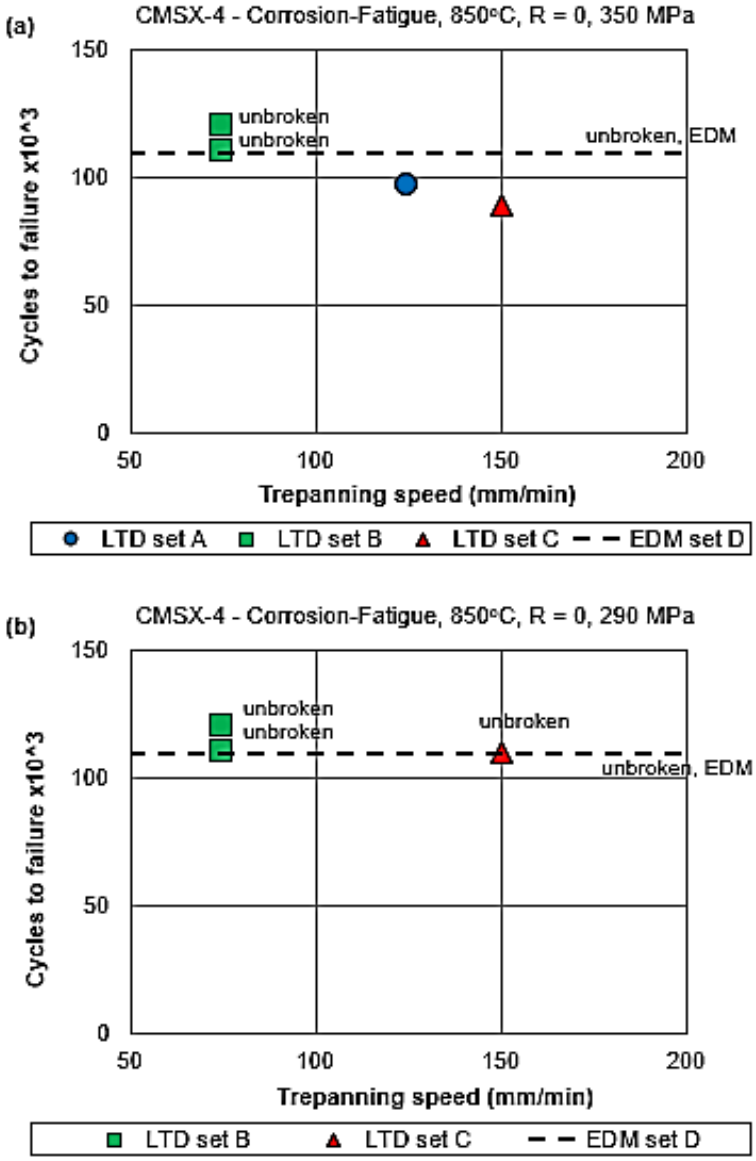

Figure 6-3. Effect of trepanning speed on the HT LCCF life of CMSX-4 laser drilled acute angled holes at (a) 350 MPa and (b) 290 MPa.

6.3 Summary

The effects of recast layer thickness on corrosion-fatigue lives of nickel base CMSX-4 angled holes at 850 °C were investigated in this chapter. In addition, relationship between trepan speed, recast layer thickness and corrosion-fatigue life was established. The key observations in this chapter are as follow:

1. The fatigue life of CMSX-4 un-drilled specimens at 850ºC is significantly greater in air than in hot corrosion environment, there is a life debit of approximate 15-20% associated with corrosion-fatigue interaction. Moreover, when comparing drilled specimens there is a fatigue life debit of 30-50%, suggesting greater impact of surface damage induced by laser and EDM process.
2. RLT produced by die-sink EDM was up to a maximum of 25 µm, not typical of normal production (10-15 µm) had similar corrosion fatigue lives as of tested LTD set A and C specimens. This could be due to the high thermal tensile residual stresses induced by dielectric sparks on the hole surface, resulting in brittle recast microstructure and decrease in fatigue strength.
3. The effect of cyclic stress was more prominent at 550 MPa where all the laser drilled specimens failed below 10,000-20,000 cycles. This strongly suggests that cyclic stresses above 550 MPa, mechanical fatigue is the main driver for crack initiation and crack growth rate. At intermediate and low cyclic stresses, the corrosion-fatigue was dominant in both stages of crack initiation and short crack growth. Metallography analysis of fracture surfaces are discussed in Chapter 7.
4. The corrosion-fatigue life of all specimens tested improved as the stress reduced to 290 MPa, suggesting endurance limit bellow 300 MPa for all laser drilled and EDMed specimens independent of recast layer thicknesses generated (48-79 µm).
5. The effect of trepan speed at the lower level at 75 mm/min proved to be beneficial for corrosion-fatigue lives of laser drilled tested specimens (i.e. LTD set B). Implying the use of low trepan speed results in thinner recast layer and better geometry accuracy. Therefore, improves the fatigue and corrosion resistance of laser drilled cooling holes.

It has been shown that the presence of a recast layer associated with high thermal tensile residual stress produced by laser drilling process is very detrimental for turbine cooling film holes corrosion-fatigue performance. Next chapter will discuss the metallography analysis of fractured specimens to better understand the extent of recast layer thickness and environment influence on the crack initiation and crack growth.

7 METALLOGRAPHY ANALYSIS OF FRACTURE SURFACES

7.1 Introduction

The metallography analysis was conducted for better understanding of mechanisms of crack initiation and growth in laser drilled angle cooling film holes, under different fatigued specimen sets. The fracture surface of CF tested specimens were examined under an analytical optical microscope and scanning electron microscope (SEM) and presented in sections 7.2. The corrosion compounds on the fractured surfaces and in the nucleation site were analysed under energy dispersive X-rays spectroscopy (EDS). The recast layer thickness measurements were similar to the outlined in Chapter 3, in order to confirm the obtained average RLT_{max} on three different laser drilled specimens group and EDM specimens. In addition, finite element analysis was conducted to assess sites of stress concentration and potential sites of crack nucleation around the cooling holes.

Moreover, prior to the fracture analysis, a background literature (Colangelo, 1978; Mogul, 1978; Russo, 1978) was performed on the fatigue of metals, particularly fracture surfaces in the nickel superalloys at high temperature in order to understand the failure mechanisms and fracture morphology in single crystal superalloys (Duquette and Gell, 1971; Crompton and Martin, 1984; Okazaki, Imai and Nohmi, 1992).

7.2 Results and discussion

7.2.1 Fractography

Figures 7-1 and 7-2 show images of fractured corrosion-fatigue specimen's laser drilled at LTD set A and LTD set C. The observations show that most of the holes failed from the end holes. The summary of the failed holes observed in all the fracture specimens are provided in Table 7-1. Figure 7-3 show images of representative fracture path observed in angled holes of a fatigued specimen. In all cases, cracks were found to start at acute corners and grew perpendicular to the direction of applied load until the final fracture. This location found to be similar to that reported by (Sun, Heffernan and Helmink, 2011) and more recently (J. Liang *et al.*, 2016; Zhou *et al.*, 2017).

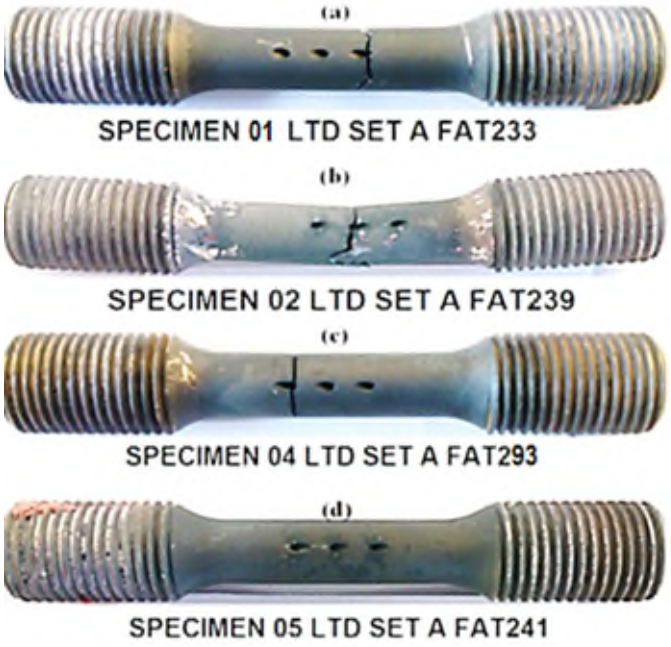

Figure 7-1. Digital image of CMSX-4 fatigued specimens with angled cooling holes in LTD set A.

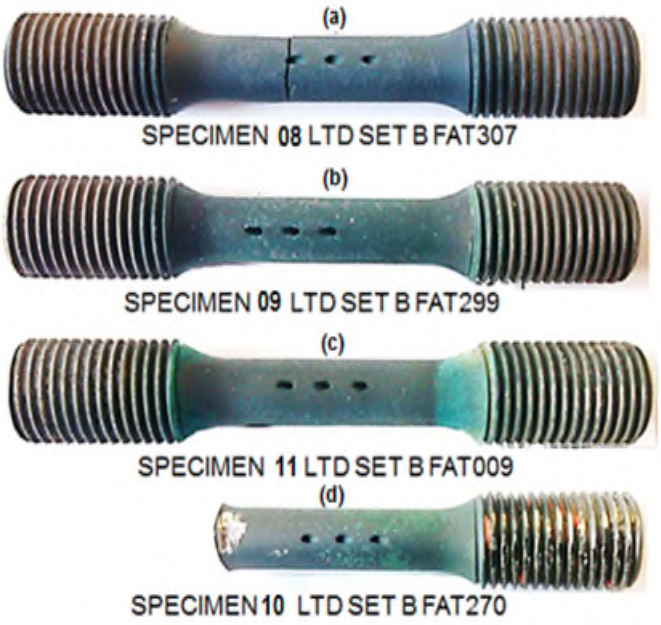

Figure 7-2. Digital image of CMSX-4 fatigued specimens with angled cooling holes in LTD set C.

Figure 7-4 show SEM micrographs of an unbroken fatigued specimen detailing multiple micro cracks around the holes. The micrographs depicted in Figure 7-4b to 7-4d are higher magnifications of Figure 7-4a. The red arrows indicate the recast layer; the yellow arrows point out the micro cracks; white arrows show the direction of the cracks, and the black

arrow is the load direction. There is a clear evidence of crack initiation from the recast layer and propagating into the parent material. These cracks are perpendicular applied load direction, along [111] slip planes. The presence of secondary cracks is due to the local stresses acting near the holes. Further, there is a similarity to damage observed at remaining holes that did not fail from fractured fatigued specimens. The environmental influence from the hot corrosion on the crack nucleation and crack growth are discussed in sections 7.2.2 and 7.2.3.

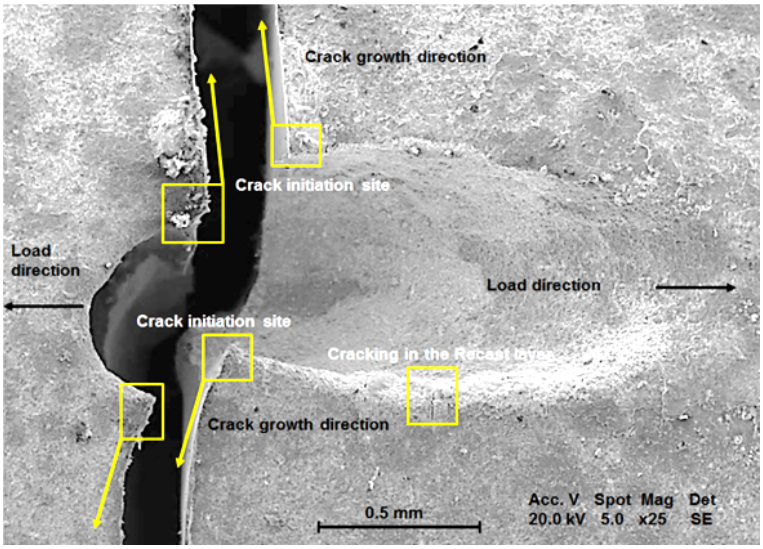

Figure 7-3. SEM micrograph of a fractured fatigue specimen FAT250 (hole 1) showing an example of observed sites of crack initiation sites and crack growth direction in laser drilled elliptical holes.

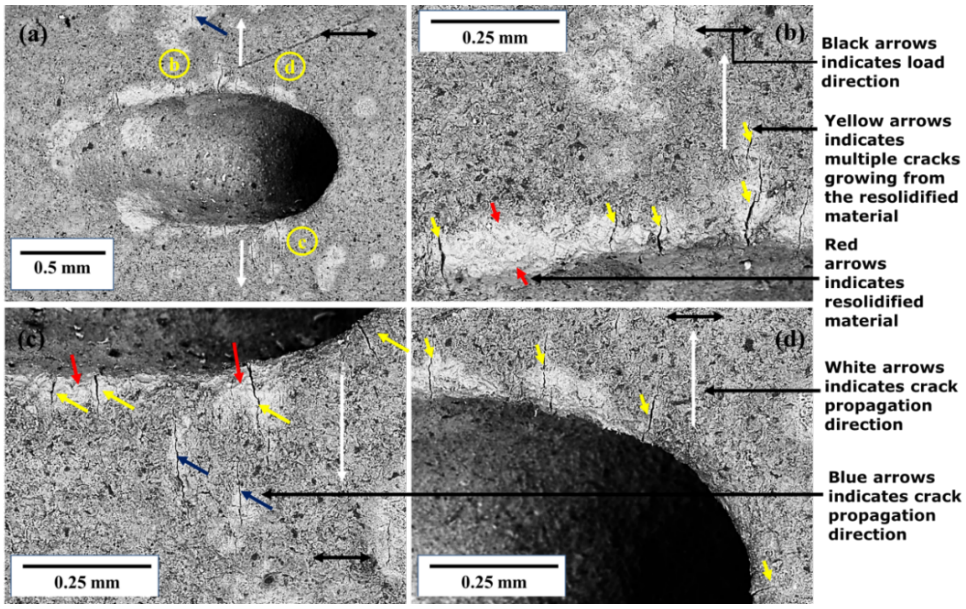

Figure 7-4. Scanning electron microscopy images showing an example of multiple cracks observed on an unbroken specimen.

Table 7-1. Summary of the fractured holes in all fatigue specimens tested.

Group	Specimen No.	Hole		
		1	2	3
LTD Set A	LTD 01	Fractured	-	-
	LTD 02	-	Fractured	-
	LTD 03	Fractured	-	-
	LTD 04	-	-	Fractured
	LTD 05	Unbroken	Unbroken	Unbroken
LTD Set B	LTD 06	Fractured	-	-
	LTD 07	Fractured	-	-
	LTD 08	Fractured	-	-
	LTD 09	Unbroken	Unbroken	Unbroken
	LTD 10	Unbroken	Unbroken	Unbroken
	LTD 11	Unbroken	Unbroken	Unbroken
	LTD 12	Unbroken	Unbroken	Unbroken
	LTD 13	Unbroken	Unbroken	Unbroken
LTD Set C	LTD 14	-	-	Fractured
	LTD 15	-	-	Fractured
	LTD 16	Fractured	-	-
	LTD 17	Fractured	-	-
	LTD 18	Unbroken	Unbroken	Unbroken
EDM Set D	EDM 01	Fractured	-	-
	EDM 02	-	-	Fractured
	EDM 03	Unbroken	Unbroken	Unbroken

The metallography analysis, revealed in all likelihood fatigued specimens with acute angled laser drilled holes, cracks were found to initiate within the recast layer, mostly located where the angled holes overlap with the thin-wall specimen surface. The surface cracks propagated internally through stage I in form of thumbnail and stage II crack growth, perpendicular to the applied load direction. The fracture morphology of tested specimens shows that all specimens that failed had a crystallographic fracture facets along [111] plane. The specimens tested at higher stress level suggest the fatigue crack Stages I and II were primarily dominated by the mechanical fatigue. Whilst, the specimens tested at an intermediate and low stress levels the corrosion-fatigue dominated the crack stage I and II after a brittle rupture within the recast layer (see Figure 7-5).

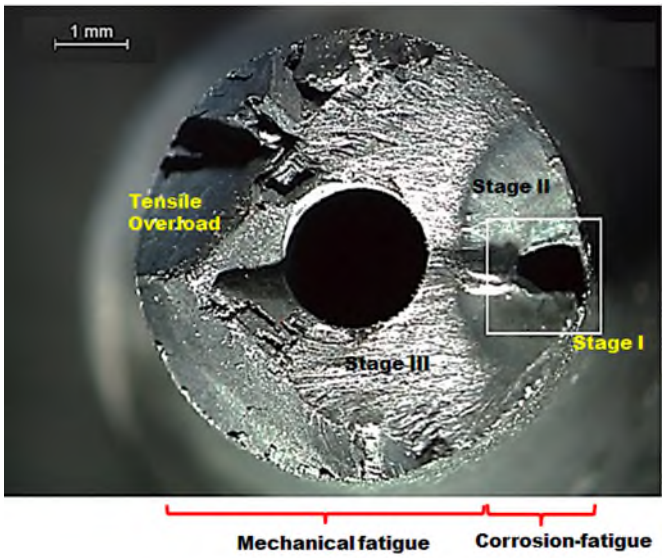

Figure 7-5. Example of a fracture surface of a tested fatigue specimen (LD 17).

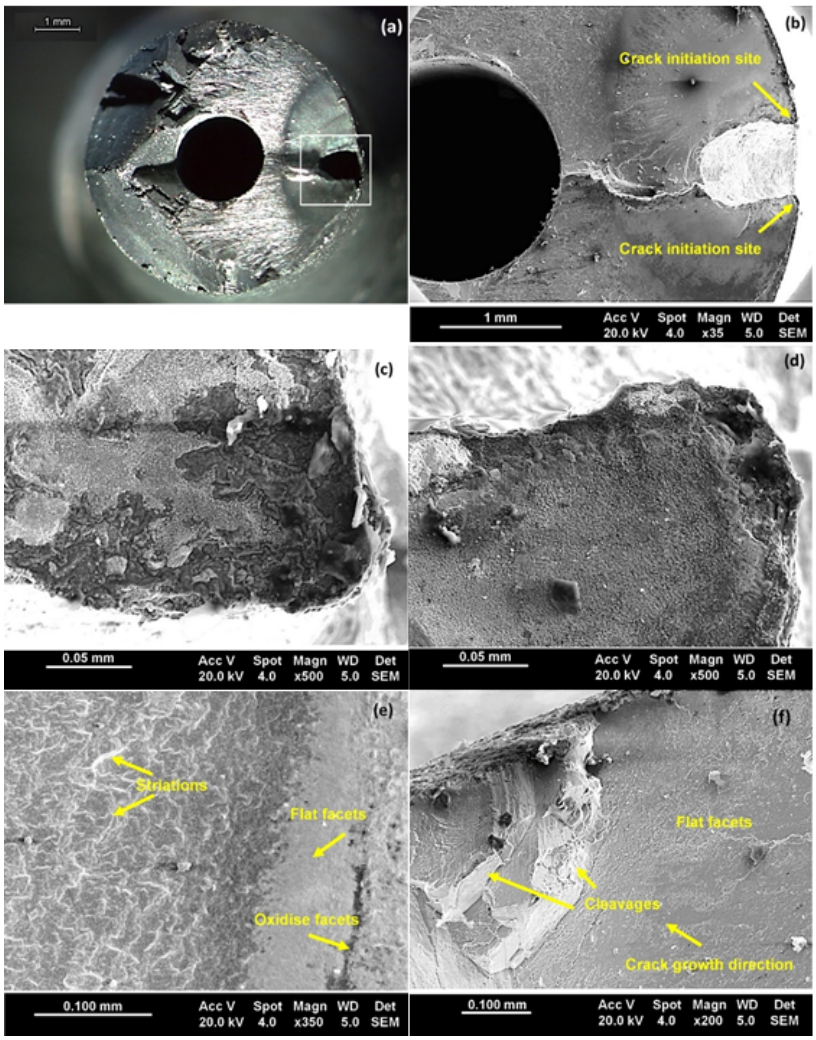

Figure 7-6. Examples of SEM micrographs of LTD C drilled specimen (LTD 17), tested in LCF at 350 MPa and 850°C at hot corrosion environment.

The annotations in Figure 7-6 micrographs show: (a) typical appearance of the fracture surface and the site of crack initiation, (b) crack initiation site from the acute corner section of the hole in a higher magnification, (c-d) surface morphology near crack initiation site (stage I), (e) flat facets and fatigue striations (stage III), and (f) cleavage and flat facets in the final fracture site (tensile overload). The examination of the final fracture zone suggests that fracture morphology resembling tensile and brittle overloading with visible planar and cleavage facets. This is indeed the case for all the specimens tested in this research work. Secondary cracks were also observed at multiple sites of the fatigued specimens, mainly located at the periphery of the holes (see Figures 7-3 and 7-4). This is likely attributed to the combination of local thermal stress/strain gradients and environmental effect either from oxidation or sulphidation.

The presence of existing micro-cracks generated during the laser drilling process may also lead to premature crack propagation, leaving out the crack initiation stage of fatigue failure mechanism. Figure 7-7 confirms the presence of surface cracks induced by laser drilling process, inside the recast zone and within the areas of high stress concentration. Moreover, it should be emphasized that these surface cracks will grow faster in areas of high stress concentration compared to other pre-existing cracks or even formed during the testing. Fractography examinations, also suggest that the crack growth at base substrate was mostly dependent on the mechanical stresses and severity of the corrosive species diffused into the crack tip.

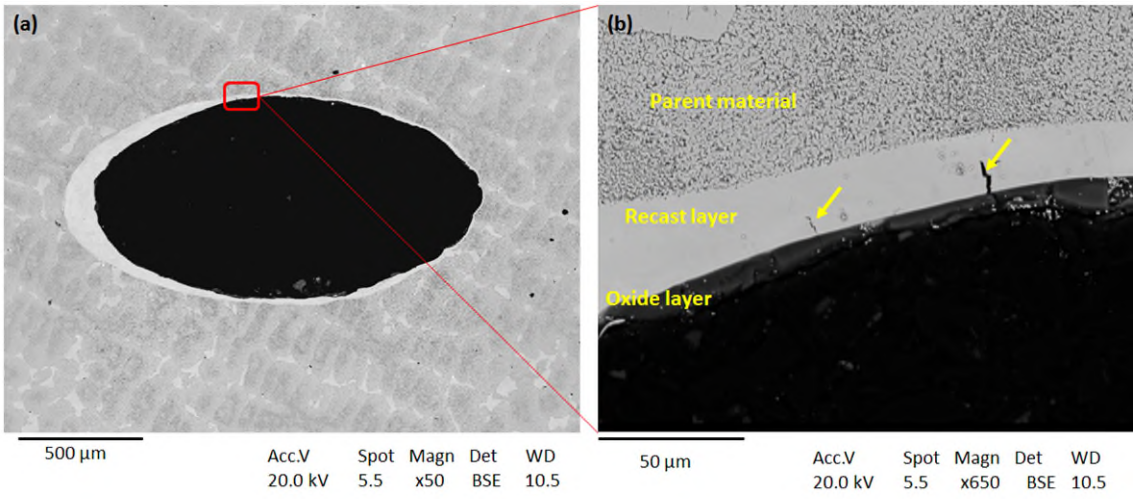

Figure 7-7. SEM micrographs show an example of micro cracks observed on the top surface of a LTD set A sample after drilling.

For further understanding the fracture faces of specimens at high and low cyclic stresses and how environmental interaction influenced the crack growth and final fracture, specimens in the highest to lowest stress levels in the range tested were analysed and shown in Figures 7-8 to 7-11. Figure 7-7 shows two examples of fracture surfaces tested at high stress level, 550 MPa. SEM examination of fractured features was more consistent with a tensile dominated fracture mode due to applied cyclic stress applied. The mechanical fatigue was dominant in crack initiation and crack advance up to tensile overload. The observed fracture facets are typical of stage I short crack growth (Duquette and Gell, 1971; Seo, Yandt and Kim, 2013).

The stage II crack propagation was dominated by the shear fracture mode towards final fracture (stage III), a mix of brittle and ductile overstress (Barnard *et al.*, 2012). The micrograph examination also shows that the period of crack initiation was short in LTD set A specimen (see Figure 7-5b) relative to LTD set B specimen tested at same stress level. This suggests that the tested fatigue specimens with a laser drilled holes with thicker recast layer has influenced the early crack initiation and further short crack advance driven by corrosion-fatigue. Both specimens exhibit crack growth direction at approximately 45-55 degrees downwards from the crack initiation site and crack growth zone (stage II) resembling river line patterns. For all the specimens tested at 550 MPa, the final fracture can be characterised by mechanical fatigue and tensile overload with an evidence of rough fracture features including cleavages and large slip bands.

Figure 7-8 shows an example of the fracture features of two specimens tested at a low stress level, 350 MPa. The examination shows that the stage I crack zone at 350 MPa was longer compared to counterpart specimens tested at 550 MPa and 450 MPa. The fractured facets show evidence of some resistance to short crack growth. However, once crack open there is a gradual crack propagation (stage II), extending in the form of thumbnail-shaped, followed by a flat fracture mode until a rough type surface with slip bands and river lines is observed. Majority of specimens tested at 350 MPa did not fail, except from LTD set A and C specimens.

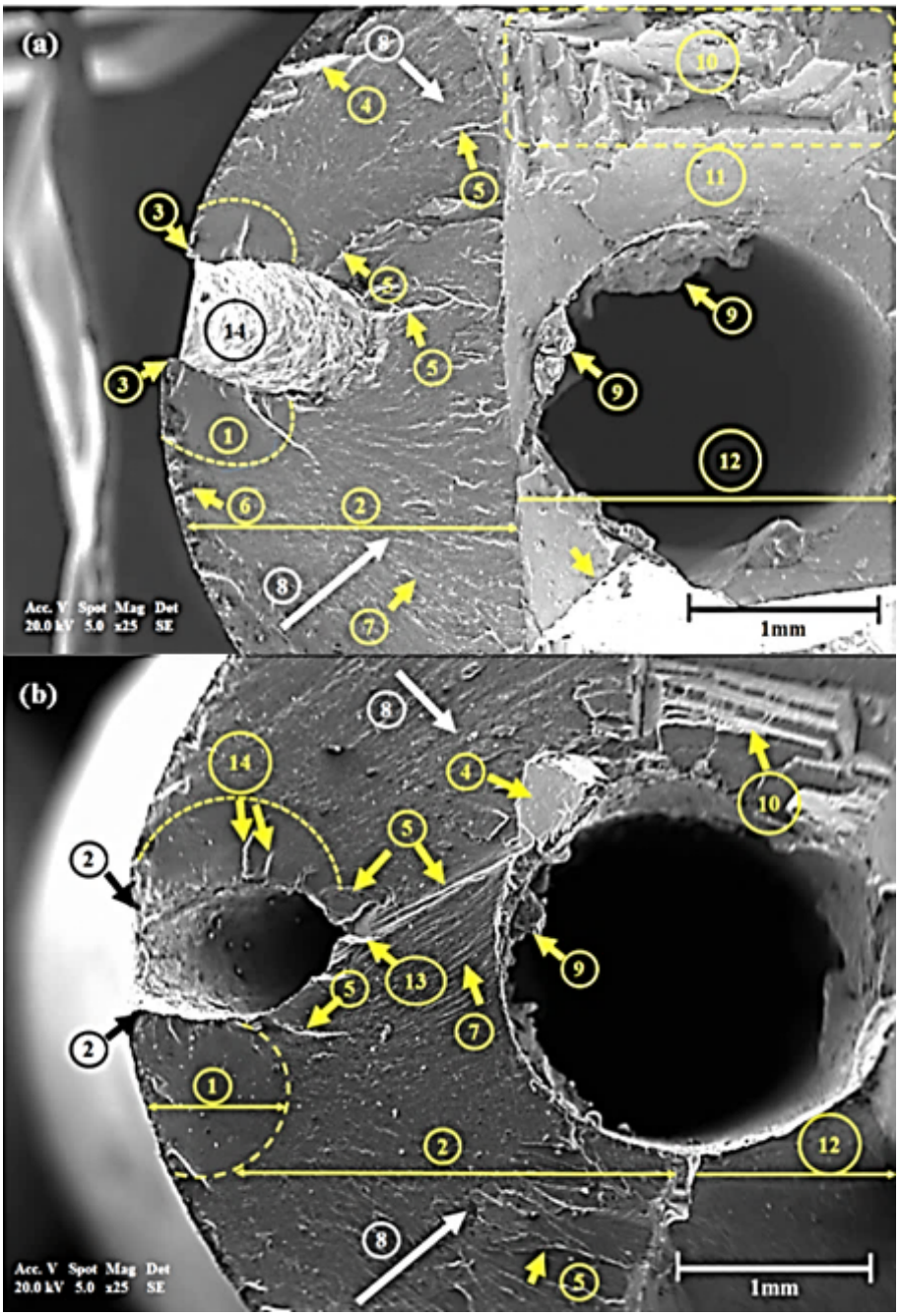

Figure 7-8. SEM micrographs showing two examples of fractured surfaces in specimens tested at 550 MPa: (a) LTD set A specimen 01 (6,353 cycles) and (b) LTD set B specimen 07 (17,716 cycles).

The numbered arrows in the Figure 7-5 indicate fracture features as follow: (1) stage I crack zone; (2) stage II crack zone; (3) crack initiation site; (4) resolidified layer; (5) river lines fracture; (6) ductile fracture (short); (7) striations; (8) direction of crack growth; (9) dross (re-solidified debris); (10a) cleavage fracture; (10b) slip bands (11) brittle overload; (12) stage III crack zone (final fracture); (13) secondary fracture; and (14) micro-cracks.

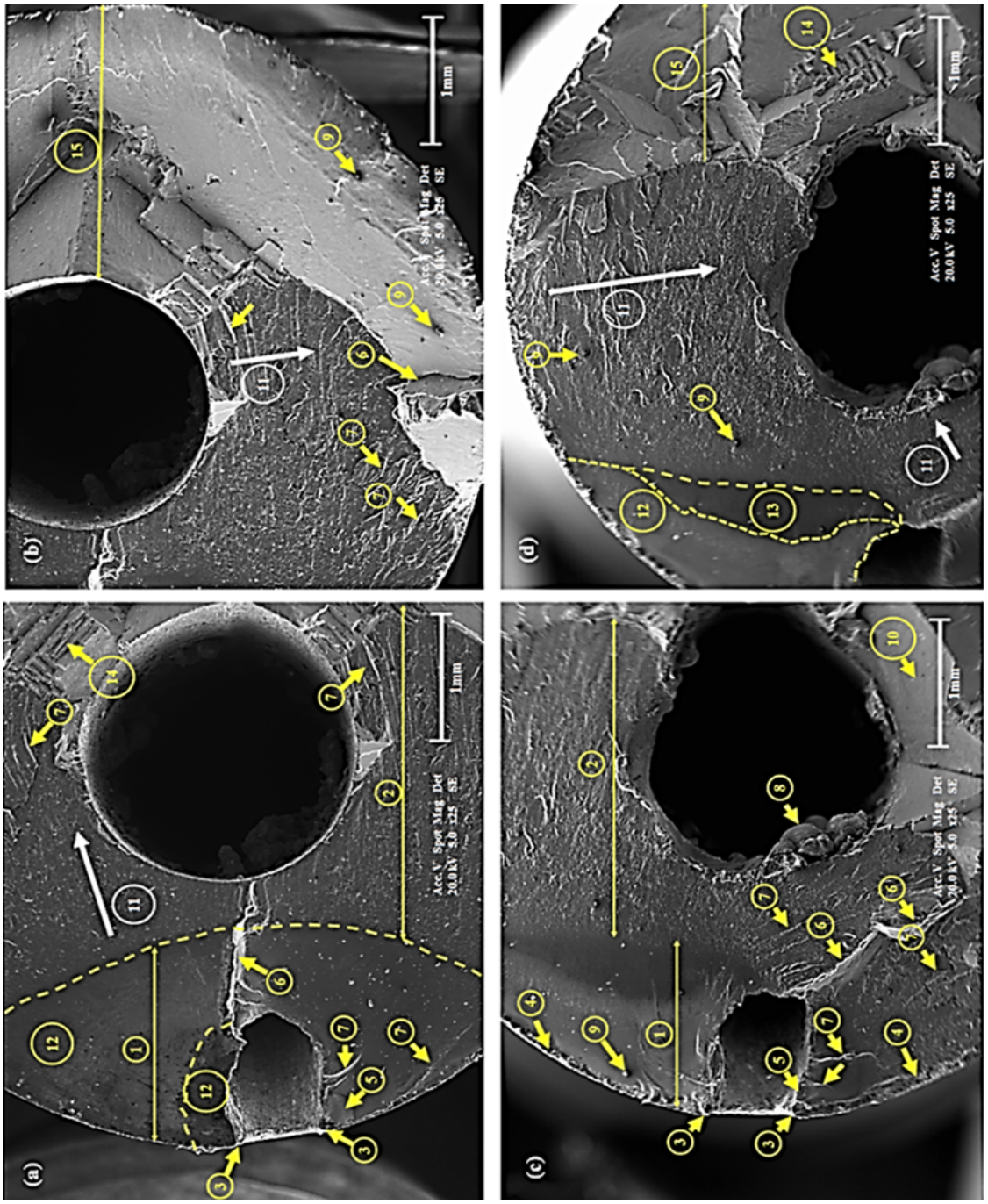

Figure 7-9. SEM micrographs showing two examples of fracture surfaces in specimens tested at 350 MPa: (a-b) LTD set C specimen 17 (89,076 cycles) and (c-d) LTD set A specimen 04 (97,247 cycles).

The numbered arrows in the Figure 7-6 indicate fracture features as follow: (1) stage I crack zone; (2) stage II crack zone; (3) crack initiation site; (4) ductile fracture; (5) thumbnail-like fracture; (6) cleavage; (7) slips; (8) dross (re-solidified debris); (9) dimples; (10) facet fracture mode; (11) direction of crack growth; (12) flat facet/shear fracture mode; (13) environmental effect; (14) slip bands; (15) stage III final fracture.

Evidence of environmental effects, such as hot corrosion and oxidation were in all specimens tested at lower stresses. These are shown as dark patches (see Figure 7-9), within the Stage I crack zone, suggesting the surface being heavily oxidised and signs of hot corrosion process. The presence of corrosive particles such as NaCl and SO_3 in the fracture surface and diffused in the crack initiation site suggests degradation due to hot corrosion (Nicholls and Simms, 2010). The presence of corrosive compounds enhances the crack growth after a crack is opened (Colangelo, 1978), thus, allowing diffusion of sulphides into the material down the crack faces, which then advancing through the remaining section of the material until it cannot longer bear the load, resulting in fast overload fracture. Further discussion on the elemental analysis and corrosion mapping of fracture facets and on crack tip opening facets are discussed in the next section. In this research, fatigue specimens tested at low cyclic stress levels (290, 350 and 400 MPa) and not failed suggests that initially they have undergone to corrosion-assisted cracking which is exposure time dependent. Therefore, these specimens had incubation phase and short crack growth stages of corrosion fatigue. Small cracks ranging between 100-300 µm were observed on the specimens tested at lower stress as above mentioned.

Figure 7-10 shows an example of high magnification crack initiation site, seen in Figure 7-8b. It can be observed that the crack initiation started within the surface recast layer adjacent to the edge of the hole, particularly at the leading-edge side of the hole. In all fatigued test specimens, the crack initiation site had a similar appearance as depicted in Figure 7-3, which implies that the initiation mechanisms are similar under each of the different fatigue specimen conditions. The SEM microscopy examination revealed the presence of micro cracks in the recast layer, as would be expected (see Figure 7-7). These multiple cracks inside the wall and edges of the hole could have formed due to high thermal cycling experienced by the work surface during the laser drilling process, or developed during the cyclic stress experienced during the test from the brittle recast layer.

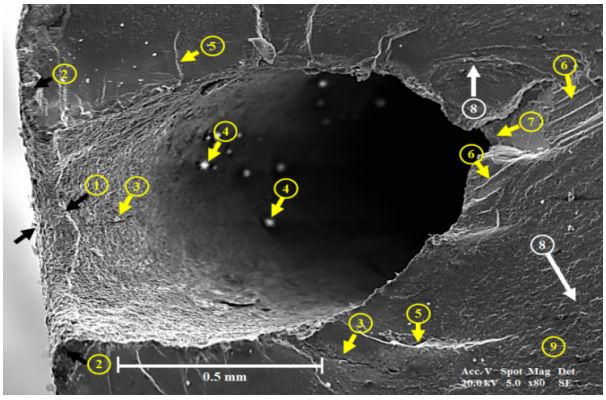

Figure 7-10. Micrograph showing fracture surface of LTD set B specimen 07.

The arrows with numbers in the Figure 7-10 indicate fracture features of an area of crack initiation. These are: (1) recast layer thickness; (2) likely oxides; (3) micro cracks in the recast layer and propagating into substrate; (4) salts particles (NaCl); (5) light cleavage/river lines; (6) slips; (7) secondary crack/fracture initiation; (8) crack growth direction; and (9) rough surface (stage II crack).

Overall, the presence of thick recast layers and the severity of pre-cracks were detrimental on stage I cracking for all tested specimens, except for the bare tested specimens. The fracture morphology of non-drilled fatigue specimens had matted appearance with few fracture steps and few river lines type facets (see Figure 7-11).

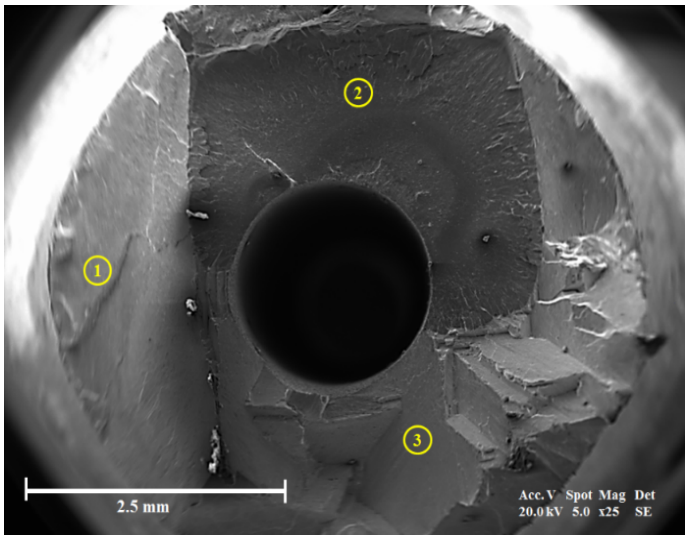

Figure 7-11. SEM micrograph showing an example of fracture surface in specimen tested at 700 MPa (Bare 03).

Figure 7-11 shows an example of fractured surface of a non-drilled specimen, bare CMSX-4 at 700 MPa. For this group of specimens, surface of gauge section of the specimens was examined by SEM. It was found that the cracks began on the gauge mid-section of the tested specimens, where the stress is expected to be higher. The cyclic stress was the dominant factor for the crack growth, and the final overload was dominated by ductile type fracture. There is limited evidence of any environmental effect, such as hot corrosion, as the main driver for the crack initiation on the surface of these specimens. Nevertheless, there are some signs of oxidation in the surface breaking site, but not enough to cause significant damage. In addition, it should be mentioned that these specimens were only tested at a higher stress levels, where the time is too short for surface to degrade by hot corrosion and corrosion to fully develop. Despite recent research work

(Chapman *et al.*, 2017), there still a need for understanding of corrosion-fatigue of bare CMSX-4 superalloy in gaseous environment at low cyclic stresses to assess the impact of salt and sulphur flux influence on crack nucleation, crack tip and crack growth.

7.2.2 FEM of stress concentrations in angled elliptical cooling holes

For further understanding of site of crack nucleation and regions of high stress concentration around angled and elliptical holes, a finite element (FE) analysis was conducted on the 3D CAD model of fatigue cylindrical specimen with three cooling holes configuration.

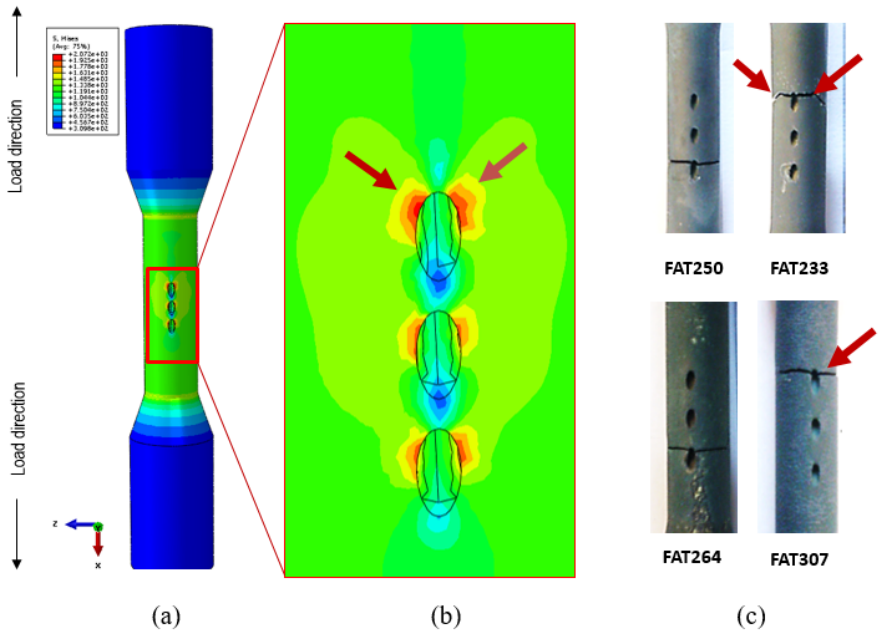

Figure 7-12. (a) Resultant stress distribution in fatigue specimen; (b) stress distribution around the cooling holes' region with highest stress concentration at the leading-edge corners of top of the elliptical holes; (c) fractography of fatigued specimens.

Figure 7-12a illustrates the 3D CAD geometry used for the FE analysis and details of boundary conditions, load, meshing and material properties are detailed in Chapter 3 (section 3.4.1). It can be seen from Figure 7-12b that the regions of high stress concentration were found along the upper lateral side part of the elliptical holes, as shown in Figure 7-12b. This location is consistent with the crack initiation site observed in all fractured laser drilled and EDMed specimens, as shown in Figure 7-12c and Figure 7-13a-b. The FE analysis indicates that the end holes in the direction of the applied load will be at high tensile stress due to local plastic deformation. Therefore, higher probability

of fatigue cracks to initiate and grow from high stress concentration fields. Whilst, low stress field found in the remaining holes is because the first hole in the row and closed position in the direction of the applied load will absorb most of the strain energy sheltering the remaining holes. This explains the surface breaking holes position observed in the fracture specimens (see Table 7-1). Past studies, reported that features such as acute corners with thin-wall sections are generally likely to act as stress raisers.

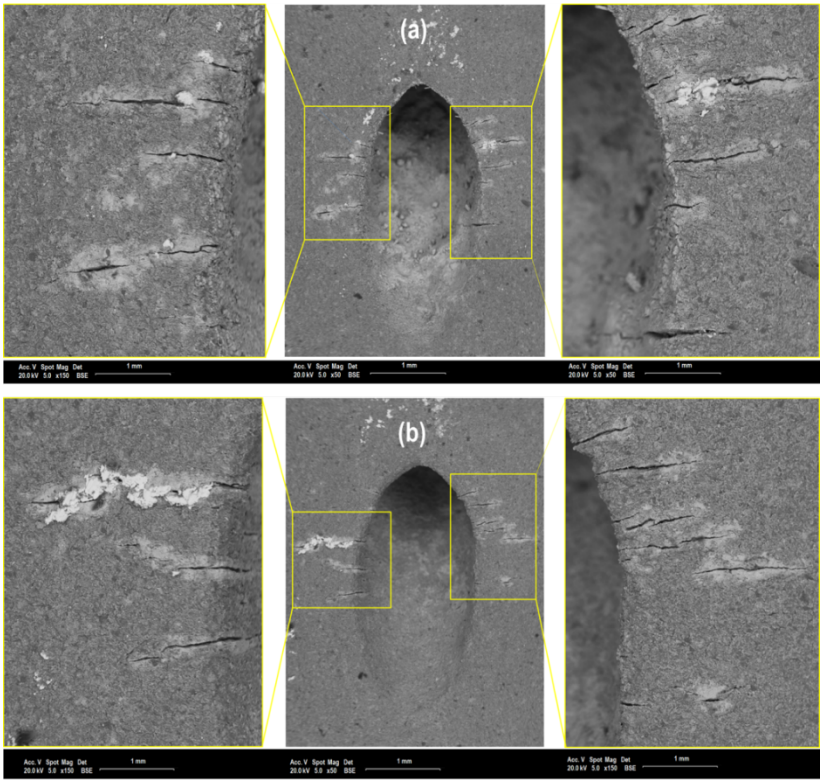

Figure 7-13. Micrographs of an unbroken non-polished fatigued specimen LTD 05.

7.2.3 Energy dispersive x-rays spectroscopy analysis

Energy dispersive X-ray spectroscopy (EDS) has been conducted on selected fracture surfaces and in the crack initiation sites to examine the presence of corrosive compounds such as oxides, chlorides, sodium, and sulphides. Figure 7-14 show an SEM micrograph and Table 7-2 related quantitate elemental by atomic weight percentage. All spectrums covered in the analysis show an evidence of surface crack initiation and surrounding crack propagation zone rich in oxygen. This is expected for specimens tested at a higher temperature. The oxygen diffusion into the surface and internal fracture surface results in the formation of protective oxide layers and diffusion of oxygen and sulphur into the

crack tips, respectively. The protective layer consist of alumina, chromium and nickel rich layer and its degradation and rupture is highly dependent upon temperature, sulphur concentration, cyclic stress and the alloying dynamics.

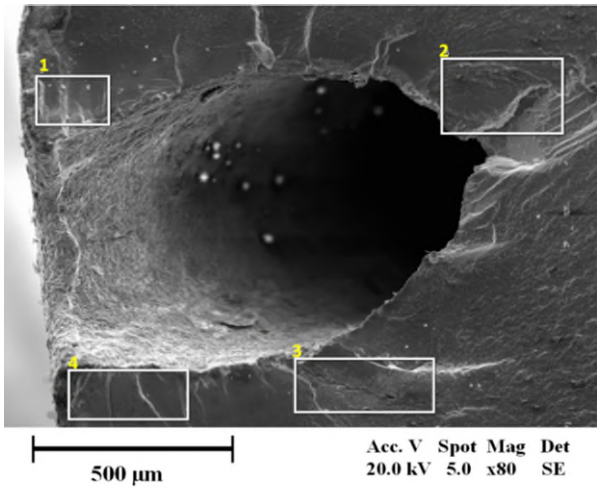

Figure 7-14. SEM micrograph showing various spectrums of EDS analysis performed on a fracture surface of a LTD set B specimen 07.

Table 7-2. Results of the EDS analysis on the selected fracture surface of specimen 07.

Elements	Atomic weight %			
	Spectrum			
	1	2	3	4
O	24.1	15.5	19.9	17.8
Al	2.6	2.4	1.6	1.1
Ti	1.8	0.9	0.9	2.4
Cr	11.8	6.2	5.8	17.2
Co	8.4	11.4	11.1	10.1
Ni	39.6	57.8	59.3	48.5
Ta	7.5	2.8	0.5	1.6
W	3.8	3.0	-	-
S	0.5	0.9	0.6	0.5
Total	100	100	100	100

It can be seen from Table 7-2 that there is a little of sulphur found near and bottom of fractured surface on tested specimens at a high stress level. Therefore, it is unclear whether the sulphur flow rate used during the fatigue testing was low or if it was the low cycle fatigue regime that did not allowed the sulphidation fully take place. However, first and fourth spectrums show evidence of nickel and aluminium depletion and increase in

the chromium atomic percentage suggesting presence of chromium oxides. The presence of sulphur in the corrosion environment contributes substantially to depletion of nickel, titanium and later chromium and titanium, hence, metal loss through formation of sulphides or synergistically in combination with chlorides (Pettit *et al.*, 1984). Implying the vulnerability of recast layer to corrosion resistance to substrate alloy.

Figure 7-15a-b show SEM micrographs of fractured facets of specimens tested at low stress level highlights the spectrums selected covering the areas of elemental analysis. Table 7-3 show the atomic percentage of selected spectrums in Figure 7-13a-b. EDS analysis indicates the presence of Na, Cl, and S diffused near the crack initiation site. According to the previous publications (Sumner *et al.*, 2013; Haight *et al.*, 2015), authors reported that NaCl prevents the formation of protective scale in the initial stage and subsequently induces internal crack by allowing other corrosive compounds such as sulphur. It was also reported that Na_2SO_4 in presence of gaseous mixture leads to the formation of sulphides (SO_3), causing internal sulphidation below the oxide scale (Birks, Meier and Pettit, 2006). The sulphur slowly penetrates beneath the protective scale and forming sulphide oxides (rich in Cr and Ti). These oxides deplete the Cr on the Cr_2O_3 and at the substrate interface inducing stress and causing breakdown of protective scales (Ni_2O_3 and Al_2O_3). Further, sulphur concentration at the crack tip act as a stress raiser enhancing the corrosion-fatigue crack growth.

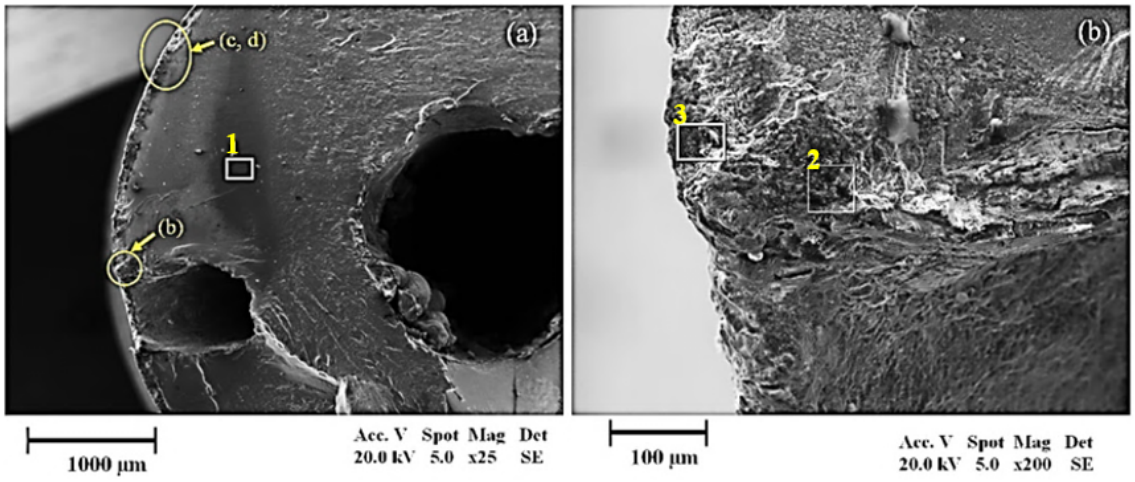

Figure 7-15. SEM images showing various spectrums of EDS analysis performed on a fracture surface of a LTD set C specimen 04.

Table 7-3. Results of the EDS analysis on the selected fracture surface of specimen 04.

Elements	Atomic weight %		
	Spectrum		
	1	2	3
O	16.1	22.3	21.5
Na	-	-	1.1
Al	-	11.0	10.2
S	-	0.4	-
Cl	0.5	0.4	-
Ti	-	1.8	1.9
Cr	1.7	10.6	11.5
Co	9.2	12.2	12.6
Ni	74.5	41.2	40.9
Total	100	100	100

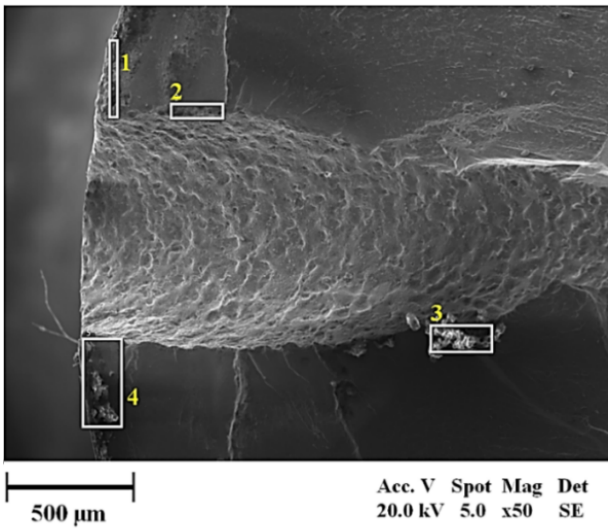

Figure 7-16. SEM micrograph showing selected areas for EDS analysis of fracture facet of a specimen EDM 01.

Figure 7-16 show SEM micrograph of a fracture surface from an EDMed specimen with spectrums covering selected areas, as highlighted and numbered. The spectrum 2, 3 and 4 covers the crack initiation site. The EDS analysis show evidence and traces of Na and Cl residues (see Table 7-4). There is also the presence of oxides rich in Al, Ni and Cr in the crack initiation site in spectrum compared to remaining fracture surfaces. There is some level of uncertainty regards to corrosive elements being part of initial crack initiation as opposed to recast layer thickness or even pre-existing cracks.

Table 7-4. Results of the EDS analysis on the selected fracture surface of EDM 01.

	Atomic weight %			
	Spectrum			
Element	1	2	3	4
O	11.1	16.8	15.3	19.7
Na	1.3	-	4.5	1.9
Al	2.1	3.5	11.2	3.9
Cl	-	-	2.8	-
Ti	1.1	0.7	-	1.3
Cr	17.4	4.3	6.0	11.4
Ni	47.4	63.5	44.4	45.0
Co	7.2	11.4	12.4	8.6
Co	7.3	11. 6	12.2	8.7
Ta	6.4	-	-	8.1
Total	100	100	100	100

7.2.4 Corrosion mapping

EDS examination of fractured fatigue specimens confirms the presence of a significant oxidise scale near the recast zone and surrounding the surface breaking holes, as shown in Figure 7-17. Previous section showed that the oxidised scale is rich in Al, Ni and Cr. These elements are easily oxidised at high temperature, particularly at the edges of recast surface boundaries. The increase of Al_2O_3 content weakens the recast microstructure, becoming more brittle, and thus, the reason for the rapid crack initiation and growth between the oxide and recast layer interface. The formation of the oxide scale above the recast layer and at the specimen surface act as outer protective layer until is depleted by the oxidation and sulphur (S) attack (see Figure 7-17). Thus, decreases Ni and Co content around the recast layer. The dissolution of Ni leads to the formation of chromium sulphides and depletion of surrounding alloys. The sulphide particles are known to enhance the crack growth (Carter, 2005), preferably form at adjacent to crack opening and at the crack tip and can deplete the alloy chemistry and enhance crack advance from the open cracks within the recast layer and surrounding surface.

In the case of single crystal CMSX-4, either gamma matrix or precipitated gamma prime is attacked first by oxidation until it weakens and degrades, and thus, leading to de-alloying process. This is a time-dependent process and it is typical until a crack is open under a cyclic load. Often, under the high temperature corrosion-fatigue, crack nucleation

is driven by the level of corrosive contaminants (i.e. gas flux and chemical compounds) and mechanical load. The open cracks allow the diffusion of sulphur and oxygen into the base alloy down the crack tip accelerating the corrosion and further degrading alloy properties. As consequence, leads to a faster crack growth rate and sudden fracture.

Hot corrosion at high temperature occurs in the temperature range of 750 ºC to 950 ºC, as previously stated. The surface degradation due to HCHT starts from sodium sulphate (Na_2SO_4) and sodium chloride (NaCl) attacking the protective oxide scale and continuously reaching the base metal, depleting alumina and chromium (Birks, Meier and Pettit, 2006). This causes accelerated oxidation of the base metal and sulphidation underneath the protective oxide scale. The EDS was used for corrosion mapping and identify corrosion compounds formed at the surface of the HT CF tested specimens at different stress levels.

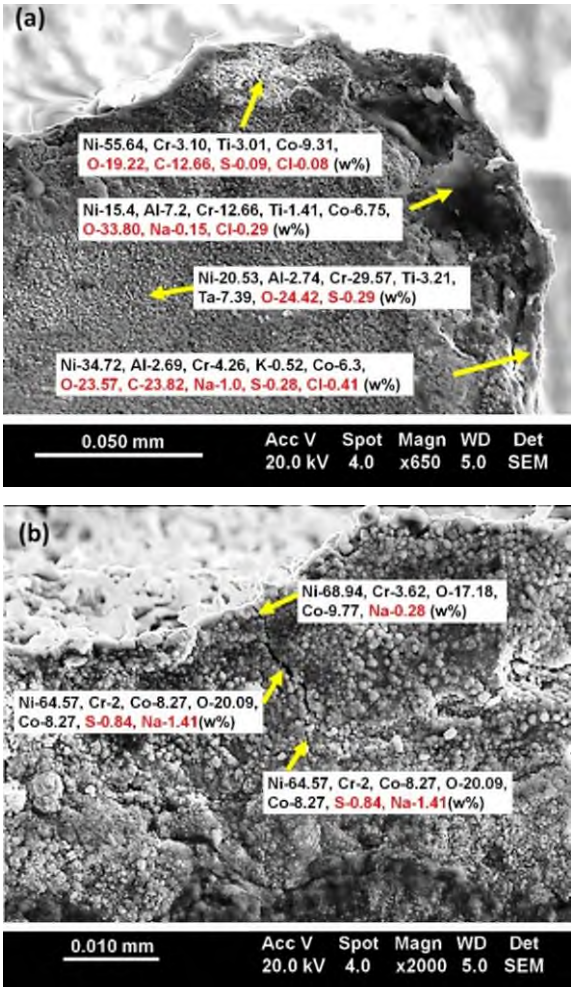

Figure 7-17. Example of SEM micrographs showing elemental analysis along the fracture surface near the crack initiation site indicating diffused corrosive compounds.

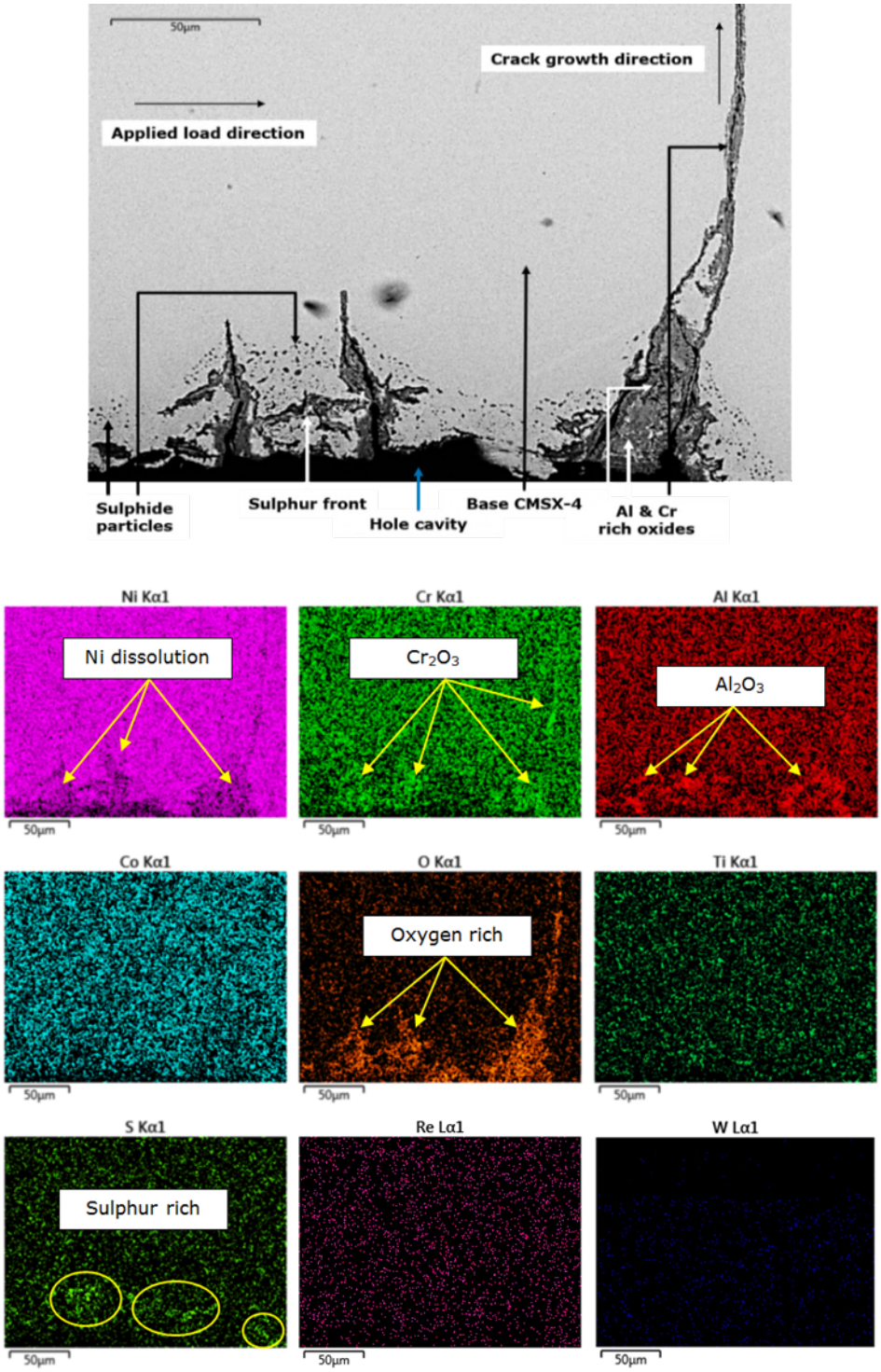

Figure 7-18. SEM micrograph and EDS mapping around the section of the hole edge of laser drilled specimen 04, tested at 350 MPa, 850 oC under HTHC environment.

Figure 7-18 show an example of EDS mapping of a crack initiation site around the edge of a hole surface of a specimen tested at a lower cyclic stress (specimen LTD 04). The EDS analysis confirms the presence of high concentration of mixed oxides, rich in Al and Cr around the open cracks. It is likely that oxygen diffused through the cracks, forming

an outer protective oxide scale. There is also evidence of nickel depletion allowing internal sulphidation to take place below the Cr and Al oxide scale. During this process, sulphides diffuse deeper into the base substrate as it depletes the surrounding alloying elements, accelerating the internal attack and increasing the crack growth rate. The sulphur map in Figure 7-18 clearly indicates a high concentration of sulphur underneath the oxide scale. Therefore, it can be understood from the SE/EDS examination confirms that at low cyclic stresses where specimens have longer life cycles, the incubation and growth phases of the HTHC fully takes place.

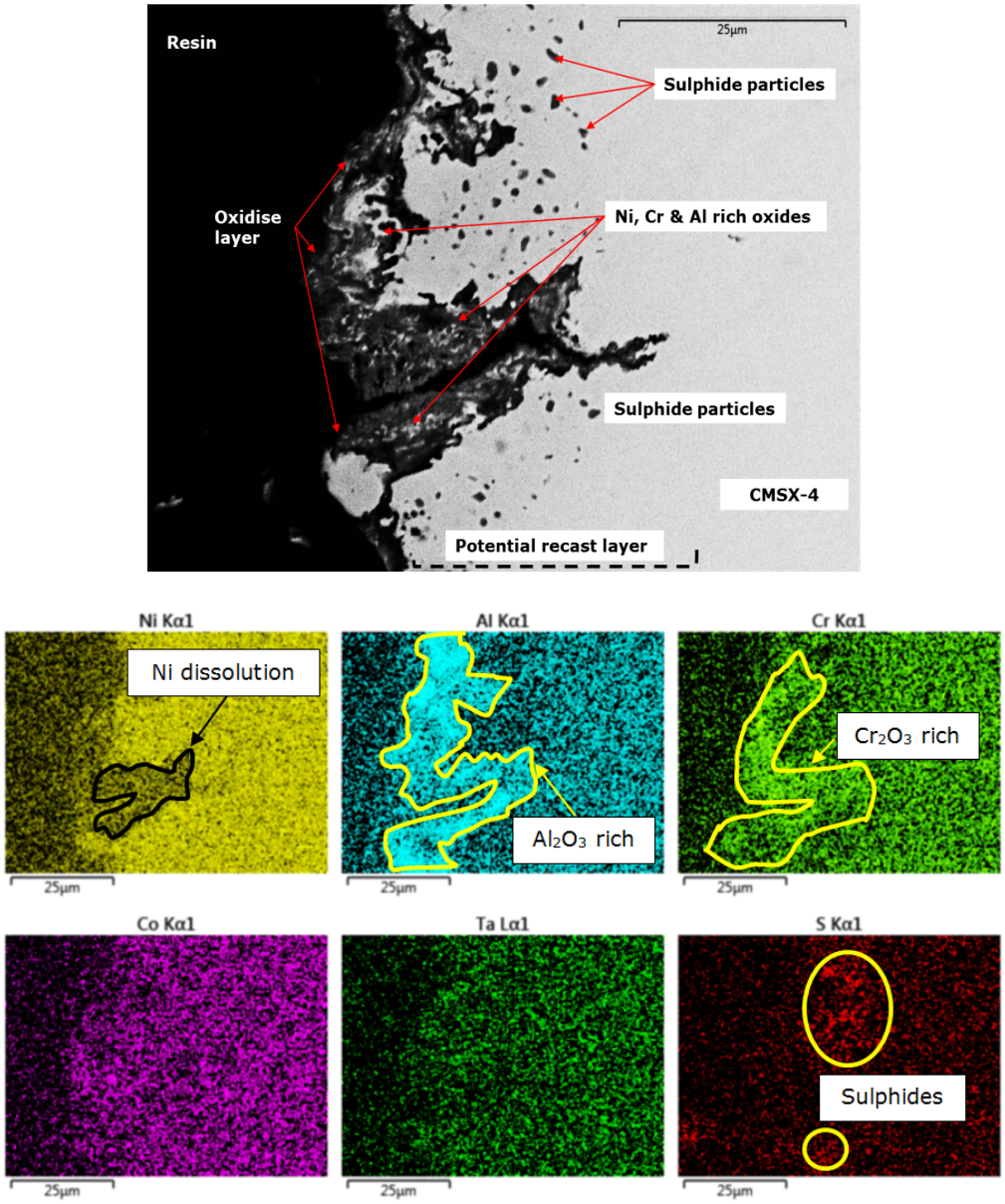

Figure 7-19. SEM micrograph and EDS mapping around the section of the hole edge of a laser drilled specimen 02, tested 450 MPa, 850 ºC under HTHC environment.

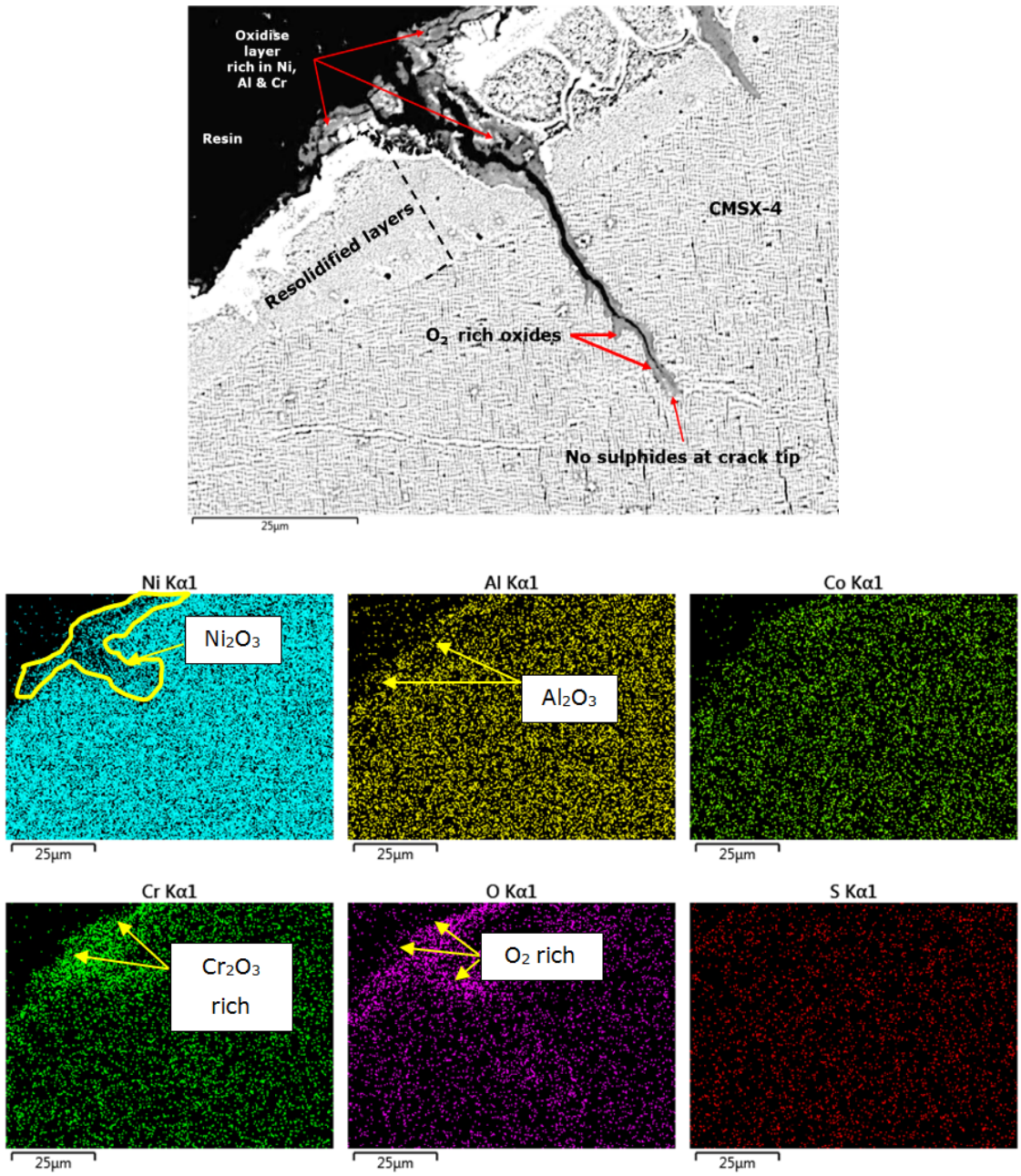

Figure 7-20: Microstructure and EDS corrosion mapping of cross-section of a CMSX-4 laser drilled specimen 14 tested at 550 MPa, 850 °C under HTHC environment.

Figure 7-19 show a SE/EDS mapping of a cross-sectioned surface near the edge of the hole. It highlights the susceptibility of the material to oxidation and sulphidation in the recast layer zone compared to the base metal. The recast layer being brittle causes early crack initiation under thermal and mechanical load. The open cracks form a path for oxygen and sulphur to diffuse into the recast zone and subsequently to the base metal zone. The maps in Figure 7-19 confirms the presence of alumina and chromium scale around the crack opening area. Further, presence of decorated sulphide particles

surrounding the recast zone clearly indicate that the recast zone with open cracks when exposed to a hot corrosion environment becomes vulnerable to internal oxidation and sulphur diffusion into the cracks and continuing the attack to the base metal.

Figure 7-20 shows SE/EDS mapping of a cross-sectioned of a laser drilled hole surface of a specimen tested under high cyclic stress. The maps in Figure 7-20 highlight the protective oxide scale rich in Ni, Al and Cr formed around the recast zone and open crack. For the specimen tested at higher stress level, there is little or no traces of sulphides below the oxide scale or in the open crack. This could be due to (i) SO_2 flux is lower inside of the hole compared to the external surface as expected; or (ii) the time of exposure (6353 cycles) was too short to incubation steps of HTHC fully take place.

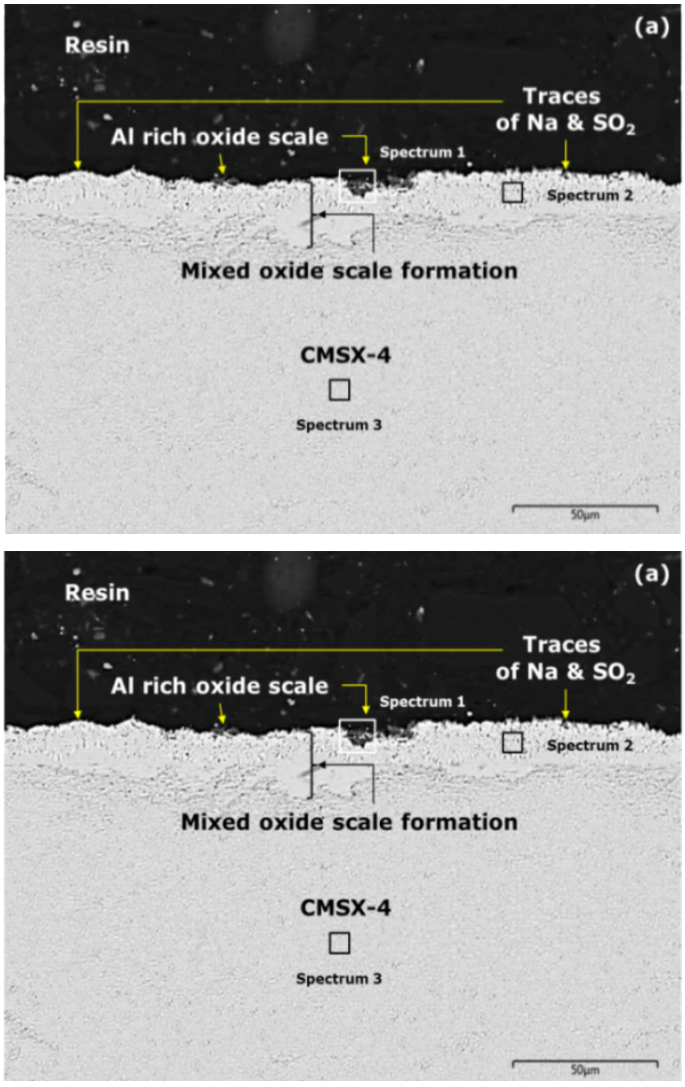

Figure 7-21. Examples of cross-section micrographs of specimen 01 and 08 near gauge mid-section surface tested at 550 MPa and 450 MPa, respectively, under 850 ºC HTHC environment.

Figure 7-21a-b show SEM micrographs of polished and etched cross-section of specimen gauge mid-section after CF tests. It is evident from the micrographs shown in Figure 7-21a-b that the cracking did not occur in gauge region away from the holes. This may be due to low magnitude of stress concentration. However, formation of oxide scale rich in Al, Ni and Cr did occur across the surface of the specimen. Figure 7.21b show indications of sulphide particles below the oxidise layer. This suggests that environment had some influence on the base alloy, however, recast layer thickness and cyclic load were dominant drivers. Moreover, it should be mentioned that these specimens had less exposure time to hot corrosion, under 5,000 to 55,000 cycles, thus, only limiting to the incubation phase. A summary of elemental analysis of fracture facets depicted in Figure 7-21a-b are provided in Table 7-5.

Table 7-5. EDS spectrum analysis of specimens depicted on Figure 7-15.

	Specimen LTD 01 (a)			Specimen LTD 08 (b)		
Elements	1	2	3	1	2	3
O	39.5	7.2	6.0	54.2	2.2	7.9
Al	29.7	11.6	12.0	39.2	5.0	12.9
S	0	0.4	0.0	0.2	0.0	0
Ti	0.3	1.6	0.1	0.4	0.6	1.4
Cr	3.9	4.0	3.6	2.6	5.8	4.6
Co	4.5	8.0	7.1	0.5	10.7	8.0
Ni	19.5	61.2	64.2	2.4	70.0	60.3
Mo	0.4	1.7	1.4	0.0	0.4	0.7
Ta	0.9	2.2	1.5	0.3	2.1	1.9
W	0.8	1.8	1.8	0.2	2.2	2.4
Re	0.3	0.8	0.1	0	1.0	0
Total	100	100	100	100	100	100

Figure 7-22(a) SE micrograph show depletion of the outer protective oxide scale, which leads to cracking of the base metal under HTHC and cyclic mechanical load. The maps depicted in the Figure 7-22(b) shows depletion of the Ni and Al in the subsurface and in the crack surroundings. It also shows a high concentration of sulphate below the oxide scale, which diffused deeper into the base metal, depleting surrounding alloying elements. The severity of surface degradation due to HTHC was more prominent in the specimens tested at lower cyclic stress compared to specimens tested at high cyclic stresses as depicted in Figure 7-21a-b. One reason, the exposure time has shown to have an influence on the surface degradation and crack initiation under HTHC environment. However, this

could be superimposed in the case of pre-existing crack, resulting in an accelerated corrosion and faster crack growth rate.

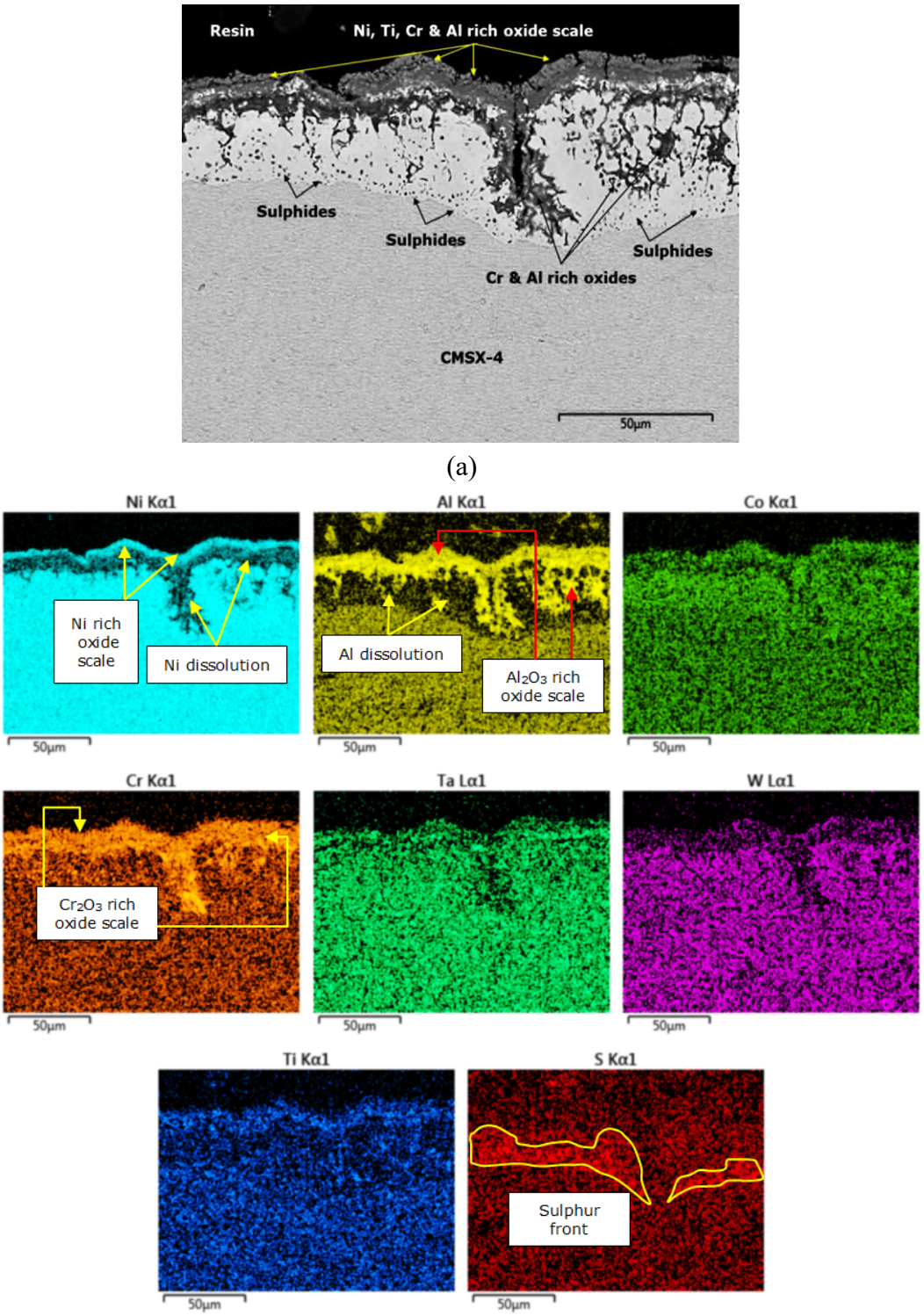

Figure 7-22. SE/EDS mapping on a cross-sectioned specimen 05, gauge mid-section surface, tested at 350 MPa, 850 oC under HTHC environment.

7.2.5 Recast layer thickness measurements

The recast layer thickness measurements were performed to confirm that the down selected laser drilling conditions obtained values closer to the estimated average of RLT_{max}. The fractured fatigue specimens were examined by metallography, in which, specimens of each of the four sets including EDM were sectioned perpendicular to the axes of the holes and ground back such as that the plane section was midway through the test piece. Measurements were made using SEM and measuring points across the sectioned hole were similar to the described in previously (see Chapter 3). Examples of cross-sectioned of fatigue test specimens are shown in Figure 7-23. SEM examination of cross-sectioned fatigue specimen's shows that the actual average of RLT_{max} were close to the estimated values, assumed for each laser trepanning drilling parameters set (see Figure 7-24). The measured values fall under 95 % prediction confidence intervals.

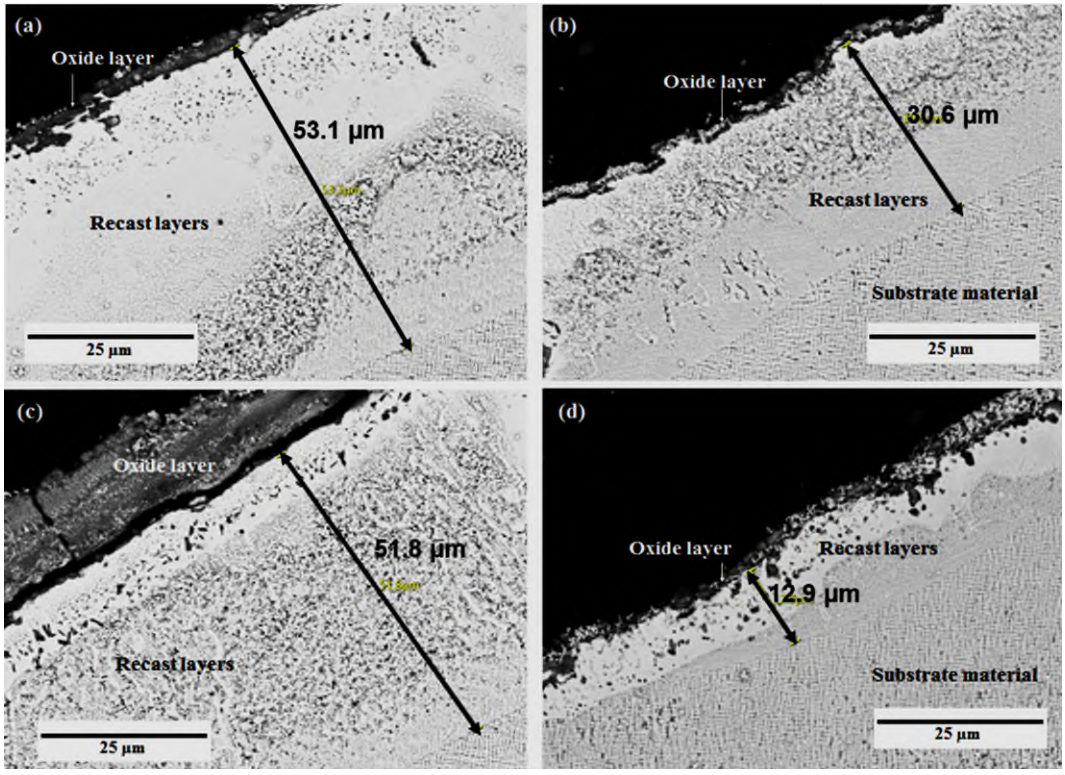

Figure 7-23. Examples of SEM micrographs showing the recast layer morphology under different drilling conditions tested: (a) LTD set A; (b) LTD set B; (c) LTD set C; and (d) Die-Sink EDM set D.

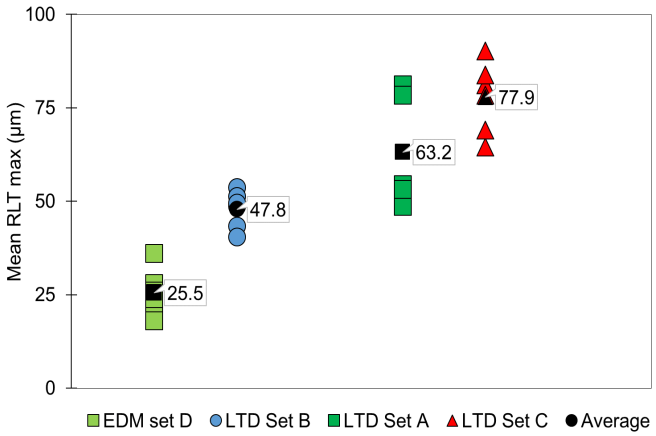

Figure 7-24. Mean of maximum recast layer thickness distribution in all cross-sectioned fatigue drilled specimens.

Figure 7-24 show the measured values of the recast layer thickness performed on the cross-sectioned of fatigue specimens, as it shows the recast layer thickness data versus laser peak power of the specimens tested. Metallographic measurements confirm that the recast layer thickness was variable up to a maximum average of ≤ 26 µm for the EDM set D, ≤ 50 µm for the LTD set B, ~ 65 µm for the LTD set A, and ≥ 75 µm for the LTD set C specimens.

7.3 Summary

The main output of this chapter can be summarised as follows:

1 SEM observation of fractured specimens show that the recast layer is the main site for the crack initiation, and the acute corners of the elliptical hole are regions of high stress concentration. Therefore, recast layer zone becomes more susceptible to cracking under hot corrosion type environment.

2 Cyclic load had a significant influence on the fatigue crack stages of specimens tested at 550 MPa. Corrosion-fatigue type fracture facets was evident on specimens tested at low cyclic stresses (450 and 350 MPa), but the severity of corrosion damage was relatively up incubation phase and short crack growth for specimens that not failed (350 and 290 MPa), under LCF regime.

3 The fracture morphology of tested specimens shows that all specimens that failed had a crystallographic fracture facets along [111] plane. The specimens tested at

higher stress level suggest the fatigue crack Stages I and II were primarily dominated by the mechanical fatigue. Whilst, the specimens tested at an intermediate and low stress levels the corrosion-fatigue dominated the crack stage I and II after a brittle rupture within the recast layer

4 EDS analysis confirms the presence of corrosion species and formation of oxide layers rich in Ni, Al and Cr for all the specimens examined. However, the severity of sulphidation and oxidation attack was dependent on the exposure time. The sulphides were found mostly surrounding the recast layer zone and surface breaking cracks.

5 Another critical observation is that the EDS analysis indicates that corrosion-fatigue had more influence on the crack growth than nucleation. This is due to the dominant effect of the recast layer has on the crack nucleation on the fatigue life when pre-cracking is already present. The findings, also suggest that further study is required to investigate corrosion-fatigue behaviour of CMSX-4 laser drilled angled holes, under a high cycle fatigue regime.

6 Corrosion mapping shows that the open cracks lead to diffusion of oxygen and sulphur through the crack tips, depleting surrounding alloy elements such as nickel, aluminium and chromium. This has led a further diffusion of sulphides into the substrate, resulting in an accelerated crack propagation and faster degradation of the specimen surfaces.

Overall, metallography examination with aid of FE analysis confirms that the surface crack initiation on cooling holes is facilitated by the brittle recast layer along with acute corner regions where the stress concentration is high. The SEM observation of fracture facets and EDS elemental analysis suggest corrosion-fatigue crack growth was mostly dependent on cyclic load applied and severity of the corrosive species diffused into the crack tip, most likely gaseous sulphur and oxygen. From this understanding, surface crack initiation is strongly related to the recast layer produced by laser drilling process and growth is dependent on the corrosion–fatigue up to short crack growth and mechanical fatigue for large crack growth up to final fracture. Therefore, laser drilled holes with high surface quality is required. Smoother surfaces lead to lower local stress concentration, resulting in a longer initiation time to crack nucleation and critical crack size to propagate. As consequence, resulting in an increase of life expectancy of laser drilled components.

8 STRESS-LIFE PREDICTION MODEL CONSIDERING SURFACE FLAW SIZE EFFECTS

8.1 Introduction

The surface flaws produced by machining operations can significantly affect the fatigue performance of a component during service life. These surface flaws act as localised stress raisers similar to notches and can become potential sites of fatigue crack nucleation and subsequent crack advance may result in premature failure or replacement of a component.

Existing stress-life prediction models such as Basquin law, Walker model(E. K. Walker, 1970), Smith, Watson and Topper (SWT) equation (Smith, Watson and Topper, 1970) consider mean stress effects, stress ratios, stress concentration factor and notch sensitivity (Basquin, 1910; K. Walker, 1970; Smith, Watson and Topper, 1970). Therefore, fatigue life prediction models considering the mean stress, stress ratios and notched sensitivity has been extensively reported for different types of metals (Fang and Berkkovits, 1994; Qylafku *et al.*, 1999; Dowling, 2004; Liu and Mahadevan, 2005; Al-Rubaie, 2008; McEvily *et al.*, 2008; Filippini, 2011b; Ince, 2017). However, there still remains a limited amount of work related to fatigue prediction models considering surface flaw size effects (Guu and Hocheng, 2001; Fleury and Nowell, 2017; Shen *et al.*, 2017).

The purpose of this paper is to propose a general stress-life model incorporating surface flaw size effects produced by a machining process on fatigue performance. The proposed model is tested on CMSX-4 laser drilled fatigue data and may extrapolate fatigue lives of different surface flaw size values that were not considered in the data. Therefore, reducing the number of fatigue tests at various sizes of surface flaw.

8.2 Model

The proposed model is based on Basquin's law (Basquin, 1910), which is mostly used for fitting the observed stress-life data (Dowling, Calhoun and Arcari, 2009) within the finite life region of S-N curve (Suresh, 1998). Basquin's equation describes the linear

relationship between the log cyclic applied stress (S_a) in the y-axis and the log number of cycles to failure (N_f) in the x-axis plotted, see Figure 8-1.

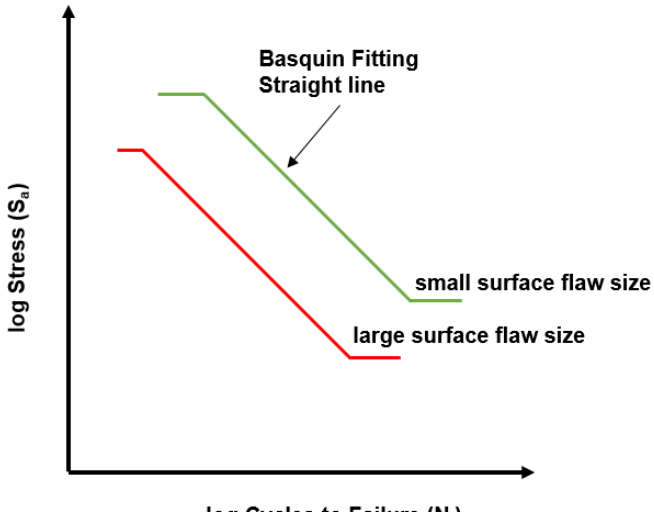

Figure 8-1. Log-log stress-life S-N curves showing Basquin fitting and effects of surface flaw size on fatigue life.

Basquin law can be found in the form as:

$$S_a = AN_f^B \tag{8-1}$$

The parameters A and B are fitting parameters of the log-log scale S-N curve. In this work, to incorporate the effects of surface flaw size (S_{flaw}) on fatigue life, Basquin equation (1) is modified by adding an extra input parameter S_{flaw} and related coefficient parameter φ, as follows:

$$S_a = AN_f^B = S_a\,(S_{flaw})^{\varphi} \tag{8-2}$$

The general stress-life prediction model considering the surface flaw effects may be re-written as:

$$N_f = \left[S_a(S_{flaw})^{\varphi}\frac{1}{A}\right]^{\frac{1}{B}} \tag{8-3}$$

The logarithmic form of equation (3) may be written as:

$$log\ N_f = \frac{1}{B}\ log\ S_n + \frac{\varphi}{B}\ log\ S_{flaw} - \frac{1}{B}\ log\ A \tag{8-4}$$

The next section presents a detailed methodology to determine the model parameters A, B and φ. The S_{flaw} value may be obtained by applying the method of least squares to the observed data or using a specific value of interest under the range of values tested.

8.3 Discussion

8.3.1 Testing and validation

In the present work, laser drilled CMSX-4 fatigue data was used to test the proposed model. The detailed test conditions are reported in previous Chapter 6. Moreover, it should be mentioned that the environmental effects on fatigue life were not considered for the present modelling. This is because environmental factors such as temperature and gaseous flux were held constant through the entire tests. The fatigue specimens were split in three groups based on laser drilling conditions and related recast layer thickness range. Thus, S_{flaw} is assumed as the recast layer thickness (RLT) for testing the proposed model, which is a typical metallurgical anomaly produced during the laser drilling process.

As previously mentioned, S_{flaw} value may be obtained by applying a method of least squares to experimental laser drilling data for estimating fatigue lives of untested specimens with desired RLT up to a maximum of 90-100 µm. The average RLTmax ranging from 45-80 µm were observed and tested, and 15-110 µm reported elsewhere (Sezer *et al.*, 2006; Leigh *et al.*, 2010), during the laser drilling of nickel-base angled micro holes. Therefore, S_{flaw} values from 15-100 µm may be applicable for testing the model and prediction of untested data.

The best fit of the laser drilling parameters-recast layer thickness data by multiple regression analysis yielded the following semi-natural log function (see Section 5.2.3):

$$S_{flaw} = \ln RLT_{max} = 3.62 + 0.01PP^2 - 0.04TS^2 - 0.002\,(PP \times TS) \qquad (8\text{-}5)$$

Where PP is the peak power (Joules per second) and TS is trepanning speed (mm/sec) as the laser drilling input parameters. The obtained R^2 statistics and adjusted R^2 are 0.98 and 0.92, respectively. Hence, adequate for prediction of the recast layer thickness based on the range of values of input parameters tested. Statistical modelling of the recast layer thickness is detailed in Chapter 5 (Section 5.2.3). Table 8-1 presents a small sample of

fatigue data of laser drilled CMSX-4 specimens used for stress-life fitting incorporating the surface flaw size effect. The data covers S_a levels of 550, 450 and 350 MPa for S_{flaw} mean values of 63.2, 47.8 and 7.79 µm. Moreover, the fatigue data in which fatigue lives exceeded more than 10^5 cycles were considered run-out and excluded. Thus, enabling to fit the Basquin's suggested log-log straight line S-N relationship.

Table 8-1. Fatigue data used for proposed model.

Fatigue data				log transformed data for fitting		
Data No.	Maximum, (MPa) S_a	Mean, Observed (m) S_{flaw}	Mean, Life (Cycles) N_f	x_1 $\log S_a$	x_2 $\log S_{flaw}$	y $\log N_f$
1	550	6.32E-05	6,353	2.74	-4.20	3.80
2	450	6.32E-05	54,490	2.65	-4.20	4.74
3	350	6.32E-05	108,624	2.54	-4.20	5.04
4	550	4.78E-05	18,660	2.74	-4.32	4.27
5	450	4.78E-05	80,768	2.65	-4.32	4.91
6	350	4.78E-05	240,000	2.54	-4.32	5.38
7	550	7.79E-05	4,333	2.74	-4.11	3.64
8	450	7.79E-05	38,336	2.65	-4.11	4.58
9	350	7.79E-05	89,076	2.54	-4.11	4.95

The multiple linear regression analysis can be found in the form of Equation (8-5), and detailed methodology for determining the fitting parameters is given by (Dowling, Calhoun and Arcari, 2009):

$$y = m_1 x_1 + m_2 x_2 + c \tag{8-6}$$

Where,

$$y = \log N_f \qquad x_1 = \log S_a \qquad x_2 = \log S_{flaw} \tag{8-7}$$

$$m_1 = \frac{1}{B} \qquad m_2 = \frac{\varphi}{B} \qquad c = -\frac{1}{B} log\ A \tag{8-8}$$

The computed parameters for the proposed model are presented in Table 8-2. The obtained coefficients are statistically significant since their P-values are smaller than 0.05 levels of confidence limit (CL).

Table 8-2. Estimated coefficients of the proposed model.

Parameter	Coefficients	Std Error	t Stat	P-value	Lower CL 95%	Upper CL 95%
c	11.4113	3.717039	3.069998	0.021942	2.316035	20.50657
m_1	-6.09414	0.789928	-7.7148	0.000249	-8.02703	-4.16126
m_2	-2.20989	0.730053	-3.02702	0.023187	-3.99626	-0.42351

Once the fitting coefficients m_1, m_2 and c are determined, the main parameters of Equation (8-3) are easily calculated, as:

$$B = \frac{1}{m_1} = -0.1641, \quad \varphi = Bm_2 = \frac{m_2}{m_1} = 0.3626, \quad A = 10^{-c/m_1} = 74.56 \qquad (8\text{-}9)$$

Finally, applying the obtained values of A, B and φ parameters into Equation (8-3) provides the predicted lifing data considering surface flaw size effects, i.e. recast layer thickness. Or alternatively, using Equation (8-5) and then applying the Equation (8-3) fatigue lives of laser drilled specimens with angled holes may be estimated based on the laser process parameters used. The latter approach enables one to optimise the laser drilling parameters based on the desired fatigue life performance.

There are many statistical techniques to validate the adequacy and the goodness of fit of a model (Montgomery and Runger, 2012). The most widespread is the evaluation of residuals, differences between the actual and model predicted values, and statistical analysis of variance (Bower, 2000). Figure 8-2 illustrates that the relationship between the residuals and the normal scores is almost linear. Data points are close to the straight reference line and are randomly distributed on both sides of 0. Therefore, suggesting that the data points appears to be normally distributed. This type of plot indicates that the vertical deviations from the straight reference line are the actual residuals of the fit. A residual is positive if the corresponding data point is above the straight line and negative if the data point is below the straight line.

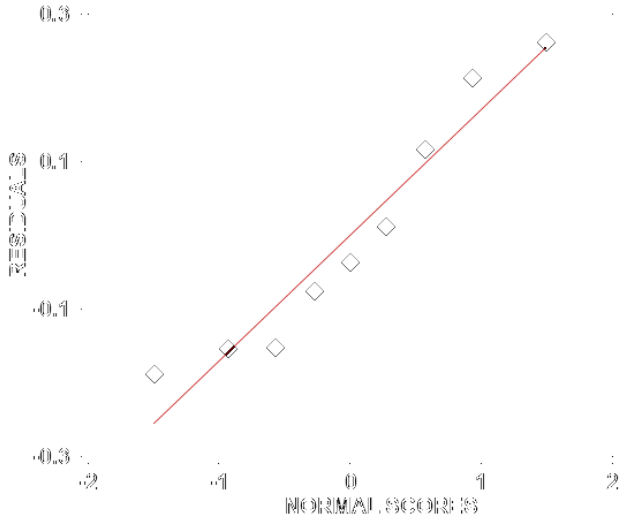

Figure 8-2. Normal probability plot of residuals.

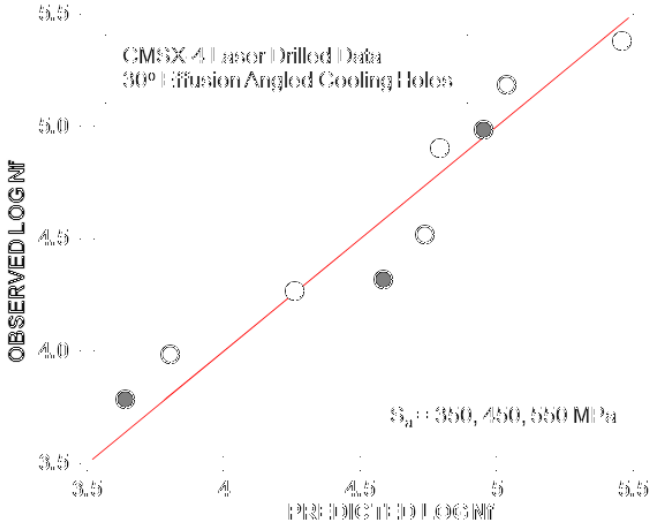

Figure 8-3. Observed log cycles to failure (N_f) versus predicted log cycles to failure (N_f), based on the small sample fatigue data.

Figure 8-33 illustrates a comparison between observed and predicted corrosion-fatigue lives for laser drilled CMSX-4 fatigued specimens. It can be seen from Figure 8-3 that there is a good correlation between the observed N_f and predicted log N_f values. It can be concluded that for a small sample of nine mean data points, the proposed model estimates fatigue lives very close with those observed, under 95% confidence limits. The statistical analysis of variance results presented in Table 8-3 confirms that is the case, where the obtained standard error of the estimate (S) of 0.19 is a small value, thus, observation data points are closer to the fitted line. Furthermore, the F-value is larger than the standard tabulated critical F-value ($F_{0.05,\ 2,\ 6}$) (Roy, 2010), implying that the model is adequate

within 95% confidence limits. Therefore, the general stress-life model incorporating surface flaw size may be applied to interpolate fatigue lives of laser drilled specimens. Moreover, the proposed model (Equation 8-3) can be applied to interpolate fatigue lives based on small sample data of other types of surface flaws produced by other machining methods with minimum number of testing effort.

Table 8-3. Results of statistical analysis of variance.

	Df, Degree of freedom	SS, Sum of Squares	MS, Mean of Squares	F-Ratio	P-value
Regression	2	2.487334	1.243667	34.34054	0.000519
Residual	6	0.217294	0.036216	-	-
Total	8	2.704629	-	-	-
S = 0.19		R^2 = 0.92		Adjusted R^2 = 0.89	

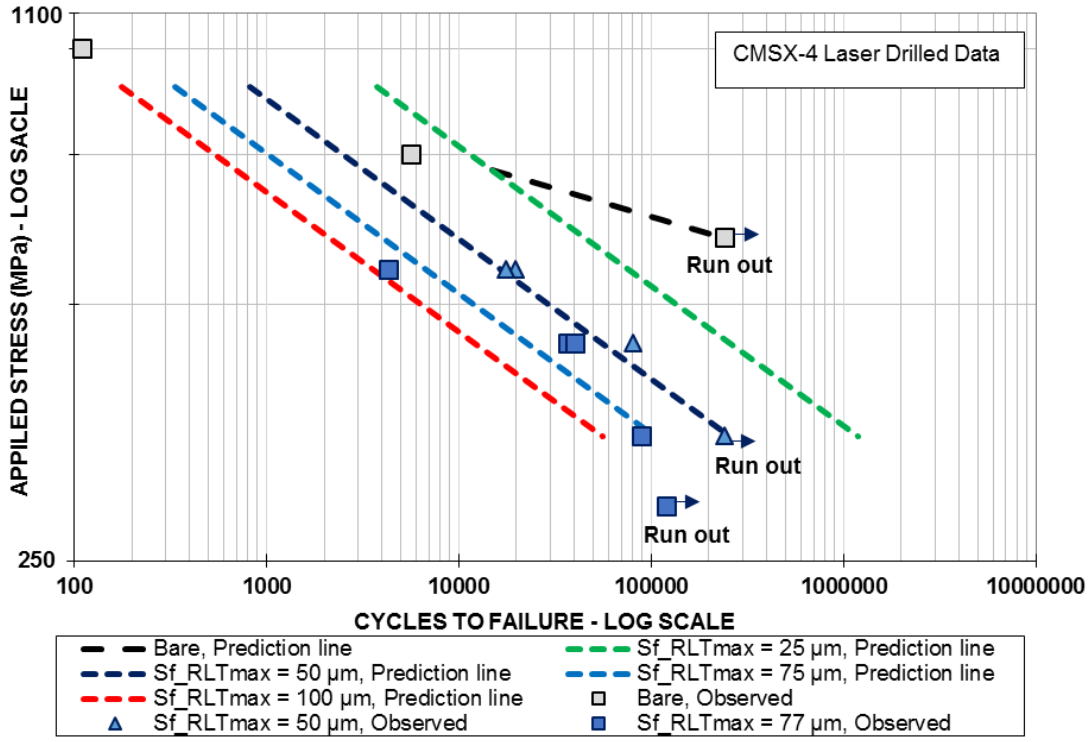

Figure 8-4. Stress-life of CMSX-4 laser drilled specimens at different surface flaw sizes, RLT_{max} from 25, 50, 75 and 100 µm.

Figure 8-4 illustrates the stress-life plot considering the effect of surface flaw size (S_f) on fatigue life performance under simulated Air+SO_2 environment. Most of the observed data points lie close to the prediction line, hence suggests that the proposed model is adequate. The obtained R^2 statistic of 0.92 and adjusted R^2 statistic of 0.89 are closer to

1.0, confirming that the proposed model is satisfactory and capable of estimating fatigue life values within 95% confidence limits. Moreover, the proposed model may offer a good approximation for untested data. For example, that is the case of fatigue specimens with surface flaw recast layer thickness of 25 and 100 µm as shown in Figure 8-4. However, it may require a small number of tests to confirm the untested data trend.

Another critical observation from Figure 8-4 is that the fatigue life debit of laser drilled specimens is less for S_{flaw} of 25 µm prediction line than of S_{flaw} of 50 µm prediction line, when comparing to CMSX-4 base line at similar conditions. One reason is that the magnitude of thermally induced tensile stress is dependent of the power density inflicted on the targeted area, which in turn, affects the number formation of accumulated recast layers and thickness (Sezer *et al.*, 2006; Morar *et al.*, 2018). Therefore, different thicknesses of the recast layer may yield dissimilar morphology and altered strength properties. As this could be the case of thin recast layers less than 25 µm yielding fine microstructure, thereby giving high strength and limiting the crack advance in case of existing short cracks. Further tests may be required to confirm this trend since no crack growth measurements during the tests were performed in this research work.

8.4 Summary

This chapter introduced a novel modified stress-life prediction model which extends on the best existing best practice models such as the Basquin equation. The modified stress-life model gives a unique versatility compared to other stress-life methods when considering surface flaw effects. The proposed model is particularly suited for prediction of fatigue life of critical machined features and associated surface defects. The model has been thoroughly tested on fatigue data from laser drilled CMSX-4 samples experiencing a high temperature hot corrosion environment. The material has been chose due to its high relevance for the aerospace industry. To consider the surface flaw size effects, the recast layer thickness produced by laser drilling of effusion cooling holes has been used as an additional parameter for modelling. The ANOVA results show that the proposed model is accurate. The results feature the model ability to estimate the life of untested specimens even when only small fatigue data samples are available.

9 CONCLUSIONS

This chapter outlines the limitations and challenges encountered in the present research work. In addition, reflects the main research contributions by remarking the gaps found in the literature. Finally, the concluding remarks of the thesis including key findings and directions for the future work.

9.1 Limitations of the research

Although this research has achieved its aim and objectives, this section outlines three limitations found in this research that requires discussion. First, difficulties in accessing the relevant service experience information and manufacturing procedures for critical mechanical components within sponsor organisation (i.e. laser drilling parameters). This created difficulty in the initial stages of the research, particularly in the design of the research and initial industrial case study. This has delayed the entire research programme. Nevertheless, data capture of in-service experience information of critical mechanical components was conducted with limited information. The remaining causal information was gathered from the published peer reviewed papers and reports. These papers reported failure and root cause analysis of critical aeroengine mechanical components from different organisations around the world. It would be better if all the relevant information were captured from one organisation and then compared with information from other organisations in order to make the degradation analysis more broad, sensible and robust.

Second, the range of parameters and values investigated in the preliminary experiments were limited. This is because the experimental trials and laser drilled fatigue specimens to generate lifing data were conducted in two stages, which only lasted for four continuous weeks, two days each week. Therefore, eight working days are not enough to investigate a broad range of parameters. Therefore, Taguchi orthogonal array (OA) L9 with three input factors and additional confirmation trials was a feasible option. It would be better if it was performed through a full factorial analysis or L16 OA design considering other input factors such as pulse duration, pulse energy, pulse frequency, gas pressure, focal position and trepan speed.

Third, because of the time limit and inherent costs, the corrosion-fatigue testing was conducted on a small size of samples for each laser drilling group, limited to 120,000

cycles. Five fatigue specimens for each group might not represent full S-N diagram. The research should have involved more fatigue specimens for each laser drilling group, base line, and EDMed specimens. This would have generated A or B class lifing data applicable for process optimisation.

Nevertheless, the correlation between the laser drilling parameters, recast layer thickness and corrosion-fatigue life has established in this research. Moreover, the lifing data generated in thesis provides reasonable trends for lifing of cooling holes geometry. In addition, information for laser drilling parameters optimisation to minimise the recast and cracks formation in cooling holes at manufacturing stages.

9.2 Research contribution

The research main contributions, in summary, are as follows:

1. The effects of laser trepanning drilling parameters such as peak power, pulse frequency and trepan speed on the recast layer thickness and surface crack formation in CMSX-4 angled holes have been established (Chapters 4 and 5).

The research work presented in Chapter 5 is unique and fills the knowledge gap regarding understanding of surface cracks formation in laser trepan drilled angled holes, and adds further knowledge to previous investigations conducted elsewhere regarding laser drilling of micro-holes for cooling film holes application in the aerospace industry. To address this, surfaces cracks in the recast layer were analysed by crack number density, which is a new approach for quantifying the surface cracks produced by laser drilling. Furthermore, recast layer morphology and hardness in acute angled holes is analysed and discussed (Chapter 4).

To the author's knowledge, much of the work published on laser drilling of Ni-based superalloys were focused on the hole geometry (i.e. taper ratio, roundness), drilling time and recast layer formation in non-angled holes. Also, studies on the optimisation and modelling of laser drilling process were conducted in the last decade, mostly on the pulsed Nd:YAG percussion laser drilling method. There is limited and detailed research work published on the pulsed Nd:YAG laser trepan drilling. Moreover, analysis presented in this research is of key importance for selecting processing parameters for eliminating or

minimising the surface cracks inside the recast layers and understand the potential impact of such metallurgical anomalies on the fatigue crack initiation and consequent in through-life performance of laser drilling holes in service.

2. The relationship between laser trepan drilling, recast layer thickness and corrosion-fatigue life has been established for Ni-based CMSX-4 angled cooling holes (Chapters 6 and 7).

Past and recant studies have reported the effects of cooling holes geometry on the thermal mechanical fatigue and creep behaviour. There are no studies published in the open literature reporting the high temperature corrosion-fatigue behaviour of cooling holes due to presence of different recast layer thickness produced by laser trepan drilling. The research work presented in Chapters 6 and 7 fills the knowledge gap in this subject area and the thesis main contributions to the knowledge.

3. A general stress-life empirical model considering initial surface flaw size effects has been proposed. The empirical model is based on the Basquin's stress-life relationship (Chapter 8).

The proposed model is unique since it correlates laser drilling process parameters, surface defects, and fatigue life performance. Based on the results, proposed model may well be adequate to estimate the life of untested specimens based on the small sample of fatigue data. Moreover, the proposed model can be extended to other manufacturing methods. Past studies have only developed empirical models on either machining data or simulation data for optimisation purpose. In summary, the present research work fills the existing knowledge gaps in areas of laser drilling, corrosion-fatigue and lifing of cooling film holes for aeroengine blades and vanes. In addition, adds further knowledge to existing investigations elsewhere on laser drilling where none of author's reported the process parameters contribution to surface micro cracks formation in the recast layer (Sezer *et al.*, 2006; Chien and Hou, 2007; Leigh *et al.*, 2010; Antar *et al.*, 2016).

9.3 Thesis concluding remarks

The present research involved collaboration between the EPSRC Centre for Innovative Manufacturing in Through-life Engineering Services at Cranfield University and Rolls-

Royce Aeroengines, in support of flagship the Project 3 "Characterisation of in-service component feedback for system design and manufacturing". This research established the dependencies between laser drilling process parameters, recast layer thickness and corrosion-fatigue life for turbine vane cooling holes. The delineated research objectives were achieved and the postulated influences of manufacturing process and parameters on the fatigue life of a critical aerospace component feature has been answered.

From this research, following conclusions can be drawn:

1. There is a strong correlation between the laser drilling process parameters and recast layer thickness. The trepan speed and peak power had significant influence on the thickness of the recast layer and surface cracks formation respectively, both statistically and physically under the range of values tested.
2. The recast layer produced by laser drilling process on the sidewalls of angled cooling holes found to be detrimental to fatigue strength and corrosion resistance. Nano indentions tests shown that the recast layer hardness values were higher than the base alloy, suggesting the brittle nature of the recast layer may have influence the early crack initiation. In case of pre-existing cracks, less resistant to crack growth than the base alloy.
3. Metallography observations show that the recast layer microstructure is of nano-crystalline structure with grains ranging between 50-250 nm. This due to re-crystallisation occurring during the laser drilling process leads to re-precipitation, mostly at solidification stage of molten material. Thus, resultant re-precipitation leads to nano size grains. The selected diffraction patterns show that both recast layer and CMSX-4 corresponds to similar FCC crystallographic structure of [112] planes.
4. Elemental analysis on the recast layer show significant alterations in alloy chemistry in the recast layer, thus, potential alterations in mechanical properties and high temperature resistance. Understanding of the microstructure and chemistry of the recast layers obtained after laser drilling enables to recognise the potential impact of this layer on the performance of laser drilled components.
5. The effects of different recast layer thicknesses on high temperature corrosion-fatigue life of CMSX-4 angled cooling holes have been investigated. For the first-

time fatigue specimens with laser drilled holes were tested on an environmental fatigue rig simulating hot corrosion environment. There is a fatigue life debit of 40 % compared to bare specimens tested. The specimens with recast layer thickness under 50 μm had better performance than counter specimens with 65 and 77 μm. The results suggest that thin recast layers less than 45 μm could significantly improve life of laser drilled components. More tests are needed to confirm this trend.

6. The S-N curves obtained suggest that the corrosion-fatigue limit for laser drilled specimens produced in this research for cooling holes is below 350-290 MPa, independent of recast layer thickness obtained.

7. Metallography of fracture specimens indicate that cracks nucleated from the recast layer and extending to base alloy. The crack nucleation sites found to be at acute corners where high stress concentrations are typically predominant. The recast layer along with environmental influence act as stress raiser accelerating the nucleation. The elemental analysis has shown that the hot corrosion environment had influence on the fatigue strength degradation of cooling holes. The crack growth was typical of crystallographic fracture and along [111] planes.

8. The corrosion maps of fracture surface show formation of oxide scale rich in aluminium and depletion of nickel alloy on the top surface of the specimens. Beneath the alumina layer, another oxide layer rich in chromium was formed as well as presence of diffused sulphides around the open cracks. The elements maps produced in this research provides evidence of corrosion-fatigue assisted cracking experienced by fatigued specimens tested.

9. The research establishes that corrosion-fatigue in cooling holes is influenced by combined interaction of recast layer thickness, cyclic load and hot corrosion chemistry (i.e. oxidation and sulphidation). Although, recast layer facilitates the crack nucleation the cyclic load and sulphur concentration promotes accelerated crack growth. That was indeed the case for fatigue specimens that did not fail had experienced the incubation phase and short crack growth under low cyclic load.

10. Stress-life model considering surface flaw is proposed based on the Basquin's equation. The proposed model uses both laser drilling experiments and lifing data

to determine the model parameters, making this model robust to extrapolate S-N curves with minimal testing effort. The estimated lifing data could be reused for design and process parameters improvement.

11. Lastly, the main contribution of this research falls under subject areas of materials processing and lifing of turbine components, particularly in laser drilled cooling holes where there is lack of understanding and knowledge of high temperature corrosion-fatigue behaviour, recast layer thickness and pre-existing surface cracks impact.

9.4 Future work

The scopes for future research work based on the present thesis are as follows:

1. To further understand the mechanics of fatigue crack growth on effusion cooling holes in single crystal and polycrystalline Ni-base superalloys. The study should use compact test fatigue coupons to generate FCG data, at different crack lengths observed in the laser drilled holes. In addition, detailed metallography analysis to understand the crystallography fracture in cooling hole configurations
2. To extend the study to other emerging drilling methods for cooling holes such as water jet drilling (WJD) and fiber laser drilling impact on the corrosion-fatigue life. The number of fatigue specimens should be larger than the present research to make the lifing data more meaningful and statistically significant.
3. To investigate the influences of low temperature hot corrosion in both impingement and film cooling holes. This could provide a full insight on the degradation of corrosion-fatigue strength of turbine blades and vanes cooling system.
4. The present research did not investigate the influence of assist gas pressure on the recast layer and surface crack formation. Past studies have reported the effects of processing gas types on recast layer and cracks, but no studies have reported the effects of mass flow rate in laser trepan drilling of cooling holes. Therefore, mass flow rate could be thoroughly investigated within a range of 10 to 20 Nm^3/hour.

REFERENCES

ABET (2016) *Engineering Design*. Available at: http://www.me.unlv.edu/Undergraduate/coursenotes/meg497/ABETdefinition.htm (Accessed: 28 October 2016).

Ai, X., Gao, H.-S., Wen, Z.-X., Liu, D.-S. and Yue, Z.-F. (2014) 'Creep behavior of thin-walled plate with cooling holes of nickel-based single crystal superalloy DD6 under high temperature', *Hangkong Dongli Xuebao/Journal of Aerospace Power*, 29(5).

Al-Rubaie, K. S. (2008) 'A general model for stress-life fatigue prediction', *Materialwissenschaft und Werkstofftechnik*, 39(6), pp. 400–406.

Von Allmen, M. (1976) 'Laser drilling velocity in metals', *Journal of Applied Physics*, 47(12), pp. 5460–5463.

Antar, M., Chantzis, D., Marimuthu, S. and Hayward, P. (2016) 'High Speed EDM and Laser Drilling of Aerospace Alloys', in *Procedia CIRP*, pp. 526–531.

Anthony, C. (2007) 'Linear Elastic Fracture Mechanics', in *Introduction to Contact Mechanics*. Boston, MA: Springer US, pp. 31–48.

Antolovich, B. (1996) 'Fatigue and fracture of nickel-base superalloys', in *Fatigue And Fracture*. ASM International, pp. 854–868.

Arakere N, S. G. (2002) 'Effect of crystal orientation on fatigue failure of single crystal nickel base turbine blade superalloys', *Journal of Engineering for Gas Turbines and Power*, 124(1), pp. 161–176.

Arrell, D., Hasselqvist, M., Sommer, C. and Moverare, J. (2004) 'On TMF damage, degradation effects, and the associated TM in influence on TMF test results in γ/γ′ alloys', in *Proceedings of the International Symposium on Superalloys*, pp. 291–294.

Askeland, D. R., Fulay, P. P. and Wright, W. J. (2010) *The Science and Engineering of Materials*. 6th edn. Stamford, USA: Cengage Learning.

ASTM E1820-15a (2015) 'Standard Test Method for Measurement of Fracture Toughness, E1820-15a', *American Society for Testing and Materials*. American Society for Testing and Materials: ASTM International, pp. 1–38.

ASTM E2368-10 (2010) ‘E2368-10 Standard Practice for Strain Controlled Thermomechanical Fatigue Testing, E2368-10’, *American Society for Testing and Materials*. Philadelphia: ASTM International, pp. 1–10.

ASTM E399-12 (2013) ‘Standard Test Method for Linear-Elastic Plane-Strain Fracture Toughness KIC of Metallic Material, E399 - 12’, *American Society for Testing and Materials*. Philadelphia: ASTM International, pp. 1–33.

ASTM E6 (2000) ‘Standard Terminology Relating to Methods of Mechanical Testing 1, E6’, *American Society for Testing and Materials*. Philadelphia: ASTM International, E 6, pp. 1–10.

ASTM E606 (2012) ‘Standard Test Method for Strain-Controlled Fatigue Testing, E606/E606M - 12’, *American Society for Testing and Materials*. Philadelphia: ASM International, p. 16.

ASTM E647 − 15e (2015) ‘Standard Test Method for Measurement of Fatigue Crack Growth Rates, E647 − 15e’, *American Society for Testing and Materials*. Philadelphia, pp. 1–50.

ATSB (2014) *Power plant failures in turbofan-powered aircraft 2008 to 2012*. Sydney.

Bagnall, S. M. (2008) *Fatigue life prediction in turbine components: Lecture notes*. Bristol: Rolls-Royce.

Bagnall, S., Shaw, D. and Mason-Flucke, J. (2000) ‘Implications of’Power by the Hour’on Turbine Blade Lifing’, in *Design for Low Cost Operation and Support*. Ottawa, Canada: DTIC.

Bandyopadhyay, S., Gokhale, H., Sundar, J., Sundararajan, G. and Joshi, S. (2005) ‘A statistical approach to determine process parameter impact in Nd:YAG laser drilling of IN718 and Ti-6Al-4V sheets’, *Optics and Lasers in Engineering*, 43(2), pp. 163–182.

Bandyopadhyay, S., Sarin, S. J., Sundararajan, G. and Joshi, S. (2002) ‘Geometrical features and metallurgical characteristics of Nd:YAG laser drilled holes in thick IN718 and Ti–6Al–4V sheets’, *Journal of Materials Processing Technology*, 127(1), pp. 83–95.

Barbosa, C., Nascimento, J., Caminha, I. and Abud, I. (2005) ‘Microstructural aspects of the failure analysis of nickel base superalloys components’, *Engineering Failure*

Analysis, 12(3), pp. 348–361.

Barnard, N., Maclachlan, D., Jones, N., Mason-Flucke, J., Bagnall, S. and Bache, M. (2012) 'Low cycle fatigue of CMSX-4 in off-axis orientations and the effect of a multi-axial stress state', in *Superalloys 2012*. John Wiley and Sons, pp. 293–300.

Basquin, O. H. (1910) 'The exponential law of endurance tests', in *Proceedings of American Society for Testing and Materials, vol.10*. West Conshohocken, Pa, USA: ASTM, pp. 625–630.

Bathe, R. and Padmanabham, G. (2014) 'Evaluation of laser drilling of holes in thermal barrier coated superalloys', *Materials Science and Technology*. Maney Publishing Suite 1C, Joseph's Well, Hanover Walk, Leeds LS3 1AB, UK, 30(14), pp. 1778–1782.

Beck, T. (2011) 'Laser drilling in gas turbine blades Shaping of holes in ceramic and metallic coatings', *Laser Technik Journal*, 8(3), pp. 40–43.

Beck, T., Bostanjoglo, G., Kugler, N., Richter, K. and Weber, H. (1997) 'Laser beam drilling applications in novel materials for the aircraft industry', in *Laser Institute of America, Proceedings*, pp. E93–E102.

Bhaumik, S., Bhaskaran, T., Rangaraju, R., Venkataswamy, M., Parameswara, M. and Krishnan, R. (2002) 'Failure of turbine rotor blisk of an aircraft engine', *Engineering Failure Analysis*, 9(3), pp. 287–301.

Bhaumik, S., Sujata, M., Venkataswamy, M. and Parameswara, M. (2006) 'Failure of a low pressure turbine rotor blade of an aeroengine', *Engineering Failure Analysis*, 13(8), pp. 1202–1219.

Białas, M. (2008) 'Finite element analysis of stress distribution in thermal barrier coatings', *Surface and Coatings Technology*, 202(24), pp. 6002–6010.

Birks, N., Meier, G. H. and Pettit, F. S. (2006) *Introduction to the High Temperature Oxidation of Metals*, *Engineering*. London, UK: Cambridge University Press.

Blanchard, A. (2011) *Review of thermo-mechanical fatigue models for aero-engines*. phdthesis. MSc Thesis. Cranfield, England: Cranfield University.

Bower, K. M. (2000) 'Analysis of Variance (ANOVA) Using MINITAB', *Scientific Computing & Instrumentation*, (2), pp. 0–5. Available at:

http://12.230.216.10/uploadedFiles/Shared_Resources/Documents/Articles/analysis_of_variance.pdf.

Boyce, M. (2012) 'Gas Turbine Engineering Handbook', *Gas Turbine Engineering Handbook*. Elsevier, pp. 357–383.

Brandon, D. and Kaplan, W. D. (2008) 'Transmission Electron Microscopy', in Brandon, D. and Kaplan, W. D. (eds) *Microstructural Characterization of Materials*. 2nd edn. Wiley, pp. 179–260.

Broek, D. (1986) *Elementary Engineering Fracture Mechanics*. 4th edn. Dordrecht, The Netherlands: Martinus Nijhoff.

Broek, D. (2012) *Elementary engineering fracture mechanics*. Springer Science & Business Media.

Brooks, C. R. and Choudhury, A. (2002) *Failure Analysis of Engineering Materials*. 1st edn. United States: McGraw-Hill Education - Europe.

Cai, C., Liaw, P. K., Ye, M. and Yu, J. (1999) 'Recent developments in the thermomechanical fatigue life prediction of superalloys', *J. Mater.-e,(JOM-e)*, pp. 51–54.

Campbell, F. C. (2008) 'Elements of Metallurgy and Engineering Alloys', *ASM International*. ASM International, pp. 243–262.

Campbell, F. C. (2012) 'Fatigue and fracture, Understanding the basics', *ASM International*. ASM International, 1, pp. 55–100.

Carter, T. J. (2005) 'Common failures in gas turbine blades', *Engineering Failure Analysis*, 12(2), pp. 237–247.

Chan, K., Enright, M. and P. Moody, J. (2013) 'Development of a Probabilistic Methodology for Predicting Hot Corrosion Fatigue Crack Growth Life of Gas Turbine Engine Disks', *Journal of Engineering for Gas Turbines and Power*.

Chan, K. S., Enright, M. P., Moody, J. P. and Fitch, S. H. K. (2016) 'Physics-Based Modeling Tools for Predicting Type II Hot Corrosion in Nickel-Based Superalloys', in *Superalloys 2016: 13th International Symposium*, pp. 917–926.

Chapman, N., Brooking, L., Sumner, J., Gray, S. and Nicholls, J. (2017) 'Corrosion

fatigue testing: the combined effect of stress and high temperature corrosion', *Materials at High Temperatures*. Taylor & Francis, 0(0), pp. 1–8.

Chen, L., Hu, W., Wen, Z., Yue, Z. and Y., G. (2014) 'Effects of roundness of laser formed film cooling holes on fatigue life of nickel based single crystal', *Materials at High Temperatures*, 31(1), pp. 18–26.

Chen, X. (2005) 'Foreign object damage on the leading edge of a thin blade', *Mechanics of Materials*, 37(4), pp. 447–457.

Chiang, K.-T., Pettit, F. and Meier, G. (1983) 'Low temperature hot corrosion', *International Corrosion Conference Series*.

Chien, W. T. and Hou, S. C. (2007) 'Investigating the recast layer formed during the laser trepan drilling of Inconel 718 using the Taguchi method', *International Journal of Advanced Manufacturing Technology*, 33(3–4), pp. 308–316.

Child, D., Meldrum, J. and Onwuarolu, P. (2016) 'Corrosion-fatigue testing of Ni-based superalloy RR1000', *Materials Science and Technology*, 11(4), pp. 1040–1047.

Chryssolouris, E. L. K. . (1991) *Laser Machining: Theory and Practice*. New York: Springer-Verlag.

Clarke, D. R. and Phillpot, S. R. (2005) 'Thermal barrier coating materials', *Materials Today*, 8(6), pp. 22–29.

Coffin, L. F. (1954) 'A study of the effects of cyclic thermal stresses on a ductile metal', *Transactions of the ASME*, 76, pp. 931–950.

Colangelo, V. (1978) 'Metallographic Analysis of Corrosion Failures', in McCall, J. L. and French, P. M. (eds) *Metallography in Failure Analysis*. Boston, MA: Springer US, pp. 121–140.

Coppola, T., Risciful, S., Tassa, O. and Pasquero, G. (2008) 'Thermo-mechanical fatigue behaviour of bare and coated CMSX-4', in *Proceedings of the ASME Turbo Expo*, pp. 431–436.

Corcoran, A. and Sexton, L. (2000) 'The laser drilling of multi-layer Rene80 and X40

material systems', *Laser Materials Processing*. Laser Institute of America, Orlando, FL (United States), 89, pp. 163–172.

Corcoran, A., Sexton, L., Seaman, B., Ryan, P. and Byrne, G. (2002) 'The laser drilling of multi-layer aerospace material systems', *Journal of Materials Processing Technology*. Elsevier, 123(1), pp. 100–106.

Cowles, B. A. (1996) 'High cycle fatigue in aircraft gas turbines - an industry perspective', *International Journal of Fracture*, 80(2), pp. 147–163.

Cox, D. C., Roebuck, B., Rae, F. and Reed, R. C. (2003) 'Recrystallisation of single crystal superalloy CMSX-4', *Materials Science and Technology*. Taylor & Francis, 19(4), pp. 440–446.

Craig, B. D. (2005a) 'Material failure modes, part I: A brief tutorial on fracture, ductile failure, elastic deformation, creep, and fatigue', *Journal of Failure Analysis and Prevention*, 5(5), pp. 13–14.

Craig, B. D. (2005b) 'Material failure modes, part II: A brief tutorial on impact, spalling, wear, brinelling, thermal shock, and radiation damage', *Journal of Failure Analysis and Prevention*, 5(6), pp. 7–12.

Craig, B. D. (2006) 'Material failure modes, part III: A brief tutorial on corrosion-related material failure modes', *Journal of Failure Analysis and Prevention*, 6(2), pp. 12–19.

Crompton, J. S. and Martin, J. W. (1984) 'Crack growth in a single crystal superalloy at elevated temperature', *Metallurgical Transactions A*, 15(9), pp. 1711–1719.

Cui, W. (2002) 'A state-of-the-art review on fatigue life prediction methods for metal structures', *Journal of Marine Science and Technology*, 7(1), pp. 43–56.

D, V. (2008) *Energy Dispersive X-ray Microanalysis An Introduction*. California: Thermo Fisher Scientific. Available at: https://tools.thermofisher.com/content/sfs/brochures/D17000~.pdf.

Dahotre, N. B. and Harimkar, S. P. (2008) 'Laser drilling', in N.B. Dahotre, S. P. H. (ed.) *Laser Fabrication and Machining of Materials*. New York: Springer, pp. 97–143.

Das, D. K. and Pollock, T. M. (2009) 'Femtosecond laser machining of cooling holes in thermal barrier coated {CMSX4} superalloy', *Journal of Materials Processing*

Technology, 209(15–16), pp. 5661–5668.

Degeilh, R., Bonnand, V. and Pacou, D. (2013) 'Study and 3D analysis of the drilling process influence on notched single crystal superalloy specimens', *ICMFF9*.

Deodeshmukh, V. and Gleeson, B. (2008) 'Environmental and compositional effects on the hot-corrosion behavior of Ni-based alloys and coatings', in *Corrosion 2008*. New Orleans, LA: NACE International.

Dhar, S., Saini, N. and Purohit, R. (2006) 'A review on laser drilling and its techniques', *Proceedings of the International Conference on Advances in Mechanical Engineering*, 2006(Ame). Available at: http://sushidhar.tripod.com/New_Folder/laserdrilling.pdf.

van Dijk, M. H. (1992) '"Drilling of aero-engine components: Experiences from the shop floor."', in Belforte, D. and Leviit, M. (eds) *The Industrial Laser Handbook*. Springer, pp. 113–118.

Dimov, S., Petkov, P., Minev, R. and Pham, D. (2008) 'Laser Milling: Pulse duration effects on surface integrity', *Proceedings of the Institution of Mechanical Engineers, Part B: Journal of Engineering Manufacture*, 222(1), pp. 35–45.

Dowling, N. E. (2004) 'Mean Stress Effects in Stress-Life and Strain-Life Fatigue', *2nd SAE Brasil International Conference on Fatigue*.

Dowling, N. E., Brose, W. R. and Wilson, W. K. (1977) 'Notch member fatigue life predictions by local strain approach', in *Fatigue under complex loading -Analysis and experiments*. Warrandale: Society of Automotive Engineers, pp. 55–84.

Dowling, N. E., Calhoun, C. A. and Arcari, A. (2009) 'Mean stress effects in stress-life fatigue and the Walker equation', *Fatigue & Fracture of Engineering Materials & Structures*. USA: Blackwell Publishing, 32(3), pp. 163–179.

Duan, W., Dong, X., Wang, K., Fan, Z., Mei, X., Wang, W. and Lv, J. (2016) 'Effect of temporally modulated pulse on reducing recast layer in laser drilling', *The International Journal of Advanced Manufacturing Technology*, 87(5), pp. 1641–1652.

Duan, W., Wang, K., Dong, X., Mei, X., Wang, W. and Fan, Z. (2015) 'Study on machining of high-quality micro-holes by laser trepan drilling', *Hsi-An Chiao Tung Ta Hsueh/Journal of Xi'an Jiaotong University*, 49(3), pp. 95–112.

Duan, W., Wang, K., Dong, X., Mei, X., Wang, W. and Fan, Z. (2014) 'Experimental characterizations of burr deposition in Nd:YAG laser drilling: a parametric study', *The International Journal of Advanced Manufacturing Technology*, 76(9–12), pp. 1529–1542.

Dubey, A. K. and Yadava, V. (2008) 'Laser beam machining - A review', *International Journal of Machine Tools and Manufacture*, 48(6), pp. 609–628.

Duquette, D. J. and Gell, M. (1971) 'The effect of environment on the mechanism of Stage I fatigue fracture', *Metallurgical Transactions*, 2(5), pp. 1325–1331.

Dutta Majumdar, J. and Manna, I. (2003) 'Laser processing of materials', *Sadhana*, 28(3), pp. 495–562.

Eady, C. (2000) 'Modes of Gas Turbine Component Life Consumption', in Sapsard, M. (ed.) *Recomended Practices For Monitoring Gas Turbine Engine Life Consumption*. RTO TR-28, pp. 4–12.

Ejaz, N., Qureshi, I. N. and Rizvi, S. A. (2011) 'Creep failure of low pressure turbine blade of an aircraft engine', *Engineering Failure Analysis*, 18(6), pp. 1407–1414.

Eliaz, N., Shemesh, G. and Latanision, R. M. (2002a) 'Hot corrosion in gas turbine components', *Engineering Failure Analysis*, 9(1), pp. 31–43.

Eliaz, N., Shemesh, G. and Latanision, R. M. (2002b) 'Hot corrosion in gas turbine components', *Engineering Failure Analysis*, 9(1), pp. 31–43.

Encinas-Oropesa, A., Simms, N., Nicholls, J., Oakey, J., Heikinheimo, L. and Tuurna, S. (2014) 'Effect of biofuel-derived contaminants on coated industrial gas turbines blade materials', *Materials and Corrosion*, 65(2), pp. 206–216.

Epishin, A., Link, T., Brückner, U., Klingelhöffer, H. and Portella, P. (2005) 'Influence of high temperature creep damage on low cycle fatigue of CMSX-4', in *Materials Science and Technology*, pp. 231–239.

Epishin, A., Link, T., Klingelhöffer, H., Fedelich, B. and Portella, P. (2010) 'Creep damage of single-crystal nickel base superalloys: Mechanisms and effect on low cycle fatigue', *Materials at High Temperatures*, 27(1), pp. 53–59.

Eshelby, J. D. (1961) 'Elastic inclusions and inhomogeneities', *Progress in Solid*

Mechanics, 2, pp. 89–140.

Evans, W., Lancaster, R., Steele, A., M., W. and Jones, N. (2009) 'Plain and notched fatigue in nickel single crystal alloys', *International Journal of Fatigue*, 31(11–12), pp. 1709–1718.

Fang, D. N. and Berkkovits, A. (1994) 'Mean stress models for low-cycle fatigue of a nickel-base superalloy', *International Journal of Fatigue*, 16(6), pp. 429–437.

Farahmand, B. (2001) 'Linear Elastic Fracture Mechanics (LEFM) and Applications', in *Fracture Mechanics of Metals, Composites, Welds, and Bolted Joints: Application of LEFM, EPFM, and FMDM Theory*. Boston, MA: Springer US, pp. 52–117.

Fedelich, B., A., E., Link, T., Klingelhöffer, H., Künecke, G. and Portella, P. (2012) 'Rafting during high temperature deformation in a single crystal superalloy: Experiments and modeling', in *Proceedings of the International Symposium on Superalloys*, pp. 491–500.

Feist, W. D., Mook, G., Taylor, S., Söderberg, H., Mikic, A. and Stepinski, T. (1994) 'Non-destructive evaluation of manufacturing anomalies in aero-engine rotor disks', in *16th World conference on non-destructive testing, Montreal*.

Fernandes, P., Roy, R., Mehnen, J. and Harrison, A. (2011) 'An Overview on Degradation Modelling for Service Cost Estimation', in Hesselbach, J. and Herrmann, C. (eds) *Functional Thinking for Value Creation: Proceedings of the 3rd CIRP International Conference on Industrial Product Service Systems*. Berlin, Heidelberg: Springer Berlin Heidelberg, pp. 309–314.

Filippini, M. (2011a) 'Creep-fatigue at high temperature of notched single crystal superalloys', *ASTM Special Technical Publication*, 8(6), pp. 348–374.

Filippini, M. (2011b) 'Notched fatigue strength of single crystals at high temperature', *Procedia Engineering*, 10, pp. 3787–3792.

Fischer-Cripps, A. C. (2011) 'Nanoindentation Testing', in Fischer-Cripps, A. C. (ed.) *Nanoindentation*. 3rd edn. New York: Springer-Verlag New York, pp. 21–37.

Fleury, R. M. N. and Nowell, D. (2017) 'Evaluating the influence of residual stresses and surface damage on fatigue life of nickel superalloys', *International Journal of Fatigue*,

105, pp. 27–33.

Ford, D., Fullagar, K., Bhangu, H., Thomas, M., Burkholder, P., Korinko, P., K., H. and Wahl, J. (1999) 'Improved performance rhenium containing single crystal alloy turbine blades utilising PPM levels of the highly reactive elements lanthanum and yttrium', *Journal of Engineering for Gas Turbines and Power*, 121(1), pp. 138–143.

Freedman, D. (2005) *Statistical models: Theory and practice*, *Cambridge University Press*.

French, P. M. W., Naeem, M., Sharp, M. and Wartkins, K. G. (2006) 'Investigation into the influence of pulse shaping on drilling efficiency', in *Icaleo 2006*, pp. 166–172.

French, P. W., Naeem, M., Sharp, M., Watkins, K. G. and Valley, S. (2006) 'Investigation into the influence of pulse shaping on drilling efficiency', *ICALEO 2006*. Laser Institute of America, Orlando, FL (United States), 310, pp. 1–7.

French, P. W., Naeem, M. and Watkins, K. G. (2003) 'Laser Percussion Drilling of Aerospace Material using a 10kW Peak Power Laser using a 400 μm Optical Fibre Delivery System', in *ICALEO 2003 - 22nd International Congress on Applications of Laser and Electro-Optics, Congress Proceedings*. Laser Institute of America, pp. 1–9.

Frost, J. (2013) 'Regression Analysis: How to Interpret S, the Standard Error of the Regression | Minitab', *Minitab*, pp. 1–17.

Fu, C. H., Liu, J. F., Guo, Y. B. and Zhao, Q. Z. (2016) 'A Comparative Study on White Layer Properties by Laser Cutting vs. Electrical Discharge Machining of Nitinol Shape Memory Alloy', *Procedia CIRP*, 42(Isem Xviii), pp. 246–251.

Fuchs, H. O., Stephens, R. I. and Saunders, H. H. (1981) 'Metal Fatigue in Engineering', *Journal of Engineering Materials and Technology*. ASME, 103(4), pp. 59–92.

Fullagar, K. P. L., Broomfield, R. W., Hulands, M., Harris, K., Erickson, G. L. and Sikkenga, S. L. (1996) 'Aero engine test experience with CMSX-4® alloy single-crystal turbine blades', *Journal of Engineering for Gas Turbines and Power*, 118(2), pp. 380–388.

Fullagar, K. P. L. and et Al. (1996) 'Aero-Engine tests experience with CMSX4 alloy SX turbine blades', *Trans of the ASME*, 118.

Gabb, T., Telesman, J., Hazel, B. and Mourer, D. (2010) 'The effects of hot corrosion pits on the fatigue resistance of a disk superalloy', *Journal of materials engineering and performance*. Springer, 19(1), pp. 77–89.

Gabriel, B. L. (1985) *SEM: A user's manual for materials science*. United States: American Society for Metals.

Gangloff, R. P. (2005) 'Environmental Cracking - Corrosion Fatigue', *Corrosion Tests and Standards: Application and Interpretation*, pp. 1–20.

Garofano, J., Marcus, H. and Aindow, M. (2009) 'Characterization of microstructural effects in a percussion laser-drilled powder metallurgy Ni-based superalloy', *Journal of Materials Science*, 44(2), pp. 680–684.

Garofano, J., Marcus, H. and Aindow, M. (2010) 'Extraction replication studies of near-surface microstructures in laser-drilled samples of the powder metallurgy Ni-based superalloy IN100', *Materials Characterization*. Elsevier Inc., 61(10), pp. 929–936.

Gayda, J. and Miner, R. V. (1983) 'Fatigue crack initiation and propagation in several nickel-base superalloys at 650°C', *International Journal of Fatigue*, 5(3), pp. 135–143.

Gell, M. and Leverent, G. R. (1973) 'Mechanisms of High-Temperature Fatigue', in *Fatigue at Elevated Temperatures*. ASTM STP 5. American Society for Testing ans Materials, pp. 37–67.

Gemma, A. E. and Phillips, J. S. (1977) 'The application of fracture mechanics to life prediction of cooling hole configurations in thermal-mechanical fatigue', *Engineering Fracture Mechanics*, 9(1), pp. 25–36.

Gibson, G. J., Perkins, K. M., Gray, S. and Leggett, A. J. (2016) 'Influence of shot peening on high-temperature corrosion and corrosion-fatigue of nickel based superalloy 720Li', *Materials at High Temperatures*, 33(3), pp. 225–233.

Gibson, G., Perkins, K., S., G. and Leggett, A. (2016) 'Influence of environmental factors on the corrosion-fatigue response of a nickel-based superalloy', *Materials Science and Technology*, 33(3), pp. 225–233.

Gibson, J., Schröders, S., C., Z. and Korte-Kerz, S. (2016) 'Towards nanoindentation at application-relevant temperatures – A study on CMSX-4 alloy and amdry-386 bond coat',

in ECI Symposium Series (ed.) *Beyond Nickel-Based Superalloys II*. South Africa: ECI Archives, pp. 1–19.

Giorgetti, A., Monti, C., Tognarelli, L. and Mastromatteo, F. (2017). 'Microstructural evolution of René N4 during high temperature creep and aging'. *Results in physics*, *7*, pp.1608-1615.

Goebel, J. A., Pettit, F. S. and Goward, G. W. (1973) 'Mechanisms for the hot corrosion of nickel-base alloys', *Metallurgical Transactions*, 4(1), pp. 261–278.

Goodhew, P. J., Humphreys, J. and Beanland, R. (2001) 'Electron Microscopy and Analysis', *Taylor and Francis*, 30, p. 132.

Goodman, J. (1899) 'Stress, Strain, and Elasticity', in *Mechanics Applied to Engineering*. 1st edn. London: Longmans, pp. 240–289.

Goyal, R. and Dubey, A. K. (2014) 'Quality improvement by parameter optimization in laser trepan drilling of superalloy sheet', *Materials and Manufacturing Processes*, 29 (11–12), pp. 1410–1416.

Grafton-Reed, C. (2008) 'Brief insight into Rolls-Royce laser manufacturing technologies', *Industrial opportunities in laser micro and nano processing - AILU Technology Workshop*. Cheshire, UK, pp. 1–9.

Grandt Jr, A. F. (2003) 'Introduction to Fatigue', in *Fundamentals of structural integrity: damage tolerant design and nondestructive evaluation*. John Wiley & Sons, pp. 6–16.

Griffith, A. A. (1920) 'The phenomenon of rupture and flow in solids', *Philosophical Transactions of the Royal Society*, 221(A221), pp. 163–198.

Guinard, C., Guipont, V., H.Proudhon, Jeandin, M., Girardot, J., Schneider, M., Berthe, L. and Martin, A. (2012) 'Study of delamination induced by laser-drilling of thermally-sprayed TBC interfaces', in *Thermal Spray 2012: Proceedings of the International Thermal Spray Conference (ASM International)*. ASM International, pp. 114–119.

Gunston, B. (2007) 'The Development of Jet and Turbine Aero Engines', *Aircraft Engineering and Aerospace Technology*. Emerald Group Publishing Limited, 79(1), p. 253.

Gunturi, S. S. K., MacLachlan, D. W. and Knowles, D. M. (2000) 'Anisotropic creep in

CMSX-4 in orientations distant from <001>', *Materials Science and Engineering A*, 289(1–2), pp. 289–298.

Guu, Y. H. and Hocheng, H. (2001) 'High cycle fatigue of electrical-discharge machined AISI D2 tool steel', *International Journal of Materials & Product Technology - INT J MATER PROD TECHNOL*, 16.

Hafner, B. (2007) 'Scanning Electron Microscopy Primer', *Cities*, pp 1-29.

Haight, H., Potter, A., Sumner, J. and Gray, S. (2015) 'New technique to map hot corrosion damage: CMSX-4 example', *Oxidation of Metals*, 84(5), pp. 607–619.

Harper, H. (2009) 'Detection of Defects and Assessment of Servicebility', in Rees D. Rawlings (ed.) *Materials and Science*. 3rd edn. Oxford: EOLSS/UNESCO, pp 1-47.

Harrison, G. F. and Winstone, M. R. (1996) 'Modelling and lifing of structural materials for future aeroengine components', *Advanced Performance Materials*. Springer, 3(3–4), pp. 263–278.

He, R., Gahlawat, S., Guo, C., Chen, S., Dahal, T., Zhang, H., Liu, W., Zhang, Q., Chere, E., White, K. and Ren, Z. (2015) 'Studies on mechanical properties of thermoelectric materials by nanoindentation', *physica status solidi (a)*, 212.

He, Y., Hou, X., Tao, C. and Han, F. (2011) 'Recrystallization and fatigue fracture of single crystal turbine blades', *Engineering Failure Analysis*, 18(3), pp. 944–949.

Herbert, C., Kwong, J., Kong, M., Axinte, D., Hardy, M. and Withers, P. (2012) 'An evaluation of the evolution of workpiece surface integrity in hole making operations for a nickel-based superalloy', *Journal of Materials Processing Technology*, 212(8), pp. 1723–1730.

Holdsworth, S. R. (1980) 'The significance of defects in nickel base superalloys', in *Superalloys 1980*. The Minerals, Metals and Materials Society, pp. 375–383.

Hong, H., Kang, J., Choi, B., Kim, I., Yoo, Y. and Jo, C. (2011) 'A comparative study on thermomechanical and low cycle fatigue failures of a single crystal nickel-based superalloy', *International Journal of Fatigue*, 33(12), pp. 1592–1599.

Horn, A., Weichenhain, R., Albrecht, S., Kreutz, E. W., Michel, J., Niessen, M.,

Kostrykin, V., Schulz, W., Etzkorn, A., Bobzin, K. and Lugscheider, E. (2000) 'Microholes in zirconia coated Ni-superalloys for transpiration cooling of turbine blades', *Proceedings of SPIE - The International Society for Optical Engineering*. SPIE, 4065, pp. 218–226.

Hou, J., Wicks, B. and Antoniou, R. (2002) 'An investigation of fatigue failures of turbine blades in a gas turbine engine by mechanical analysis', *Engineering Failure Analysis*, 9(2), pp. 201–211.

Hou, N., Gou, W., Wen, Z. and Yue, Z. (2008) 'The influence of crystal orientations on fatigue life of single crystal cooled turbine blade', *Materials Science and Engineering: A*. Elsevier, 492(1), pp. 413–418.

Ince, A. (2017) 'A generalized mean stress correction model based on distortional strain energy', *International Journal of Fatigue*, 104, pp. 273–282.

Ince, A. and Glinka, G. (2011) 'A modification of Morrow and Smith-Watson-Topper mean stress correction models', *Fatigue and Fracture of Engineering Materials and Structures*, 34(11), pp. 854–867.

Infante, V., Silva, J., de Freitas, M. and Reis, L. (2009) 'Failures analysis of compressor blades of aeroengines due to service', *Engineering Failure Analysis*, 16(4), pp. 1118–1125.

Irwin, G. R. (1948) 'Fracture Dynamics', *Fracturing of Metals*, (40A), pp. 147–166.

Irwin, G. R. (1960) 'Plastic zone near a crack and fracture toughness', in *Proceedings of the Seventh Sagamore Ordance Materials Conference, Vol. IV*. New York, pp. 63–78.

Jagtap, S. and Johnson, A. (2010) 'Requirements and use of in-service information in an engineering redesign task: Case studies from the aerospace industry', *Journal of the American Society for Information Science and Technology*, 61(12), pp. 2442–2460.

Jagtap, S. and Johnson, A. (2011) 'In-service information required by engineering designers', *Research in Engineering Design*, 22(4), pp. 207–221.

Jahangiri, M. R. and Fallah, A. A. (2011) 'Effects of welding defects on reducing lifetimes of first stage nozzles of a 123MW gas turbine made of FSX-414 alloy',

Materials and Design, 32(1), pp. 424–432.

Jianting, G., Ranucci, D., Picco, E. and Strocchi, P. (1984) 'Effect of environment on the low cycle fatigue behaviour of cast nickel-base superalloy IN738LC', *International Journal of Fatigue*, 6(2), pp. 95–99.

Jianwei, L. and Zhixun, W. (2015) 'Numerical Simulation on the Creep Damage Evolution of Nickel-Based Single Crystal Specimens with Slant-Angled Film Cooling Holes', *Rare Metal Materials and Engineering*, 44(11), pp. 2656–2660.

Johnson, J. and Pfledderer, M. (1989) 'Deep hole drilling with lasers', 62, pp. 53–63.

Kamalu, J., Byrd, P. and Pitman, A. (2002) 'Variable angle laser drilling of thermal barrier coated nimonic', *Journal of Materials Processing Technology*, 122(2–3), pp. 355–362.

Kang, J., Hong, H., Choi, B., Kim, I., Kang, N. and Jo, C. (2011) 'Deformation and failore behavior during thermo-mechanical fatigue of a nickel-based single crystal superalloy', *Journal of Korean Institute of Metals and Materials*, 49(2), pp. 112–120.

Kersey, R., A, S., Dudzinski, D. and Genest, M. (2013) 'Thermomechanical fatigue crack growth from laser drilled holes in single crystal nickel based superalloy', *International Journal of Fatigue*, 55, pp. 183–193.

Kianicová, M. and Pokluda, J. (2014) 'Fatigue fracture of turbine blades: Case studies', *Key Engineering Materials*, 592–593, pp. 712–715.

Kim, H. (2009) 'Study of the fracture of the last stage blade in an aircraft gas turbine', *Engineering Failure Analysis*, 16(7), pp. 2318–2324.

Kim, S., Hwang, Y., Kim, T. and Shu, C. (2008) 'Failure analysis of J85 Engine turbine blades', *Engineering Failure Analysis*, 15(4), pp. 394–400.

Klingelhöffer, H., Epishin, A. and Link, T. (2009) 'Low cycle fatigue of the single-crystal nickel-base superalloy CMSX-4-anistropy and effect of creep damage', *Materialpruefung/Materials Testing*, 51(5), pp. 291–294.

Koener, C., Mayerhofer, R., Hartmann, M. and Bergmann, H. W. (1996) 'Physical and

material aspects in using visible laser pulses of nanosecond duration for ablation', *Applied Physics A*, 63(2), pp. 123–131.

Kool, G., van den Elshout, J., Vogelaar, E., van Gestel, R. and Mom, A. (2008) 'EVITA study: Evaluation of unscheduled aircraft and industrial gas turbine part failure cases.', *ASME Turbo Expo 2008: Power for Land, Sea, and Air*, 1, pp. 487–494.

Koster, A., Alam, A. M. and Rémy, L. (2002) 'A physical-base model for life prediction of single crystal turbine blades under creep-fatigue loading and thermal transient conditions', *European Structural Integrity Society*, 29(C), pp. 203–212.

Kreutz, E. W., Trippe, L., Walther, K. and Poprawe, R. (2007) 'Process Development and Control of Laser Drilled and Shaped Holes in Turbine Components', *Journal of Laser Micro/Nanoengineering*, 2(2), pp. 123–127.

Kumar, S., Dubey, A. K. and Pandey, A. K. (2013) 'Computer-aided genetic algorithm based multi-objective optimization of laser trepan drilling', *International Journal of Precision Engineering and Manufacturing*, 14(7), pp. 1119–1125.

Kurz, R. (2005) 'Gas turbine performance', *Proceedings of the 34th Turbomachinery Symposium*, pp. 131–146.

Kurzydłowski, K. J., Lewandowska, M., Świ\keszkowski, W. and Lewandowska-Szumieł, M. (2007) 'Degradation of Engineering Materials--Implications to Regenerative Medicine', in *Macromolecular Symposia*, pp. 1–9.

Lee, B., Suh, J., Lee, H. and Kim, T. (2011) 'Investigations on fretting fatigue in aircraft engine compressor blade', *Engineering Failure Analysis*, 18(7), pp. 1900–1908.

Leigh, S., Sezer, K., Li, L., Grafton-Reed, C. and Cuttell, M. (2009) 'Statistical analysis of recast formation in laser drilled acute blind holes in CMSX-4 nickel superalloy', *International Journal of Advanced Manufacturing Technology*, 43(11–12), pp. 1094–1105.

Leigh, S., Sezer, K., Li, L., Grafton-Reed, C. and Cuttell, M. (2010) 'Recast and oxide formation in laser-drilled acute holes in CMSX-4 nickel single-crystal superalloy', *Proceedings of the Institution of Mechanical Engineers, Part B: Journal of Engineering Manufacture*, 224(7), pp. 1005–1016.

Levine, D. M., Szabat, K. A. and Stephan, D. (2008) *Statistics for Managers Using Microsoft Excel*. 5th edn. Prentice Hall.

Leyens, C., Wright, I. G. and Pint, B. A. (2001) 'Hot corrosion of nickel-base alloys by alkali-containing sulfate deposits', *Materials Science Forum*, 369–372(II), pp. 571–578. doi: 10.4028/www.scientific.net/MSF.369-372.571.

Li, L., Ao, L., Xie, G., Wang, X. and Cao, G. (2013) 'Influences of holes arrangement on creep characteristic of nickel-base single crystal alloy blade cooling holes', *Advances in Materials Science and Engineering*, 2013.

Liang, J. ., Ai, X. ., Wen, Z. . and Yue, Z. . (2016) 'Experimental investigation on low cycle fatigue of DZ125 with film cooling holes in different processes of laser drilling', *Engineering Failure Analysis*, 59, pp. 326–333.

Liang, J., Ai, X., Wen, Z. and Yue, Z. (2016) 'Experimental investigation on low cycle fatigue of DZ125 with film cooling holes in different processes of laser drilling', *Engineering Failure Analysis*, 59, pp. 326–333.

Liu, A. (2005) 'Mechanics and Mechanisms of Fracture : An Introduction', in *ASM International*. ASM International, pp. 59–83.

Liu, C., Zhang, B., Yang, S., He, Y. and Tao, C. (2011) 'Analysis of fracture and cracks of single crystal blades in aero-engine', *Engineering Failure Analysis*, 18(2), pp. 582–589.

Liu, Y. and Mahadevan, S. (2005) 'Multiaxial high-cycle fatigue criterion and life prediction for metals', *International Journal of Fatigue*, 27(7), pp. 790–800.

Lortrakul, P., Trice, R., Trumble, K. and Dayananda, M. (2014) 'Investigation of the mechanisms of Type-II hot corrosion of superalloy CMSX-4', *Corrosion Science*, 80, pp. 408–415.

Low, D. K. Y., Li, L. and Byrd, P. J. (2000) 'The effects of process parameters on spatter deposition in laser percussion drilling', *Optics & Laser Technology*, 32(5), pp. 347–354.

Low, D. K. Y., Li, L. and Byrd, P. J. (2001) 'The influence of temporal pulse train modulation during laser percussion drilling', *Optics and Lasers in Engineering*, 35(3),

pp. 149–164.

Low, D. K. Y., Li, L. and Byrd, P. J. (2003) 'Spatter prevention during the laser drilling of selected aerospace materials', *Journal of Materials Processing Technology*, 139(1–3 SPEC), pp. 71–76.

Low, D. K. Y., Li, L. and Corfe, A. G. (2000) 'Effects of assist gas on the physical characteristics of spatter during laser percussion drilling of NIMONIC 263 alloy', *APPLIED SURFACE SCIENCE*, 154, pp. 689–695.

Low, D. K. Y., Li, L. and Corfe, A. G. (2000) 'The influence of assist gas on the mechanism of material ejection and removal during laser percussion drilling', *Proceedings of the Institution of Mechanical Engineers, Part B: Journal of Engineering Manufacture*, 214(7), pp. 521–527.

Low, D. K. Y., Li, N. and Byrd, P. J. (2001) 'Spatter removal characteristics and spatter prevention during laser percussion drilling of aerospace alloys', *Journal of Laser Applications*, 13(2), pp. 70–78.

Lowden, P., Turcott, S., Perrin, M. and Hastie, S. (2009) 'The role of metallurgical analysis in gas turbine maintenance', in *Proceedings from the 18th Symposium of the Industrial Application of Gas Turbines Committee (2009-IAGT-303)*. Alberta, Canada: IAGT, pp. 1–15.

Lugscheider, E., Bobzin, K., Maes, M., Lackner, K., Poprawe, R., Kreutz, E. and Willach, J. (2005) 'Laser drilled microholes in zirconia coated surfaces using two variants to implement the effusion cooling of first stage turbine blades', *Advanced Engineering Materials*, 7(3), pp. 145–152.

Luxon, T. J. and Parker, D. E. (1985) *Interaction of High-Power Laser Beams with Materials: Industrial Lasers and Their Applications*. New Jersey: Prentice Hall.

Lv, F., Fu, G., Cai, Z. and Zhang, D. (2009) 'Failure analysis of components in compressor vane', *Engineering Failure Analysis*, 16(5), pp. 1703–1710.

M. Ruselowski, J. (1987) 'Laser Selection For Drilling', pp. 106–123.

MacLachlan, D. W. and Knowles, D. M. (2000) 'Creep-behavior modeling of the single-crystal superalloy CMSX-4', *Metallurgical and Materials Transactions A: Physical*

Metallurgy and Materials Science, 31(5), pp. 1401–1411.

MacLachlan, D. W., Wright, L. W., Gunturi, S. and Knowles, D. M. (2001) 'Constitutive modelling of anisotropic creep deformation in single crystal blade alloys SRR99 and CMSX-4', *International Journal of Plasticity*, 17(4), pp. 441–467.

Mahobia, G., Paulose, N., Mannan, S., Sudhakar, R., Chattopadhyay, K., Santhi Srinivas, N. and Singh, V. (2014) 'Effect of hot corrosion on low cycle fatigue behavior of superalloy IN718', *International Journal of Fatigue*, 59, pp. 272–281.

Manson, S. S. (1954) *Behavior of materials under conditions of thermal stress, NACA Report 1170*. article. Cleveland.

Marchionni, M. (2002a) 'Low cycle and thermomechanical fatigue of nickel base superalloys for gas turbine application', *European Structural Integrity Society*, 29(C), pp. 177–184.

Marchionni, M. (2002b) 'Low cycle and thermomechanical fatigue of nickel base superalloys for gas turbine application', *European Structural Integrity Society*, 29(C), pp. 425–431.

Marchionni, M., Goldschmidt, D. and Maldini, M. (1993) 'Evaluation of high-temperature behavior of CMSX4 + yttrium single- crystal nickel- base superalloy', *Journal of Materials Engineering and Performance*, 2(4), pp. 497–503.

Marimuthu, S., Antar, M. and Chantzis, D. (2015) 'High Speed Quasi-CW Fibre Laser Drilling of Aerospace Alloys', in *Proceedings of Lasers in Manufacturing*, pp. 1111–1121.

Mason, R. L., Gunst, R. F. and Hess, J. L. (2003) 'Designs and analyses for fitting response surfaces', in *Statistical Design and Analysis of Experiments*, pp. 568–613.

Masood, T., Roy, R., Harrison, A., Xu, Y., Gregson, S. and Reeve, C. (2015) 'Integrating through-life engineering service knowledge with product design and manufacture', *International Journal of Computer Integrated Manufacturing*, 28(1), pp. 59–74.

Matsumoto, K., Koizumi, Y., Kawagishi, K. and Harada, H. (2011) 'Development of NIMS burner rig and cyclic testing of nickel base superalloys', *Canadian Metallurgical Quarterly*, 50(3), pp. 311–315.

McDonald J, Ma S, Nees J, Pollock T, Y. S. (2006) 'Dynamics of ultrafast laser induced damage in single crystal Ni-based superalloy during machining', in *Symposium II – Advanced Intermetallic-Based Alloys*. (MRS Online Proceedings Library Archive), p. 0980–II05–31 (6 pages).

McEvily, A. J., Endo, M., Yamashita, K., Ishihara, S. and Matsunaga, H. (2008) 'Fatigue notch sensitivity and the notch size effect', *International Journal of Fatigue*, 30(12), pp. 2087–2093.

McFarlane, D. and Cuthbert, R. (2012) 'Modelling information requirements in complex engineering services', *Computers in Industry*, 63(4), pp. 349–360.

McNally, C. A., Folkes, J. and Pashby, I. R. (2004) 'Laser drilling of cooling holes in aeroengines: state of the art and future challenges', *Materials Science and Technology*. Maney Publishing, 20(7), pp. 805–813.

Meher-homji, B., Chaker, M. and Motiwala, H. M. (2001) 'Gas Turbine Performance Deterioration', *30th Turbomachinery Symposium, Texas A&M University, Texas*, pp. 139–176.

Meher-Homji, C. B. and Gabriles, G. (1998) 'Gas turbine blade failures -causes, avoidance, and troubleshooting', in *27th Turbomachinery Symposium, Houston, TX, Sept*, pp. 129–179.

Meijer, J. (2004) 'Laser beam machining (LBM), state of the art and new opportunities', *Journal of Materials Processing Technology*, 149(1–3), pp. 2–17.

Milella, P. P. (2013) *Fatigue and corrosion in metals*. Springer Milan, pp 767-806.

Mishra, R., Johney, T., Srinivasan, K., Vaishakhi, N. and Raghavendra, B. (2014) 'Investigation of LP turbine blade failure in a low bypass turbofan engine', *Journal of Failure Analysis and Prevention*, 14(2), pp. 160–166.

Mishra, R. K., Ahmed, S. I. and Srinivasan, K. (2013) 'Investigation of a bird strike incident of a military gas turbine engine', *Journal of Failure Analysis and Prevention*, 13(6), pp. 666–672.

Mishra, R., Thomas, J., Srinivasan, K. and Ahmed, S. (2014) 'Fatigue failure of LP compressor blade in an aero gas turbine engine', *Journal of Failure Analysis and Prevention*, 14(3), pp. 296–302.

Mishra, S. and Yadava, V. (2013a) 'Modeling and optimization of laser beam percussion drilling of nickel-based superalloy sheet using Nd: YAG laser', *Optics and Lasers in Engineering*, 51(6), pp. 681–695.

Mishra, S. and Yadava, V. (2013b) 'Modelling of hole taper and heat affected zone due to laser beam percussion drilling', *Machining Science and Technology*, 17(2), pp. 270–291.

Mogul, J. (1978) 'Metallographic Characterization of Fatigue Failure Origin Areas', in McCall, J. L. and French, P. M. (eds) *Metallography in Failure Analysis*. Boston, MA: Springer US, pp. 97–120.

Montgomery, D. C. Peck, E. A, Vining, G. G. (2012) *Introduction to linear regression analysis*. 5eds, Wiley, pp 12-108.

Mook, G., Feist, W. D., Hinken, J. H. and Perrin, G. (2006) 'Detection and Characterization of Magnetic Anomalies in Gas Turbine Disks', in *Proc. 9th Europ. Conf. On NTD, ECNDT*, pp. 25–29.

Morar, N. I., Roy, R., Mehnen, J., Marithumu, S., Gray, S., Roberts, T. and Nicholls, J. (2018) 'Investigation of recast and crack formation in laser trepanning drilling of CMSX-4 angled holes', *The International Journal of Advanced Manufacturing Technology*, pp. 1–12.

Morar, N. I., Roy, R., Mehnen, J., Redding, L. E. and Harrison, A. (2013) 'Data mining and knowledge reuse for the initial systems design and manufacturing: Aero-engine service risk drivers', in *Procedia CIRP*, pp. 130–134.

Mori, T. and Tanaka, K. (1973) 'Average stress in matrix and average elastic energy of materials with misfitting inclusions', *Acta Metallurgica*, 21(5), pp. 571–574.

Morrow, J. (1968) 'Fatigue Design Handbook', in *Advances in Engineering*. Warrendale, PA: SAE, pp. 21–29.

Motarjemi, A. and Shirzadi, A. (2006) *Structural Integrity Assessment of Engineering*

Components, *Cambridge University*. Available at: http://www.phase-trans.msm.cam.ac.uk/2006/SI/SI.html (accessed 21 June 2015).

Mottura, A. and Reed, R. C. (2014) 'What is the role of rhenium in single crystal superalloys?', in *MATEC Web of Conferences*, p. 1001.

Moverare, J. J. (2007) 'Thermal-mechanical fatigue behaviour of CMSX-4 in virgin and long term aged conditions', *Materials Science and Technology*, 23(12), pp. 1450–1453.

Moverare, J., Johansson, S. and Reed, R. C. (2009) 'Deformation and damage mechanisms during thermal–mechanical fatigue of a single-crystal superalloy', *Acta Materialia*, 57(7), pp. 2266–2276.

Mukai Y, Kagawa H, O. M. (2015) 'Thermo-mechanical and low cycle fatigue behavior of ni-base single crystal superalloy CMSX-4', in *ICOPE 2015 - International Conference on Power Engineering*.

Mustafa, A. H., Badairy, H. H. and Mehta, S. (2009) 'Gas turbine aero-engine first stage turbine blade failure investigation', *Journal of Engineering for Gas Turbines and Power*, 131(5).

N.E.R (2011) *Fracture toughness*, *NDT Education Resource Center*. Available at: https://www.nde-ed.org/EducationResources/CommunityCollege/Materials/Mechanical/FractureToughness.htm (Accessed: 8 October 2015).

Naeem, M. (2008) 'Advancement in laser drilling for aerospace gas turbines', in *3rd Pacific International Conference on Applications of Lasers and Optics, PICALO 2008 - Conference Proceedings*. Laser Institute of America, pp. 197–202.

Nandi, V., Bhat, R., Yatisha, I. and Suresh, S. (2012) 'Liquid-metal-induced embrittlement in turbine casing segment screws of an aeroengine', *Journal of Failure Analysis and Prevention*, 12(4), pp. 348–353.

Nanocrystalline Materials: Fatigue Part 1 (Nanotechnology) (2016). Available at:

http://what-when-how.com/nanoscience-and-nanotechnology/nanocrystalline-materials-fatigue-part-1-nanotechnology/ (Accessed: 9 June 2016).

Neidel, A., Riesenbeck, S., Ullrich, T., Völker, J. and Yao, C. (2005) 'Hot cracking in the HAZ of laser-drilled turbine blades made from René 80', *Materials Testing*. Carl Hanser Verlag, 47(10), pp. 553–559.

Neubauer, J. C. (1990) 'Why birds kill: Cross-sectional analysis of US Air Force bird strike data.', *Aviation, space, and environmental medicine*, 61(4), pp. 343–348.

Neuber, H. (1961) 'Theory of stress concentration for shear-strained prismatical bodies with arbitrary nonlinear stress-strain law', *Journal of Applied Mechanics*, 28(4), p. 544+.

Ng, G. K. L., Crouse, P. L. and Li, L. (2006) 'An analytical model for laser drilling incorporating effects of exothermic reaction, pulse width and hole geometry', *International Journal of Heat and Mass Transfer*, 49(7–8), pp. 1358–1374.

Nicholls, J. R. and Simms, N. J. (2010) 'Gas Turbine Oxidation and Corrosion', in Cottis, B., Graham, M., Lindsay, R., Lyon, S., Richardson, T., Scantlebury, D., and Stott, H. (eds) *Shreir's Corrosion*. Oxford: Elsevier, pp. 518–540.

Nicholls, J. R., Simms, N. J. and Encinas-Oropesa, A. (2007) 'Modelling hot corrosion in industrial gas turbines', *Materials at High Temperatures*, 24(3), pp. 149–162.

Nissley, D. M. (1997) 'Thermal barrier coating life modeling in aircraft gas turbine engines', *Journal of Thermal Spray Technology*, 6(1), pp. 91-98.

Nowakowski, K. A. (2005) *Laser beam interaction with materials for microscale applications*. PhD Dissertatoin, Worcester Polytechnic Institute, Massachusetts.

Nowell, D., Dini, D. and Duó, P. (2003) 'Stress analysis of V-notches with and without cracks, with application to foreign object damage', *The Journal of Strain Analysis for Engineering Design*. SAGE Publications, 38(5), pp. 429–441.

NTSB (1989) *United Airlines Flight 232 McDonnell Douglas DC-10-10*, *National Transport Safety Bureau*. Available at: https://www.ntsb.gov/investigations/accidentreports/pages/AAR9006.aspx (Accessed: 12 October 2015).

NTSB (1996) *Uncontained Engine Failure Delta Air Lines Flight 1288 McDonnell*

Douglas MD-88, N927DA, *National Transport Safety Bureau*. Available at: https://www.ntsb.gov/news/events/Pages/Delta_Air_Lines_Flight_1288_McDonnell_Douglas_MD-88_N927DA_Pensacola_Florida_July_6_1996.aspx (Accessed: 12 October 2015).

Okazaki, M., Imai, T. and Nohmi, S.-I. (1992) 'Naturally Initiated Fatigue Small Crack Growth in a Single Crystal Ni-Base Superalloy at Elevated Temperature.', in Rie, K.-T., Grünling, H. W., König, G., Neumann, P., Nowack, H., Schwalbe, K.-H., and Seeger, T. (eds) *Low Cycle Fatigue and Elasto-Plastic Behaviour of Materials---3*. Dordrecht: Springer Netherlands, pp. 539–544.

Okazaki, M. and Sakaguchi, M. (2008) 'Thermo-mechanical fatigue failure of a single crystal Ni-based superalloy', *International Journal of Fatigue*, 30(2), pp. 318–323.

Okho, C. Roy, R., Mehnen, J. and Harrison, A. (2014) 'Development of an Ontology for Aerospace Engine Components Degradation in Service', in *Proceedings of the International Conference on Knowledge Engineering and Ontology Development*. Rome, pp. 108–119.

Oliver, W. C. and Pharr, G. M. (2004) 'Measurement of hardness and elastic modulus by instrumented indentation: Advances in understanding and refinements to methodology', *Journal of Materials Research*, 19(1), pp. 3–20.

Oliver, W. and Pharr, G. (1992) 'An improved technique for determining hardness and elastic modulus using load and displacement-sensing indentation systems', *Journal of Materials Research*, 7(6), pp. 1564–1583.

Orosz, R., Krupp, U., Christ, H.-J. and Monceau, D. (2007) 'The influence of specimen thickness on the high temperature corrosion behavior of CMSX-4 during thermal-cycling exposure', *Oxidation of Metals*, 68(3–4), pp. 165–176.

Orowan, E. (1949) 'Fracture and strength of solids', *Reports on Progress in Physics*, 12(1), p. 185.

Ott, M. and Mughrabi, H. (1999) 'Dependence of the high-temperature low-cycle fatigue behaviour of the monocrystalline nickel-base superalloys CMSX-4 and CMSX-6 on the γ/γ′-morphology', *Materials Science and Engineering A*, 272(1), pp. 24–30.

Pahlavanyali, S., Pang, H., Li, F., Bagnall, S. and Rae, C. (2014) 'On effect of salt

deposits on oxidation behaviour of CMSX-4 above 1000°C', *Materials Science and Technology (United Kingdom)*, 30(15), pp. 1890–1898.

Palumbo, B., De Chiara, G. and Marrone, R. (2009) 'Technological Process Innovation via Engineering and Statistical Knowledge Integration', in Erto, P. (ed.) *Statistics for Innovation: Statistical Design of Continuous Product Innovation*. Milano: Springer Milan, pp. 177–190.

Pan, Y., Bischoff-Beiermann, B. and Schulenberg, T. (1999) 'Material testing for fatigue design of heavy-duty gas turbine blading with film cooling', in Marquis, G. and Solin, J. B. T.-E. S. I. S. (eds) *Fatigue Design and Reliability*. Elsevier, pp. 155–162.

Pandey, N. D., Shan, H. S. and Mohandas, T. (2005) 'Quality of percussion laser drilled holes for cooling of turbine components', *High Temperature Material Processes (An International Quarterly of High-Technology Plasma Processes)*. Begel House Inc., 9(4), pp. 625–653.

Pandey, N. D., Shan, H. S. and Mohandas, T. (2006) 'Percussion laser-drilled holes: characteristics and characterization procedure', *Materials and Manufacturing Processes*, 21(4), pp. 383–391.

Paris, P. C. and Erdogan, F. (1963) 'A critical analysis of crack propagation laws', *Journal of Basic Engineering*, 85(4), pp. 528–534.

Park, M., Hwang, Y., Choi, Y. and Kim, T. (2002) 'Analysis of a J69-T-25 engine turbine blade fracture', *Engineering Failure Analysis*, 9(5), pp. 593–601.

Patel, R. S. and Brewster, M. Q. (1991) 'Gas-Assisted Laser-Metal Drilling: Theoretical Model', *JOURNAL OF THERMOPHYSICS AND HEAT TRANSFER*, 5(1), pp. 32–39.

Patil, A. A. and Shirsat, U. M. (2012) 'Study of Failure Analysis of Gas Turbine Blade', *IOSR Journal of Engineering*. National Symposium on engineering and Research, pp. 37–43.

Petronić, S., Milosavljević, A., Z., R., Drobnjak, P. and Grujić, I. (2010) 'Analysis of geometrical characteristics of pulsed ND:YAG laser drilled holes in superalloy Nimonic 263 sheets', *Tehnički vjesnik*. Strojarski fakultet u Slavonskom Brodu, Elektrotehnički fakultet u Osijeku, Građevinski fakultet u Osijeku, 17(1), pp. 61–66.

Pettit, F. (2011) ‘Hot corrosion of metals and alloys’, *Oxidation of Metals*, 76(1/2), pp. 1–21.

Pettit, F. S., Meier, G. H., Gell, M., Kartovich, C. S., Bricknel, R. H., Kent, W. B. and Radovich, J. F. (1984) ‘Oxidation and hot corrosion of superalloys’, in *Superalloys 1984*. The Metal Society AIME, Warrendale, PA, pp. 651–687.

Pieraggi, B. (1987) ‘Effect of creep or low cycle fatigue on the oxidation or hot corrosion behaviour of nickel-base superalloys’, *Materials Science and Engineering*, 88(C), pp. 199–204.

Qining, S., Zheng, Y., Ni, D. R. and Ma, Z. Y. (2015) ‘Characterization of the Corrosion Product Films Formed on the As-Cast and Friction-Stir Processed Ni-Al Bronze in a 3.5 wt% NaCl Solution’, *Corrosion*, 71, pp. 606–614.

Qylafku, G., Azari, Z., Kadi, N., Gjonaj, M. and Pluvinage, G. (1999) ‘Application of a new model proposal for fatigue life prediction on notches and key-seats’, *International Journal of Fatigue*, 21(8), pp. 753–760.

Rahmani, K. and Nategh, S. (2010) ‘Mechanical properties of uncoated and aluminide-coated rené 80’, *Metallurgical and Materials Transactions A: Physical Metallurgy and Materials Science*, 41(1), pp. 125–137.

Ramesh, N. I. (2009) ‘The role of Minitab in teaching and learning statistics’, *International Education Journal*, 5(3), pp. 275–293.

Ransom, J. B., Glaessgen, E. H. and Ratcliffe, J. G. (2013) ‘An Overview of Durability and Damage Tolerance Methodology at NASA Langley Research Center’, in *Advances in Interdisciplinary Mathematical Research*. Springer, pp. 1–34.

Rao, V., Kumar, I. and Prasad, K. (2014) ‘Failure modes/mechanisms in turbine blades of a gas turbine Engine - an overview’, *International Journal of Engineering Research and Development*. www.ijerd.com, 10(8), pp. 48–57.

Ready, J. F., Farson, D. F. and Feeley, T. (2001) *LIA Handbook of Laser Materials Processing*. 1st edn. Orlando, FL, USA: Laser Institute of America.

Redding, L., Tiwari, A., Roy, R., Phillips, P. and Shaw, A. (2015) ‘The adoption and use

of through-life engineering services within UK manufacturing organisations', *Proceedings of the Institution of Mechanical Engineers, Part B: Journal of Engineering Manufacture*, 229(10), pp. 1848–1866.

Reed, R. C. (2006) 'Superalloys for turbine disc applications', in *The Superalloys: Fundamentals and Applications*. Cambridge: Cambridge University Press, pp. 217–282.

Reed, R. C. (2006) 'The physical metallurgy of nickel and its alloys', in *The Superalloys: Fundamentals and Applications*. Cambridge: Cambridge University Press, pp. 33–120.

Reed, R. C., Matan, N., Cox, D., Rist, M. and Rae, C. (1999) 'Creep of CMSX-4 superalloy single crystals: effects of rafting at high temperature', *Acta Materialia*, 47(12), pp. 3367–3381.

Reed, R. C. and Miller, M. D. (2008) 'Comparison of low cycle (notch) fatigue behaviour at temperature in single crystal turbine blade materials', in *Proceedings of the International Symposium on Superalloys*, pp. 527–533.

Rockstroh, T. J., Chen, X. and Lotshaw, W. T. (1996) 'Influence of laser pulse duration on laser drilled hole quality in nickel based super alloy', in *Proceedings of the laser materials processing conference - ICALEO `96*. Laser Institute of America, Orlando, FL (United States), pp. 113–122.

Rockstroh X (1996) 'Laser drilling of advanced materials: Effects of peak power, pulse format, and wavelength', *Journal of Laser Applications*, 8(5), pp. 233–239.

Rolls-Royce (2005) *The Jet Engine*. 5th edn. London: Wiley.

Rolls-Royce (2016) *About Rolls-Royce*. Available at: https://www.rolls-royce.com/about.aspx (Accessed: 16 August 2015).

Rosier, H., Perkins, K., Girling, A., Leggett, J. and Gibson, G. (2014) 'Factors affecting the corrosion fatigue life in nickel based superalloys for disc applications', in *MATEC Web of Conferences*, p. 3001.

Ross, P. J. (1998) 'Loss Fuction, Orthogonal Experiments, Parameter and Tolerance Design', in *Taguchi Techniques for Quality Engineering*. McGraw Hill, pp. 276–279.

Roy, R. K. (1990) *A Primer on the Taguchi method*. 2nd edn. New York: Van Nostrand Reinhold.

Roy, R. K. (2010) *A Primer on the Taguchi Method, Second Edition*. Society of Manufacturing Engineers.

Roy, R., Shaw, A., Erkoyuncu, J. A. and Redding, L. (2013) 'Through-life engineering services', *Measurement and Control (United Kingdom)*, 46(6), pp. 172–175.

Ruf, A., Breitling, D., Berger, P., Dausnger, F. and Hugel, H. (2003) 'Modeling and investigation of melt ejection dynamics for laser drilling with short pulses', *Proc. SPIE*, 4830, pp. 73–78.

Russo, M. (1978) 'Analysis of Fractures Utilizing the SEM', in McCall, J. L. and French, P. M. (eds) *Metallography in Failure Analysis*. Boston, MA: Springer US, pp. 65–95.

Sahu, J. K., Ravi Kumar, B., Das, S. K., Paulose, N. and Mannan, S. L. (2015) 'Isothermal high temperature low cycle fatigue behavior of Nimonic-263: Influence of type I and type II hot corrosion', *Materials Science and Engineering A*, 622, pp. 131–138.

Salam, I., Tauqir, A. and Khan, A. Q. (2002) 'Creep-fatigue failure of an aero engine turbine blades', *Engineering Failure Analysis*, 9(3), pp. 335–347.

Sanya, I. O. and Shehab, E. M. (2014) 'A framework for developing engineering design ontologies within the aerospace industry', *International Journal of Production Research*, 53(July), pp. 1–27.

Sato, M., Kobayashi, Y., Matsuzak, H., Tamaki, H., Yoshinari, A., Iijima, K., Fukui, Y., Kodama, H. and Wada, K. (1995) 'High temperature strength of large size SC and DS buckets for industrial gas turbines', in *Proceedings of the ASME Turbo Expo*.

Schneider, M. (2007) 'New experimental approach to study laser matter interaction during drilling in percussion regime', *Journal of Laser Micro/Nanoengineering*, 2(2), pp. 117–122.

Schneider, M., Berthe, L., Muller, M. and Fabbro, R. (2010) 'A fast method for morphological analysis of laser drilling holes', *Journal of Laser Applications*. Laser Institute of America, 22(4), pp. 127–131.

Scholz, A., Schmidt, A., Walther, H., Schein, M. and Schwienheer, M. (2008) 'Experiences in the determination of TMF, LCF and creep life of CMSX-4 in four-point

bending experiments', *International Journal of Fatigue*, 30(2), pp. 357–362.

Scholz, A., Wang, Y., Linn, S., Berger, C. and Znajda, R. (2009) 'Modeling of mechanical properties of alloy CMSX-4', *Materials Science and Engineering A*, 510–511(C), pp. 278–283.

Schulz, W. and Eppelt, U. (2009) 'Basic Concepts of Laser Drilling', in Dowden, J. (ed.) *The Theory of Laser Materials Processing: Heat and Mass Transfer in Modern Technology*. Dordrecht: Springer Netherlands, pp. 129–165.

Scutti, J.J. and McBrine, W.J., (2002). Introduction to failure analysis and prevention. *Materials Park, OH: ASM International, 2002.*, pp.3-23.

Seerangan, M., Walunj, J. and Kumar, S. K. (2012) 'Review of the state of art in the life evaluation technologies of gas turbine parts', in *ASME 2012 Gas Turbine India Conference, GTINDIA 2012*, pp. 649–656.

Sengupta, A., Putatunda, S., Bartosiewicz, L., Hangas, J., Nailos, P., Peputapeck, M. and Alberts, F. (1994) 'Tensile behavior of a new single-crystal nickel-based superalloy (CMSX-4) at room and elevated temperatures', *Journal of materials engineering and performance*. Springer, 3(1), pp. 73–81.

Seo, D. Y., Yandt, S. and Kim, D. S. (2013) 'Microstructural changes and thermomechanical fatigue behaviour of CMSX-4 under in-phase (IP) condition in the temperature range of 500-1100°C', in *Materials Science and Technology Conference and Exhibition 2013, MS and T 2013*, pp. 82–93.

Sezer, H. K., Li, L. and Leigh, S. (2009) 'Twin gas jet-assisted laser drilling through thermal barrier-coated nickel alloy substrates', *International Journal of Machine Tools and Manufacture*, 49(14), pp. 1126–1135.

Sezer, H., Li, L., Schmidt, M., Pinkerton, A., Anderson, B. and Williams, P. (2006) 'Effect of beam angle on HAZ, recast and oxide layer characteristics in laser drilling of TBC nickel superalloys', *International Journal of Machine Tools and Manufacture*, 46(15), pp. 1972–1982.

Sezer, H., Pinkerton, A., Li, L. and Byrd, P. (2005) 'An investigation into delamination

mechanisms in inclined laser drilling of thermal barrier coated aerospace superalloys', *Journal of Laser Applications*, 17(4), p. 225.

Shen, F., Zhao, B., Li, L., Chua, C. K. and Zhou, K. (2017) 'Fatigue damage evolution and lifetime prediction of welded joints with the consideration of residual stresses and porosity', *International Journal of Fatigue*, 103, pp. 272–279.

Shipley, R. and Becker, W. (2002) *ASM Handbook, Volume 11: Vol. 11: Failure Analysis and Prevention*, *ASM Handbook*. America: ASM Handbook Committee.

Shongwe, M. B., Witcomb, M. J., Cornish, L. A. and Papo, M. J. (2012) 'TEM studies of Pt-Al-Cr-Ru Alloys', *Journal of the Southern African Institute of Mining and Metallurgy*. scieloza, 112, pp. 551–558.

Shuja, S. Z., Yilbas, B. S. and Shazli, S. Z. (2007) 'Laser repetitive pulse heating influence of pulse duty on temperature rise', *Heat and Mass Transfer/Waerme- und Stoffuebertragung*, 43(9), pp. 949–955.

Sidhu, T. S., Prakash, S. and Agrawal, R. D. (2006) 'Hot corrosion and performance of nickel-based coatings', *Current Science*, 90(1), pp. 41–47.

Silveira, E., Atxaga, G., Erauzkin, E. and Irisarri, A. (2009) 'Study on the root causes for the premature failure of an aircraft turbine blade', *Engineering Failure Analysis*, 16(2), pp. 639–647.

Silveira, E., Atxaga, G. and Irisarri, A. M. (2008) 'Failure analysis of a set of compressor blades', *Engineering Failure Analysis*, 15(6), pp. 666–674.

Simms, N. J., Encinas-Oropesa, A. and Nicholls, J. R. (2008) 'Hot corrosion of coated and uncoated single crystal gas turbine materials', *Materials and Corrosion*, 59(6), pp. 476–483.

Simms, N. J., Smith, P. J., Encinas-Oropesa, A., Ryder, S., R., N. J. and Oakey, J. E. (2001) 'Development of Type II Hot Corrosion in Solid Fuel Fired Gas Turbines', in *Lifetime Modelling of High Temperature Corrosion Processes: (EFC 34)*. Maney Publishing, pp. 246–260.

Sklenicka, V. (1996) 'Development of intergranular damage under high temperature

loading conditions mechanical behaviour of materials at high temperature', in C. Moura Branco (ed.) *Mechanical Behaviour of Materials at High Temperature*. NATO ASI s. The Netherlands: Kluwer Academic Publishing, pp. 43–58.

Smith, D. J. (2013) 'Power-by-the-hour: the role of technology in reshaping business strategy at Rolls-Royce', *Technology analysis & strategic management*. Taylor & Francis, 25(8), pp. 987–1007.

Smith, K. N., Watson, P. and Topper, T. H. (1970) 'A stress-strain function for the fatigue of metals', *Journal of Materials*, 4, pp. 767–778.

Soares, C. (2015) 'Gas Turbines: An Introduction and Applications', in *Gas Turbines*. Elsevier, pp. 1–31.

Soderberg, C. R. (1939) 'Factor of safety and working stress', *Transactions of ASME*, 59, pp. 12–28.

Song, K., Kim, S., Jung, D. and Hwang, Y. (2007) 'Analysis of the fracture of a turbine blade on a turbojet engine', *Engineering Failure Analysis*, 14(5), pp. 877–883.

Steen, W. M. and J., M. (2010) *Laser Material Processing*, *Springer-Verlag London Limited*.

Stekovic, S. (2005) 'Low cycle fatigue of single crystal nickel-base superalloy cmsx-4 coated with a new coating IC1', in *American Society of Mechanical Engineers, Materials Division (Publication) MD*, pp. 235–241.

Strangman, T. E. (1992) 'Thermo-Mechanical Fatigue Life Model for Coated Superalloy Turbine Components', *Superalloys 1992*, pp. 795–804.

Stromeyer, C. E. (1914) 'The determination of fatigue limits under alternating stress conditions', *Proceedings of the Royal Society of London. Series A, Containing Papers of a Mathematical and Physical Character*. JSTOR, 90(620), pp. 411–425.

Sugianto, A., Wardhana, R. J., Yulian, N., Wardana, I. J., Karokaro, M. and Purwaningsih, H. (2014) *Failure analysis of a first stage high pressure turbine blade in an aero engine turbine on PK-GSG boeing B747-400*.

Sumner, J., Encinas-Oropesa, A., Simms, N. and Nicholls, J. R. (2013) 'Type II hot

corrosion: Kinetics studies of CMSX-4', *Oxidation of Metals*, 80(5–6), pp. 553–563.

Sumner, J., Encinas-Oropesa, A., Simms, N. and Nicholls, J. R. (2014) 'Type II hot corrosion: Behavior of CMSX-4 and IN738LC as a function of corrosion environment', *Materials and Corrosion*, 65(2), pp. 188–196.

Sun, E., Heffernan, T. and Helmink, R. (2011) 'Stress rupture and fatigue in thin wall single crystal superalloys with cooling holes', in Huron, E. S., Reed, R. C., Hardy, M. C., Mills, M. J., Montero, R. E., Portella, P. D., and Telesman, J. (eds) *Superalloys 2012*. Hoboken, NJ, USA: John Wiley & Sons, Inc., pp. 353–362.

Sun, E., Heffernan, T. and Helmink, R. (2012) 'Stress rupture and fatigue in thin wall single crystal superalloys with cooling holes', in *Superalloys 2012*, pp. 351–362.

Suresh, K. M., Sujata, M., Venkataswamy, M. and Bhaumik, S. (2013) 'Fatigue fracture of a compressor disc of an aeroengine', *Journal of Failure Analysis and Prevention*, 13(4), pp. 437–444.

Suresh, S. (1998) *Fatigue of materials*. 2nd edn. Cambridge University Press.

Szczotok, A. and Chmiela, B. (2014) 'Effect of heat treatment on chemical segregation in CMSX-4 nickel-base superalloy', *Journal of Materials Engineering and Performance*, 23(8), pp. 2739–2747.

Tam, S., Williams, R., Yang, L., Jana, S., Lim, L. and Lau, M. (1990) 'A review of the laser processing of aircraft components', *Journal of Materials Processing Technology*, 23(2), pp. 177–194.

Tam, S., Yeo, C., Jana, S., Lau, M., Lim, L., Yang, L. and Noor, Y. (1993) 'Optimization of laser deep-hole drilling of Inconel 718 using the Taguchi method', *Journal of Materials Processing Technology*, 37(1), pp. 741–757.

Tan, B. (2013) 'Laser Material Processing for Aerospace Applications', *J Aeronaut Aerospace Eng*, 2(1), p. e120.

Tang, H., Cao, D., Yao, H., Xie, M. and Duan, R. (2009) 'Fretting fatigue failure of an aero engine turbine blade', *Papers presented at the Third International Conference on Engineering Failure Analysis (Sitges, Spain, 13-16 July 2008) Part II*, 16(6), pp. 2004–2008.

Tasker, P. (2016) *A National Strategy for Engineering Services*. Cranfield. Available at: https://www.through-life-engineering-services.org/downloads/TES_Strategy_Report.pdf.

Tatlock, G. J., Hurd, T. J. and Punni, J, S. (1987) 'High temperature degradation of nickel based alloys', *Platinum Metals Review*. Johnson Matthey, 31(1), pp. 26–31.

TES (2011) *TES Project 3: In-service component feedback*, *Through-life Engineering Services Centre*. Available at: https://www.through-life-engineering-services.org/index.php/research/core-projects/in-service-component-feedback (Accessed: 10 September 2014).

TES (2012) *What is the TES Centre?*, *Through-life Engineering Services Centre*. Available at: https://www.through-life-engineering-services.org/index.php/research/core-projects (Accessed: 12 September 2015).

Thomas, M. C. (1994) 'Allison Manufacturing, property and Turbine Engine Performances of CMSX-4® Single Crystal Alloy', *Materials for Advanced Power Engineering, Part II*, pp. 1075–1098.

Topper, T. H., Sandor, B. I. and Morrow, J. (1969) 'Cumulative damage under cyclic strain control', *Journal of Materials*, 4, pp. 189–199.

Trippe, J., Willach, J., Kreutz, E., Schulz, W., Petereit, J., Kaierle, S. and Poprawe, R. (2004) 'Melt ejection during single-pulse drilling and percussion drilling of micro holes in stainless steel and nickel-based superalloy by pulsed Nd:YAG laser radiation', in *Fifth International Symposium on Laser Precision Microfabrication*. International Society for Optics and Photonics, pp. 609–615.

Viswanathan, R. (1989) *Damage Mechanisms and Life Assessment of High-Temperature Components*, *ASM International*. ASM International.

Voisey, K. and Clyne, T. (2004) 'Laser drilling of cooling holes through plasma sprayed thermal barrier coatings', *Surface and Coatings Technology*, 176(3), pp. 296–306.

Voisey, K. T., Kudesia, S. S., Rodden, W. S. O., Hand, D. P., Jones, J. D. C. and Clyne, T. W. (2003) 'Melt ejection during laser drilling of metals', *Materials Science and Engineering A*, 356(1–2), pp. 414–424. doi: 10.1016/S0921-5093(03)00155-2.

Voisey K, Thompson J, C. T. (2001) ‘Damage caused during Laser Drilling of Thermal Spray TBCs on Superalloy Substrates’, in *20th International Congress on Applications of Lasers and Electro-Optics, ICALEO 2001 -Congress Proceedings, Vol. 103*. Laser Institute of America, pp. 257–265.

Walker, E. K. (1970) ‘The effect of stress ratio during crack propagation and fatigue for 2024-T3 and 7075-T6 aluminum’, *ASTM STP, American Society for Testing and Materials*, pp. 1–14.

Walker, K. (1970) ‘The effect of stress ratio during crack propagation and fatigue for 2024-T3 and 7075-T6 aluminum’, in *ASTM STP 462*. Philadelphia: American Society for Testing ans Materials, pp. 1–14.

Walsh, P. P. and Fletcher, P. (2004) ‘Gas Turbine Engine Components’, in *Gas Turbine Performance*. 2nd edn. Wiley-Blackwell, pp. 159–247.

Walsh, W. S., Thole, K. A. and Joe, C. (2006) ‘Effects of sand ingestion on the blockage of film-cooling holes’, *Volume 3: Heat Transfer, Parts A and B*, 2006, pp. 81–90.

Walther, K., Brajdic, M., Dietrich, J., Hermans, M., Witty, M., Horn, A., Kelbassa, I. and Poprawe, R. (2008) ‘Manufacturing of shaped holes in multi-layer plates by Laser-drilling’, in *In 3rd Pacific International Conference on Applications of Lasers and Optics, PICALO 2008*, pp. 789–794.

Wang, H., Zuo, H., He, X., Lin, Q. and Hu, X. (2007) ‘Failure analysis of 3rd turbine blade of aero-engines’, *Failure Analysis and Prevention*, 1, p. 9.

Wang, K., Duan, W., Mei, X. and Wang, W. (2012) ‘Technology to drill micro-holes without recast layer by laser on nickel-based alloy’, in *Advanced Materials Research*, pp. 303–307.

Wang, X., Lu, P., Dai, N., Li, Y., Liao, C., Zheng, Q. and Liu, L. (2007) ‘Noncrystalline micromachining of amorphous alloys using femtosecond laser pulses’, *Materials Letters*, 61(21), pp. 4290–4293.

Wang, X. M., Liu, H., Zhou, Q. T., Li, L., Deng, C. H. and Yue, Z. F. (2013) ‘Influences of ellipse cooling holes on creep crack initiation and surface morphology of nickel based superalloys’, *Materials Science and Technology*, 29(3), pp. 337–341.

Wang, X. Y., Ng, G. K. L., Liu, Z., Li, L. and Bradley, L. (2004) 'EPMA microanalysis of recast layers produced during laser drilling of type 305 stainless steel', in *Thin Solid Films*, pp. 84–88.

Weman, K. (2003) *Welding Processes Handbook*, *Welding Processes Handbook*.

Wen, Z., Huang, S., Gao, H. and Yue, Z. (2017) 'Experimental investigation on low cycle fatigue properties of GH3536 alloy with film cooling holes in different drilling processes', *Engineering Failure Analysis*, 82, pp. 190–197.

Wilby, A. J. and Neale, D. P. (2012) 'Defects introduced into metals during fabrication and service', *Materials Science and Engineering A*, 3, pp. 1–11.

Willach, J., Kreutz, E., Michel, J., Niessen, M., Schulz, W. and Poprawe, R. (2003) 'Melt expulsion by a coaxial gas jet in trepanning of CMSX-4 with microsecond Nd:YAG laser radiation', *Fourth International Symposium on laser Precision Microfabrication*. International Society for Optics and Photonics, 5063, pp. 435–440.

Williams, David B., Carter, C. B. (2009) 'Kikuchi Diffraction', in *Transmission Electron Microscopy: A Textbook for Materials Science*. 2nd edn. Springer US, pp. 311–322.

Williams, D. B. and Carter, C. B. (2009a) *Transmission Electron Microscopy: A Textbook for Materials Science*, *Materials Science*.

Williams, D. B. and Carter, C. B. (2009b) *Transmission Electron Microscopy: A Textbook for Materials Science*, *Materials Science*.

Witek, L. (2006) 'Failure analysis of turbine disc of an aero engine', *Engineering Failure Analysis*, 13(1), pp. 9–17.

Wöhler, A. (1867) 'Wöhler's experiments on the strength of metals', in *Engineering*, pp. 160–161.

Wöhler, A. (1870) 'Über die Festigkeitversuche mit Eisen und Stahl', *Zeitschrift für Bauwesen*. Berlin: Ernst & Korn, 20, pp. 73–106.

Wu, X., Miller, M., Zhang, Z., Miller, J. and Reed, P. (2005) 'Fracture mechanics analysis of notch fatigue of a single crystal superalloy - CMSX-4', in *11th International Conference on Fracture 2005, ICF11*, pp. 245–249.

Xi, N., Zhong, P., Huang, H., Yan, H. and Tao, C. (2000) 'Failure investigation of blade

and disk in first stage compressor', *Engineering Failure Analysis*, 7(6), pp. 385–392.

Xie, M., Zhong, P., Xi, N., Zhang, Y. and Tao, C. (2000) 'Analysis of fracture failure of fir-tree serrations of stage II turbine disks', *Engineering Failure Analysis*, 7(4), pp. 249–260.

Xie, Y., Wang, M., Zhang, G. and Chang, M. (2006) 'Analysis of superalloy turbine blade tip cracking during service', *Engineering Failure Analysis*, 13(8), pp. 1429–1436.

Xu, J., Reuter, S. and Rothkegel, W. (2008) 'Tensile and bending thermo-mechanical fatigue testing on cylindrical and flat specimens of CMSX-4 for design of turbine blades', *International Journal of Fatigue*, 30(2), pp. 363–371.

Yan, H., Zhong, P., Xi, N. and Tao, C. (2000) 'A case study of cracks in aeroengine compressor discs', *Engineering Failure Analysis*, 7(3), pp. 181–188.

Yandt, S., Wu, X., Tsuno, N. and Sato, A. (2012) 'Cyclic Dwell Fatigue Behaviour of Single Crystal Ni-Base Superalloys with/without Rhenium', *Superalloys 2012*, pp. 501–508.

Yang, X., Li, S. and Qi, H. (2015) 'Effect of high-temperature hot corrosion on the low cycle fatigue behavior of a directionally solidified nickel-base superalloy', *International Journal of Fatigue*, 70, pp. 106–113.

Yeo, C., Tam, S., Jana, S. and Lau, M. (1994) 'A technical review of the laser drilling of aerospace materials', *Journal of Materials Processing Technology*, 42(1), pp. 15–49.

Yilbas, B. S. (1985) 'The study of laser produced plasma behaviour using streak photography', *Japanese Journal of Applied Physics*, 24(11 R), pp. 1417–1420.

Yilbas, B. S. (1995) 'Study of liquid and vapor ejection processes during laser drilling of metals', *Journal of Laser Applications*, 7(3), pp. 147–152.

Yilbas, B. S. (1997) 'Parametric study to improve laser hole drilling process', *Journal of Materials Processing Technology*, 70(1–3), pp. 264–273.

Yilbaş, B. S. (1993) 'Analytical solution for the heat conduction mechanism appropriate to the laser heating process', *International Communications in Heat and Mass Transfer*, 20(4).

Yilbas, B. S. and Aleem, A. (2004) 'Laser hole drilling quality and efficiency

assessment', in *Proceedings of the Institution of Mechanical Engineers, Part B: Journal of Engineering Manufacture*, pp. 225–233.

Yilbas, B. S. and Yilbas, Z. (1988) 'Some aspects of laser-metal vapour interaction', *Pramana*, 31(5), pp. 365–381.

Yu, Q. M., Yue, Z. F. and Wen, Z. X. (2008) 'Creep damage evolution in a modeling specimen of nickel-based single crystal superalloys air-cooled blades', *Materials Science and Engineering A*, 477(1–2), pp. 319–327.

Zhang, H., Zhou, M., Wang, Y., Zhang, X., Yan, Y. and Wang, R. (2016) 'Development of a quantitative method for the characterization of hole quality during laser trepan drilling of high-temperature alloy', *Applied Physics A: Materials Science and Processing*, 122(2), pp. 1–11.

Zhang, H., Zhou, M., Wang, Y., Zhang, X., Yan, Y. and Wang, R. (2016) 'Development of a quantitative method for the characterization of hole quality during laser trepan drilling of high-temperature alloy', *Applied Physics A*, 122(2), pp. 1–11.

Zhang, W., Li, Y., Liu, G., Zhao, A., Tao, C., Tian, J. and Yao, G. (2004) 'Recrystallization and fatigue failure of DS alloy blades', *Engineering Failure Analysis*, 11(3), pp. 429–437.

Zhao, Y., Harrison, A., Roy, R. and Mehnen, J. (2011) 'Aircraft engine component deterioration and Life Cycle Cost estimation', in *Glocalized Solutions for Sustainability in Manufacturing - Proceedings of the 18th CIRP International Conference on Life Cycle Engineering*, pp. 657–662.

Zhou, Z. J., Wang, L., Wen, J. L., Lou, L. H. and Zhang, J. (2015) 'Effect of skew angle of holes on the tensile behavior of a Ni-base single crystal superalloy', *Journal of Alloys and Compounds*, 628, pp. 158–163.

Zhou, Z. J., Yu, D. Q., Wang, L. and Lou, L. H. (2017) 'Effect of skew angle of holes on the thermal fatigue behavior of a Ni-based single crystal superalloy', *Acta Metallurgica Sinica (English Letters)*, 30(2), pp. 185–192.

Zhu, X.-K. and Joyce, J. A. (2012) 'Review of fracture toughness (G, K, J, CTOD, CTOA) testing and standardization', *Engineering Fracture Mechanics*. Elsevier, 85, pp. 1–46.

APPENDICES

Appendix A - HPT NGV

The first stage HPT NGV is a static component that is fixed and does not rotate, located right after the combustor section and before the HPT rotor blades, see Figure A-1a. The main function of the HPT NGV is to direct the hot gases from the combustor to stage one HPT rotor blades, where it extracts the energy from the hot exhaust gas stream to convert into kinetic energy to drive the rotating compressor stages and the fan via rotating shafts. The HPT NGV consist of two airfoil joined through an upper and lower platform sections (see Figure A-1b). These aerofoils are coated with ceramic thermal barrier coating (TBC) and film cooling holes to protect the base material, shielding from the hot gasses and providing circulation of cooling air externally and internally, respectively. The ceramic coating and film cooling holes provides longer life while operating at aggressive environment (i.e. hot corrosion type environment), without affecting the integrity of the vane. The cooling air is taken from the compressor stages and fed into vanes to cool the airfoils (see Figure A-2).

Typical base material used in the HPT NGV are cast nickel-based superalloys such as CMSX-4 and/or René 80, providing high resistance to stress-rupture, creep, hot corrosion and thermal fatigue. Most of the HPT NGV are turbine vanes are manufacture through in the investment casting in vacuum and casted in the single-crystal form. In Figure A-3, the various stages in the manufacture of HPT NGV, from casting to final assembly is given. Figure A-4 shows a service exposed HPT NGV. The airfoils and inner platform sections have been seen to undergo severe thermal distress, burn and oxidation. The leading-edge section showed evidence of heavy burns, oxidation and thermal cracking (or spalling) in the thermal barrier coating near the film cooling holes. Multiple cracking branching within film cooling holes was also observed. Thermal cracking is also seen in the trailing-edge section of the airfoil and near the cooling holes. This is because of trailing edge section has a thinner wall than the leading-edge and thus thermal strains are higher than the rest of the vane. Figure A-5 shows typical damage and degradation mechanisms reported in the company service experience data and some from the open literature.

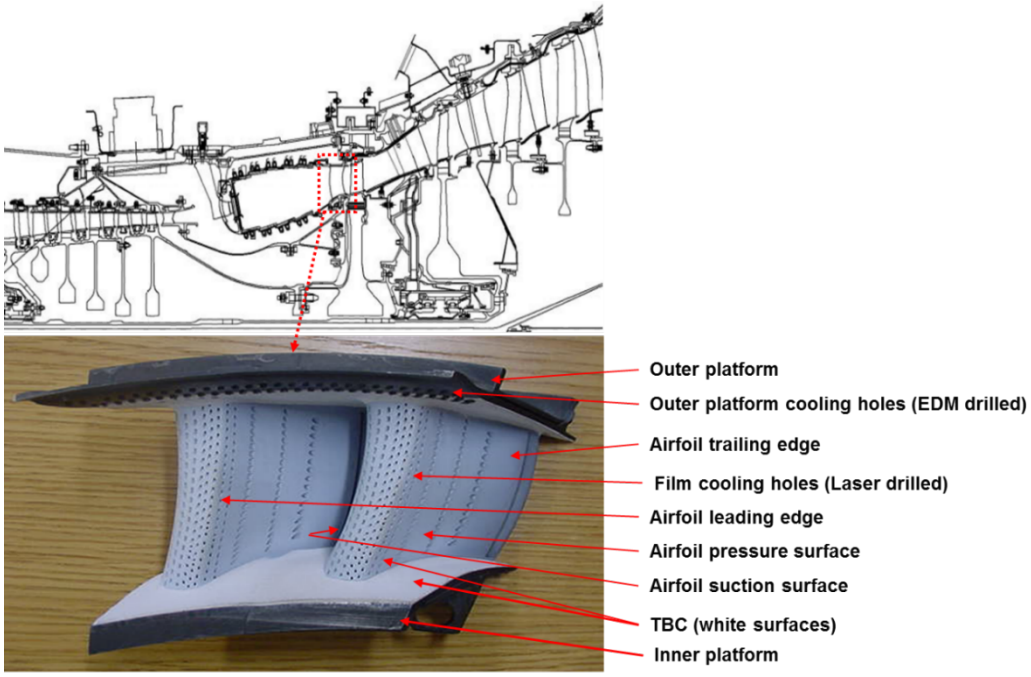

Figure A-1: Illustration of (a) general arrangement of HPT NGV location and (b) show key design features (courtesy of Rolls-Royce).

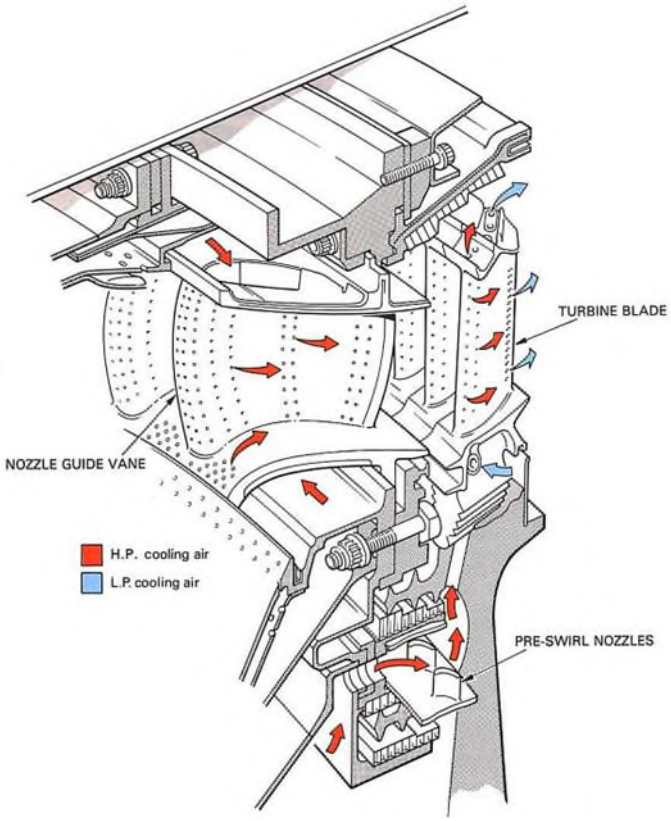

Figure A-2: circuit diagram showing how cooling air is delivered to vane and blade airfoils (courtesy of Rolls-Royce).

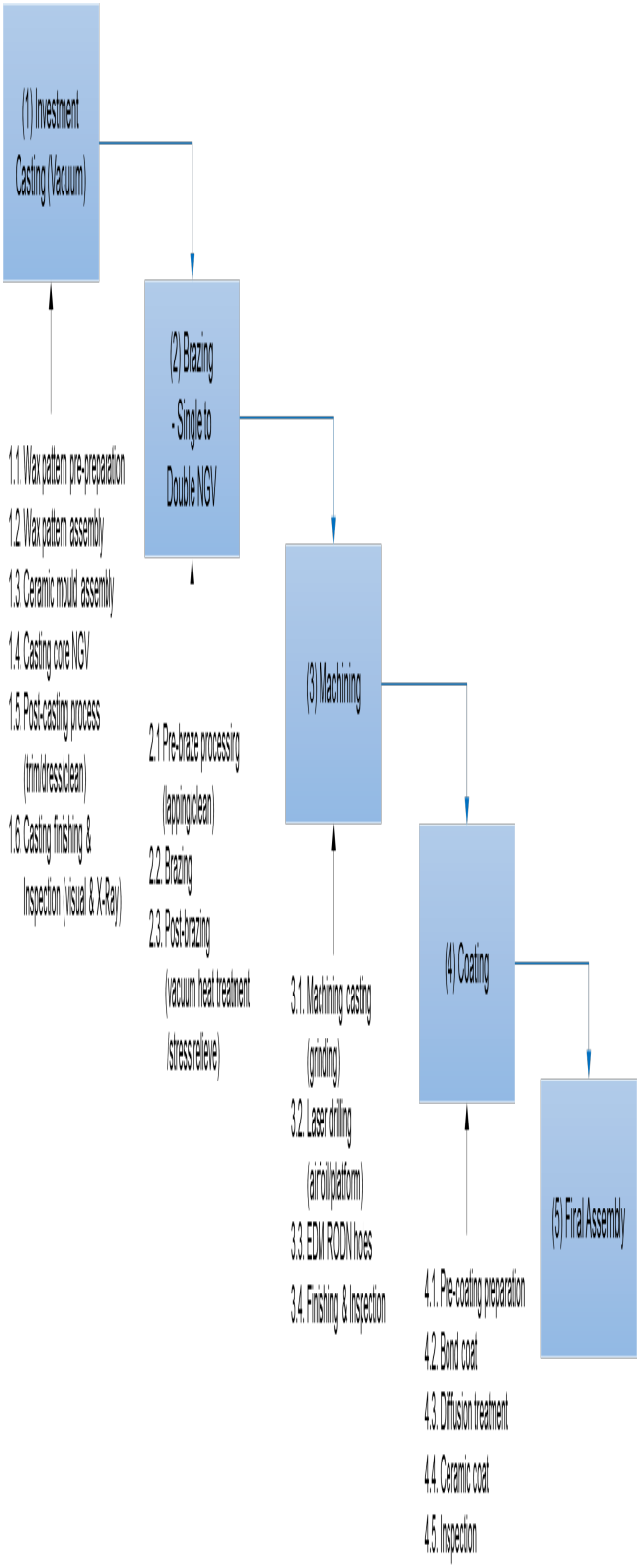

Figure A-3: Illustration of the various processes of the manufacture of cast single crystal HPT Nozzle Guide Vanes.

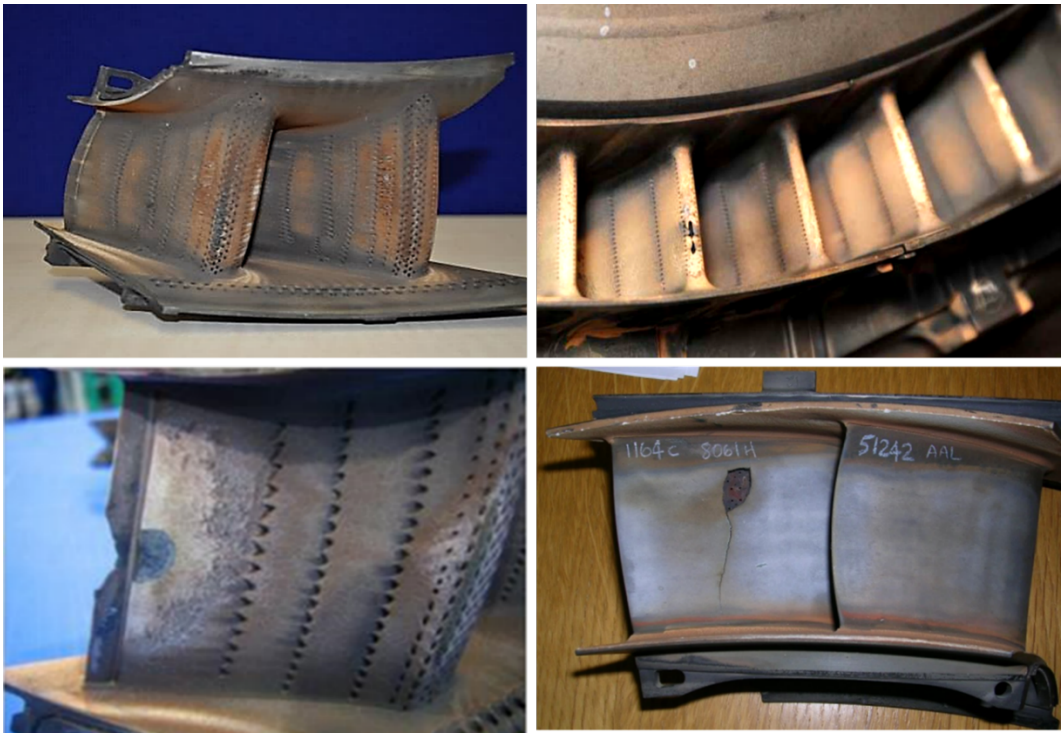

Figure A-4: Examples of service exposed HPT NGV's (courtesy of Rolls-Royce).

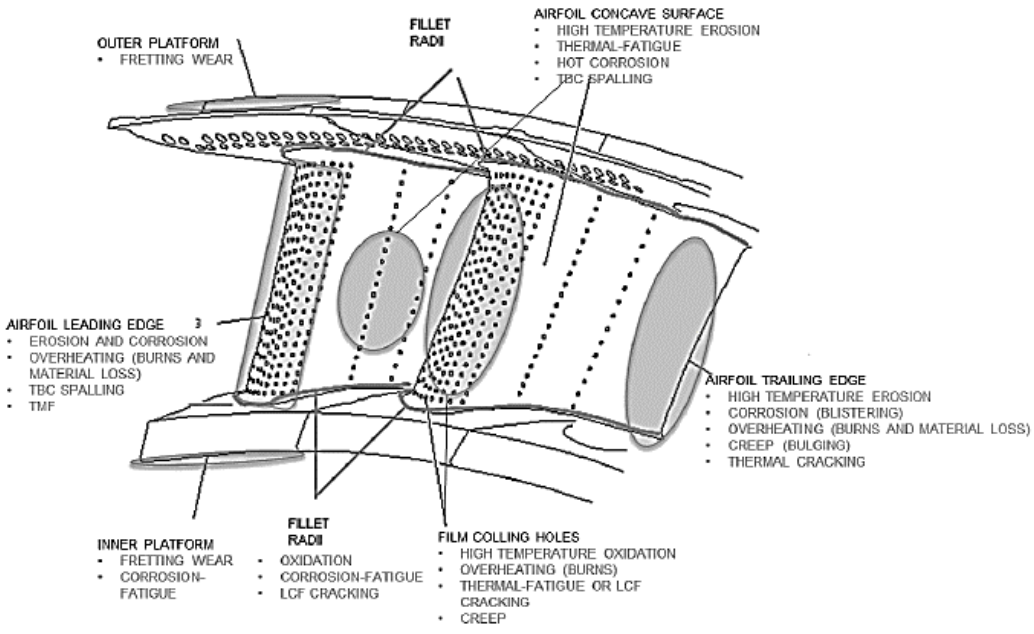

Figure A-5: Typical locations of degradation mechanisms in HPT NGV's.

Appendix B – Laser drilling trials data

Table B-1: RLT measurements from OA L9 trials 1-3.

Recast points measurements	Experimental trials no.											
	1				2				3			
	Hole 1	Hole 2	Hole 3	Hole 4	Hole 1	Hole 2	Hole 3	Hole 4	Hole 1	Hole 2	Hole 3	Hole 4
1	10.2	11.2	12.5	16.2	17.2	16.1	15.3	21	45	10	73.1	34.5
2	34	48	39	36.8	32	32.6	47.9	53.6	59	47	78.1	61.5
3	19	40	34	42.1	23.4	27.5	31.5	41.2	64.5	52	72.5	62.1
4	29	23	46	39.5	17.6	25.2	32.6	25.1	42.5	55.2	33.1	27.2
5	29	44	25	26.5	38.2	19.2	29.6	36.2	35	49.5	41.5	59.2
6	44	29	18	22.8	25.1	36.4	18.6	24.9	49	59.5	40.5	72.4
7	23	20	45	23.5	46.3	27.3	25.2	40.2	52.5	54.2	34.5	81.6
8	29	45	38	45.6	44.5	48.2	49.2	23.6	65.2	43.2	62.1	40.2
9	15	6.5	21	36.9	21.2	28.7	12.6	17.2	58.6	53.5	67.2	67.6
10	36	11	37	38.2	32.6	40.2	38	38.2	61.8	66.1	28.1	82.3
11	39	40	42	36	42.7	29.5	49.8	37.6	66.2	64.7	72.3	56.4
12	44	21	49	32.5	38.2	45	43.2	32.5	69.2	79	56.2	57.8
13	44	38	46	39.2	61.6	34.2	42	49.2	56.2	65.5	44.1	65.1
14	32	29	51	46.2	35	29.7	38.2	61.4	58.5	45.2	52	77.3
15	36	36	34	48.2	38.2	40.5	48.6	28.4	67.2	23.5	51.7	78.6
16	44	25	53	26.5	17.6	16.5	15.9	21.5	15	12.5	74.2	45.2
Mean	31.7	29.2	36.9	34.8	33.2	31.1	33.6	33.9	54.1	48.8	53.9	60.6
Min	10.2	6.5	12.5	16.2	17.2	16.1	12.6	17.2	15	10	28.1	27.2
Max	44	48	53	48.2	61.6	48.2	49.8	53.6	69.2	79	78.1	82.3
Mean p/trial	33.1				33.0				54.3			
Mean, Max	**48.3**				**53.4**				**77.1**			

Reading points 1-8 is left side of hole (see Figure 5-10)

Reading points 9-16 is right side of hole (see Figure 5-10)

*= Damaged during cutting operations.

Table B-2: RLT measurements from OA L9 trials 4-6.

Recast points measurements	Experimental trials no.											
	4				5				6			
	Hole 1	Hole 2	Hole 3	Hole 4	Hole 1	Hole 2	Hole 3	Hole 4	Hole 1	Hole 2	Hole 3	Hole 4
1	32	25	41	21.2	13	11	*	8	12	18.3	15	*
2	37	42.5	33.2	33.2	32	60	*	50	27	12.1	48.2	*
3	41	17	28.5	38.6	19	36	21	23	37	43.1	27	*
4	27	32	23.5	16.5	24	17	22	29	31	19.5	32.1	*
5	23	40.2	42.1	21.2	27	17	23	34	23	17.2	28	25.2
6	25	17.2	33.2	51.2	23	25	12.5	31	20	29.5	29	49.5
7	29	24.1	26.5	31.2	33	31	29	34	27	34.5	33	29.2
8	33	52.8	14	26.2	35	62	42	25	42	19.5	29	36.1
9	53	23	16.2	35.6	34	8	21	8	54	43.5	12.5	38.2
10	38	42	29.5	36.5	38	33	44	32	55.6	25.6	33	26.1
11	36	29	37.5	42.2	29	42	33	29	34	21	29	21.2
12	27	23	40.2	22.5	36	44	39	48	36	26	41.2	26.5
13	42	40	35.4	28.5	32	36	40	53	24.5	21.2	22.3	32.1
14	44	48	19.5	29.5	34	48	42	42.5	19	41.2	29	35.6
15	37	36	22.5	25.6	24	29	21	27	38	28.2	14	30.2
16	19	44	42.8	43.2	83	50	60	48	41	23	12	45.2
Mean	33.9	33.5	30.4	31.4	32.3	34.3	32.1	32.6	32.6	26.5	27.1	32.9
Min	19.0	17.0	14.0	16.5	13.0	8.0	12.5	8.0	12.0	12.1	12.0	21.2
Max	53.0	52.8	42.8	51.2	83.0	62.0	60.0	53.0	55.6	43.5	48.2	49.5
Mean p/trial	32.3	-	-	-	32.8	-	-	-	29.8	-	-	-
Mean, Max	**53.0**	**-**	**-**	**-**	**64.5**	**-**	**-**	**-**	**49.2**	**-**	**-**	**-**

Reading points 1-8 is left side of hole (see Figure 5-10)

Reading points 9-16 is right side of hole (see Figure 5-10)

*= Damaged during cutting operations.

Table B-3: RLT measurements from OA L9 trials 7-9.

Recast points measurements	Experimental trials no.											
	7				8				9			
	Hole 1	Hole 2	Hole 3	Hole 4	Hole 1	Hole 2	Hole 3	Hole 4	Hole 1	Hole 2	Hole 3	Hole 4
1	32.5	44.2	12	*	-	31.9	46.6	18.6	26.5	23	27.8	20
2	48	32.6	42	*	50.7	34.4	33	29.4	32	32	34	33
3	38	54.2	36	*	27.8	52.3	42	44.2	60	57	42.5	56.2
4	55	62.5	55.3	*	21.2	58.2	29	24.4	59	24	49	48
5	60.2	43.8	59.8	*	17.2	36.5	13	27.8	42	42.5	36	32
6	52.3	49.5	45.8	*	54.4	33.6	41.3	12.5	53	33.6	27	27.8
7	42.5	42.3	57.2	*	36.4	32	43.5	14.7	26	34.4	53	62.3
8	55	51.2	42.3	*	68.4	40.1	42.1	34	41	32	46	56.6
9	27.2	23.8	27.2	*	76.7	34.4	32.9	36	42	24	31.7	41.2
10	73	44	44.1	*	63.4	43.5	36	48	63.8	66	45	64.7
11	45.6	60	53	*	52.2	53.1	45	42.5	46.6	46.6	53.2	38.4
12	69	32	62	*	25.3	60.9	38.4	42	27.8	59.7	46.6	56.7
13	61	34	56.3	*	58.4	39.5	45	52.3	35.6	34.4	55.6	63.4
14	49.2	44	54	*	72.5	56.3	21.2	51.6	40	40.1	29.4	61.2
15	53	31	36.5	*	36	60.2	32	49.9	27.8	27.2	46.6	59.4
16	17	71	33.6	*	44.7	71.5	44	50.7	54.3	69.6	42	58.5
Mean	48.7	45.0	44.8	*	47.0	46.2	36.6	36.2	42.3	40.4	41.6	48.7
Min	17.0	23.8	12.0	*	17.2	31.9	13.0	12.5	26.0	23.0	27.0	20.0
Max	73.0	71.0	62.0	*	76.7	71.5	46.6	52.3	63.8	69.6	55.6	64.7
Mean p/trial	46.2	-	-	-	41.5	-	-	-	43.3	-	-	-
Mean, Max	**68.7**	**-**	**-**	*	**61.8**	**-**	**-**	**-**	**63.4**	**-**	**-**	**-**

Reading points 1-8 is left side of hole (see Figure 5-10)

Reading points 9-16 is right side of hole (see Figure 5-10)

*= Damaged during cutting operations.

Table B-4: Cracks measurements from OA L9 trials 1-3.

Trial no.	Cracks	Crack length (µm)				Max.no.	CNDmax (no./mm^2)
		Hole 1	Hole 2	Hole 3	Hole 4		
1	**Transverse**	**29.6**	**19.6**	**23.3**	**15.7**	**4**	**1**
		-	**-**	**20.8**	**11.5**		
		-	**-**	**19.9**	**19.7**		
		-	**-**	**30.1**	**-**		
	Longitudinal	18.9	18.9	-	20.2		
		9.49	9.49	-	51.2		
		13.3	13.3	-	-		
		15.4	15.4	-	-		
		27.5	27.5	-	-		
2	**Transverse**	**22.2**	**28.9**	**28.4**	**30.7**	**5**	**2**
		25.8	**7.8**	**22.3**	**10.3**		
		-	**11.9**	**8.35**	**30.2**		
		-	**12.4**	**24.6**	**-**		
		-	**-**	**41.1**	**-**		
		-	**-**	**30.3**	**-**		
		-	**-**	**39.1**	**-**		
		-	**-**	**10.1**	**-**		
	Longitudinal	21.7	41.4	12.6	-		
		-	20.2	36.2	-		
		-	16.7	29.5	-		
3	**Transverse**	**26.9**	**12.9**	**-**	**21.4**	**5**	**1.25**
		14.3	**22.2**	**-**	**15.3**		
		19.4	**-**	**-**	**21.2**		
		25.1	**-**	**-**	**14.8**		
		28.6	**-**	**-**	**-**		
	Longitudinal	-	143	22.5	20.9		
		-	25.8	-	12.2		

Table B-5: Cracks measurements from OA L9 trials 4-5.

Trial no.	Cracks	Crack length (µm)				Max.no.	CNDmax (no./mm^2)
		Hole 1	Hole 2	Hole 3	Hole 4		
4	**Transverse**	**30.8**	**32.5**	**26.8**	**12.5**	**6**	**1.5**
		20.9	**24.1**	**-**	**15.5**		
		21.6	**-**	**-**	**-**		
		26.4	**-**	**-**	**-**		
		34.6	**-**	**-**	**-**		
		15.1	**-**	**-**	**-**		
	Longitudinal	-	58.8	-	15.2		
		-	11.4	-	-		
5	**Transverse**	**10.4**	**15.3**	**18.7**	**15.3,**	**11**	**2.75**
		9.8	**35.2**	**19.4**	**35.2**		
		9.7	**18.7**	**16.5**	**18.7**		
		22.9	**23.3**	**7.9**	**23.3**		
		29.7	**16.8**	**16.5**	**16.8**		
		23.2	**9.7**	**20.1**	**9.7**		
		27.4	**18.6**	**19.1**	**18.6**		
		16.2	**8.3**	**15.5**	**8.3**		
		15.1	**-**	**13.9**	**-**		
		-	**-**	**13.2**	**-**		
		-	**-**	**12.5**	**-**		
	Longitudinal	13.2	29.9	39.5	24,1		
		21.8	25.7	33.2	35.3		
		-	-	41.5	45.1		
		-	-	33.6	76.9		
		-	-	-	31.4		
		-	-	-	63.1		

Table B-6: Cracks measurements from OA L9 trials 6-9.

Trial no.	Cracks	Crack length (μm)				Max.no.	CNDmax (no./mm^2)
		Hole 1	Hole 2	Hole 3	Hole 4		
6	**Transverse**	**20.6**	**26.9**	**14.1**	**20.1**	**10**	**2.5**
		16.3	**11.8**	**13.9**	**7.5**		
		18.4	**20.8**	**12.5**	**12.1**		
		9.2	**9.46**	**25.7**	**12.3**		
		15.7	**10.6**	**9.5**	**5.3**		
		18.3	**18.3**	**17.8**	**5.6**		
		11.8	**14.1**	**-**	**14.5**		
		14,2	**21.7**	**-**	**15.1**		
		39.2	**15.5**	**-**	**24.3**		
		-	**12.4**	**-**	**10.2**		
	Longitudinal	24.1	11.3	71.9	17.5		
		35.3	-	-	26.4		
		45.1	-	-	-		
		76.9	-	-	-		
		31.4	-	-	-		
		63.1	-	-	-		
7	**Transverse**	**11.2**	**20.5**	**10.6**	**12.5**	**5**	**1.25**
		15.4	**28.2**	**22.5**	**16.5**		
		10.5	**-**	**9.5**	**-**		
		12.6	**-**	**-**	**-**		
		18.2	**-**		**-**		
	Longitudinal	19.5	31.5	-	-		
			27.5				
8	**Transverse**	**-**	**19.6**	**-**	**-**	**1**	**0.25**
	Longitudinal		81.6				
			29.5				
9	**Transverse**	**32.9**	**-**	**54.6**	**40.8**	**2**	**0.5**
		12.6	**-**	**-**	**22.5**		
	Longitudinal		141	36.2	-		

Micrographs of laser drilled cross-sectioned samples

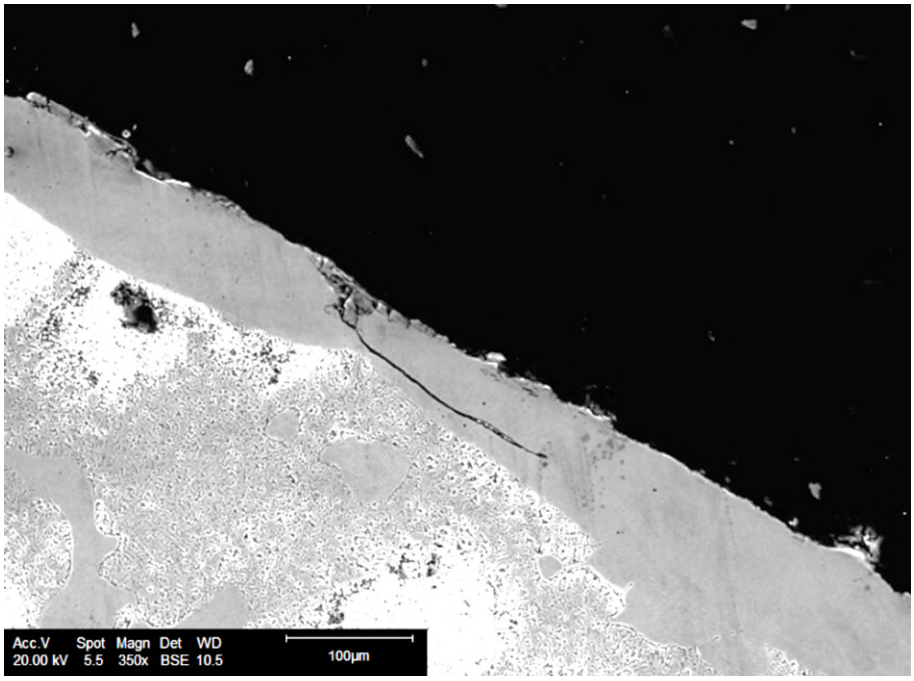

Figure B-1: SEM micrographs showing trial 8, hole no. 2 trailing edge entrance section side (PP = 12.5 kW; PF = 22.5 Hz; TS = 75 mm/min).

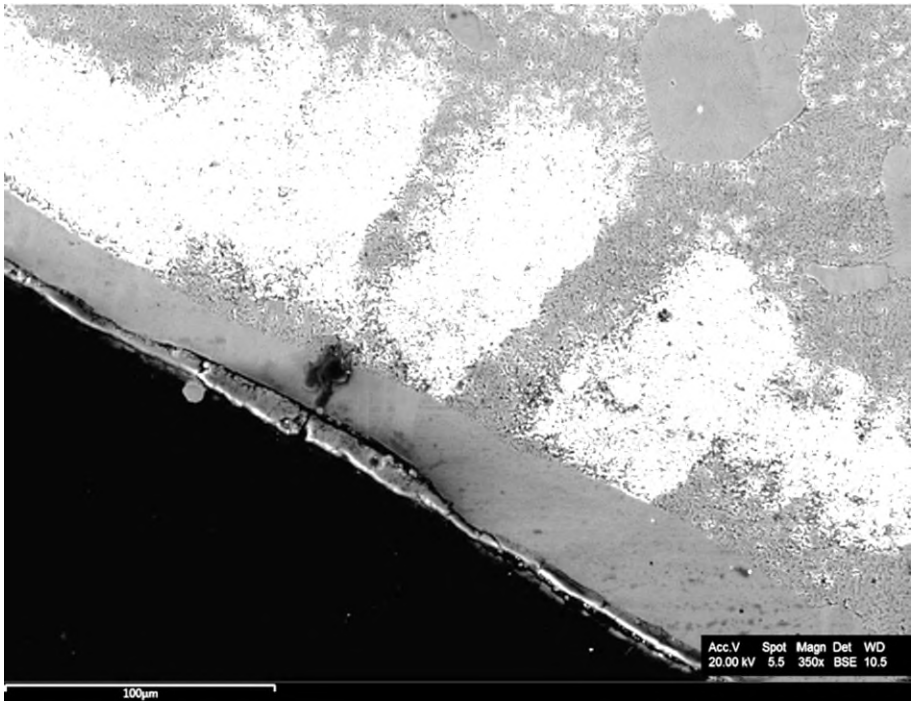

Figure B-2: SEM micrographs showing trial 8, hole no. 2 right mid-section side (PP= 12.5 kW; PF = 22.5 Hz; TS = 75 mm/min).

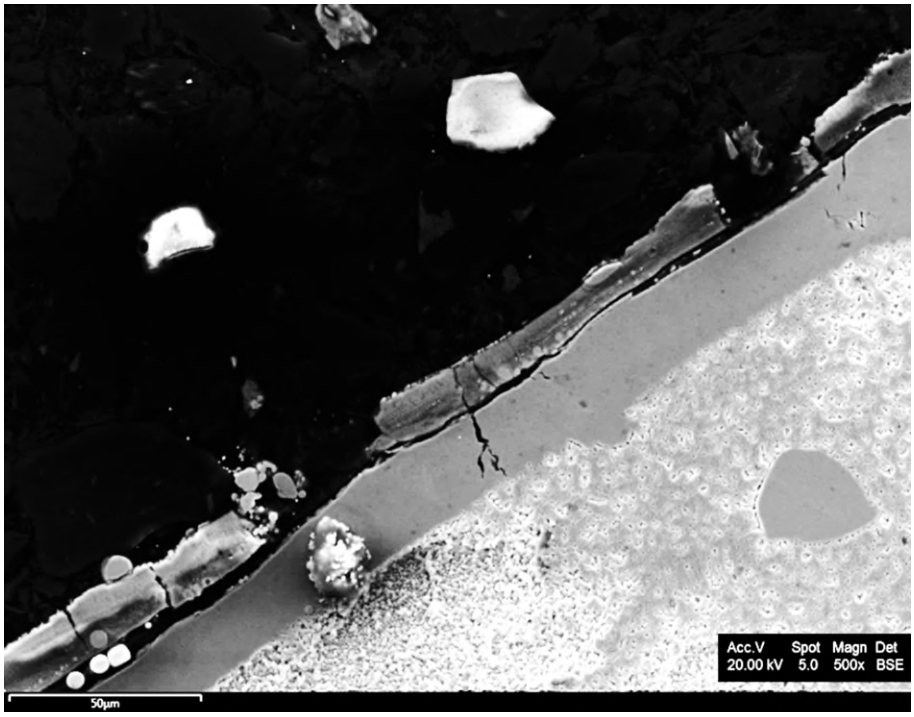

Figure B-3: SEM micrographs illustrating trial 5, hole no. 3 trailing edge entrance side (PP = 10 kW; PF = 22.5 Hz; TS = 125 mm/min).

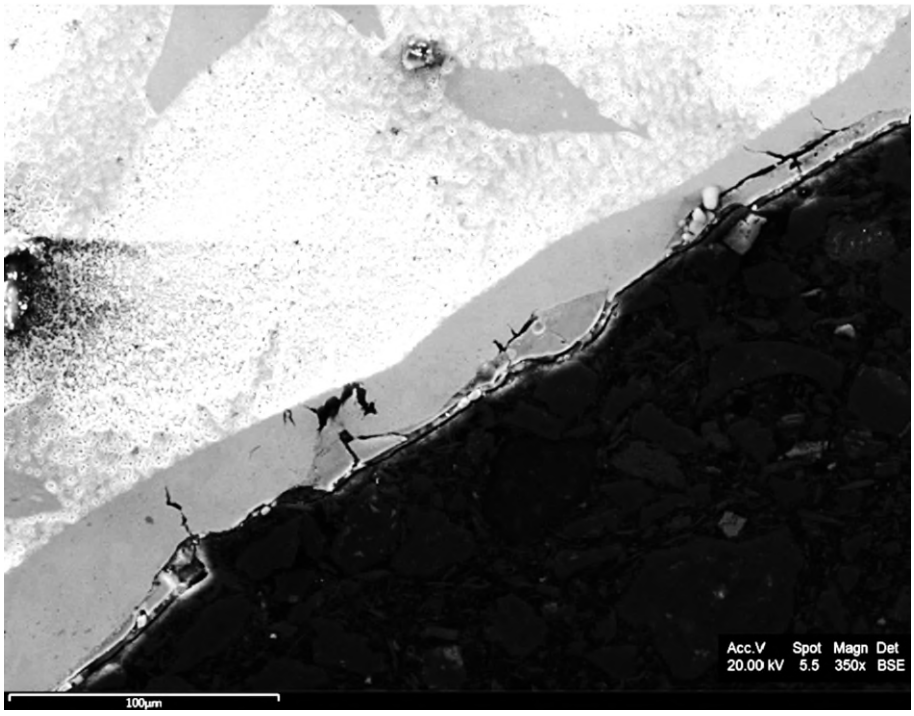

Figure B-4: SEM micrographs showing trial 5, hole no. 4 leading edge mid-section side (PP = 10 kW; PF = 22.5 Hz; TS = 125 mm/min).

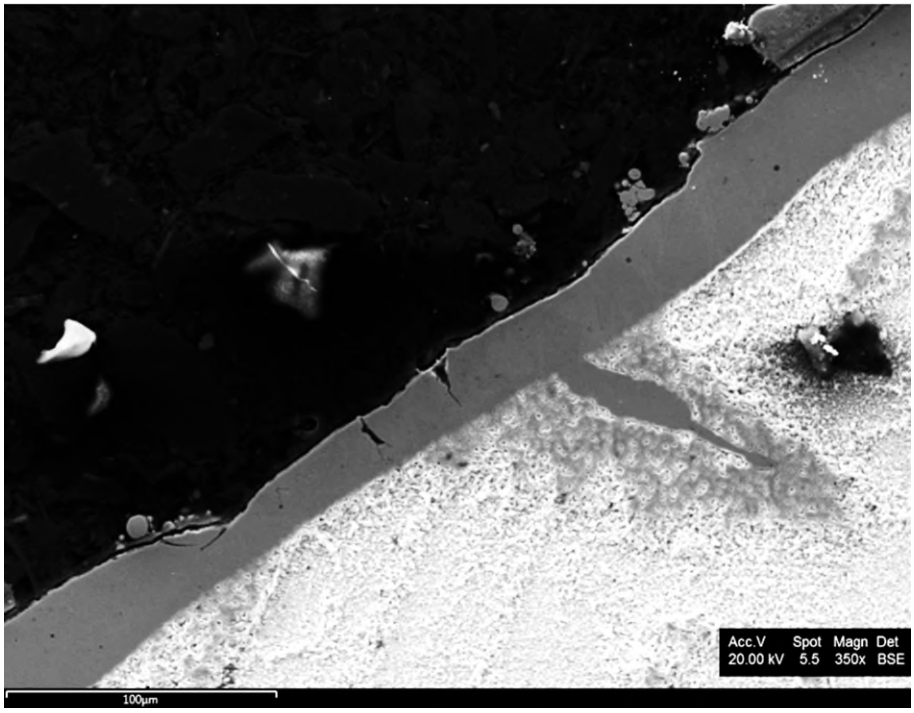

Figure B-5: SEM micrographs illustrating trial 6, hole no. 4 trailing edge mid-section side (PP = 10 kW; PF = 25.0 Hz; TS = 75 mm/min).

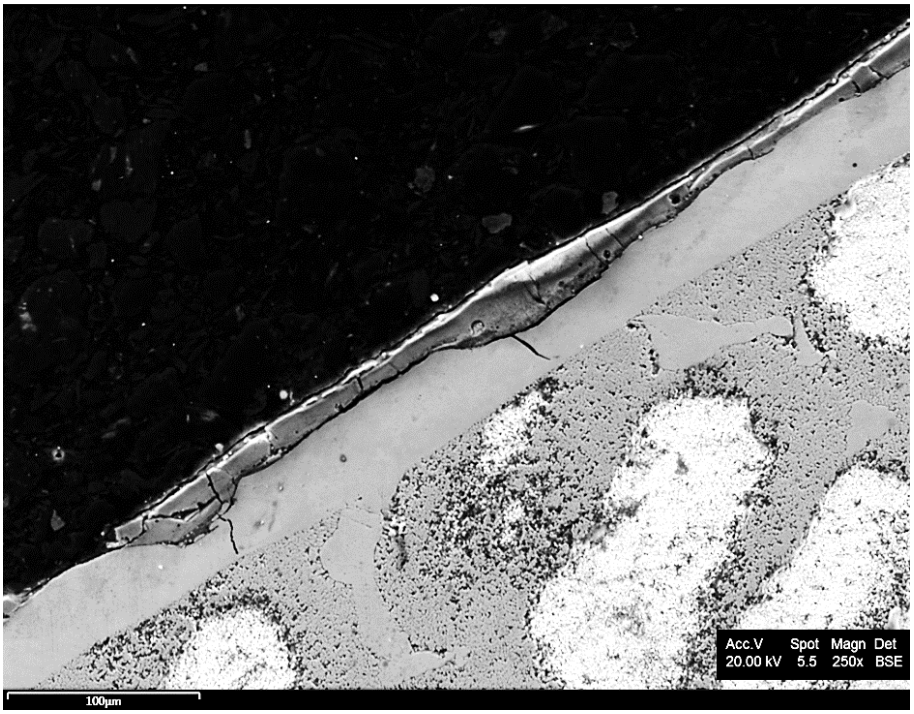

Figure B-6: SEM micrographs showing trial 1, hole no. 3 trailing edge mid-section end side (PP = 8.3 kW; PF = 20.0 Hz; TS = 75 mm/min).

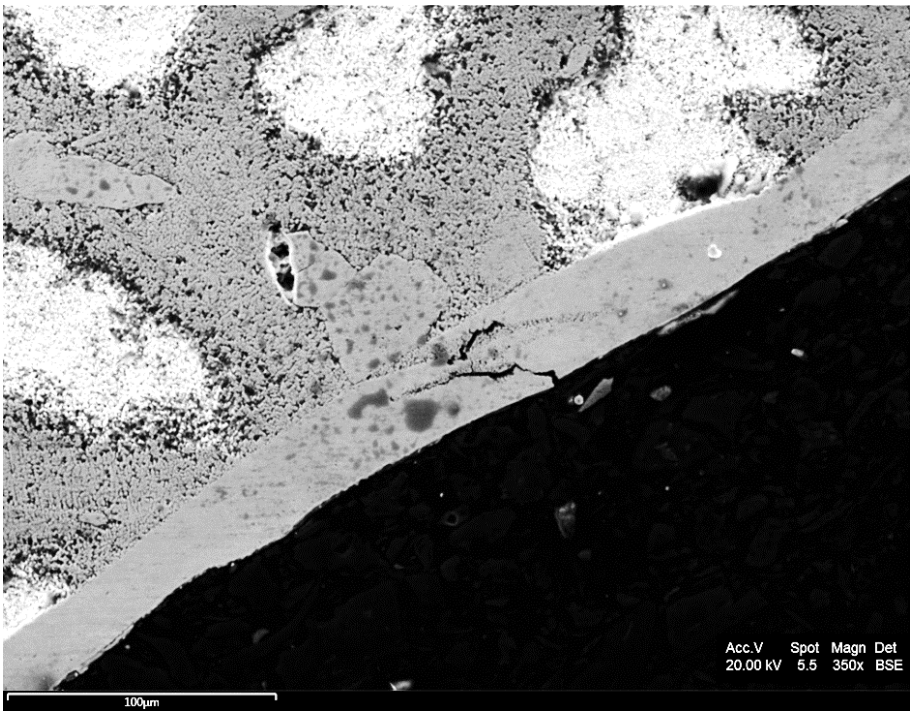

Figure B-7: SEM micrographs showing trial 1, hole no. 4 leading edge mid-section side (PP = 8.3 kW; PF = 22.5 Hz; TS = 75 mm/min).

Appendix C - Fractography of fatigued specimens

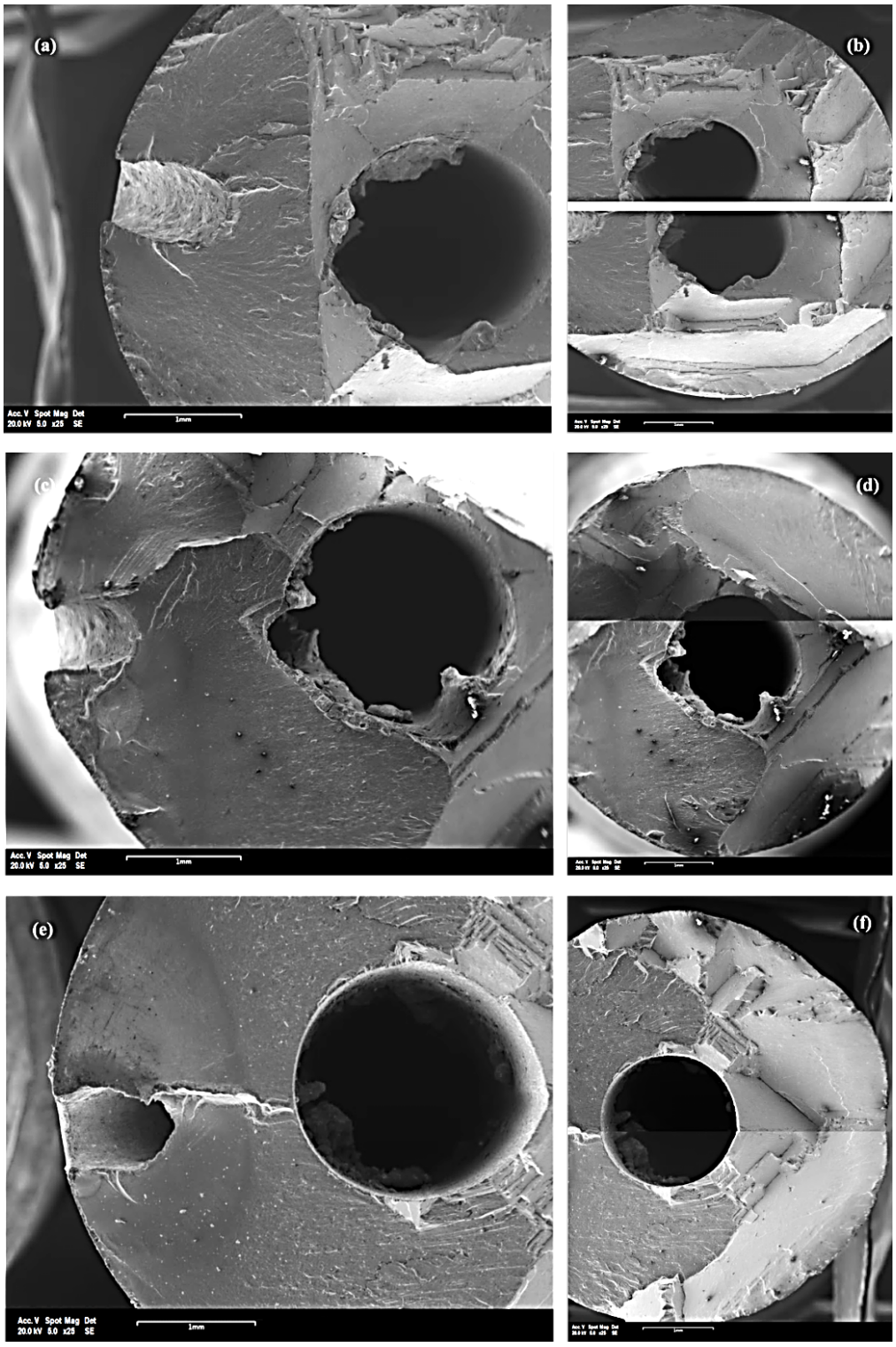

Figure C-1: Micrographs of fractured surfaces of specimens: (a-b) LTD 01 (FAT233), (c-d) LTD 02 (FAT239) and (e-f) LTD 17 (FAT250).

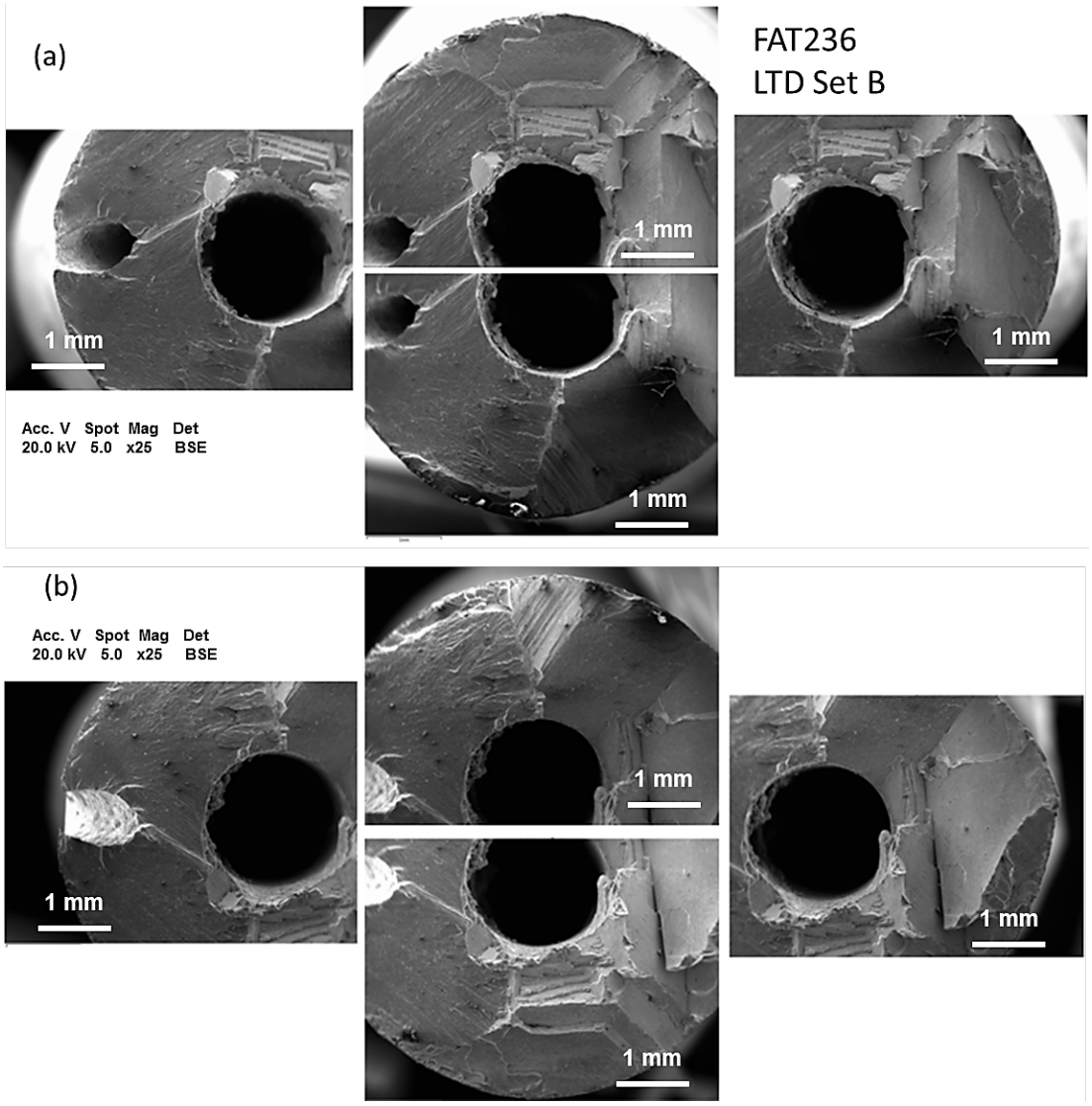

Figure C-2: Example of micrographs of fractured faces of fatigued specimen LTD 07 (FAT236): (a) right side and (b) left side.

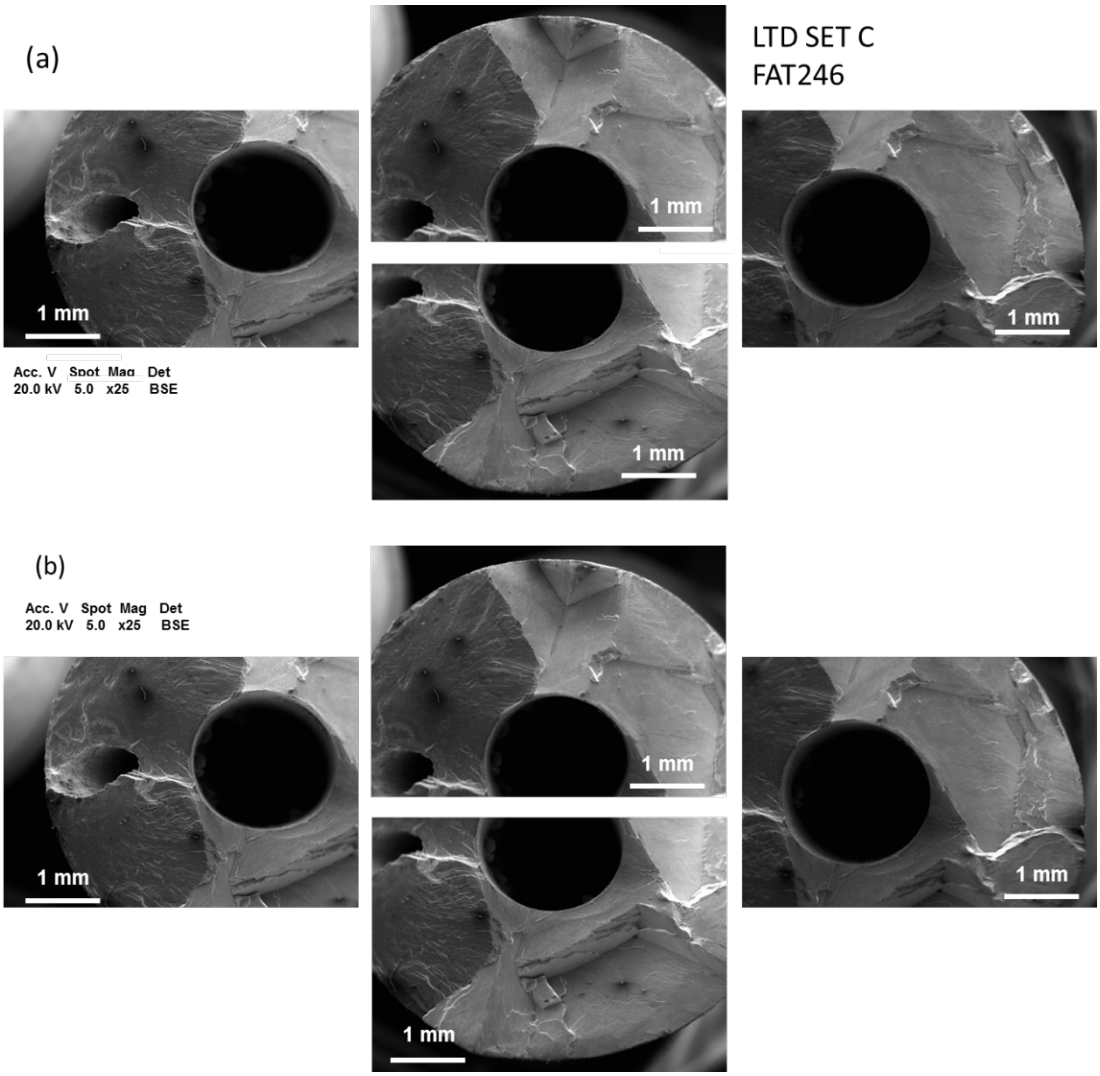

Figure C-3: Example of micrographs of fractured faces of fatigued specimen LTD 06 (FAT246): (a) right side and (b) left side.

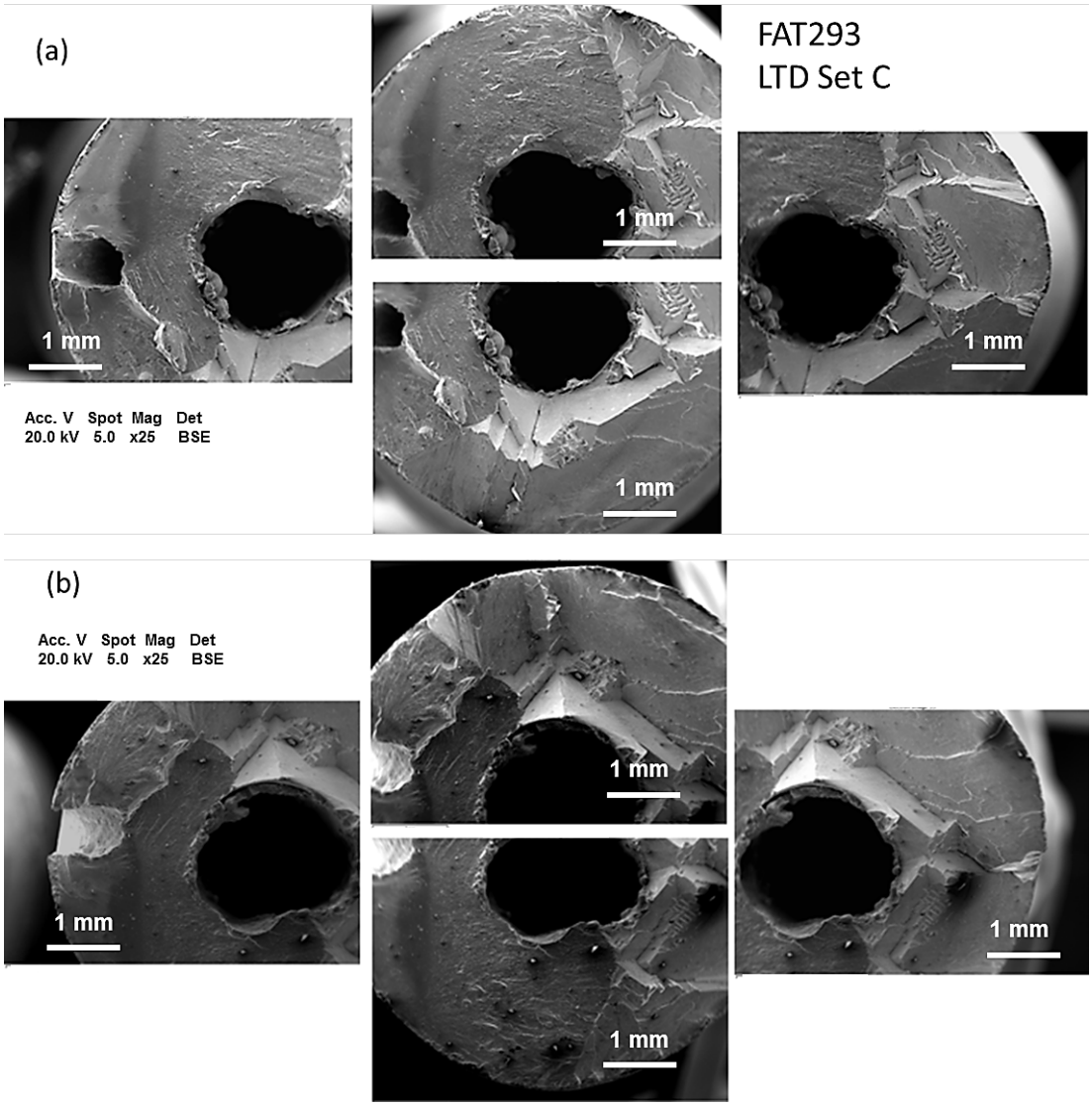

Figure C-4: Example of micrographs of fractured faces of fatigued specimen (04) FAT293: (a) right side and (b) left side.

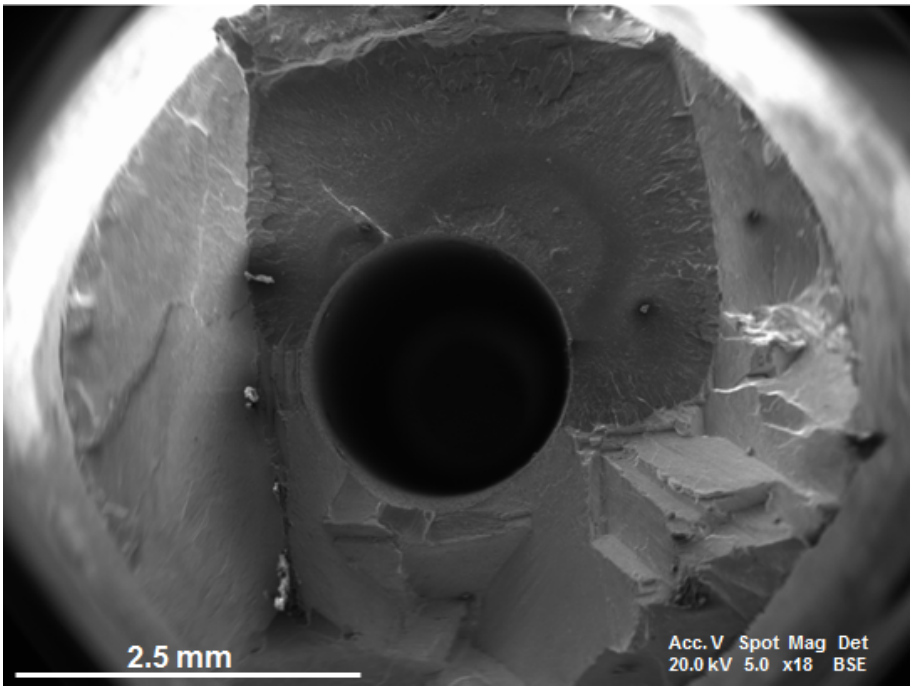

Figure C-5: Example of micrographs of fractured faces of bare CMSX-4 fatigued specimen LTD 14 (FAT311).

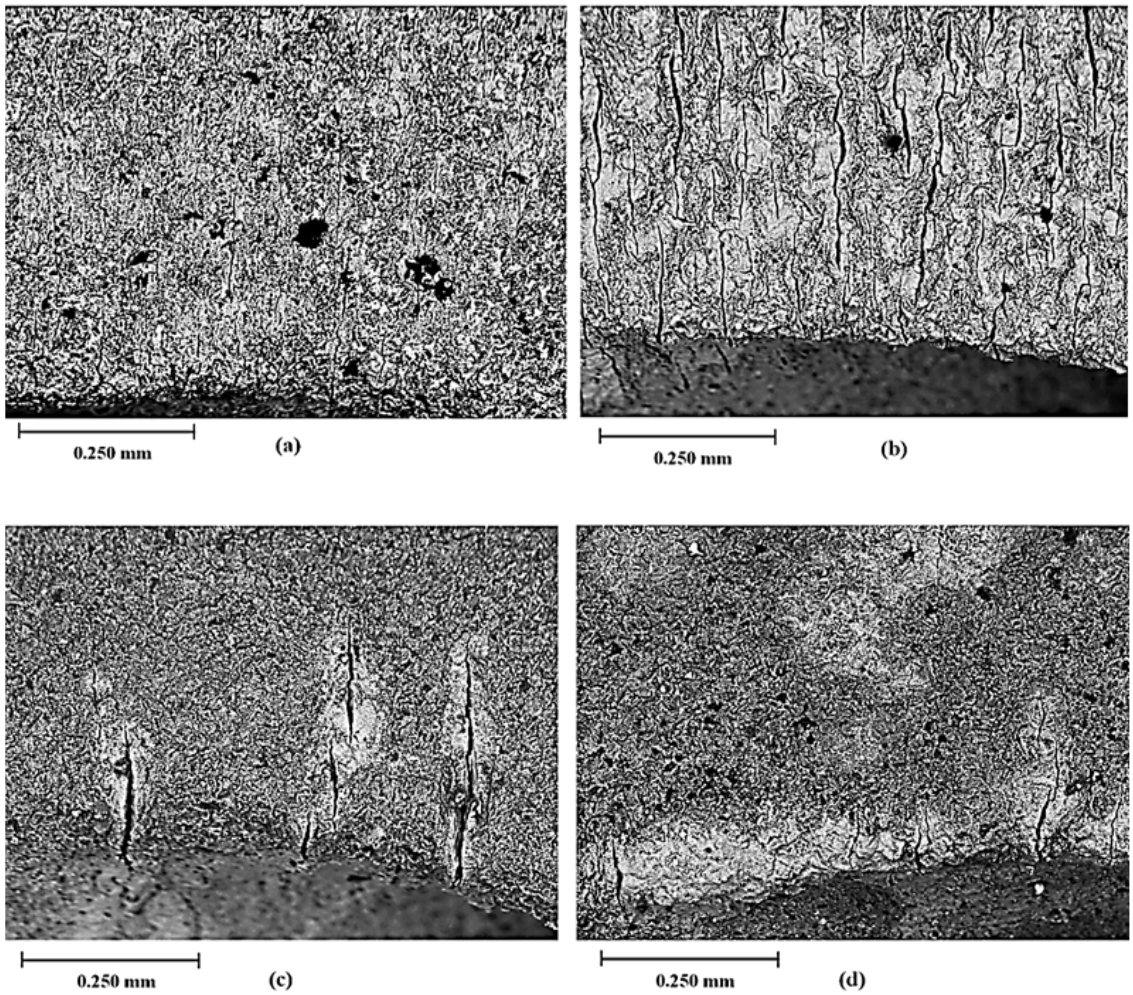

Figure C-6: Examples of surface cracks initiation from the recast in the fatigue tested specimen LTD 05 (FAT241).

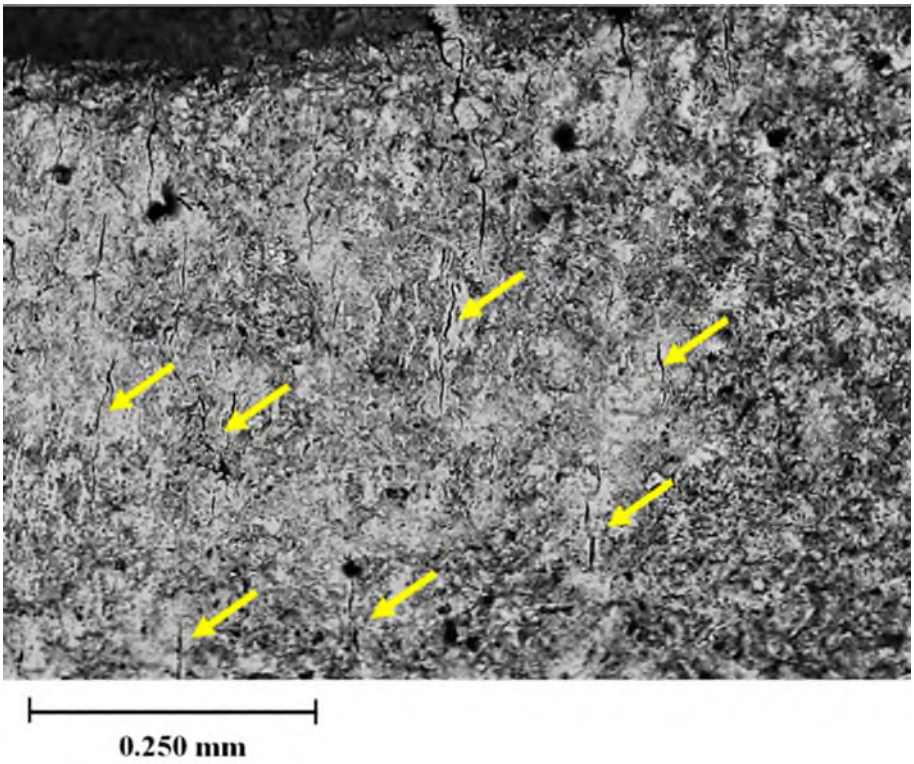

Figure C-7: Example of surface cracks formed outside the recast periphery (base alloy) in the fatigued specimen LTD 14 (FAT247).

RLT measurements on the fatigue specimens

Table C-1: RLT measurements of cross-sectioned fractured specimens, LTD set A.

RP	LTD set A					
	LTD 01			LTD 02		
	H1	H2	H3*	H1	H2	H3
1	14.43	63.3	-	22.5	27	21.6
2	51.2	35.2	-	44.4	32.4	35.2
3	53.2	32.4	-	36.9	29.8	53.24
4	45.9	43.4	-	18.9	32.4	41.8
5	43.2	37.8	-	48.5	35.3	40.5
6	29.7	51.35	-	27.3	37.8	45.9
7	40.5	48.6	-	32.4	48.6	34.5
8	81.1	42.3	-	37.8	40.5	27.1
9	37.8	51.4	-	29.7	43.3	25.2
10	27.02	35.2	-	40.5	24.3	38.7
11	51.4	48.6	-	48.6	36.5	29.735
12	72.9	62.2	-	54.5	48.6	-
13	24.3	59.5	-	13.5	40.5	-
14	32.4	78.4	-	32.4	29.7	-
15	41.5	54.05	-	-	-	-
16	63.1	67.56	-	-	-	-
RP = Reading points						
Reading points 1-8 is left side of hole (see Figure 5-10)						
Reading points 9-16 is right side of hole (see Figure 5-10)						
*= Fractured						

Table C-2: RLT measurements of cross-sectioned fractured specimens, LTD set B.

RP	LTD set B								
	LTD 08			LTD 12			LTD 11		
	H1	H2	H3*	H1	H2	H3	H4	H5	H6
1	15.9	36.1	20.7	8.1	8.3	-	10.8	40.5	8.1
2	22.7	30.5	31	13.5	16.2	-	16.2	29.7	43.5
3	28.3	36.4	26.1	16.5	17.5	-	18.9	42.4	21.6
4	29.9	40.5	48.6	19.7	21.6	-	32.4	39.2	45.9
5	40.2	31.2	46.7	32.4	18.9	-	27	37.2	40.5
6	45.3	34.3	48.6	40.5	29.7	-	45.9	41.8	45.6
7	53.7	21.6	40.5	21.6	32.4	-	51.3	48.6	29.7
8	50.3	43.2	32.4	32.4	40.5	-	21.6	32.43	48.9
9	42.3	40.5	35.3	24.3	48.2	-	35.1	*	40.5
10	45.6	27.2	40.5	27	24.3	-	22.9	*	27.02
11	32.4	43.2	44.6	14.1	16.3	-	43.2	*	49.5
12	45.9	29.7	27.1	29.7	28.6	-	21.6	*	25.6
13	37.8	19.2	43.2	21.6	43.3	-	27.1	*	22.9
14	43.5	33.9	14.4	27	-	-	40.4	*	-
15	27.1	27.6	-	24.5	-	-	-	*	-
16	46.1	43.4	-	34.2	-	-	-	*	-
17	51.4	29.7	-	28.4	-	-	-	*	-
18	48.6	-	-	37.8	-	-	-	*	-
RP = Reading points									
Reading points 1-8 is left side of hole (see Figure 5-10)									
Reading points 9-16 is right side of hole (see Figure 5-10)									
*= Fractured									

Table C-3: RLT measurements of cross-sectioned fractured specimens, LTD set C.

RP	LTD set C specimens					
	LTD 18			LTD 15		
	H1	H2	H3*	H1	H2	H3
1	13.5	46.5	20.3	43.9	42.2	44.6
2	35.1	49.2	29.7	35.8	51.4	45.9
3	37.8	38.6	41.9	35.5	42.7	62.2
4	39.2	40.5	43.2	31.1	64.9	17.4
5	45.9	41.9	56.8	51.4	44.6	41.7
6	38.4	37.3	44.6	50.3	62.2	61.6
7	40.5	50.0	56.8	54.1	69.2	65.2
8	24.3	48.6	51.4	45.9	56.8	50.0
9	20.3	39.2	56.8	51.4	63.5	39.2
10	39.2	47.3	59.5	39.2	50.0	62.2
11	35.1	50.0	55.4	50.0	48.6	58.1
12	39.9	59.5	44.6	41.9	33.8	51.4
13	54.1	33.8	50.0	31.1	36.5	66.2
14	81.1	27.0	45.9	35.1	29.7	33.8
15	-	31.1	42.2	64.5	56.8	39.2
16	-	33.8	39.2	-	39.2	78.4
17	-	24.3	31.1	-	41.1	-
18	-	32.4	33.8	-	51.4	-
19	-	35.1	75.3	-	44.6	-
20	-	56.8	82.5	-	-	-
21	-	65.7	-	-	-	-
RP = Reading points						
1/2 Reading points is the left side of hole (see Figure 5-10)						
1/2 Reading points is the right side of hole (see Figure 5-10)						
*= Fractured						

Appendix D Empirical model data

Table D-1: Predicted mean responses for ln transformed SD_{RLTmax}.

No.	Equation 7					
			95% CI		95% PI	
	Predicted	SE fit	Lower bound	Upper bound	Lower bound	Upper bound
1	3.87457	0.0343311	3.72685	4.02228	3.66426	4.08487
2	3.98772	0.0227333	3.88991	4.08554	3.80890	4.16654
3	4.35600	0.0338987	4.21015	4.50185	4.14700	4.56500
4	4.00445	0.0246507	3.89839	4.11052	3.82099	4.18792
5	4.15321	0.0225238	4.05630	4.25012	3.97488	4.33154
6	3.92165	0.0332854	3.77844	4.06487	3.71448	4.12883
7	4.22418	0.0342946	4.07662	4.37173	4.01398	4.43437
8	4.11096	0.0335258	3.96671	4.25521	3.90308	4.31885
9	4.15466	0.0332517	4.01159	4.29773	3.94759	4.36173

Table D-2: Predicted mean responses for SD_{RLTmax}.

No.	Equation 8					
			95% CI		95% PI	
	Predicted (µm)	SE fit	Lower bound (µm)	Upper bound (µm)	Lower bound (µm)	Upper bound (µm)
1	48.1988	1.56339	41.4721	54.9255	38.5748	57.8228
2	53.9413	1.00269	49.627	58.2555	45.8181	62.0645
3	77.5409	1.56339	70.814	84.2676	67.9168	87.1649
4	54.4813	1.12396	49.6453	59.3173	46.0694	62.8932
5	64.1600	1.12396	59.3240	68.9960	55.7481	72.5719
6	50.5707	1.51159	44.0668	57.0745	41.1011	60.0402
7	68.4690	1.58557	61.6468	75.2912	58.7780	78.1600
8	61.2004	1.53189	54.6093	67.7916	51.6706	70.7302
9	63.5376	1.53189	56.9464	70.1288	54.0078	73.0674

Table D-3: **Predicted mean responses for ln transformed CF_{850C}.**

No.	Batch	Equation 9					
				95% CI		95% PI	
		Predicted	SE Fit	Lower bound	Upper bound	Lower bound	Upper bound
1	LD set A	12.0106	0.285667	11.2762	12.7449	10.5320	13.4891
2	LD set A	10.3435	0.178683	9.88416	10.8028	8.98045	11.7065
3	LD set A	9.00981	0.274719	8.30362	9.71600	7.54503	10.4746
4	LD set B	13.6430	0.453940	12.4761	14.8099	11.9085	15.3775
5	LD set B	11.4790	0.283937	10.7491	12.2089	10.0026	12.9553
6	LD set B	9.74775	0.436543	8.62558	10.8699	8.04300	11.4525
7	LD set C	11.4411	0.375732	10.4753	12.4070	9.83497	13.0473
8	LD set C	9.94738	0.235019	9.34325	10.5515	8.52898	11.3658
9	LD set C	8.75239	0.361333	7.82355	9.68122	7.16821	10.3366

Table D-4: Predicted mean responses for CF_{850C}.

No.	Batch	Equation 11					
				95% CI		95% PI	
		Predicted	SE Fit	Lower bound	Upper bound	Lower bound	Upper bound
1	LD set A	170671	73424	78920.79	342799.2	37496.39	721508.9
2	LD set A	32055	22435	19617.16	49158.25	7946.207	121358
3	LD set A	8433	2080	4038.465	16580.79	1891.319	35404.71
4	LD set B	880273	119727	262000.1	2703073	148523.7	4768298
5	LD set B	100632	19864	46588.08	200566.3	22083.81	423073
6	LD set B	17810	850	5572.394	52569.95	3111.935	94136.39
7	LD set C	95032	5956	35429.5	244507.2	18675.54	463842.3
8	LD set C	21310	17026	11421.47	38234.75	5059.283	86318.57
9	LD set C	6458	2125	2498.76	16014.02	1297.52	30840.99

Table D-5: Predicted mean responses for CF_{850C} at RLT_{max} = 25 µm.

		Ln transformed						Equation 9
SD_{RLTmax} (µm)	**Stress (MPa)**	**SD_{RLTmax}**	**Stress**	**Predicted CF_{850C}**	**SE Fit**	**95 %CI Lower**	**95% CI Upper**	**Predicted CF_{850C}**
25	1050	3.22	6.96	11.60	4.122	1.006	22.197	96853.6
25	950	3.22	6.86	11.67	3.679	2.217	21.133	105178.2
25	850	3.22	6.75	11.70	3.227	3.496	20.088	115271.6
25	750	3.22	6.62	11.82	2.602	5.128	18.506	127792.7
25	650	3.22	6.48	11.97	2.056	6.687	17.259	143783.1
25	550	3.22	6.31	12.08	1.377	8.542	15.62	164998.5
25	450	3.22	6.11	12.27	0.8702	10.0357	10.0357	194661.6
25	350	3.22	5.86	12.46	1.238	9.275	15.639	239442.4

Table D-6: Predicted mean responses for CF_{850C} at RLT_{max} = 35 µm.

		Ln transformed						Equation 9
SD_{RLTmax} (µm)	**Stress (MPa)**	**SD_{RLTmax}**	**Stress**	**Predicted CF_{850C}**	**SE Fit**	**95 %CI Lower**	**95% CI Upper**	**Predicted CF_{850C}**
35	1050	3.56	6.96	9.832	2.983	2.164	17.5	15057.7
35	950	3.56	6.86	10.038	2.656	3.21	16.867	18977.5
35	850	3.56	6.75	10.333	2.357	4.274	16.39	24541.9
35	750	3.56	6.62	10.534	1.883	5.694	15.373	32777.0
35	650	3.56	6.48	10.911	1.518	7.01	14.812	45628.9
35	550	3.56	6.31	11.284	1.033	8.628	13.941	67136.5
35	450	3.56	6.11	11.7415	0.6245	10.1362	13.3468	106764.8
35	350	3.56	5.86	12.3239	0.8017	10.2632	14.3847	190872.3

Table D-7: Predicted mean responses for CF_{850C} at RLT_{max} = 50 µm.

		Ln transformed						Equation 9
SD_{RLTmax} (µm)	Stress (MPa)	SD_{RLTmax}	Stress	Predicted CF_{850C}	SE Fit	95 %CI Lower	95% CI Upper	Predicted CF_{850C}
50	1050	3.91	6.96	7.696	1..605	3.57	11.822	2093.5
50	950	3.91	6.86	8.079	1.427	4.411	11.747	3089.6
50	850	3.91	6.75	8.505	1.236	5.329	11.682	4761.6
50	750	3.91	6.62	8.9284	0.9533	6.4778	11.379	7747.3
50	650	3.91	6.48	9.527	0.7619	7.5684	11.4855	13515.8
50	550	3.91	6.31	10.1654	0.4919	8.9009	11.4298	25881.5
50	450	3.91	6.11	10.9321	0.3271	10.0912	11.7729	56482.5
50	350	3.91	5.86	11.9125	0.5453	10.5108	13.3142	150097.3

Table D-8: Predicted mean responses for CF_{850C} at RLT_{max} = 65 µm.

		Ln transformed						Equation 9
SD_{RLTmax} (µm)	**Stress (MPa)**	**SD_{RLTmax}**	**Stress**	**Predicted CF_{850C}**	**SE Fit**	**95 %CI Lower**	**95% CI Upper**	**Predicted CF_{850C}**
65	1050	4.17	6.96	6.1632	0.8917	3.8711	8.4554	490.4
65	950	4.17	6.86	6.6793	0.7942	4.6378	8.7207	812.9
65	850	4.17	6.75	7.238	0.685	5.4772	8.9989	1425.3
65	750	4.17	6.62	7.8381	0.5435	6.441	9.2351	2681.4
65	650	4.17	6.48	8.5694	0.4173	7.4966	9.6421	5522.8
65	550	4.17	6.31	9.3847	0.28	8.665	10.1043	12837.5
65	450	4.17	6.11	10.4167	0.2151	9.8636	10.9697	35360.2
65	350	4.17	5.86	11.7067	0.3447	10.8207	12.5927	125776.7

Table D-9: Predicted mean responses for CF_{850C} at RLT_{max} = 75 µm.

SD_{RLTmax} (µm)	Stress (MPa)	Ln transformed						Equation 9
		SD_{RLTmax}	Stress	Predicted CF_{850C}	SE Fit	95 %CI Lower	95% CI Upper	Predicted CF_{850C}
75	1050	4.32	6.96	5.5699	0.8376	3.4168	7.7231	222.2
75	950	4.32	6.86	6.1302	0.7456	4.2137	8.4067	392.4
75	850	4.32	6.75	6.7774	0.6453	5.1186	8.4362	738.2
75	750	4.32	6.62	7.4217	0.5309	6.057	8.7864	1503.3
75	650	4.32	6.48	8.2856	0.4081	7.2365	9.3347	3389.7
75	550	4.32	6.31	9.1894	0.2724	8.4893	9.8895	8757.8
75	450	4.32	6.11	10.3099	0.1814	9.8434	10.7763	27388.9
75	350	4.32	5.86	11.7768	0.3004	11.0046	12.549	114215.8

Table D-10: Predicted mean responses for CF_{850C} at RLT_{max} = 85 µm.

SD_{RLTmax} (µm)	Stress (MPa)	Ln transformed						Equation 9
		SD_{RLTmax}	Stress	Predicted CF_{850C}	SE Fit	95 %CI Lower	95% CI Upper	Predicted CF_{850C}
85	1050	4.44	6.96	4.706	1.07	1.956	7.456	111.2
85	950	4.44	6.86	5.3548	0.9437	2.929	7.7806	207.5
85	850	4.44	6.75	6.0463	0.8182	3.9431	8.1494	415.2
85	750	4.44	6.62	6.779	0.7205	4.9269	8.6311	906.2
85	650	4.44	6.48	7.7314	0.5256	6.3802	9.0826	2211.8
85	550	4.44	6.31	8.7236	0.3964	7.7046	9.7426	6267.9
85	450	4.44	6.11	9.9767	0.2535	9.3251	10.6284	21904.9
85	350	4.44	5.86	11.5764	0.3261	10.738	12.4147	104978.6